LEPTONIC DECAYS
AND
KAON IDENTIFICATION
AT THE NA62 EXPERIMENT AT CERN

by

Angela Romano

Thesis submitted to
the University of Birmingham
for the degree of
Doctor of Philosophy

Supervisors:

Dr. Cristina Lazzeroni
Dr. Evgueni Goudzovski

Particle Physics Group

School of Physics and Astronomy
The University of Birmingham
December 2012

Abstract

A study of the radiative leptonic $K^+ \to e^+ \nu_e \gamma$ kaon decay is reported, using a partial sample of data collected by the NA62 experiment at CERN in 2007. The signal event selection, the study of trigger efficiencies and the measurement of form factors are presented. The main systematic uncertainties associated to the analysis are discussed and preliminary results on form factor parameters are obtained:

$$V_0 = 0.0946 \pm 0.0018_{stat} \pm 0.0170_{syst}$$
$$\lambda = 0.521 \pm 0.055_{stat} \pm 0.052_{syst}$$

with a statistical correlation between parameters of -0.94 and $\sim 100\%$ correlation between systematic errors.

The outcome of a test run performed at CERN in October 2011 for the commissioning of a Cherenkov differential counter to be used for the charged kaon identification in the near-future NA62 research programme, is reported. The counter's ability to distinguish between kaons and pions is validated by pressure scan results. Tests of various combinations of standard and new read-out technology and electronics are presented. The time resolution of the new photon detector technology (Hamamatsu R7400-U03 PMT) to be replaced for the detector upgrade in NA62 is measured:

$$\sigma_T = (251 \pm 2)\text{ps} \ .$$

Declaration

I declare that the dissertation is my own work, unless otherwise specified; whereas contributions are coming from other people, explicit references are used. No other qualifications have been achieved with the work reported in here.

To my dear family and lovely friends..

Contents

List of Tables

List of Figures

ix

xviii

Introduction

Kaon physics plays an important role in the comprehension of the flavour structure of the Standard Model (SM). The study of kaon decays allows the exploring of a wide range of flavour physics: some examples are quark mixing, charge-parity (CP) violation, the suppression of flavour-changing neutral currents (FCNC) and lepton flavour violation (LFV). Since the discovery of kaons, the studies of kaon decays have helped in shaping the SM, unravelling the underlying symmetries and dynamics of interactions in the flavour sector. Due to the interplay between strong, electromagnetic and weak dynamics, kaon decays have a large sensitivity and can provide stringent tests of weak interactions universality and quantum chromodynamics (QCD).

The work accomplished for this PhD thesis has been carried out within the NA62 fixed-target experiment at CERN. NA62 represents the current kaon physics research programme at CERN and it is a third upgrade of the NA48 detector located in the *Super Proton Synchroton* (SPS) north area. The NA62 research programme had a preliminary phase devoted to a precision test of Lepton Flavour Universality (LFU) [1] but its main purpose is the study of the ultra-rare kaon $K^+ \to \pi^+ \nu \bar{\nu}$ decay. During the former phase, in 2007, data were collected with the beam line and setup from the predecessor NA48/2 experiment to measure the ratio R_K of charged kaon leptonic decay rates: $K \to e\nu_e/K \to \mu\nu_\mu$. Exploiting the same data set, the study of other interesting kaon decay channels came as a by-products. The latter phase, currently undergoing, foresees a technical run with almost 70% of the NA62 detector layout in place (October 2012); the final data taking is scheduled in about two years from this run.

The PhD thesis is organised into two parts: one describes the study of the radiative leptonic $K^+ \to e^+\nu_e\gamma$ (SD$^+$) kaon decay performed with the data collected by NA62 in 2007, and one refers to the current research and development status of the NA62 detector. The first chapter combines the underlying theoretical frameworks: the Chiral Perturbation Theory (χPT) for the description of low-energy hadronic dynamics, which dominates in $K^+ \to e^+\nu_e\gamma$ (SD$^+$), and the theoretical mechanism of suppressed high-order quantum loop interactions (penguin and box diagrams), which describe

1

the $K^+ \to \pi^+ \nu \bar{\nu}$ decay. The second chapter gives a description of the NA48/2 beam line, experimental apparatus and data acquisition system with particular care to the sub-detectors involved in the $K^+ \to e^+ \nu_e \gamma$ (SD$^+$) analysis. In the third chapter the signal event selection, the study of trigger efficiencies and the measurement of form factors are presented; a study of the main systematic uncertainties associated with the analysis and the preliminary results on form factors are shown. The fourth chapter introduces the second part of the thesis with an overview of the NA62 beam line and detector; the strategy for the measurement of the branching ratio BR($K^+ \to \pi^+ \nu \bar{\nu}$) is presented here. The fifth chapter focuses on a Cherenkov differential detector to be used for both the $K^+ \to \pi^+ \nu \bar{\nu}$ event reconstruction and the background suppression. The principle of operations of the detector and a simulation of the readout system are discussed; some tests of the technology for the Cherenkov photon detection are illustrated. The last chapter reports the procedures and findings of a test run performed at CERN in October 2011 for the Cherenkov detector commissioning: the counter ability to distinguish between kaons and pions is validated. Tests of various combinations of standard and new read-out technology and electronics are presented. The detector performance in terms of kaon identification efficiency ($> 95\%$) and time resolution ($\sim 100 \, \mathrm{ps}$) is discussed.

Chapter 1

Theoretical framework

Depending on the type of particles produced in a kaon decay, it is possible to distinguish between several overlapping categories such as: leptonic, semi-leptonic and hadronic decays. The QCD, describing strong interactions between quarks and gluons in the Standard Model (SM), has a non-perturbative nature below the energy scale of the chiral symmetry breaking ($E \ll \Lambda_\chi \sim 1\,\text{GeV}$). The dynamics of these low-energy hadronic interactions can be studied in an appropriate theoretical framework (Chiral Perturbation Theory - χPT [2, 3]), which provides a parameterisation of the strong interactions in terms of momenta and light meson masses using a small number of unknown coupling constants, the so-called low-energy constants (LECs). χPT is an effective low-energy theory of the SM which allows to extract predictions on many kaon decays, including rare and radiative modes. An overview of χPT can be found in [4–7].

By definition, radiative leptonic kaon decays involve leptons and photons in the final state. Similarly to the approach described above, the decay amplitude for electroweak interactions is expanded in terms of momenta and quark masses. To obtain reliable predictions from χPT, the expansion parameters need to be small compared to the physical scale of the chiral symmetry breaking. This is indeed the case for kaon decays because $m_K < 1\,\text{GeV}$. The quality of χPT predictions relies to a large extent on the knowledge of the LECs involved in the parameterisation of the interactions. In radiative leptonic kaon decays the corresponding LECs, up to $\mathcal{O}(p^4)$, have already been experimentally determined. As a consequence, high precision has been achieved in the theoretical predictions for a large number of channels; this makes these processes worth investigating and enhances their potential to catch sight of new physics (NP). As an example, the study of lepton polarisation effects, depending on the vector

and axial-vector form factors of the structure-dependent parts, can lead to indirect evidence of physics beyond the SM [8,9].

1.1 The $K^+ \to e^+ \nu_e \gamma$ decay
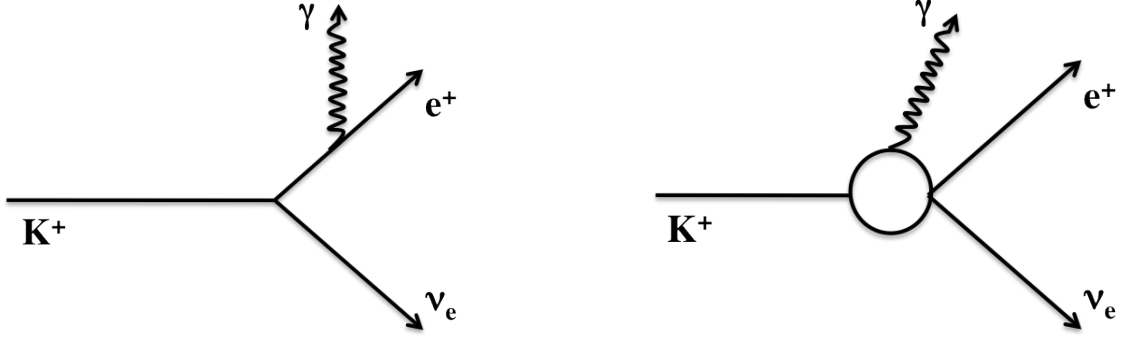
Figure 1.1: Feynman diagrams contributing to the $K^+ \to e^+ \nu_e \gamma$ process: "Inner Bremsstrahlung" (left) and "Structure Dependent" (right).

The $K^+ \to e^+ \nu_e \gamma$ ($K^+_{e2\gamma}$) process receives three contributions to the total decay amplitude: "Inner Bremsstrahlung" (IB), "Structure Dependent" (SD) and a term of interference INT between the IB and SD components [10, 11]. The Feynman diagrams contributing to the process $K^+_{e2\gamma}$ are shown in Fig. 1.1. The IB part is purely electromagnetic as the photon is emitted by the positron via bremsstrahlung. At the lowest order this component can be predicted from the non-radiative K^+_{e2} amplitude [12]. The SD part receives electro-weak and hadronic contributions and is sensitive to the kaon structure: the effective kaon coupling to the photon proceeds through vector and axial-vector currents, which are parameterised in terms of vector and axial-vector form factors (F_V, F_A). The kaon is spin-less so that the coupling depends only on the momentum transfer $p = p_K - q$, where p_K and q are the kaon and photon four-momenta. In order for the corresponding matrix element to be Lorentz invariant the coupling is a function of the Lorentz scalar $p^2 = (p_K - q)^2$, thus implying a p^2-dependence for (F_V, F_A). Depending on the polarisation of the radiative photon two SD components can be distinguished[1]: one with positive photon helicity (SD$^+$, sensitive to $F_V + F_A$ couplings) and one with negative (SD$^-$, sensitive to $F_V - F_A$ couplings). Their corresponding interference terms with IB are denoted as INT$^+$ and INT$^-$. Terms of given helicity may

---

[1]There is no interference term between the two SD components.

be disentangled from kinematical analysis and lead to a deeper understanding of the kaon structure. Predictions for $F_V(p^2)$ and $F_A(p^2)$ exist from low-energy systematic operator expansion (χPT up to the next-to-next-to-leading order [13], for example vector meson dominance (VMD) and chiral constituent quark model (CQM)) and from other specific models (like light front quark model (LFQM) [9]). The $K^+_{e2\gamma}$ analysis presented in this thesis has the potential to reach an accuracy ~ 5 times better than the current experimental status. From the theoretical point of view, the importance of the $K^+_{e2\gamma}$ decay measurement is that it allows a quantitative comparison of the theoretical predictions. Moreover, it might also be useful for future experiments for which $K^+_{e2\gamma}$ is a source of background.

1.1.1 Matrix elements and form factors

Let us consider the $K^+_{e2\gamma}$ process:

$$K^+(p_K) \to e^+(p_e)\nu_e(p_\nu)\gamma(q), \tag{1.1}$$

where p_K, p_e, p_ν and q are the four-momenta of K^+, e^+, ν_e and the photon, respectively; γ is real with $q^2 = 0$. The matrix element $\mathcal{M}$ can be written in terms of IB and SD contributions [4,9,11]:

$$\mathcal{M} = \mathcal{M}_{IB} + \mathcal{M}_{SD}, \tag{1.2}$$

$$\mathcal{M}_{IB} = ie\frac{G_F}{\sqrt{2}}V^*_{us}F_K\epsilon^*_\mu K^\mu, \tag{1.3}$$

$$\mathcal{M}_{SD} = -ie\frac{G_F}{\sqrt{2}}V^*_{us}\epsilon^*_\mu H^{\mu\nu}L_\nu, \tag{1.4}$$

with

$$K^\mu = m_e\bar{u}(p_\nu)(1+\gamma_5)\left(\frac{2p^\mu_K}{2p_K\cdot q} - \frac{2p^\mu_e + \slashed{q}\gamma^\mu}{2p_e\cdot q}\right)v(p_e), \tag{1.5}$$

$$H^{\mu\nu} = i\frac{F_V(p^2)}{m_K}\epsilon^{\mu\nu\alpha\beta}q_\alpha(p_K)_\beta - \frac{F_A(p^2)}{m_K}(q\cdot pg^{\mu\nu} - p^\mu q^\nu), \tag{1.6}$$

$$L_\mu = \bar{u}(p_\nu)\gamma_\mu(1-\gamma_5)v(p_e), \tag{1.7}$$

$$p^\mu = (p_K - q)^\mu = (p_e + p_\nu)^\mu. \tag{1.8}$$

The coupling constants appearing in both IB and SD terms are the electron charge e, the Fermi constant G_F and the Cabibbo-Kobayashi-Maskawa (CKM) matrix element V_{us}; these come from the electro-weak decay structure and the transition between u and $\bar{s}$ quark states embedded into the K^+ meson. The photon polarisation vector ϵ_μ

satisfies the gauge condition $q^\mu \epsilon_\mu = 0$ and the leptonic states (outgoing positron and neutrino) are described by the spinors $u(p_\nu)$, $v(p_e)$.

The IB matrix element ($\mathcal{M}_{\mathcal{IB}}$) is factorized into the kaon decay constant F_K and a leptonic charged weak current K^μ between the positron and the neutrino in the final state. The kaon structure is embedded into F_K, while p_K contributes to K^μ as a point-like particle in electro-weak interactions. For the computation of this term the covariant form of Dirac equations for the positron and neutrino fermionic states are used: $(\not{p}_e - m_e)v(p_e) = 0$ and $\bar{u}(p_\nu)\not{p}_\nu = 0$, where $\not{p} = \gamma_\mu p^\mu$ is the usual contraction between the Dirac gamma matrices (γ_μ) [14] and four-vectors. The positron equation gives the electron mass m_e in $\mathcal{M}_{\mathcal{IB}}$. The gamma matrices γ_μ, with $\mu = 0, 1, 2, 3$, allow to define the function $\bar{u} \equiv u^\dagger \gamma_0$, where $u^\dagger$ represents the hermitian conjugate, and the matrix $\gamma_5 = i\gamma_0\gamma_1\gamma_2\gamma_3$. The definition of $\not{q}$ is the same as for $\not{p}$.

The SD matrix element ($\mathcal{M}_{\mathcal{SD}}$) contains an antisymmetric tensor $H^{\mu\nu}$ acting on a leptonic charged weak current L_ν; the former is parameterised in terms of the form factors $F_V(p^2)$ and $F_A(p^2)$. The transferred momentum p has been defined above; m_K is the kaon mass; $\epsilon^{\mu\nu\alpha\beta}$ and $g^{\mu\nu}$ are metric tensors running on four-vector components. The dot (or scalar) product between four-vectors is defined as the sum over repeated indices: $q \cdot p = q^\mu p_\mu$. The contravariant form of a vector is obtained from its covariant form as follows: $q^\mu = g^{\mu\nu}q_\nu$. Both K^μ and L_ν show the vector and axial-vector ($V \pm A$) structure which characterises the weak currents; this translates into the presence of $(1 \pm \gamma_5)$ projection operators encoding the parity violation.

Theoretical predictions for the IB part do not depend on a specific model. The SD part depends on F_A and F_V, which are analytical functions of p^2 in the physical allowed region: $m_e^2 \leq p^2 \leq m_K^2$. At the leading order in χPT (tree level), which from previous considerations is $\mathcal{O}(p^2)$, both form factors do not contribute ($F_A = F_V = 0$) and the only non-vanishing term of the amplitude comes from $\mathcal{M}_{\mathcal{IB}}$ [15]. At next-to-leading order in χPT (one-loop level), which corresponds to $\mathcal{O}(p^4)$ because the chiral counting proceeds in double powers of p, the predictions still rule out any dependence on p^2 and both form factors are constant:

$$
\begin{aligned}
F_A &= \frac{4\sqrt{2}m_K}{F_K}(l_9^r + l_{10}^r), \\
F_V &= \frac{m_K}{4\sqrt{2}F_K\pi^2},
\end{aligned}
\tag{1.9}
$$

where l_9^r and l_{10}^r are renormalised low-energy couplings [4]. At next-to-next-to-leading order in χPT (two-loop level), corresponding to $\mathcal{O}(p^6)$, the form factors exhibit a dependence on p^2: more renormalised low-energy couplings (up to 100) and additional

terms in p^2 are used in the explicit expression of the form factors, which can be summarised as follows:

$$F_A(p^2) = \frac{4\sqrt{2}m_K}{F_K}(l_9^r + l_{10}^r) + C_A + C_A' p^2,$$

$$F_V(p^2) = \frac{m_K}{4\sqrt{2}F_K\pi^2} + C_V + C_V' p^2. \tag{1.10}$$

The first terms entering Eqs. 1.10 correspond to the χPT predictions at $\mathcal{O}(p^4)$ (Eqs. 1.9), while $C_{A,V}$ and $C_{A,V}'$ are constants including the renormalised low-energy couplings used in the chiral expansion at $\mathcal{O}(p^6)$. A detailed computation of both form factors in χPT at $\mathcal{O}(p^6)$ is reported in [13]. The numerical predictions of $F_{A,V}$ in χPT at $\mathcal{O}(p^4)$ and $\mathcal{O}(p^6)$, as well as in LFQM, are reported in the next section.

1.1.2 Kinematics

In order to describe the kinematics of the $K_{e2\gamma}^+$ decay, two dimensionless Lorentz-invariant variables are introduced [15]:

$$x = \frac{2p_K \cdot q}{m_K^2}, \quad y = \frac{2p_K \cdot p_e}{m_K^2}. \tag{1.11}$$

These variables satisfy the following constraints:

$$0 \leq x \leq 1 - r_e, \quad 1 - x + \frac{r_e}{1 - x} \leq y \leq 1 + r_e,$$

where $r_e = m_e^2/m_K^2$. The relation between the momentum transfer p^2 and x is:

$$p^2 = m_K^2(1 - x). \tag{1.12}$$

In the kaon rest frame, x (y) is proportional to the photon (positron) energy:

$$x = \frac{2E_\gamma^*}{m_K}, \quad y = \frac{2E_e^*}{m_K}. \tag{1.13}$$

The partial decay rate for $K_{e2\gamma}^+$ can be written as [16]:

$$d\Gamma(K_{e2\gamma}^+) = \frac{1}{(2\pi)^3}\frac{1}{8m_K}|\mathcal{M}|^2 dE_\gamma^* dE_e^*,$$

where $\mathcal{M}$ is defined in Eq. 1.2. Using Eqs. 1.3-1.8 and 1.13 one can obtain the double differential decay rate of $K_{e2\gamma}^+$ in the kaon rest frame:

$$\frac{d^2\Gamma(K_{e2\gamma}^+)}{dxdy} = \frac{m_K^5}{64\pi^2}\alpha G_F^2|V_{us}|^2(1 - \lambda)A(x,y), \tag{1.14}$$

7

where $\lambda = (x + y - 1 - r_e)/x$ and $\alpha = e^2/4\pi$ is the fine-structure constant. The amplitude $A(x, y)$ can be written as the sum of the contributions [9]:

$$A(x, y) = A_{IB}(x, y) + A_{SD\pm}(x, y) + A_{INT\pm}(x, y),$$

$$A_{IB}(x, y) = \frac{4 r_e |F_K|^2}{m_K^2 \lambda x^2} \left[x^2 + 2(1 - r_e) \left(1 - x - \frac{r_e}{\lambda} \right) \right], \qquad (1.15)$$

$$A_{SD^+}(x, y) = |F_V + F_A|^2 \frac{x^2 \lambda^2}{1 - \lambda} \left(1 - x - \frac{r_e}{\lambda} \right), \qquad (1.16)$$

$$A_{SD^-}(x, y) = |F_V - F_A|^2 x^2 (y - \lambda), \qquad (1.17)$$

$$A_{INT^+}(x, y) = -\frac{4 r_e}{m_K} Re \left[F_K (F_V + F_A)^* \right] \left(1 - x - \frac{r_e}{\lambda} \right), \qquad (1.18)$$

$$A_{INT^-}(x, y) = \frac{4 r_e}{m_K} Re \left[F_K (F_V - F_A)^* \right] \left(\frac{1 - y + \lambda}{\lambda} \right). \qquad (1.19)$$

Due to the smallness of the electron mass, the contributions to the decay rate from INT$^\pm$ (Eqs. 1.18-1.19) are negligible. The IB and SD$^\pm$ contributions to the differential decay rate are represented as functions of x and y in Fig. 1.2; the distributions are obviously different and, in principle, one can determine the rate of each term by choosing the appropriate kinematical region of observation.
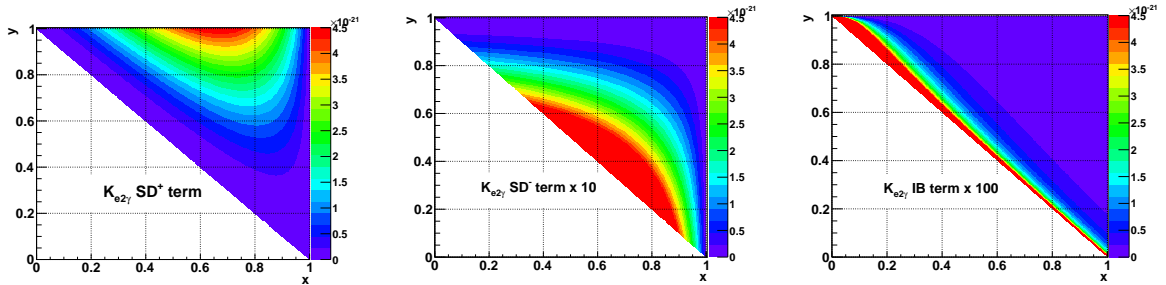
Figure 1.2: Contributions to the differential decay rate $d^2\Gamma(K_{e2\gamma}^+)/dxdy$ (expressed in GeV) from the SD$^+$ (left), SD$^-$ (centre) and IB (right) terms at $\mathcal{O}(p^6)$ in χPT .

1.1.3 Form factor predictions

Figure 1.3 shows the dependence of the form factors $F_V(p^2)$ and $F_A(p^2)$ on the transferred momentum, as predicted by χPT at order $\mathcal{O}(p^4)$, $\mathcal{O}(p^6)$ and LFQM. As already mentioned, χPT at $\mathcal{O}(p^4)$ predicts constant form factors, while at $\mathcal{O}(p^6)$ the form factors exhibit a p^2 dependence. In particular, in the framework of χPT at $\mathcal{O}(p^6)$, F_A predictions show a small (negligible) dependence on p^2 ($F_A(p^2) \simeq F_A(0)$), while

for F_V a significant slope (linear dependence) on p^2 (or equivalently on x, see Eq. 1.12) is predicted [9]:

$$F_V(x) = F_V(0) \cdot [1 + \lambda(1 - x)] . \tag{1.20}$$

In the LFQM the x dependence is more complex [9].

Model	$F_V(p^2 = 0)$	$F_A(p^2 = 0)$
$\mathcal{O}(p^4)$	0.0945	0.0425
$\mathcal{O}(p^6)$	0.082	0.034
LFQM	0.106	0.036

Table 1.1: The $K^+_{e2\gamma}$ form factors at $p^2 = 0$ in χPT at $\mathcal{O}(p^4)$, $\mathcal{O}(p^6)$ and LFQM [9].

χPT predictions at $\mathcal{O}(p^6)$ can use alternative models for the coefficients of the chiral expansion, such as the vector meson dominance (VMD) and the chiral constituent quark model (CQM) [17]. The former describes the dynamics of interactions below the chiral breaking scale with the exchange of a vector meson. The latter relies on the assumption that the vertices are associated with quark constituent loops. The χPT predictions at $\mathcal{O}(p^6)$ presented throughout this chapter are based on the VMD model, unless specified otherwise.

Theoretical predictions for the form factors $F(0)$ in the various models are summarised in Tab. 1.1. Fig. 1.4 shows the vector form factor F_V as a function of the momentum transfer p^2: the dotted line corresponds to the χPT predictions at $\mathcal{O}(p^4)$;
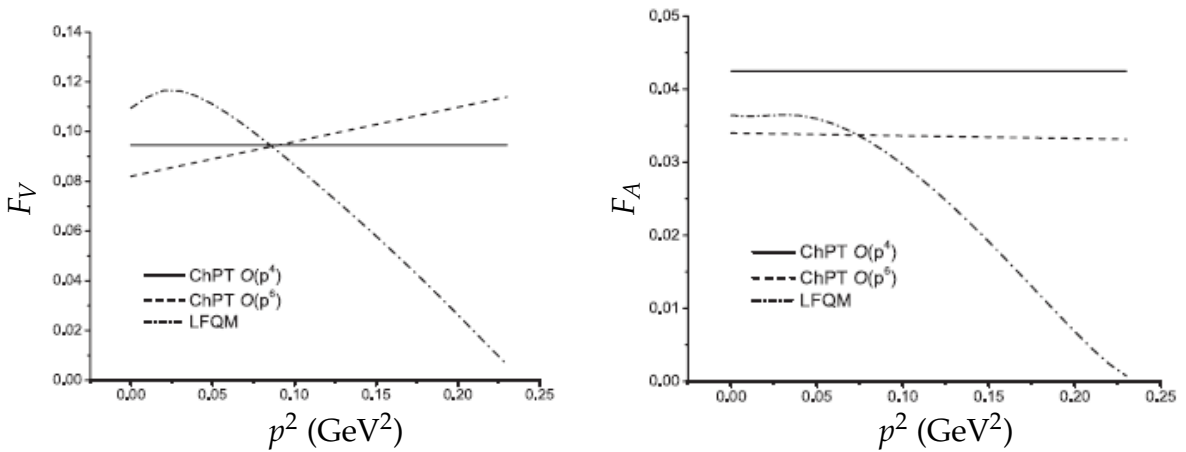
Figure 1.3: Theoretical predictions in χPT at $\mathcal{O}(p^4)$, $\mathcal{O}(p^6)$ and LFQM for F_V (left) and F_A (right) as a function of the squared momentum transfer [9].

the solid line represents the χPT predictions at $\mathcal{O}(p^6)$; the dashed line shows the χPT predictions at $\mathcal{O}(p^6)$ in the CQM model[2].
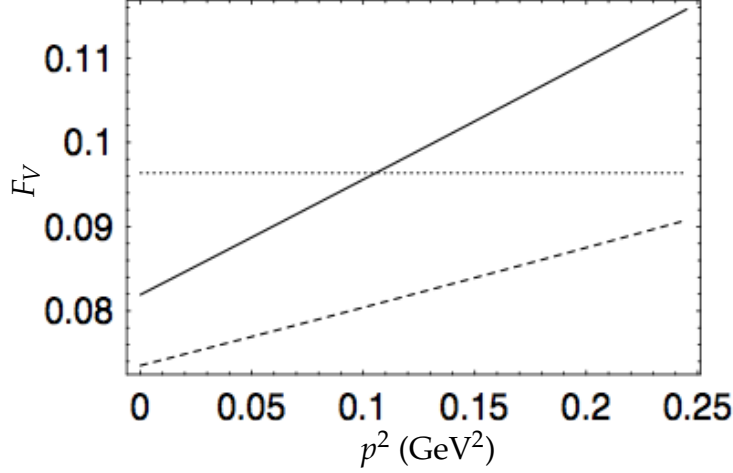
Figure 1.4: The form factor F_V as a function of the momentum transfer p^2 for $K_{e2\gamma}^+$. Dotted, solid and dashed lines are the χPT predictions at $\mathcal{O}(p^4)$, $\mathcal{O}(p^6)$ in the VMD model and $\mathcal{O}(p^6)$ in the CQM model, respectively [13].

The theoretical errors on the form factors are not quoted in [9, 13]; an estimate of the uncertainties in the framework of χPT can be found in [19] and is reported in Tab. 1.2. The central values for $F_V(0)$ and λ are obtained from Fig. 1.4 and correspond to the mean values between χPT predictions at $\mathcal{O}(p^6)$ in VMD and CQM models. The corresponding errors for $F_V(0)$ and λ are taken as half of the difference between the two models shown in Fig. 1.4. The central values for $F_V(0) \pm F_A(0)$ are computed using $F_A(0)$ as predicted in χPT at $\mathcal{O}(p^6)$ from Tab. 1.1. Their uncertainty is evaluated by using different computations for the low-energy constants entering the chiral lagrangian [19].

1.1.4 Branching ratio of $K_{e2\gamma}^+$

The differential branching ratio (BR) of $K_{e2\gamma}^+$ as a function of x can be obtained from Eq. 1.14:

$$
\begin{aligned}
\frac{dBR(K_{e2\gamma}^+)}{dx} &= \frac{1}{\Gamma_{tot}(K^+)} \frac{d\Gamma(K_{e2\gamma}^+)}{dx} \\
&= \frac{1}{\Gamma_{tot}(K^+)} \int_{1-x}^{1} \frac{d^2\Gamma(K_{e2\gamma}^+)}{dxdy} dy
\end{aligned}
\tag{1.21}
$$

---

[2]The dotted and solid lines in Fig. 1.4 can be directly compared with the solid and dashed theoretical predictions in Fig. 1.3 (left panel).

Form factor	χPT estimation
$F_V(0)$	0.078 ± 0.005
λ	0.3 ± 0.1
$F_V(0) + F_A(0)$	0.112 ± 0.005
$F_V(0) - F_A(0)$	0.044 ± 0.010

Table 1.2: Theoretical estimation of the form factors and their uncertainties in the χPT framework as reported in [19]. Errors are assigned by using different computations for the low-energy constants entering the chiral lagrangian.

where $\Gamma_{tot}(K^+)$ is the kaon total decay width [16]. The contributions to $\frac{dBR(K^+_{e2\gamma})}{dx}$ from SD (χPT at $\mathcal{O}(p^6)$) and IB terms are presented in Fig. 1.5.
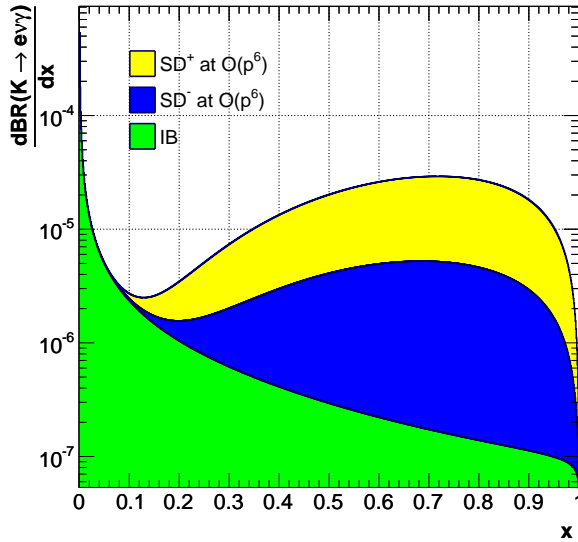
Figure 1.5: Spectra of differential branching ratio of $K^+_{e2\gamma}$ as functions of x for SD (χPT $O(p^6)$) and IB terms (logarithmic scale). The contributions from $\text{INT}^\pm$ are not plotted as they are vanishingly small ($10^{-5} < \text{BR}_{\text{INT}^\pm}/\text{BR}_{\text{SD}^\pm} < 10^{-2}$).

Fig. 1.6 shows the predictions for the total $\frac{dBR(K^+_{e2\gamma})}{dx}$ versus x in LFQM (dashed-dotted line), in χPT at $\mathcal{O}(p^4)$ (solid line) and $\mathcal{O}(p^6)$ (dashed line). All contributions from IB, $\text{SD}^\pm$ and $\text{INT}^\pm$ are considered. The numerical predictions of $\text{BR}(K^+_{e2\gamma})$, calculated by integrating over the variable x, for the single components IB, $\text{SD}^\pm$, $\text{INT}^\pm$ and their sum in χPT at $\mathcal{O}(p^4)$ and $\mathcal{O}(p^6)$, as well as in the LFQM are reported in Tab. 1.3.
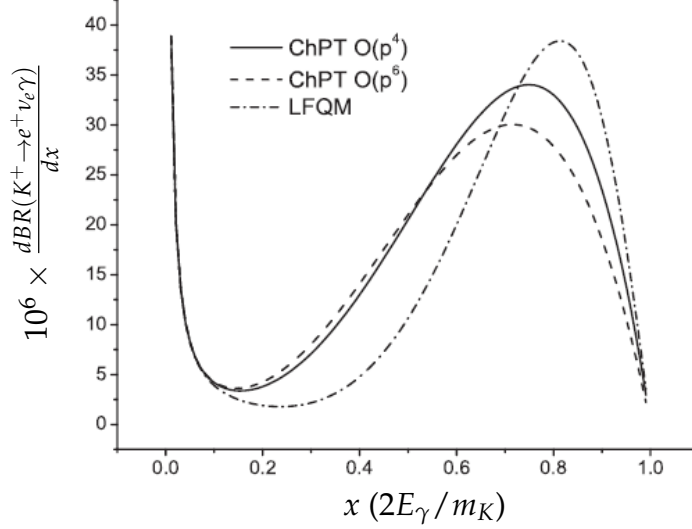
Figure 1.6: Theoretical predictions for the differential branching ratio of $K_{e2\gamma}^+$ as functions of x in LFQM (dashed-dotted line), in χPT at $\mathcal{O}(p^4)$ (solid line) and $\mathcal{O}(p^6)$ (dashed line).

Lower cuts at $x = 0.01$ and $x = 0.1$ are applied as the IB terms diverge[3] for $x \to 0$, corresponding to the maximum transferred momentum $p^2 \to p_{max}^2 = m_K^2$. The SD$^+$ component dominates the branching ratio.

Model	x Cut	IB	SD$^+$	SD$^-$	INT$^+$	INT$^-$	Total
χPT $\mathcal{O}(p^4)$	$x = 0.01$	1.65×10^{-1}	1.34	1.93×10^{-1}	6.43×10^{-5}	-1.10×10^{-3}	1.70
	$x = 0.1$	0.69×10^{-1}	1.34	1.93×10^{-1}	6.43×10^{-5}	-1.10×10^{-3}	1.60
χPT $\mathcal{O}(p^6)$	$x = 0.01$	1.65×10^{-1}	1.15	2.58×10^{-1}	6.22×10^{-5}	-1.21×10^{-3}	1.57
	$x = 0.1$	0.69×10^{-1}	1.15	2.58×10^{-1}	6.22×10^{-5}	-1.21×10^{-3}	1.47
LFQM	$x = 0.01$	1.65×10^{-1}	1.12	2.59×10^{-1}	4.33×10^{-5}	-1.29×10^{-3}	1.54
	$x = 0.1$	0.69×10^{-1}	1.12	2.59×10^{-1}	4.33×10^{-5}	-1.29×10^{-3}	1.44

Table 1.3: Differential branching ratio of $K_{e2\gamma}^+$ (in units of 10^{-5}) for the single components IB, SD$^\pm$, INT$^\pm$ and their sum (Total) in χPT at $\mathcal{O}(p^4)$ and $\mathcal{O}(p^6)$, in the LFQM, with lower cuts at $x = 0.01$ and $x = 0.1$ [9].

---

[3]The reader can refer to [20] for details on the renormalisation of the IB divergence at $x \to 0$.

1.1.5 Experimental status

Referring to Eqs. 1.14-1.19, one can state that the only unknowns of the $K^+_{e2\gamma}$ decay rate are the two real functions: $F^\pm(p^2) = F_V(p^2) \pm F_A(p^2)$. The results obtained by observing the $SD^\pm$ terms alone, with either $K_{e2\gamma}$ or $K_{\mu2\gamma}$ decays, are subject to sign ambiguities since $SD^\pm$ depend on the absolute values of $|F_V - F_A|^2$ and $|F_V + F_A|^2$. As a consequence, to determine $F_{V,A}$ uniquely one must measure the $INT^\pm$ terms as well. A direct measurement of $F^\pm$ from the interference terms $INT^\pm$ using $K_{e2\gamma}$ decays is limited by the small contribution of $INT^\pm$ in the signal kinematic region; the measurement is easier to achieve by selecting $K_{\mu2\gamma}$ decays, as described later in this section.

The PDG 2012 [16] quotes:

$$BR(K^+ \to e^+ \nu_e \gamma) = (9.4 \pm 0.4) \cdot 10^{-6}$$

in the kinematic region $10\,\text{MeV} < E^*_\gamma < 250\,\text{MeV}$ and $p^*_e > 200\,\text{MeV}$. This value was obtained by the KLOE collaboration using the DAΦNE collider in Frascati [21]. The measurement is based on the observation of 1484 $K^\pm \to e^\pm \nu_e \gamma$ candidates in the above kinematic region. The SD^- and IB contributions account for about 2% and 1.3% respectively of the total sample. The form factor parameters have been obtained by fitting the measured E^*_γ distribution with the theoretical differential decay width, assuming the vector form factor expansion at the first order of x as in Eq. 1.20. The small contribution from the SD^- component to the selected events does not allow a fit to the related $|F_V - F_A|$ component. As a consequence, in the fitting procedure $|F_V(0) - F_A(0)|$ is kept fixed at the expectation value from χPT at $\mathcal{O}(p^6)$, while $|F_V(0) + F_A(0)|$ and λ are considered as free parameters. The results are the following [21]:

$$|F_V(0) + F_A(0)| = 0.125 \pm 0.007_{stat} \pm 0.001_{syst},$$
$$\lambda = 0.38 \pm 0.20_{stat} \pm 0.02_{syst}. \tag{1.22}$$

with a correlation coefficient of -0.93. The result indicates a non-zero slope in the vector form factor F_V, which is in agreement with the λ value reported in Tab. 1.2. Among the available analyses of experimental data of the $K^+_{e2\gamma}$ decay, this is the only one attempting a measurement of $F_{V,A}$ as predicted by χPT at $\mathcal{O}(p^6)$. The results discussed below on $K^+_{l2\gamma}$ decays with $l = e^+, \mu^+$ assume constant form factors as predicted in χPT at $\mathcal{O}(p^4)$ throughout.

In 2008 the PDG world average $BR(K^+ \to e^+ \nu_e \gamma, SD^+) = (1.53 \pm 0.23) \cdot 10^{-5}$ was based on a combination of results from two experiments at CERN [22, 23]. In the first

experiment 56 $K^+_{e2\gamma}$ events were selected in the kaon rest frame energy range: $E^*_\gamma >$ 100 MeV, $E^*_e > 236$ MeV and $\theta^*_{e^+\gamma} > 120°$ and the ratio $\Gamma(K^+_{e2\gamma}, SD^+)/\Gamma(K_{e2})$ was measured. In the second experiment the measurement of the ratio $\Gamma(K^+_{e2\gamma}, SD^+)/\Gamma(K_{\mu2})$ was performed with 51 $K^+_{e2\gamma}$ events selected in the kaon rest frame kinematical region: $E^*_e > 235$ MeV, $E^*_\gamma > 48$ MeV and $\theta^*_{e^+\gamma} > 140°$. Both experiments were sensitive to the structure dependent (SD^+) term only, proportional to $|F_V + F_A|^2$. Under the assumption of constant form factors the following estimations were obtained:

$$|F_V(0) + F_A(0)| = 0.150^{+0.018}_{-0.023},$$
$$|F_V(0) + F_A(0)| = 0.147 \pm 0.011$$

The $BR(K^+_{e2\gamma}, SD^+)$ was measured with an experimental uncertainty ($\sim 15\%$) not suitable to discriminate between the theoretical models.

The E787 collaboration at BNL reported the first measurement of a SD component in the decay $K_{\mu2\gamma}$, in the kaon rest frame kinematic region where the muon kinetic energy is > 137 MeV and the photon energy is > 90 MeV [24]. In the $K_{\mu2\gamma}$ decay the IB term is not suppressed by helicity and the INT term (interference term between IB and SD) is comparable in size to the SD term. As mentioned above, the measurement of the INT term allows to establish the sign and magnitude of the form factors. The final sample comprised 2693 $K_{\mu2\gamma}$ events; a shape fit of the IB, SD and INT components allowed the extraction of the form factor combinations:

$$|F_V(0) + F_A(0)| = 0.165 \pm 0.007_{stat} \pm 0.011_{syst},$$
$$F_V(0) - F_A(0) = 0.102 \pm 0.073_{stat} \pm 0.044_{syst},$$

where $|F_V(0) + F_A(0)|$ from $K_{\mu2\gamma}$ differs from the value measured with $K_{e2\gamma}$ at a 3σ level.

A more accurate determination came from the E865 experiment at the Brookhaven AGS [25]. For the first time all form factors from $K^+ \rightarrow l^+\nu_l e^+e^-$ (K_{l2ee}) decays, with $l = e, \mu$, were measured using 410 K_{e2ee} events (in the invariant mass region $m_{ee} > 150$ MeV with 10% background contamination) and 2679 $K_{\mu2ee}$ events ($m_{ee} > 145$ MeV, 19% background contamination). The form factor measurement was performed with a combined likelihood fit, the fit function used being the sum of $K_{\mu2ee}$ and K_{e2ee} log-likelihood functions. The following combined results were achieved: $F_V(0) = 0.112 \pm 0.018$, $F_A(0) = 0.035 \pm 0.019$ and

$$|F_V(0) + F_A(0)| = 0.147 \pm 0.026,$$
$$F_V(0) - F_A(0) = 0.077 \pm 0.028.$$

No inconsistency between $K_{\mu2ee}$ and K_{e2ee} form factors was found.

Very recently the ISTRA+ collaboration has reported the study of the $K_{\mu2\gamma}^-$ decay. The measurement of the difference $F_V - F_A$ was performed by observing the interference term between IB and SD$^-$ components (INT$^-$) in a sample of about 22,000 $K_{\mu2\gamma}^-$ events. In the fit procedure the sum $F_V + F_A$ was fixed at the value measured in [24], assuming a p^2 dependence. The ISTRA+ results relative to two alternative analyses [26, 27]:

$$F_V(0) - F_A(0) = 0.126 \pm 0.027_{stat} \pm 0.047_{syst},$$
$$F_V(0) - F_A(0) = 0.21 \pm 0.04_{stat} \pm 0.03_{syst}$$

are respectively about 1.5 and 3σ above the χPT predictions reported in Tab. 1.2.

The theoretical expectations and experimental results for the form factor combinations, $F_V + F_A$ and $F_V - F_A$, are summarised in Fig. 1.7. χPT predictions at $\mathcal{O}(p^4)$ are computed using the values reported in Tab. 1.1, where no errors are available (representation as a single point); χPT at $\mathcal{O}(p^6)$ are taken from Tab. 1.2. The KLOE analysis is the only one assuming the form factors as predicted by χPT at $\mathcal{O}(p^6)$ and a linear parametrization of F_V on p^2 (see Eq. 1.20). The other analyses assume constant form factors as predicted in χPT at $\mathcal{O}(p^4)$. The width of the bands corresponds to the sum in quadrature of statistical and systematic errors. For experiments providing the measurement of both form factor combinations, the results are represented with a 1σ contour in the ($F_V - F_A$, $F_V + F_A$) plane; no correlation is assumed.

1.2 $K \to \pi \nu \bar{\nu}$ decays

Within the Standard Model (SM) the transitions $K^+ \to \pi^+ \nu \bar{\nu}$ and $K_L \to \pi^0 \nu \bar{\nu}$ are Flavour-Changing Neutral-Current processes [28] particularly interesting to study the physics of flavour: their rates can be computed with high precision and provide determinations of less-well known fundamental physics parameters. Concisely, the main motivations for studying the $K \to \pi \nu \bar{\nu}$ decay channels are listed below, while a more detailed discussion will follow in Sec. 1.2.3.

- The branching ratios (BR) of $K \to \pi \nu \bar{\nu}$ decays are theoretically well calculated observables. The predicted non-parametric relative uncertainties are BR($K^+ \to \pi^+ \nu \bar{\nu}$) $\approx$ 4% and BR($K_L \to \pi^0 \nu \bar{\nu}$) $\approx$ 2% [29];

- The decays $K \to \pi \nu \bar{\nu}$ are sensitive to the CKM matrix element V_{td}: this fundamental parameter can be extracted from their BR with a theoretical intrinsic
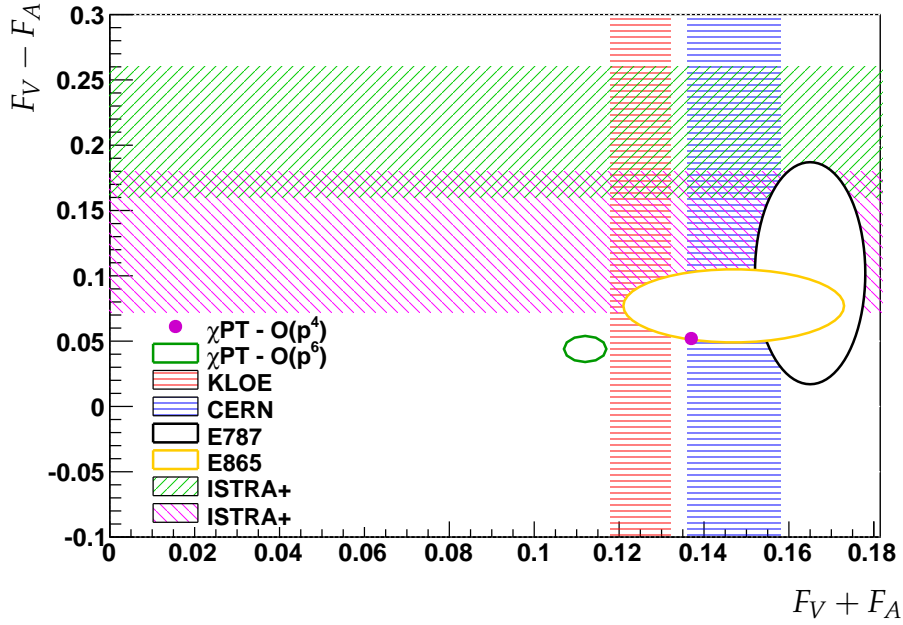
Figure 1.7: Theoretical expectations for $F_V \pm F_A$ in χPT at $\mathcal{O}(p^4)$ (magenta marker) and $\mathcal{O}(p^6)$ (green ellipse). Results on the form factor combinations from KLOE [21], CERN [22,23] and ISTRA+ [26,27] collaborations; 1σ contours in the ($F_V - F_A$, $F_V + F_A$) plane, assuming no correlation, from E787 [24] and E865 [25] experiments at BNL.

relative uncertainty of $\sim 3\%$;

- FCNC processes are strongly suppressed within the SM, thus very sensitive to new physics (NP) and can be used to test several SM extensions and NP scenarios;

- The processes $K \to \pi \nu \bar{\nu}$ allow to test charge-parity symmetry: V_{td} is one of the two CKM matrix elements containing CP violation information in the SM;

- Simultaneous BR measurements of $K^+ \to \pi^+ \nu \bar{\nu}$ and $K_L \to \pi^0 \nu \bar{\nu}$ decays provide determinations of CKM parameters and the unitarity triangle in a complementary and independent way with respect to the study of B decays.

1.2.1 The CKM framework

The Cabibbo 2×2 matrix [31] expresses how the charged (or flavour-changing) current couples $u \to d$ or $c \to s$ quark states. This happens through intermediate states, d' and s', which are orthogonal combinations of the physical (mass) eigenstates

of quarks of definite flavour d, s:

$$\begin{pmatrix} d' \\ s' \end{pmatrix} = \begin{pmatrix} \cos\theta_C & \sin\theta_C \\ -\sin\theta_C & \cos\theta_C \end{pmatrix} \begin{pmatrix} d \\ s \end{pmatrix}. \tag{1.23}$$

The quark mixing is described by a single real parameter: the Cabibbo angle $\theta_C \simeq 13°$ that can be determined from experimental information on the corresponding quark flavour transition. For example, the amplitudes of the processes $c \to su\bar{d}$ and $c \to \bar{s}ud$ are respectively proportional to $\sim \cos^2\theta_C$ and $\sim \sin^2\theta_C$; since $\cos^2\theta_C \gg \sin^2\theta_C$ the latter process is Cabibbo suppressed.

The 3×3 quark-mixing CKM matrix [32] generalizes the Cabibbo one by including a third coupling of quark states $t \to b$:

$$\begin{pmatrix} d' \\ s' \\ b' \end{pmatrix} = \begin{pmatrix} V_{ud} & V_{us} & V_{ub} \\ V_{cd} & V_{cs} & V_{cb} \\ V_{td} & V_{ts} & V_{tb} \end{pmatrix} \begin{pmatrix} d \\ s \\ b \end{pmatrix}. \tag{1.24}$$

The matrix can be expressed in the Wolfenstein parameterisation [33]:

$$V = \begin{pmatrix} 1 - \lambda^2/2 & \lambda & A\lambda^3(\rho - \iota\eta) \\ -\lambda & 1 - \lambda^2/2 & A\lambda^2 \\ A\lambda^3(1 - \rho - \iota\eta) & -A\lambda^2 & 1 \end{pmatrix} + O(\lambda^4), \tag{1.25}$$

where λ is used as an expansion parameter; A and λ are defined to be positive and satisfy the relations: $\lambda = \sin\theta_{12}$, $A\lambda^2 = \sin\theta_{23}$ and $A\lambda^3(\rho - \iota\eta) = \sin\theta_{13}e^{-i\phi}$, with θ_{ij} denoting three real parameters (Cabibbo-like angles) and $e^{-i\phi}$ a phase factor. Unlike the Cabibbo matrix, the CKM is complex: the phase encodes the CP violation. The elements of the CKM matrix are fundamental parameters of the SM and it is important to determine them precisely. The current status of the experimental situation is summarised in the following [34]:

$$\begin{pmatrix} |V_{ud}| = 0.97425 \pm 0.00022 & |V_{us}| = 0.2252 \pm 0.0009 & |V_{ub}| = (4.15 \pm 0.49) \times 10^{-3} \\ |V_{cd}| = 0.230 \pm 0.011 & |V_{cs}| = 1.006 \pm 0.023 & |V_{cb}| = (40.9 \pm 1.1) \times 10^{-3} \\ |V_{td}| = (8.4 \pm 0.6) \times 10^{-3} & |V_{ts}| = (42.9 \pm 2.6) \times 10^{-3} & |V_{tb}| = 0.89 \pm 0.07 \end{pmatrix}. \tag{1.26}$$

The values reported above are obtained by averaging various measurements. It can be noted that:

- Diagonal elements are clearly dominant and reflect the most allowed transitions: $u \to d, c \to s, t \to b$.

- The off-diagonal elements represent transitions suppressed at a certain level, depending on their amplitude. The value reported for $|V_{us}|$ comes from the measurement BR($K^+ \rightarrow \mu^+ \nu(\gamma)$) [35] and a combined result of $K_L^0 \rightarrow \pi e \nu$, $K_L^0 \rightarrow \pi \mu \nu$, $K^\pm \rightarrow \pi^0 e^\pm \nu$, $K^\pm \rightarrow \pi^0 \mu^\pm \nu$ and $K_S^0 \rightarrow \pi e \nu$ decays [36]. As shown in Sec. 1.2.3 precise determinations of $|V_{td}|$ and $|V_{ts}|$ cannot be achieved with tree-level processes involving top quarks, which are suppressed. At present, the study of $B^0 - \bar{B}^0$ oscillations mediated by box diagrams, including top quarks, and the analysis of loop-mediated rare decays in the K and B meson sectors offer the possibility to measure these two CKM matrix elements. For example, the inclusive BR($B \rightarrow X_s \gamma$) is sensitive to $V_{tb} V_{ts}^*$ [37]; a theoretically clean determination of $|V_{td} V_{ts}^*|$ is possible from the $K^+ \rightarrow \pi^+ \nu \bar{\nu}$ decay [38] and the ratio $|V_{ts}/V_{cb}|$ can be extracted from the the ratio $BR(B \rightarrow X_s \gamma)/BR(B \rightarrow X_c e \bar{\nu})$ [39]. These latter CKM elements also determine the $B_s \rightarrow \mu^+ \mu^-$ decay rate [40]. Values of $|V_{td}|$ and $|V_{ts}|$ reported in Eq. 1.26 are obtained by the measurements of the mass difference of two neutral B^0 meson mass eigenstates performed by the CDF [41] and LHCb [42] experiments.

1.2.2 The unitarity triangle

The CKM matrix unitarity [43] imposes nine conditions on the CKM matrix elements: $\sum_i V_{ij} V_{ik}^* = \delta_{jk}$ and $\sum_j V_{ij} V_{kj}^* = \delta_{ik}$, where $i = u, c, t$ and $j, k = d, s, b$ with

$$\delta_{\alpha\beta} = \begin{cases} 1 & \text{if } \alpha \neq \beta \,, \\ 0 & \text{otherwise} \,. \end{cases}$$

The three equations on the diagonal elements give information on the magnitude of the CKM elements. The six vanishing combinations can be represented as triangles in a complex plane. A powerful test of the SM flavour sector is to measure the CKM matrix elements and test the matrix unitarity; any significant deviations from the SM predictions would be hint of physics beyond the SM. The combination most referred to is:

$$V_{ud} V_{ub}^* + V_{cd} V_{cb}^* + V_{td} V_{tb}^* = 0 \,. \tag{1.27}$$

The above can be interpreted as the sum of three vectors in a complex plane and represented with the triangle in Fig. 1.8 by dividing each side by the best-known one: $V_{cd} V_{cb}^*$.
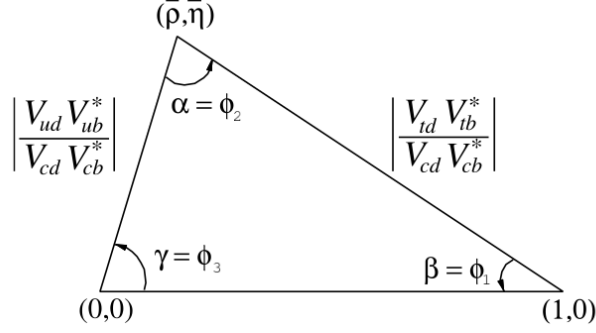
Figure 1.8: Unitarity triangle corresponding to the condition 1.27.

The angles of the unitarity triangle in Fig. 1.8 are:

$$\beta = \phi_1 = \arg\left(-\frac{V_{cd}V_{cb}^*}{V_{td}V_{tb}^*}\right),$$

$$\alpha = \phi_2 = \arg\left(-\frac{V_{td}V_{tb}^*}{V_{ud}V_{ub}^*}\right),$$

$$\gamma = \phi_3 = \arg\left(-\frac{V_{ud}V_{ub}^*}{V_{cd}V_{cb}^*}\right). \tag{1.28}$$

In the Wolfenstein parameterisation (1.25) the CKM unitarity condition in Eq. 1.27 is written as:

$$1 + \frac{V_{td}V_{tb}^*}{V_{cd}V_{cb}^*} = -\frac{V_{ud}V_{ub}^*}{V_{cd}V_{cb}^*} = \bar{\rho} + i\bar{\eta}, \tag{1.29}$$

where

$$\bar{\rho} = \rho\left(1 - \frac{\lambda^2}{2}\right); \qquad \bar{\eta} = \eta\left(1 - \frac{\lambda^2}{2}\right).$$

As a consequence, the vertex coordinates of the unitarity triangle in Fig. 1.8 are exactly $(0,0)$, $(1,0)$, and $(\bar{\rho},\bar{\eta})$.

1.2.3   BR($K \to \pi \nu \bar{\nu}$)

At the quark level the $K \to \pi \nu \bar{\nu}$ processes arise from the flavour changing quark transition $s \to d \nu \bar{\nu}$, which in the SM receives one-loop contributions from Z-penguin and W-box, as shown in figure 1.9.

In these graphs the u, c, and t quarks appear as internal lines. Separating the contributions to the one-loop level amplitude one has [44]:

$$A(s \to d \nu \bar{\nu}) = \sum_{q=u,c,t} V_{qs}^* V_{qd} A_q \ ,$$
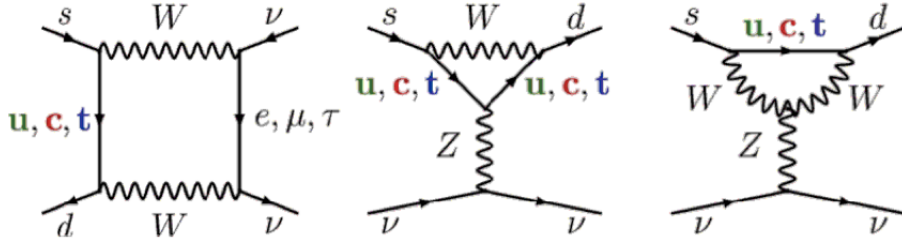
Figure 1.9: One-loop diagrams contributing to the $s \to d\nu\bar{\nu}$ process. From left: a W-box diagram and two Z-penguin diagrams.

where V_{ij} denote the elements of the CKM matrix. Considering the magnitude of CKM matrix elements, as reported in 1.26, up-quark and charm-quark contributions should be favoured. However, as flavour-changing transitions such as $s \to d$ are forbidden at tree-level, high order quantum loops contribute at the leading order and the amplitude is written in terms of $A_q \sim (m_q^2/M_W^2)^\alpha$, with $\alpha > 0$. Because of its mass, the top-quark contribution becomes the dominant term and the transition $s \to d$ is described by short-distance quark dynamics. As a consequence, the QCD corrections are small and calculable in perturbation theory [45]. The $s \to d\nu\bar{\nu}$ process is well described by means of a Fermi-like coupling between a quark and a lepton neutral weak currents [46]:

$$H_{eff} = \frac{G_F}{\sqrt{2}} \frac{\alpha}{2\pi \sin^2 \theta_W} \sum_{l=e,\mu,\tau} [\lambda_c X^l + \lambda_t Y(x_t)](\bar{s}d)_{V-A}(\bar{\nu}_l \nu_l)_{V-A} , \qquad (1.30)$$

where

1. G_F is the Fermi coupling constant;

2. α is the fine-structure constant;

3. θ_W is the Weinberg angle[4];

4. $\lambda_q = V_{qs}^* V_{qd}$, with $q = c, t$;

5. $x_t = m_t^2/M_W^2$ where m_t is the top-quark mass and M_W is the W boson mass;

6. $Y(x_t)$ is a function encoding the sole or the dominant top-quark loop contribution to the neutral or the charged $K \to \pi\nu\bar{\nu}$ decay modes, respectively. $Y(x_t)$ is known at the next-to-leading order (NLO) accuracy in QCD [47]. The associated theoretical uncertainty is small: the parametric part is essentially determined by

---

[4]The Weinberg angle, or weak mixing angle, is a parameter in the Weinberg-Salam theory of the electroweak force.

the experimental error on m_t ($\sim 3\%$ relative); the intrinsic part has been recently pushed down by computing two-loop electro-weak corrections to $Y(x_t)$. In total the result is:

$$Y(x_t) = 1.469 \pm 0.017 \pm 0.002, \tag{1.31}$$

where the first error comes from QCD NLO corrections, while the second error comes from the two-loop electro-weak corrections.

7. X^l with $l = e, \mu, \tau$ are functions describing the charm-quark contribution in the loop. The total charm-quark term is conveniently described by the parameter [46, 48]:

$$P_0(X) = \frac{1}{\lambda^4} \left[\frac{2}{3} X^e + \frac{1}{3} X^\tau \right] = 0.42 \pm 0.06, \tag{1.32}$$

in which the functions $X^e = X^\mu$ and X^τ, all known at NLO [49], and the Wolfenstein parameter $\lambda = \sin\theta_{12} = 0.2240 \pm 0.0036$ have been used. For the $K^+ \to \pi^+ \nu\bar{\nu}$ decay, the charm-quark exchange is non negligible: it amounts to about 30% of the total magnitude of $A(s \to d\nu\bar{\nu})$ and the NLO uncertainty, coming from Eq. 1.32, translates into an error of about 10% in the SM estimate of $BR(K^+ \to \pi^+ \nu\bar{\nu})$. This uncertainty can be reduced to below 4% with calculations of X^l at Next-to-Next-to-Leading Order (NNLO) accuracy [38] [48].

8. u and $\bar{s}$ are the quark states embedded into the K^+ meson;

9. $(\bar{s}d)_{V-A}$ and $(\bar{\nu}_l \nu_l)_{V-A}$ are the quark and lepton neutral weak currents showing the vector - axial vector $(V - A)$ structure: $[\bar{s}\gamma_\mu(1 - \gamma_5)d][\bar{\nu}\gamma_\mu(1 - \gamma_5)\nu]$; the Dirac gamma matrices (γ_μ) [14] have been introduced in Sec. 1.1.1.

The structure of the effective Hamiltonian in Eq. 1.30 shows that the amplitude is dominated by one single semi-leptonic operator acting on left-handed fermionic states $(\bar{s}_L \gamma^\mu d_L)(\bar{\nu}_L \gamma_\mu \nu_L)$. The hadronic matrix elements can be extracted by isospin symmetry with negligible error from the measured BR of the semi-leptonic kaon decay $K^+ \to \pi^0 e^+ \nu$ (K_{e3}^+). Using the functions defined above, the BR can be written as [49,50]:

$$BR(K^+ \to \pi^+ \nu\bar{\nu}) = \frac{\bar{k}_+}{\lambda^2} \left[(Im\lambda_t)^2 Y^2(x_t) + (\lambda^4 Re\lambda_c P_0(X) + Re\lambda_t Y(x_t))^2 \right], \tag{1.33}$$

where the coefficient $\bar{k}_+$ includes the dependence on the CKM matrix element $V_{us} = \lambda$, the kaon mass m_K, the charged kaon lifetime $\tau(K^+)$, the K^+ and π^+ decay constants and a phase space factor. Since the same factors appear in $BR(K^+ \to \pi^0 e^+ \nu_e)$ one can then write:

$$\bar{k}_+ = r_{K^+} BR(K^+ \to \pi^0 e^+ \nu), \tag{1.34}$$

where $BR(K^+ \rightarrow \pi^0 e^+ \nu) = (5.08 \pm 0.05) \times 10^{-2}$ [16] and $r_{K+} = 0.901$ is a parameter including the isospin breaking corrections necessary to relate the final states $\pi^+ \nu \bar{\nu}$ and $\pi^0 e^+ \nu$. The $BR(K^+ \rightarrow \pi^+ \nu \bar{\nu})$ estimation depends on the "free" parameters: V_{ts} from $Im\lambda_t$, V_{cd} from $Re\lambda_c$ and V_{td} from $Re\lambda_t$. In our approximation, (1.25), $V_{ts} \approx -V_{cb}$, which is determined accurately from semi-leptonic B meson decays [34], and $|V_{cd}|$ is well measured from charmed particles decay [38] [48]. The resulting theoretical error is $\sim 5 - 7\%$ on the determination of $|V_{td}|$ [29].

For completeness, but without discussing in detail, it is possible to summarise the situation for $K_L \rightarrow \pi^0 \nu \bar{\nu}$, for which the theoretical predictions are even more precise. The lepton pair $\nu \bar{\nu}$ is produced in a definite state of CP, which is not the same as for K_L; this implies that the leading contribution to $K_L \rightarrow \pi^0 \nu \bar{\nu}$ is CP-violating. Due to the CP structure only the imaginary part in Eq. 1.30 contributes to the amplitude. The charm-quark contribution in the loop is negligible and the direct-CP-violating leading term is completely saturated by the top-quark loop contribution, for which the QCD corrections are suppressed and rapidly convergent [45]. Using the functions as defined above the BR can be written as [49, 50]:

$$BR(K_L \rightarrow \pi^0 \nu \bar{\nu}) = \frac{\bar{k}_L}{\lambda^2}(Im\lambda_t)^2 Y^2(x_t), \tag{1.35}$$

where $\bar{k}_L$ is the neutral version of $\bar{k}_+$ and can be analogously written as [51]:

$$\bar{k}_L = r_{K_L} BR(K^+ \rightarrow \pi^0 e^+ \nu), \tag{1.36}$$

$r_{K_L} = 0.944$ being the parameter including the isospin breaking corrections resulting from the usage of $BR(K^+ \rightarrow \pi^0 e^+ \nu_e)$.

In the SM, the theoretical expectations for the charged and neutral mode are therefore [29]:

$$BR(K^+ \rightarrow \pi^+ \nu \bar{\nu}) = \left(7.81^{+0.80}_{-0.71} \pm 0.29\right) \times 10^{-11};$$
$$BR(K_L \rightarrow \pi^0 \nu \bar{\nu}) = \left(2.43^{+0.40}_{-0.37} \pm 0.06\right) \times 10^{-11}, \tag{1.37}$$

where the first error is related to the uncertainties in the input parameters and is dominated by the CKM parameter V_{cb}. The second error quantifies the remaining intrinsic theoretical uncertainties: in the charge mode, those are dominated by the charm-quark contribution.

1.2.4 Unitarity triangle from $K \to \pi \nu \bar{\nu}$

Let us consider the orthogonality condition[5]:

$$V_{ud}V_{us}^* + V_{cd}V_{cs}^* + V_{td}V_{ts}^* = 0 \qquad (1.38)$$

and its representation as a unitarity triangle in a complex plane. Recalling that $\lambda_t = V_{ts}^* V_{td}$, it is possible to observe that:

- The length of the vector $V_{us}^* V_{ud}$ is determined from the K_{e3} decay, as it was seen in Sec. 1.2.1;

- The length of the third side $V_{ts}^* V_{td}$, namely $(Im\lambda_t)(Re\lambda_t)$, is measured by $K^+ \to \pi^+ \nu \bar{\nu}$ (see Eq. 1.33);

- The height of the triangle, $Im\lambda_t$, can be measured by $K_L \to \pi^0 \nu \bar{\nu}$ (see Eq. 1.35).

Therefore the branching ratio measurements of the two $K \to \pi \nu \bar{\nu}$ decay modes, along with the well known K_{e3}, will completely determine this unitarity triangle. In the Wolfenstein parameterisation (1.25) this translates into the determination of the parameter λ from K_{e3}, and the determination of $\bar{\rho}$ and $\bar{\eta}$ from the $K^+ \to \pi^+ \nu \bar{\nu}$ and $K_L \to \pi^0 \nu \bar{\nu}$ processes, respectively. Fig. 1.10 shows the triangle corresponding to Eq. 1.38. The $K^+ \to \pi^+ \nu \bar{\nu}$ decay rate defines the dashed side and the horizontal displacement of the right down vertex is due to the charm-quark contribution; the $K_L \to \pi^0 \nu \bar{\nu}$ decay rate gives the η parameter, namely the triangle height.

An important goal of flavour physics is to check the SM for consistency by using as many independent observables as possible. In this respects several scenarios are available for the determinations of the unitarity triangle and so the CKM matrix. For example, the measurements of CP asymmetries in $B_d \to J/\psi K_s$ and $B_d \to \pi\pi$ allow to extract $\sin 2\beta$ and $\sin 2\alpha$, thus constraining $\bar{\rho}$ and $\bar{\eta}$. In view of these facts the two $K \to \pi \nu \bar{\nu}$ kaon decay modes offer a complementary and independent tool to test the SM flavour dynamics.

1.2.5 Experimental status

The searches for the $K^+ \to \pi^+ \nu \bar{\nu}$ decay started in 1969; the early experiments used stopped-kaon beams. The earliest result was published by a heavy-liquid bubble

---

[5]The orthogonality condition in Eq. 1.38 is written with the elements in the first two columns of the CKM matrix, whereas the one reported in Eq. 1.27 with the ones in the first and third columns.
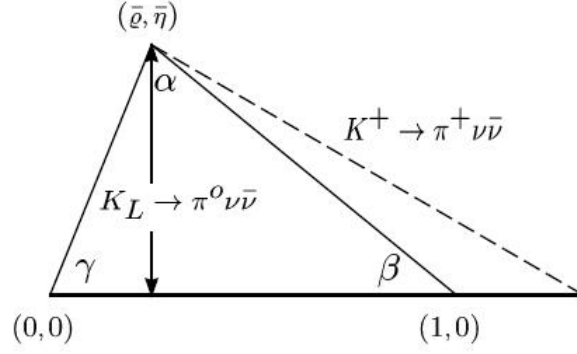
Figure 1.10: Unitarity triangle corresponding to the condition 1.38. The $K^+ \to \pi^+ \nu \bar{\nu}$ decay rate defines the dashed side and the displacement of the right down vertex is due to the charm-quark contribution; the $K_L \to \pi^0 \nu \bar{\nu}$ decay rate gives the η parameter, namely the triangle height.

chamber experiment at the Argonne Zero Gradient Synchrotron [52]: a 90% C.L. upper limit BR($K^+ \to \pi^+ \nu \bar{\nu}$) < 10^{-4} was obtained.

In 1973 a spark chamber experiment at the Berkeley Bevatron improved the limit down to BR($K^+ \to \pi^+ \nu \bar{\nu}$) < 5.6×10^{-7} [53]. The collaboration performed a combined measurement in two kinematic regions, above and below that of the potential background $K^+ \to \pi^+ \pi^0$, referred to as the $\pi \nu \bar{\nu}(1)$ and $\pi \nu \bar{\nu}(2)$ regions.

After a decade the measurement was further improved down to BR($K^+ \to \pi^+ \nu \bar{\nu}$) < 1.4×10^{-7} by an experiment at the KEK Proton Synchrotron [54]; the only kinematic region accessible by the experiment was the $\pi \nu \bar{\nu}(1)$ one.

In the early 80's a series of experiments at Brookhaven National Laboratory (BNL) started. The E787 collaboration [55] studied the $K^+ \to \pi^+ \nu \bar{\nu}$ decay from kaons at rest: in these conditions the event signature is a π^+ track and pion decay products. A secondary K^+ beam was obtained by impinging primary protons of $\sim 20\,\text{GeV}/c$, from the Alternating Gradient Synchroton (AGS), on a target. Pions and protons, produced along with the kaons, were swept out of the beam axis by means of electromagnetic separators. Kaons at $\sim 700\,\text{MeV}/c$ were selected and identified with Cherenkov counters, tracking and energy loss counters. After this stage, $\sim 27\%$ of kaons stopped in a scintillating-fiber target. The signal region is predefined in terms of the range (R), momentum (M) and kinetic energy (E) of charged decay products. These observables were measured with the target, a large acceptance solenoidal spectrometer and an hermetic (4π) photon veto. The main requirements for the selection of a signal candidate

24

are: a π^+ in the expected kinematic regions of R, M and E; the detection of the decay chain $\pi^+ \to \mu^+ \to e^+$; no other decay products (including photons) or beam particles (visible in the 4π detectors); a clean pattern in the target. The main background is due to $K^+ \to \mu^+ \nu_\mu(\gamma)$ and $K^+ \to \pi^+ \pi^0$ decays: the former is rejected by time-constraining the decay chain $\pi^+ \to \mu^+ \to e^+$; the latter is suppressed by detecting the two photons from the $\pi^0 \to \gamma\gamma$ decay. Redundant measurements were necessary to suppress backgrounds from beam pion scattering and K^+ charge-exchange process in the target inducing $K^0_L \to \pi^+ l^- \bar{\nu}_l$. A blind data analysis strategy was used: the signal region was kept masked until the selection criteria were determined and the background sources were identified and estimated with data-driven techniques. The simulation was only used to determine the signal geometrical acceptance. With a series of runs at different pion energy sensitivity, upper limits for BR($K^+ \to \pi^+ \nu\bar{\nu}$) were obtained in both $\pi\nu\bar{\nu}(1)$ and $\pi\nu\bar{\nu}(2)$ regions. E787 collected data from 1995 until 1998 and the major results are shown in Fig. 1.11:

- the red-circle markers within the box in the top-right area of the plot represent two $K^+ \to \pi^+ \nu\bar{\nu}$ candidates in the $\pi\nu\bar{\nu}(1)$ region (pion momentum between $(211,229)\,\mathrm{MeV}/c$), which leads to BR($K^+ \to \pi^+ \nu\bar{\nu}$) $= \left(1.57^{+1.75}_{-0.82}\right) \times 10^{-10}$ [55], with an estimated background of 0.15 ± 0.05 in a sample of 6×10^{12} stopped K^+.

- the green downward-pointing triangle marker within the box in the bottom-left area of the plot corresponds to one $K^+ \to \pi^+ \nu\bar{\nu}$ candidate in the $\pi\nu\bar{\nu}(2)$ region (pion momentum between $(140,195)\,\mathrm{MeV}/c$), leading to BR($K^+ \to \pi^+ \nu\bar{\nu}$) $< 42 \times 10^{-10}$ at 90% C.L [56], with an estimated background of 0.73 ± 0.18 in a sample of 1.1×10^{12} stopped K^+.

In the low momentum region ($\pi\nu\bar{\nu}(2)$), the $K^+ \to \pi^+ \pi^0$ background was mainly caused by pions losing energy via nuclear interactions in the target material near the kaon decay vertex. For these events the pion range and kinetic energy populate the signal low-momentum region $\pi\nu\bar{\nu}(2)$.

The follow-up experiment E949 [57] is an upgrade of E787, with an expected sensitivity increased by a factor of 5. The predictions on the detector performances quoted $\sim 10\ K^+ \to \pi^+ \nu\bar{\nu}$ events collected in the same running time of E787. The improvements relied on the photon veto detection efficiency, tracking, trigger efficiency and data acquisition. Several runs in both $\pi\nu\bar{\nu}(1)$ and $\pi\nu\bar{\nu}(2)$ regions gave the results shown in Fig. 1.11:

- the blue upward-pointing triangle marker within the box in the top-right area

of the plot corresponds to one $K^+ \to \pi^+ \nu \bar{\nu}$ candidate near the upper kinematic limit, leading to BR($K^+ \to \pi^+ \nu \bar{\nu}$) = $(0.96^{+4.09}_{-0.47}) \times 10^{-10}$. E787 and E949 results were combined and the branching ratio was determined: BR($K^+ \to \pi^+ \nu \bar{\nu}$) = $(1.47^{+1.30}_{-0.89}) \times 10^{-10}$ [57], based on three events observed in the pion momentum range (211,229) MeV/c (region $\pi\nu\bar{\nu}(1)$).

- the black-square markers within the box in the bottom-left area of the plot represent three $K^+ \to \pi^+ \nu \bar{\nu}$ events in the pion momentum range (140,199) MeV/c (region $\pi\nu\bar{\nu}(2)$), which leads to BR($K^+ \to \pi^+ \nu \bar{\nu}$) = $\left(7.89^{+9.26}_{-5.10}\right) \times 10^{-10}$ [58] in an exposure of 1.71×10^{12} stopped kaons, with an estimated total background of $0.93 \pm 0.17(\text{stat.})^{+0.32}_{-0.24}(\text{syst.})$ events.

The combined measurement obtained by E787-E949 collaborations, based on 7 candidates consistent with $K^+ \to \pi^+ \nu \bar{\nu}$ decays, is reported in [58]:

$$\text{BR}(K^+ \to \pi^+ \nu \bar{\nu}) = \left(1.73^{+1.15}_{-1.05}\right) \times 10^{-10}. \tag{1.39}$$

The experimental result is consistent with the SM expectation given the large statistical uncertainty. A summary of the BR($K^+ \to \pi^+ \nu \bar{\nu}$) results achieved over the past 40 years is illustrated in Fig. 1.12.

The decay $K_L \to \pi^0 \nu \bar{\nu}$ is even more experimentally challenging for several reasons including:

- the theoretical expectations for BR($K_L \to \pi^0 \nu \bar{\nu}$), reported in Eq. 1.37, which are smaller than the one for BR($K^+ \to \pi^+ \nu \bar{\nu}$);

- the event signature with only two photons in the final state, with the invariant mass of a π^0 (to be compared with the $\sim$ 34% probability of K_L^0 producing at least one π^0);

- the initial and final states being electrically neutral (no tracking for kaons and charged decay products as for $K^+ \to \pi^+ \nu \bar{\nu}$);

- the K_L production cross section, which is lower than the $K^\pm$ one, for primary protons at a given energy.

According to [59] an indirect model-independent upper limit on BR($K_L \to \pi^0 \nu \bar{\nu}$) can be derived from BR($K^+ \to \pi^+ \nu \bar{\nu}$) using the following relation:

$$\text{BR}(K_L \to \pi^0 \nu \bar{\nu}) < 4.4 \times \text{BR}(K^+ \to \pi^+ \nu \bar{\nu}).$$
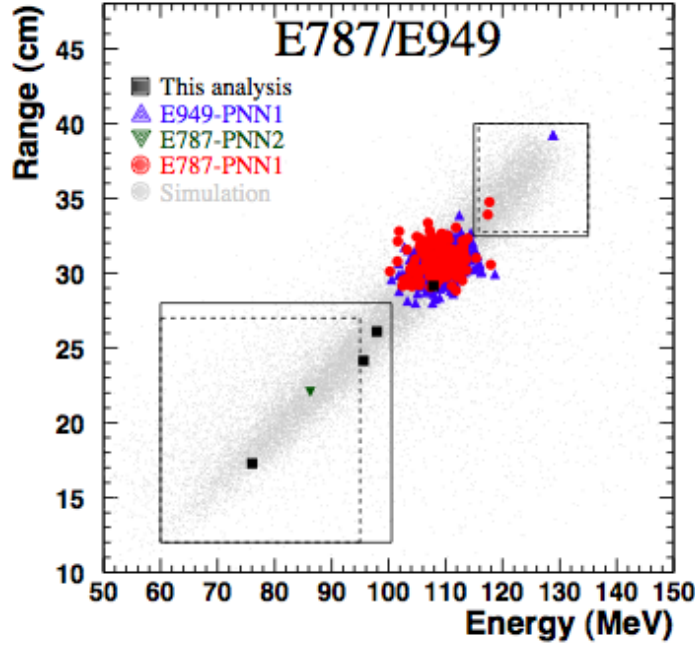
Figure 1.11: Distribution of the pion range as a function of the pion kinetic energy for events passing the $K^+ \to \pi^+ \nu \bar{\nu}$ analysis event selection. The square markers represent the events observed by E949 [58] (source of the plot) in $\pi \nu \bar{\nu}(2)$. The downward-pointing triangle marker represents the event observed by E787 in the same region. The circle and upward-pointing triangle markers represent the events selected by E787 and E949 in $\pi \nu \bar{\nu}(1)$. The solid (dashed) lines represent the limits of the $\pi \nu \bar{\nu}(1)$ and $\pi \nu \bar{\nu}(2)$ signal regions for the E949 (E787) analyses. The markers outside the boxes correspond to $K^+ \to \pi^+ \pi^0$ events surviving the photon veto cuts and passing the analysis event selection. The light gray points are simulated $K^+ \to \pi^+ \nu \bar{\nu}$ events.

Assuming the E787-E949 combined measurement of $K^+ \to \pi^+ \nu \bar{\nu}$, as reported in Eq. 1.39, one obtains the best limit at 90% C.L.:

$$\mathrm{BR}(K_L \to \pi^0 \nu \bar{\nu}) < 1.7 \times 10^{-9} \ .$$

In order to extract an independent constraint on the CKM matrix elements it is desirable to perform a direct measurement of the $K_L \to \pi^0 \nu \bar{\nu}$ decay rate. A typical major limitation in experimental programmes devoted to the search for rare decays comes from the background, which must be kept below several orders of magnitude to reach the required signal sensitivity. In the study of the $K_L \to \pi^0 \nu \bar{\nu}$ decay the main background source is due to the $K_L^0 \to \pi^0 \pi^0$ decay (BR $\sim 10^{-3}$), with two missing photons out of four produced in the $\pi^0 \to \gamma\gamma$ decays. Other sources are due to:
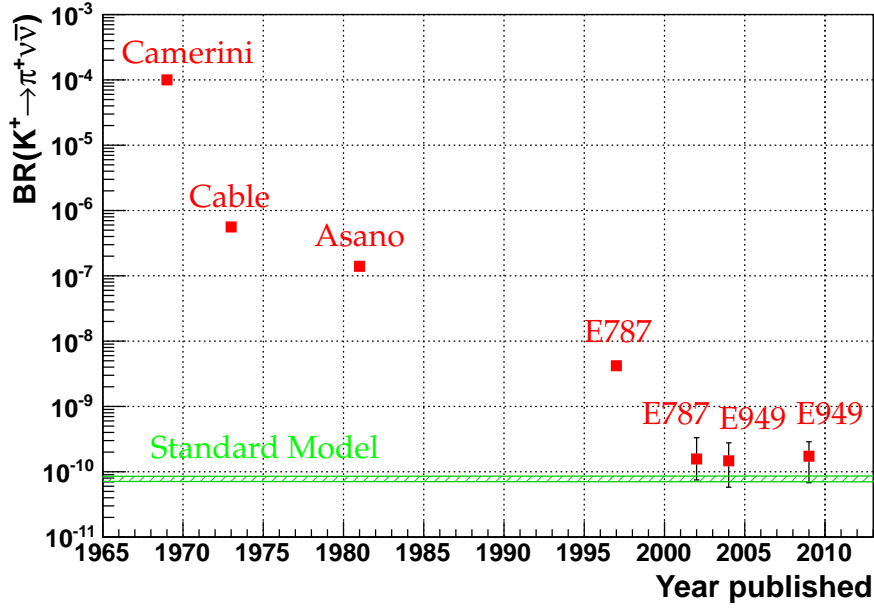
Figure 1.12: Summary of the BR($K^+ \to \pi^+ \nu\bar{\nu}$) experimental status over the years.

neutrons and kaons in the neutral beam interacting with residual gas in the decay volume and producing π^0s; halo beam neutrons interacting in the detector material; the $K_L^0 \to \gamma\gamma$ decay which has the same particles in the final state; hyperon decays such as $\Lambda \to \pi^0 n$. As a matter of principle any other kaon decay with at least two photons in the final state and with the other decay products, all being undetected, provides a source of background. As a consequence the background rejection must rely on a hermetic (4π) and highly efficient photon and charged particle vetoes.

The first direct limit on $K_L \to \pi^0 \nu\bar{\nu}$ was obtained by the E799-II experiment using the KTeV detector at Fermilab [60]. The strategy was based on the detection of the π^0 Dalitz decay $\pi^0 \to e^+ e^- \gamma$; the charged particles in the final state provided a better event signature for suppressing the background. The data were collected during 44 days in 1997 and from the full data set no signal events were observed, with an expected background of $0.12^{+0.05}_{-0.04}$, leading to BR($K_L \to \pi^0 \nu\bar{\nu}$) $< 5.9 \times 10^{-7}$ at 90% C.L. Due to the small BR($\pi^0 \to e^+ e^- \gamma$) the strategy is not optimal for high sensitivity searches and future experiments plan to use the more abundant $\pi^0 \to \gamma\gamma$ mode.

The upper limit was improved by the E391a experiment at the High Energy Accelerator Research organisation (KEK) 12 GeV proton synchrotron [61]. The strategy comprised the usage of a highly collimated "pencil"[6] K_L^0 beam, which allowed for the

---

[6] The beam has a 100 mm × 100 mm (r.m.s) beam profile in the plane orthogonal to the beam line.

28

reconstruction of the longitudinal coordinate of the neutral decay vertex, Z_{vtx}, and the π^0 transverse momentum[7], $P_T(\pi^0)$, with a reduced uncertainty due to the finite size of the beam. The fiducial decay volume and the detector were housed in vacuum to suppress the background from neutrons interacting with the residual gas. A cylindrical veto barrel surrounding the neutral beam (made of an array of CsI modules) and lead scintillator counters, filling the remaining uncovered gaps from CsI, were used as an hermetic veto. The signal-background separation relied on cuts on the reconstructed Z_{vtx} and $P_T(\pi^0)$. The single event sensitivity reached was 1.11×10^{-8}. No signal events were observed inside the signal region and a new upper limit at 90% C.L on $\mathrm{BR}(K_L \to \pi^0 \nu \bar{\nu}) < 2.6 \times 10^{-8}$ was set. In this result the main background source observed was from halo-neutron interactions, namely neutrons apart from the beam centre hitting a detector subsystem and producing a π^0.

The KOTO (KO at Tokai, where the J-PARC is located) experiment [62] aims at the first observation of the rare decay $K_L \to \pi^0 \nu \bar{\nu}$ by using the upgraded KEK-E391a detector and a high-intensity K_L beam at J-PARC. KOTO is designed to reduce the halo-neutron events down to five orders of magnitudes by using a new dedicated beam line and with detector upgrades. Knowing the beam direction, the full reconstruction of two photons in the calorimeter and the assumption of the π^0 invariant mass allow to reconstruct the neutral decay vertex; the pion transverse momentum is evaluated assuming the decay vertex in the centre of the beam line. Events with only two energy depositions in the calorimeter, no other activity in the detector and $P_T(\gamma\gamma) > 120\,\mathrm{MeV}/c$ are considered as signal candidate. This high transverse momentum cut provide: the kinematic rejection of $K_L \to \gamma\gamma$ decays; the requirement of high energy for the missing photons, thus reducing the probability for them to be undetected; the suppression of $K_L \to \pi^0\pi^0$ decay with two high-energy photons from different π^0 being detected. The KOTO detector will use primary protons at $30\,\mathrm{GeV}$ corresponding to a K_L^0 decay probability of $\sim 4\%$ (it was $\sim 2\%$ in KEK-E931a) in the given fiducial region. The first physics run is scheduled for March 2013; the first goal is to make the first observation of the decay. The number of expected signal events is 3.5, with a signal-to-noise S/N ratio of 1.4.

---

[7]The π^0 momentum component along the beam line.

Chapter 2

The NA62 detector for $K^+ \rightarrow e^+ \nu_e \gamma$
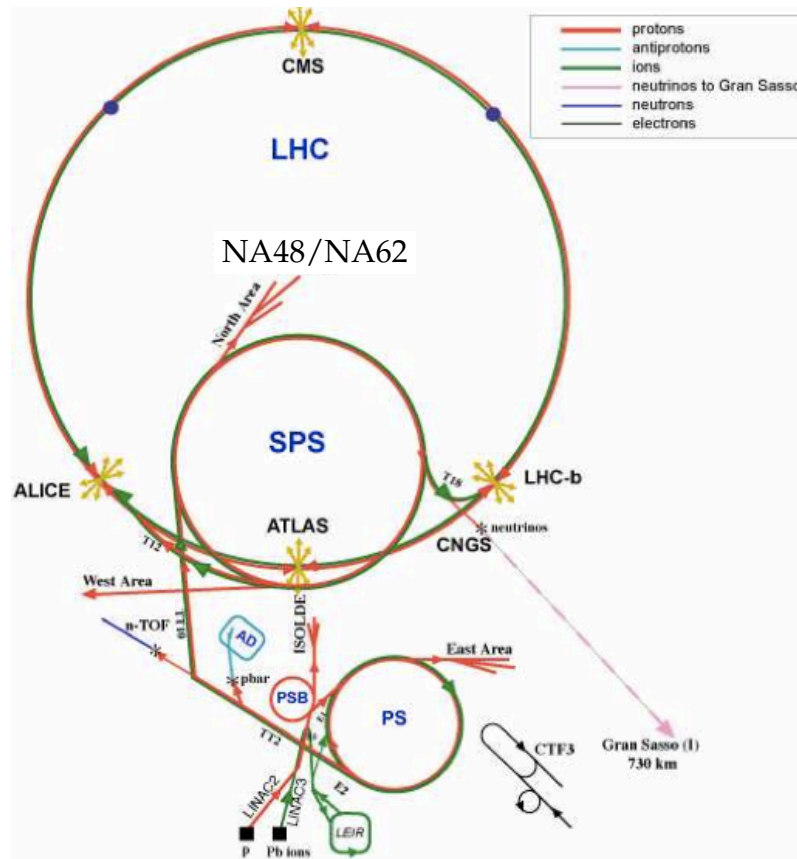
Figure 2.1: Accelerator complex at CERN. The NA62 experiment is located in the North Area of the SPS.

The NA62 (North Area 62) experiment [63] at the CERN Super Proton Synchrotron (SPS), shown in Fig. 2.1, is designed for the study of rare kaon decays. It represents the current kaon physics programme at CERN and offers a complementary approach, with respect to the Large Hadron Collider high energy frontier, to probe new physics at short distances, corresponding to energy scales up to $\sim 100\,\text{TeV}$.

In 2007 the NA62 experimental programme had a phase devoted to a precision test of lepton flavour universality [1]: four months of data taking with minimum bias trigger were accomplished using the beam line and setup of the existing NA48/2 apparatus [64, 65]. In the near future other results based on the same data sample are expected, including χPT tests with $K^+ \to \pi^+ \gamma \gamma$ and $K^+ \to e^+ \nu_e \gamma$ decays (the latter is discussed in the present thesis). The NA48/2 beam line and sub-detectors relevant to the $K^+ \to e^+ \nu_e \gamma$ data analysis are described in this chapter.

2.1 The beam line and detector
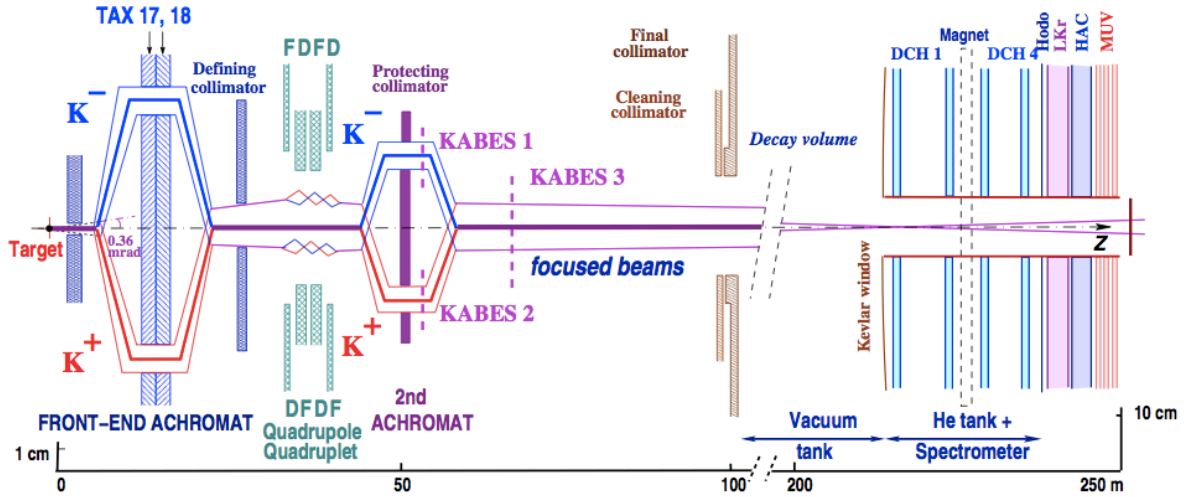
Figure 2.2: The NA48/2 beam line and detector [64, 65].

The NA48/2 beam line provides high intensity kaon beams of both charges (Fig. 2.2). The hadron beams are produced by $400\,\mathrm{GeV}/c$ momentum primary SPS protons[1] impinging on a beryllium target ($2\,\mathrm{mm}$ diameter and $400\,\mathrm{mm}$ length), which corresponds to one interaction length. A system of dipole magnets (front-end achromat in Fig. 2.2), with opposite-sign fields, separates beams of different charge and selects kaons in a narrow momentum band with a central momentum of $74.0\,\mathrm{GeV}/c$ and a spread of $1.4\,\mathrm{GeV}/c$ (rms); kaons are not separated from the other particles produced by the proton interactions in the target. After a stage of collimators and focusing quadrupoles a second achromat system again separates and recombines positive and

---

[1]The intensity of the proton beam is $\sim 10^{11}$ protons per pulse.

negative beams. In the original NA48/2 beam line, a kaon beam spectrometer (KABES in Fig. 2.2) provides the kaon tagging and momentum measurement. In the 2007 data taking the beam spectrometer was not employed and the kaon momentum was not directly measured event by event (see Sec. 3.1.4 for more details). The fiducial decay volume is 114 m long and housed in a cylindrical vacuum tank of 1.9 m to 2.4 m inner diameter. The volume is evacuated to a pressure below 10^{-4} mbar to avoid interactions of beam particles and their decay products with matter. The vacuum tank is followed by a helium-filled volume at atmospheric pressure (of 2.8 m inner diameter and $\sim$ 23 m long), which contains a magnetic spectrometer composed by four drift chambers (DCH1-4 in Fig. 2.2) and a dipole magnet. Between the two tanks (vacuum-helium) there is a thin ($\sim$ 0.4% radiation lengths X_0) Kevlar window; starting from this point, the beam, containing mainly un-decayed particles, travels in vacuum in a carbon fiber beam pipe (152 mm diameter and 1.2 mm thick), which crosses the subsequent detectors in their centre. Fig. 2.3 shows the NA48/2 detector comprising the helium tank with the magnetic spectrometer (described in Sec. 2.2) and the relevant sub-detectors to the $K^+ \rightarrow e^+ \nu_e \gamma$ data analysis: namely the hodoscope (discussed in Sec. 2.3) and the electromagnetic calorimeter (explained in Sec. 2.4).

2.2 The magnetic spectrometer

The magnetic spectrometer system is composed of four drift chambers (DCHs) [66] and a dipole magnet placed between the second and the third chambers (Fig. 2.3). The spectrometer detects charged decay products and measure their direction and momentum. As explained in Sec. 3.1.2, the information from the DCHs upstream the magnet is also used to reconstruct the kaon decay vertex. The magnet provides a field of 0.37 T in the vertical y direction. The field integral along the beam axis corresponds to a 265 MeV/c transverse momentum kick. As mentioned in the previous section, the spectrometer is housed in a stainless steel cylindrical tank, filled with helium at atmospheric pressure; this reduces multiple Coulomb scattering effects[2].

The DCHs have an octagonal shape of 2.9 m transverse width, $4.3 \times 10^{-3} X_0$ depth and a central hole of 160 mm diameter to house the beam pipe. Each chamber is formed by eight planes of 256 sense wires oriented in four different directions (views) orthogonal to the beam axis (see top picture in Fig. 2.4). Each view comprises two planes staggered by 5 mm (half distance between two consecutive wires) along the

---

[2]The amount of helium contained in the tank corresponds to $\sim 8 \times 10^{-3} X_0$.
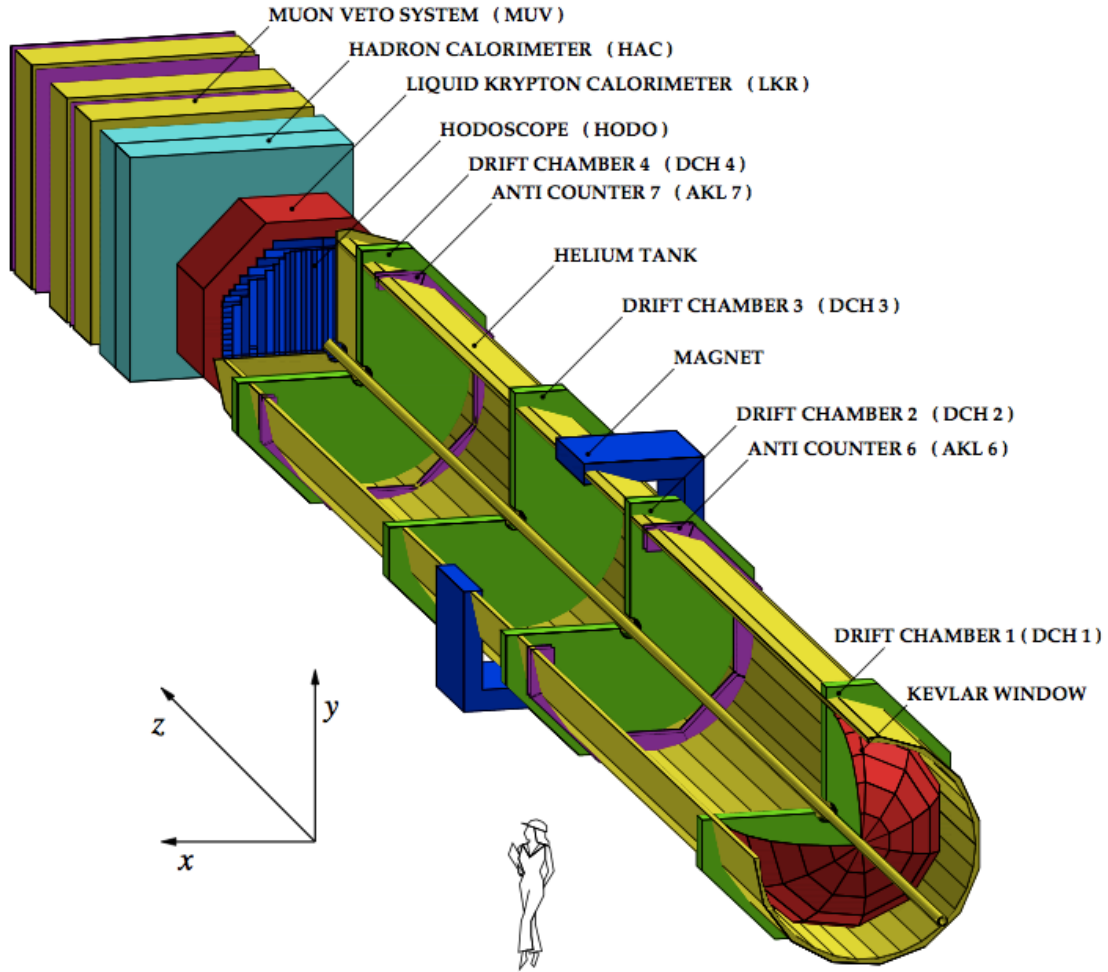
Figure 2.3: The NA48/2 detector: the helium tank comprising the magnetic spectrometer (drift chambers and magnet); the relevant sub-detectors to the $K^+ \rightarrow e^+ \nu_e \gamma$ data analysis, namely the hodoscope and the liquid krypton calorimeter.

beam axis to resolve the left-right ambiguities. The geometry of a DCH cell is sketched in Fig. 2.4 (bottom): two staggered planes forming one view are visible; the electric field is produced by two potential wire planes positioned at each side of a sense wire plane, at a distance of 3 mm. The maximum drift time is 100 ns, corresponding to the half distance (5 mm) between two consecutive wires; this is obtained by operating the DCHs with a gas mixture of Argon - Ethane $(50\% - 50\%)^3$. The spatial resolution on a reconstructed DCH space point is about 90 μm and the momentum resolution of the magnetic spectrometer can be parameterised as: $\frac{\sigma(p)}{p} = 0.48\% \oplus 0.009\% \cdot p(\text{GeV/c})$, where the first term is related to the multiple scattering in the helium tank and in the

---

[3]The drift velocity in the gas is 50 μm/ns.
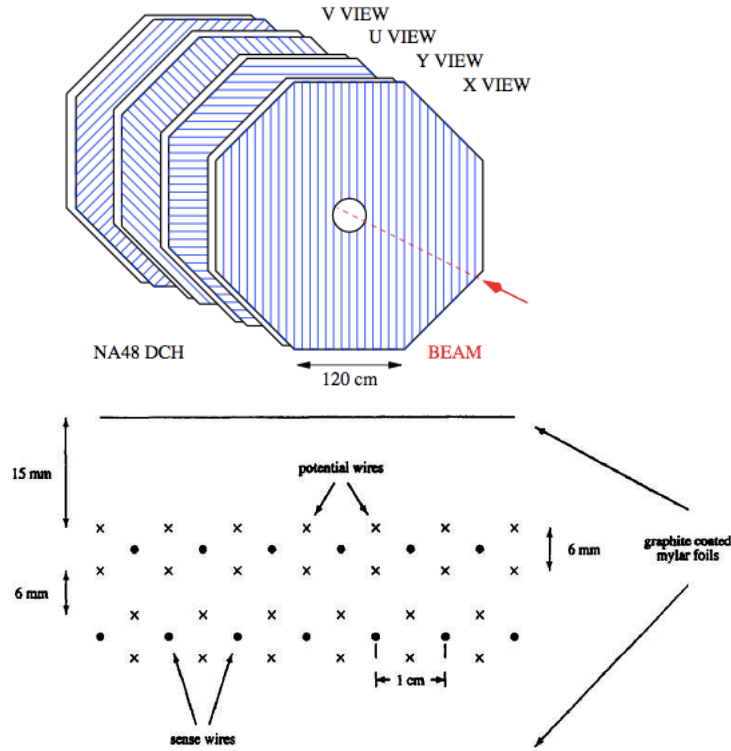
Figure 2.4: NA48 drift chambers (DCHs): (top) X,Y,U,V views; (bottom) geometry of a drift cell.

drift chambers, while the second one to the spatial point resolution of the chambers. The resolution of the track time measurement is $\sim 0.7\,\mathrm{ns}$.

2.2.1 Track reconstruction

In the study of $K^+ \rightarrow e^+ \nu_e \gamma$ events the charged track (e^+) is fully reconstructed making use of the information given by DCHs. The reconstruction algorithm is applied to raw data and it is summarized as follows:

- the raw information are hits in any DCH plane (only spatial informations are used);

- wire hits are grouped in "clusters", which are defined by at least one wire hit in both planes of all views (X,Y,U,V);

- "front segments" are reconstructed with DCH1 and DCH2 with wire hits from both planes in the same view;

- "front tracks" are defined by four front segments (one for each view);

- "space points" are defined in DCH1 and DCH2 using the front track directions and in DCH4 using the clusters;

- due to the small contribution along the y direction of the spectrometer magnetic field, a full track is reconstructed using the information from the space points: the y projection of the front track extrapolation to DCH4 is required to be within 4 cm from a space point in DCH4;

- at this stage of the reconstruction drift times from all hits are used to evaluate an average time and to define a "fit quality" variable, representing the fraction of hits near in time to the average time;

- "mini-tracks" and "mini-space points" are defined by adding the time information in order to improve the space resolution of the track impact points;

- the measured magnetic field map is used to calculate the momentum of the track;

- all parameters of the track: momentum, charge, time, positions before and after the magnet are stored in a framework (COmPACT [67]) containing the output of the reconstruction from all detectors.

2.3 The hodoscope

The hodoscope (HOD) is located downstream of the helium tank and in front of the electromagnetic calorimeter. The HOD provides the timing for charged decay products with a resolution of 200 ps: it is composed by 128 plastic scintillation counters arranged in two planes, which are separated by 75 cm. The counters are disposed horizontally in the first plane and vertically in the second one (see Fig. 2.5). The thickness of a single counter is 2 cm ($\sim 0.05 X_0$), the length varies from 60 cm up to 121 cm and the width from 6.5 cm (in the region close to the beam pipe) to 9.9 cm. The HOD has a central hole of 128 mm radius for the beam pipe. Each HOD plane is divided into four quadrants (made of 16 counters). Each quadrant is sub-divided into two sub-quadrants defined by the first 7 counters near the beam pipe and the remaining 9 ones. Considering both horizontal and vertical HOD planes the total number of sub-quadrants is 16; these are used to defined as many sets of fast logical signals (see Sec. 2.6) for trigger purposes.
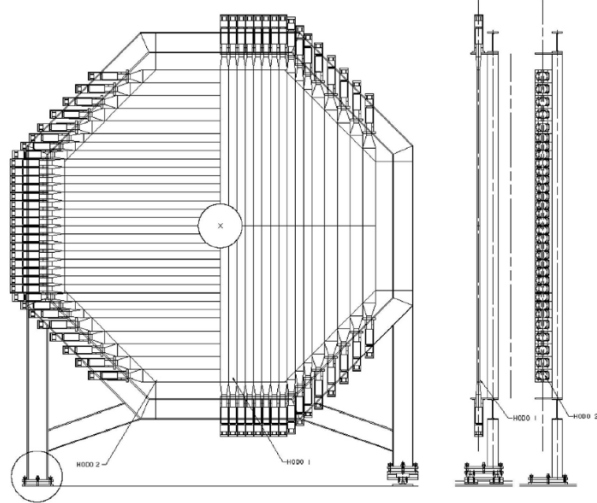
Figure 2.5: Schematic layout of the HOD detector.

2.4 The Liquid Krypton calorimeter

The NA48 Liquid Krypton (LKr) calorimeter [68] is a fundamental detector constructed for the studies of direct CP-violation in the neutral kaon system performed at CERN [69]. In the present $K^+ \rightarrow e^+ \nu_e \gamma$ data analysis the LKr is used for the positron identification and the reconstruction of the photon.

The calorimeter is a quasi-homogeneous ionization chamber; the liquid krypton was chosen as a radiator because of the energy response linearity and the capability of long term performances without ageing. The Kr radiation length ($X_0 = 4.7$ cm) and the Molière's radius ($R_M = 4.7$ cm) allow to contain high energy (> 10 GeV) electromagnetic showers in a compact detector. The LKr calorimeter has an octogonal shape (see Fig. 2.6) in the plane orthogonal to the beam axis and is 127 cm long in the longitudinal direction (corresponding to $27X_0$ in depth). The LKr has a central hole of 80 mm radius to house the beam pipe. With about 10 m^3 of liquid krypton as active material, electromagnetic showers up to 50 GeV are fully contained ($> 99\%$) in the LKr depth. The LKr has a projective readout consisting of copper/beryllium ribbons extending from the front to the back of the detector. The active volume is divided into 13, 248 readout cells with a transverse size of approximately 2×2 cm^2 each (right panel in Fig. 2.6) and no longitudinal segmentation. Only about 60 out of the 13, 248 LKr cells, known as "dead cells", have electronic faults (faulty preamplifiers, bad pedestal and/or a very unstable response to calibration pulses) preventing their utilisation. After calibration and corrections, the energy resolution of the LKr calorimeter can be
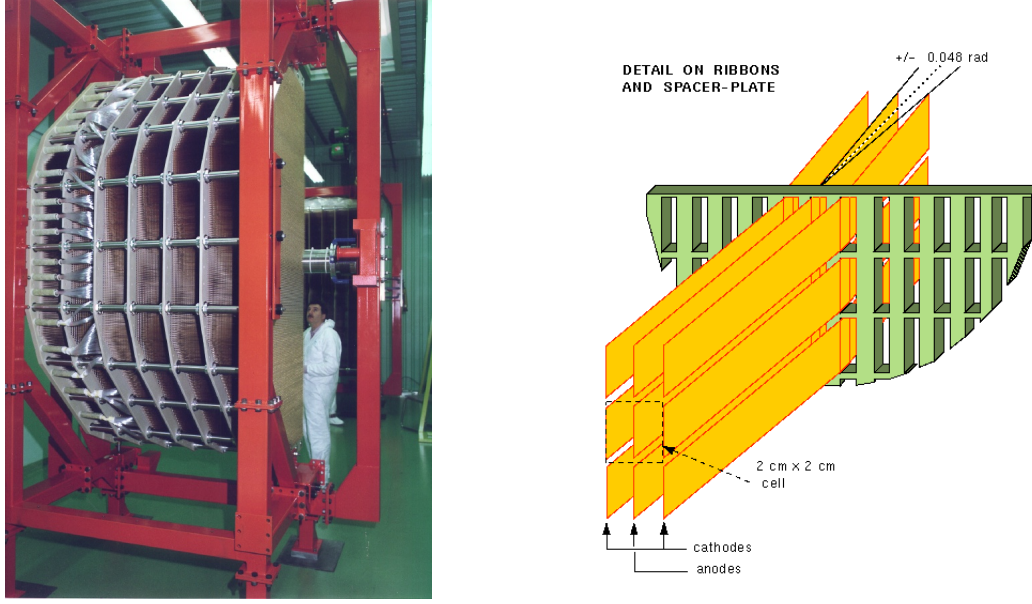
Figure 2.6: LKr calorimeter: (left) half structure while under construction; (right) details of the cell structure.

parametrized as: $\frac{\sigma(E)}{E} = \frac{3.2\%}{\sqrt{E}} \oplus \frac{9\%}{E} \oplus 0.42\%$, in units of GeV. The first term depends on stochastic sampling fluctuations, the second one on electronic noise and Kr natural radioactivity and the last one on inhomogeneities, material in front of the calorimeter and the non perfect inter-calibration of the cells. The spatial and time resolutions are (in units of GeV, cm and ns): $\sigma_{x,y} = \left(\frac{42\%}{\sqrt{E}} \oplus 5\% \right)$ and $\sigma_t = \left(\frac{2.5}{\sqrt{E}} \right)$, respectively.

2.4.1 Cluster reconstruction

In the study of $K^+ \to e^+ \nu_e \gamma$ events the photon candidate is reconstructed using the information from the LKr calorimeter. The LKr reconstruction algorithm provides energy deposition, time, position and width of a shower (cluster) produced by a particle impinging on the calorimeter. The algorithm can be summarized as follows:

- the pedestal of each cell is subtracted to evaluate the cell energy;

- a "seed" is defined if a cell has an energy larger than 100 MeV;

- a loop on all seeds is performed to identify a "cluster", which is defined by a cell with more energy than the 8 surrounding ones and such that: $E_{seed} > 0.18\text{GeV} + 1.8E_{av}$, where E_{av} is the average energy of the eight surrounding cells;

- to determine the cluster energy another loop on the LKr cells is performed: for each cell the number of clusters within 11 cm and 20 ns is evaluated and if only one is found, then the cell energy is added to the cluster energy;

- when a cell belongs to more than one cluster according to the above procedure, then the cell energy is shared among the clusters according to the expected (simulated) energy profile distribution;

- the cluster position is evaluated as the centre of gravity of the energy deposition in a box of 3×3 cells around the seed position;

- the cluster time is defined as the average time between cells in a box 5×5 cells centred on the seed position;

- the shower width (i.e. the cluster size) is evaluated separately in x and y as the r.m.s. of the energy distribution in a box of 5×5 cells centred on the seed position.

2.5   The "neutral" hodoscope

The "neutral" hodoscope (NHOD) is a plane of 256 vertical bundles of scintillating fibers positioned inside the LKr calorimeter, at the depth of $\sim 9.5 X_0$, corresponding to the maximum development of an electromagnetic shower of ~ 25 GeV. The NHOD gives an independent measurement of the timing of electromagnetic showers and it is used for trigger purposes; the signal produced by a shower provides an independent trigger (called T0N), which is used as a control signal to measure the efficiency of the main data acquisition trigger. By construction, the NHOD is fully efficient for clusters with energy ≥ 25 GeV, with a typical time resolution of $\sigma_t = 250$ ps.

2.6   The $K^+ \rightarrow e^+ \nu_e \gamma$ trigger logic and data taking

The NA62 trigger is a multilevel system, designed to cope with rates of particles in the main sub-detectors at the level of 1 MHz. The full acquisition is synchronized by a 40 MHz clock. The system is divided in two parts: the "Charged" and the "Neutral" trigger. The former collects information from the HOD and DCHs: some examples, which are relevant for this analysis, are the $Q1$ and the $1TRKLM$ signals, explained later in this section. The latter relies on calorimeter energy information and an example

is the NHOD signal, later discussed as a minimum bias trigger for efficiency studies. The two sub-systems are controlled by the Trigger Supervisor (TS) that collects all the information and takes the final decision to read-out or discard the event. The trigger signals, which arrive to the TS, are then sent to external acquisition units, called Pattern Units, for monitoring purposes and for the trigger efficiency studies.

$K^+ \rightarrow e^+ \nu_e \gamma$ events are characterized by one charged track reconstructed by the DCHs and two clusters in the electromagnetic calorimeter. Due to the signal event topology, the $K^+ \rightarrow e^+ \nu_e \gamma$ decays are selected using both "Charged" and "Neutral" trigger information. The trigger signal used to select $K^+ \rightarrow e^+ \nu_e \gamma$ events is a combination of sub-signals, $Q1 \times E_{LKr} \times 1TRKLM$, where:

- the $Q1$ requires at least one coincidence in space and time between the hits in vertical and horizontal scintillators belonging to the same HOD sub-quadrant[4]. The $Q1$ ensures the presence of at least one reconstructed charged track among the decay products;

- the E_{LKr} corresponds to a minimum energy deposition in the LKr electromagnetic calorimeter of 10 GeV;

- the $1TRKLM$ triggers events with at least 1 hit in more than 1 view and less than 15 hits in any view in DCH1-2-4. This signal rejects events with no tracks or high multiplicity (more than 56 hits per DCH) in the spectrometer.

The RAW data are processed by a software (L3) performing the event reconstruction, filtering the data and creating different output streams. The program output is in COmPACT [67] format and contains reconstructed information and physics quantities. Data were collected during the summer 2007 for a total of ~ 120 days. The sample used in this analysis corresponds to ~ 53 days of data taking with K^+ beam only.

---

[4]The definition of a HOD sub-quadrant has been given in Sec. 2.3

Chapter 3

$K^+ \to e^+ \nu_e \gamma$ (SD$^+$) measurement

The study of the radiative leptonic $K^+ \to e^+ \nu_e \gamma$ ($K_{e2\gamma}^+$) decay is based on a partial[1] sample ($\sim 40\%$) of the data collected by the NA62 experiment in 2007. The measurement of the form factors and the comparison with the current PDG average values [16] are reported in this chapter. The analysis proceeds through the following steps:

- definition of criteria for the signal event selection (see Sec. 3.1): counting of the number of candidates $N(K_{e2\gamma}^+, SD^+)$ passing the selection;

- measurement of the number of kaon decays inside a given fiducial region during the considered data taking period (see Sec. 3.2): this quantity, referred to as the kaon flux $\Phi(K^+)$, is used for the normalisation;

- determination of the trigger efficiency with a data-driven technique (see Sec. 3.3).

- estimation of the background contamination $N(bkg)$ with Monte-Carlo simulations (see 3.4);

3.1 $K^+ \to e^+ \nu_e \gamma$ (SD$^+$) event selection

The aim is to select $K_{e2\gamma}^+$ (SD$^+$) candidates and distinguish them from the background. To this purpose the selection criteria are optimised using MC simulations of the signal and background decay channels. Particular care must be taken for the rejection of $K^+ \to \pi^0 e^+ \nu_e$ and $K^+ \to \pi^+ \pi^0$ decay channels. The former may lead to a $K_{e2\gamma}^+$ (SD$^+$) signature if one photon from the $\pi^0 \to \gamma\gamma$ decay is lost. The latter may lead to a $K_{e2\gamma}^+$ (SD$^+$) signature if the π^+ is mis-identified as a e^+ and one photon

---

[1]The data sample analysed is the most suitable for the $K_{e2\gamma}^+$ study in terms of running conditions.

from the $\pi^0 \to \gamma\gamma$ decay is lost. The MC simulations are produced with the official NA62 software (CMC) [70], based on Geant3 package [71], which takes into account: the beam line geometry and optics; a detailed description of the detector layout, material and reconstruction algorithms; the main physical processes (bremsstrahlung emission, compton scattering, electron-positron annihilation, δ ray production, multiple coulomb scattering, hadronic and nuclear interactions), as well as secondary particle decays ($\pi^0 \to \gamma\gamma$, $\pi^0 \to \gamma e^+ e^-$, $\mu \to e\nu\bar{\nu}$, $\pi^\pm \to l\bar{\nu}$ with $l = \mu, e$). The simulated events are converted in the same format of experimental data (*COmPACT* [67]), so that the same analysis tools are applicable for both data and MC events. CMC allows to choose the theoretical model to be used for the generation of a decay channel. The MC event list for the $K^+_{e2\gamma}$ (SD$^+$) decay is produced with the form factors F_V, F_A measured by KLOE [21] (see Eq. 1.22) and reported in [16]. All MC event lists (signal and backgrounds) used in this analysis are the official NA62 productions [72]. Three event selection phases can be identified:

1. the collection of events with only one charged track, compatible with a positron produced in a kaon decay inside the fiducial decay region and the reconstruction of the kaon decay vertex;

2. the analysis of the energy deposition in the LKr calorimeter to identify events with two isolated electromagnetic showers, compatible with one being produced by the track and the other by the radiative photon;

3. the final separation of the signal from the main background components by means of discriminating kinematic variables.

3.1.1 Fiducial decay region
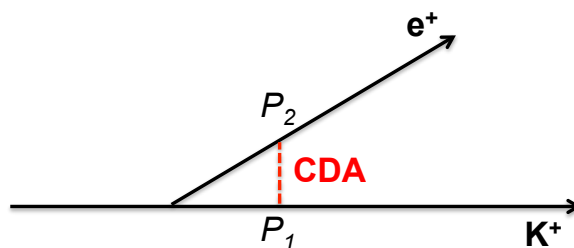
Figure 3.1: Schematic of the Closest Distance of Approach (CDA) between the kaon and the positron trajectories.

To select events with a charged track produced in a kaon decay, the Closest Distance of Approach (CDA) between the kaon and the track trajectories is computed, as shown in Fig. 3.1, using the nominal positions of the kaon beam axis and the positions of the charged track as measured in DCH. The distribution of the CDA parameter for MC $K_{e2\gamma}^+$ (SD$^+$) events is shown in Fig. 3.2 (left panel). Charged tracks with CDA < 3 cm are selected, being considered as coming from a kaon decay.

The coordinate system of the NA62 experiment is represented in Fig. 2.3. It is a cartesian reference system: the z axis is along the kaon beam line; the y direction is vertical and orthogonal to the kaon beam line (from bottom to top); the x axis determines a right-handed reference frame. The origin of the coordinate system ($x = y = z = 0$) is defined as the point, along the z axis, 120 m downstream the production target.

To select events with a charged track produced in a kaon decay inside the fiducial decay region, the longitudinal coordinate of the kaon decay vertex, z_{vtx}, is computed with the CDA as follows (Fig. 3.1):

$$z_{vtx} = \frac{z_{P_1} + z_{P_2}}{2},\tag{3.1}$$

where P_1 and P_2 are the points belonging to the kaon and track trajectories, respectively, and such that, by definition of CDA, the distance between the above lines is minimum. The distribution of z_{vtx} for MC $K_{e2\gamma}^+$ (SD$^+$) events is shown in Fig. 3.2 (right panel); the arrow corresponds to the longitudinal coordinate of the downstream plane of the final collimator on the beam line, $z_{coll} = -18$ m. Due to resolution effects some events are reconstructed with $z_{vtx} < z_{coll}$. Two fiducial regions are used throughout the analysis for historical reasons and the final result is not dependent on this choice. One fiducial region, defined by -20m $< z_{vtx} < 90$m, is chosen to evaluate the kaon flux (Sec. 3.2); the other one, defined by -16m $< z_{vtx} < 90$m is fixed for the event selection. The lower bound, $z_{vtx} = -16$ m, is chosen to avoid regions near the final collimator, whose simulation might not be optimal. The upper bound, $z_{vtx} = 90$ m, accepts all signal events, while rejecting background events decaying too close the downstream detectors and wrongly reconstructed.

3.1.2   Charged track selection

In the following procedure the purpose is to identify a well reconstructed track from the signal channel, while being independent as much as possible on the presence of tracks from accidental activity. This is useful for the background rejection and to perform an accurate extraction of the form factors. Within a first step of the track
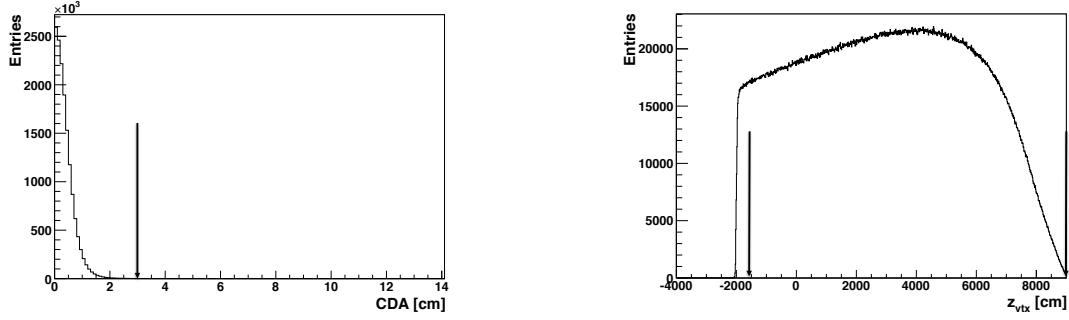
Figure 3.2: (Left) Closest Distance Approach (CDA) parameter for MC $K_{e2\gamma}^+$ (SD$^+$) events. (Right) Longitudinal decay vertex (z_{vtx}) for MC $K_{e2\gamma}^+$ (SD$^+$) events; the arrows represent the cuts applied in the event selection. $z_{vtx} = -18$ m corresponds to the position of the final collimator on the beam line.

selection a sample of "bad" tracks is identified for each event; a track is considered "bad" if it satisfies at least one of the following criteria (it is otherwise marked as "good"):

- the track is beyond the fiducial kaon decay region, namely $z_{vtx} < -20$ m or $z_{vtx} > 90$ m;

- the track momentum is $p_{trk} < 3$ GeV/c or $p_{trk} > 75$ GeV/c, that is beyond the kinematic limits allowed for 75 GeV/c kaon decays;

- the CDA is larger than 10 cm, meaning that the track is not compatible with being produced in the considered kaon decay vertex;

- the track time with respect to the trigger time is $|\Delta t| > 62.5$ ns, meaning that the track time is not compatible with the trigger time;

- the track is fake and it results from ambiguities in the reconstruction algorithm produced by hits with similar y coordinate in DCH4; the track is called "ghost". A "ghost" track is usually very close to a real one; their separation at the DCH1 plane is less than 1 cm. If a pair of tracks with 3 GeV/$c < p_{trk} < 75$ GeV/c and a distance at DCH1 below 0.5 cm is found, the track with lower reconstruction fit quality is marked as "ghost". When the fit qualities are equal, the quantity $\mathcal{Y} = |y_4^a - y_4^b|$ is evaluated for each track; y_4^b and y_4^a are the y coordinates of the track position extrapolated at DCH4, using the reconstructed track positions and directions before and after the magnet, respectively. As the magnet bends

44

the trajectories of charged particles in the horizontal plane only, the track with larger $\mathcal{Y}$ is defined as "ghost".

Bad tracks include several sources such as: secondary particles produced upstream of the final collimator (beam-induced), cosmic rays, accidentals. After the above analysis the event is accepted only if exactly one "good" track is found: this is considered to be the positron candidate track. The second step of the track selection aims at identifying the track as a positron. To be compatible with a positron the charged track must satisfy the following additional requirements:

- positive charge $q > 0$;

- track quality > 0.7; the variable corresponds to the fraction of hits, in each DCH view, which are in time with the average time of the total hit sample;

- track impact points are within the fiducial geometrical acceptance of sub-detectors (regions close to the beam pipe and detector edges are removed). This requirement defines the proper sensitive areas of sub-detectors and ensures a reliable track reconstruction. Knowing the track positions and directions at two given points before and after the magnet, the track impact point at each sub-detector is extrapolated; the following distances R are evaluated with respect to the z axis in detector front planes and required to be:

  - at DCH-1,2,4 planes: $12 \text{ cm} < R_{DCH} < 115 \text{ cm}$;

  - at the HOD plane: $14 \text{ cm} < R_{HOD} < 115 \text{ cm}$;

  - at the LKr calorimeter: $R_{LKr} > 15 \text{ cm}$; an upper octagonal-shaped cut is applied and the working conditions of certain LKr areas, masked during the data taking, are accounted for (more details can be found in [73]).

- track time as measured by the charged hodoscope[2]: $|t_{trk} - t_{trigger}| < 20 \text{ ns}$;

- minimum track distance of 2 cm from the nearest dead cell in the LKr calorimeter; this requirement ensures a reliable reconstruction of the electromagnetic shower;

- as already mentioned, the associated decay vertex must be within the fiducial decay region: $-16 \text{ m} < z_{vtx} < 90 \text{ m}$.

---

[2]Such variable is not filled for all events due to the hodoscope intrinsic inefficiency ($\sim 1\%$). When that is the case the time measurement is taken from the DCH. The default time relies on the hodoscope because of a better time resolution with respect to the DCH.

- as already mentioned, CDA < 3 cm.

- 10 GeV/c < p_{trk} < 55 GeV/c, where p_{trk} is the track momentum. The lower limit is dictated by the E_{LKr} > 10 GeV trigger condition (explained in detail in Sec. 3.3); together with the photon energy requirement it ensures more than 15 GeV energy deposit in the LKr calorimeter. The upper limit is chosen in order to minimise the $K^+ \to \pi^+\pi^0$ background contamination. Fig. 3.3 shows the squared missing mass $m^2_{miss} = (P_K - P_e - P_\gamma)^2$ distributions as functions of the track momentum for the MC signal $K^+_{e2\gamma}$ (SD$^+$) and background $K^+ \to \pi^+\pi^0$ decays passing the signal event selection. P_K, P_e and P_γ are the kaon, positron and photon reconstructed 4-momenta, respectively. For the signal (left panel) the distribution peaks at $m^2_{miss} = 0\,\text{GeV}^2/c^4$, compatible with the mass of the neutrino, while it is quite uniform over the whole track momentum range. For the background (right panel) the distribution is shifted towards negative m^2_{miss} values and it peaks in a narrow track momentum range of (60,70) GeV/c; this is a consequence of the specific kinematics of $K^+ \to \pi^+\pi^0$ events entering the signal region (the background is discussed in Sec. 3.4).
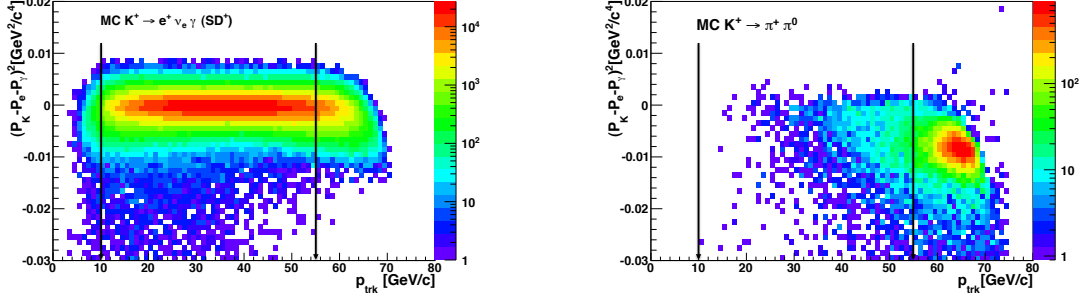
Figure 3.3: Distributions of $m^2_{miss} = (P_K - P_e - P_\gamma)^2$ vs the p_{trk} for $K^+_{e2\gamma}$ (left, signal) and $K^+ \to \pi^+\pi^0$ (right, background) MC events. The difference in the spectra suggests a cut on the track momentum in the range (10,55) GeV/c (see arrows) in order to minimise the background contamination from $K^+ \to \pi^+\pi^0$ events.

The lepton identification as a positron is based on the reconstruction of the ratio E_{LKr}/p_{trk} between the track energy deposition in the LKr calorimeter (energy of the associated cluster) and the track momentum measured by the magnetic spectrometer [1]. The associated cluster is defined as the closest cluster to the track impact point at the LKr calorimeter at a distance within 1.5 cm and in time with the track ($|\Delta t_{trk-ass.cl}| < 6$ ns). Tracks with $0.95 < E_{LKr}/p_{trk} < 1.1$ are identified as positrons (Fig. 3.4).
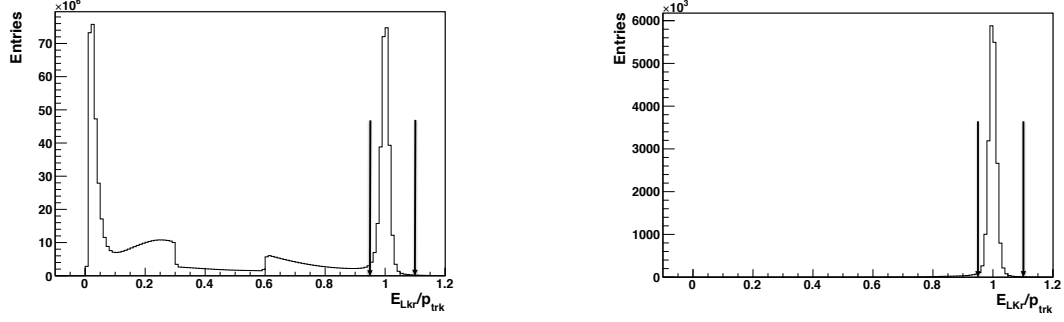
Figure 3.4: E_{LKr}/p_{trk} distributions for data (left) and $K_{e2\gamma}^+$ (SD$^+$) MC events (right) passing the charged-track selection cuts described in Sec. 3.1.2. The depletion of events in the region $0.3 < E_{Lkr}/p_{trk} < 0.6$, outside the signal region, is due to a trigger feature and is known from previous analyses. The arrows represent the cuts applied in the event selection to identify positrons.

3.1.3   Photon selection

The cluster associated to the radiative photon from $K_{e2\gamma}^+$ (SD$^+$) decay is selected among the "good" clusters in the LKr calorimeter. A "good" cluster satisfies each of the following criteria:

- the cluster is not associated to the track;

- the cluster energy is $E > 5$ GeV (Fig. 3.5). This requirement, together with the cut on the track momentum, ensures more than 15 GeV energy deposit in the LKr calorimeter and therefore high efficiency of the $E_{LKr} > 10$ GeV trigger condition (see Sec. 3.3);

- the cluster position is within the LKr acceptance, already defined for the charged track: namely the cluster distance with respect to the z axis, at the LKr calorimeter, is required to be $R_{LKr} > 15$ cm; an outer octagonal-shaped cut is applied and the working conditions of certain LKr areas, masked during the data taking, are accounted for [73];

- the cluster time with respect to the positron candidate time is: $|\Delta t_{trk-cl}| < 6$ ns (Fig. 3.6);

- the cluster distance from the nearest dead cell in the LKr calorimeter is greater than 2 cm;
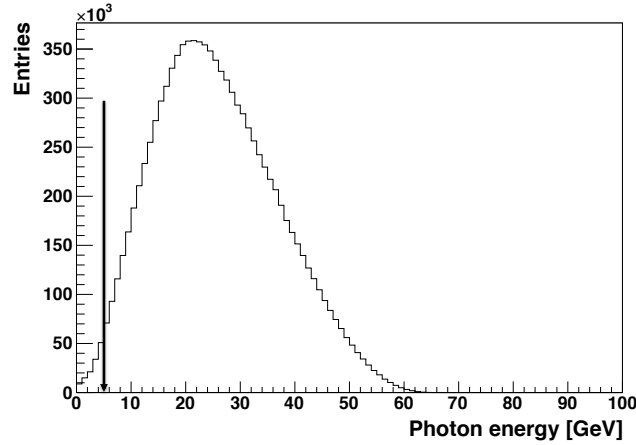
Figure 3.5: Photon energy distribution for $K_{e2\gamma}^{+}$ (SD^{+}) MC events in the lab. frame. The arrow represents the lower cut applied in the event selection.
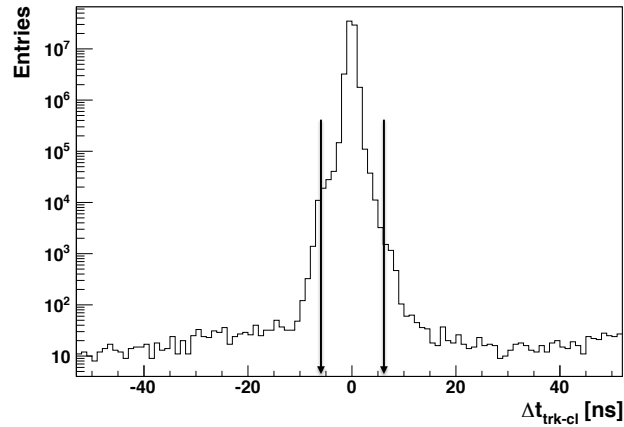
Figure 3.6: Data distribution of the time difference between the positron track and the photon cluster at LKr (Δt_{trk-cl}). The arrows represent the cut applied in the event selection.

- the cluster is isolated: its distance from any other cluster is $R_{cl-cl} > 20$ cm. This requirement avoids cluster overlapping and energy sharing, while implying a negligible reduction ($2 \cdot 10^{-4}$) in the signal acceptance.

The event is accepted only if exactly one "good" cluster is found: it is assumed to be the photon candidate cluster. A further selection is applied to this cluster.

- To reject events in which the selected cluster corresponds to a photon produced via positron bremsstrahlung, a minimum distance of 8 cm between the photon cluster and the track extrapolation at the LKr plane, without considering the

48

magnet bending, is required.

- If the photon interacts in the passive material traversed before reaching the LKr calorimeter (e.g. the DCH flanges), the selected cluster may be produced by one of its interaction products. For these events, the reconstructed squared missing mass $m_{miss}^2 = (P_K - P_e - P_\gamma)^2$ increases. Such effect has been studied with a control sample of $K^+ \to \pi^0 e^+ \nu_e$ decays. Given the photon trajectory, as introduced next in Sec. 3.1.6, the photon impact point (x_γ, y_γ) at the DCH1 front plane can be computed. The photon radius at DCH1 is then defined as $R_\gamma = \sqrt{x_\gamma^2 + y_\gamma^2}$ and its data-MC ratio for fully reconstructed $K^+ \to \pi^0 e^+ \nu_e$ events is shown in Fig. 3.7. A discrepancy for $R_\gamma < 12\,\text{cm}$ is found: this distance is compatible with the actual size of the DCH flanges and thus could indicate an inadequate description of these interactions in the MC. To make the analysis less dependent on such effect, a radial cut $R_\gamma > 12\,\text{cm}$ is imposed.

The LKr calorimeter is also used as a veto by rejecting events with additional extra clusters in time with the track ($|\Delta t_{trk-cl}| < 6\,\text{ns}$) and with energy $E_{LKr} > 2\,\text{GeV}$.
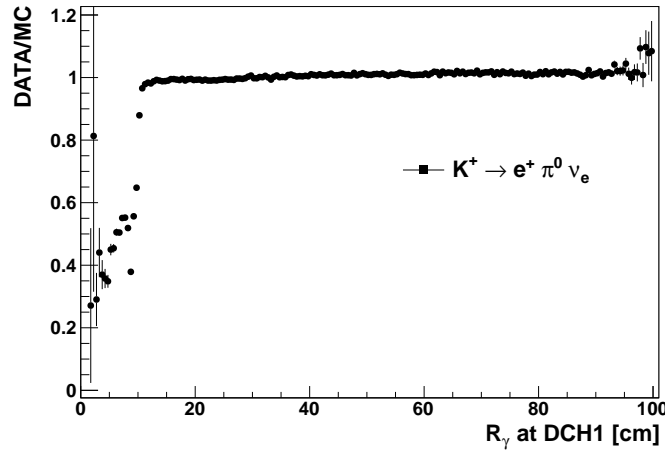
Figure 3.7: Photon radius at the DCH1: data-MC ratio for fully reconstructed $K^+ \to \pi^0 e^+ \nu_e$ events. The discrepancy for values below 12 cm is compatible with photon interactions in the DCH1 flange, which are not adequately simulated.

3.1.4 Kaon momentum

Charged kaons are delivered with a central momentum of 74 GeV/c and a spread of 1.4 GeV/c (r.m.s.). The beam transverse size at the entrance of the decay volume is

about $\delta x = \delta y = 4\,$mm (r.m.s.) and its horizontal and vertical angular divergences are about $20\,\mu$rad (r.m.s.). The kaon 3-momentum components are not directly measured for each event but the beam average, measured with reconstructed $K^+ \to \pi^+\pi^+\pi^-$ decays, is instead used to compute the $K^+_{e2\gamma}$ (SD$^+$) kinematic variables (see [74, 75] for further details). The collected data are divided into periods of ~ 100 SPS bursts with stable data taking conditions[3] and the distributions of all relevant quantities (central beam momentum, transverse position at the entrance of the vacuum tank and directions) are fitted in each time interval to extract the mean reconstructed values, which are recorded in a database. The same procedure is applied to MC simulated events with one set of constants per run (all events are generated under the same conditions within a given run). The beam mean momentum p^0_K, profile (x, y) and dy/dz slope varied slowly over time, in the ranges of about 0.1 GeV/c, 1 mm and 10μrad, respectively; the mean dx/dz slope, correlated with the magnetic spectrometer polarity, was switched between the two values of about -200μrad to $+200\mu$rad according to the magnet current.

3.1.5 Corrections

Several kinds of corrections are applied to the events in order to improve the resolution on the track momentum as well as on the energy and position of the LKr clusters. These corrections were evaluated in previous analyses [1] and studied with dedicated data samples. The procedures are documented in [72]. The main points are briefly summarised below.

3.1.5.1 LKr energy corrections

- LKr calorimeter cells are read out above a certain threshold. This results in a non-linear relation between the deposited and measured energy. The MC simulation does not reproduce such a feature and a correction must be applied to all clusters (for data only). Such correction is negligible for cluster energies above 10 GeV, while it can be otherwise parameterised as a polynomial in the measured energy.

- In order to improve the resolution and uniformity of the LKr response and to decrease the electron ID inefficiency, a LKr cell-by-cell energy calibration has been studied, separately for each period of the data taking, by using a sample

---

[3]If the run conditions changed the acquisition was ended and a new one started.

of positrons from $K^+ \rightarrow \pi^0 e^+ \nu_e$ decays. A correction is applied to the data to calibrate the LKr response.

3.1.5.2 Corrections to cluster position: projectivity and LKr to DCH alignment

The geometry of the LKr is such that the axes of the calorimeter ionization cells focus to a point P (projectivity point) at a distance $D = 10998$ cm in front of the LKr plane. The particles originating close to this point impinge on the cells with a trajectory parallel to such axes with the result that the reconstructed transverse coordinates of the clusters do not depend on the longitudinal position of the shower inside the calorimeter. However, if the decay vertex is far from the projectivity point, a small correction to the cluster position depending on the shower depth has to be applied (the projectivity correction). The depth d_{sh} depends logarithmically on the shower energy and the corrected transverse coordinates (x, y) are linked to the measured positions (x_0, y_0) by the formula:

$$(x, y) = (x_0, y_0) \cdot \left(1 + \frac{d_{sh}}{D} \right) ,$$

where $d_{sh}[\text{cm}] = 16.5 + 4.3 \ln(E[\text{GeV}])$ is the effective shower depth. The projectivity geometry of the LKr calorimeter is simulated in CMC, thus the correction must be applied to both data and MC events. In addition, the cluster positions have to be corrected for a residual mis-alignment between the LKr and the DCHs. The shift and rotation parameters of the misalignment are computed using a sample of electrons and comparing their extrapolated positions measured by the spectrometer with the correspondent LKr cluster positions. The complete correction to the cluster positions, accounting for both the projectivity and the LKr to DCH misalignment, is explained in [76, 77]. The size of the correction to the transverse cluster positions is usually less than 0.5 cm, while the typical value of the shower depth is about 30 cm. The explicit expression for the correction of data is:

$$x = (x_0 + 0.136\text{cm} + 0.87 \cdot 10^{-3} y_0) \cdot \left(1 + \frac{d_{sh}}{D} \right) ,$$

$$y = (y_0 + 0.300\text{cm} - 0.87 \cdot 10^{-3} x_0) \cdot \left(1 + \frac{d_{sh}}{D} \right) ,$$

$$z = z_{LKr} + d_{sh} ,$$

while for MC events it is:

$$x = (x_0 - 0.013\text{cm}) \cdot \left(1 + \frac{d_{sh}}{D}\right) ,$$

$$y = y_0 \cdot \left(1 + \frac{d_{sh}}{D}\right) ,$$

$$z = z_{LKr} + d_{sh} ,$$

where z_{LKr} is the longitudinal position of the LKr front plane.

3.1.5.3 Internal DCH alignment: α and β correction

The internal mis-alignment of the drift chambers and the mis-calibration of the magnetic field in the spectrometer induce a bias in the measurement of the track momentum [78]. A correction is implemented to the measured momentum p_0; the effects of mis-alignment and field mis-calibration are parametrized with two parameters, α and β. The corrected track momentum p_{trk} can be obtained using the formula [72,78]:

$$p_{trk} = p_0 \cdot (1 + q \cdot \alpha \cdot p_0) \cdot (1 + \beta)$$

where q is the charge of the track. The absolute values of α and β are time-dependent and of the order of 10^{-5}GeV^{-1} and 10^{-3}, respectively. In addition, the mean beam momentum, p_K^0, from the database, introduced in Sec. 3.1.4, has been β-corrected according to the formula:

$$p_K = p_K^0 \cdot (1 + \beta).$$

These corrections are applied to both data and MC events. The α and β parameters have been evaluated on periods of ~ 100 SPS bursts during the data taking.

3.1.5.4 Earth magnetic field effect

A stray magnetic field is present in the decay region; the source of it is due to the earth magnetic field. The trajectories of charged particles are bent with respect to their initial direction. As a consequence, the directions measured at DCHs are different from the ones at the decay vertex. As a numerical example, the discrepancy is $\sim 10^{-5}$ rad for $\sim 50\,\text{GeV}/c$ over the full tank. To correct for such an effect, the charged tracks are traced backwards through the earth field to the decay vertex position and their directions are corrected according to the measured field.

3.1.5.5 Correction for kaon momentum spectrum width

The spectra of data and MC kaon momentum slightly differ in the core width and in the high momentum tail. The effect has been studied with $K \to \pi\pi\pi$ events [72, 75, 79]. The Data/MC ratio from samples of $K_{3\pi}$ events is shown in Fig. 3.8, in arbitrary units. This shows a difference in the core width (around the nominal value of $74\,\mathrm{GeV}/c$) and also in the high momentum tail. A weight w is applied to MC events according to the formula below:

$$w = 1 + \tau \cdot (p_K^{gen} - 74\,\mathrm{GeV})^2, \tag{3.2}$$

where p_K^{gen} is the generated kaon momentum and τ is a time-dependent parameter in the range: $(-0.08 < \tau < 0.08)\,\mathrm{GeV}^{-2}$. For the partial data sample analysed in this thesis: $\tau = 0.07\,\mathrm{GeV}^{-2}$. Detailed studies and further information can be found in [75, 79].
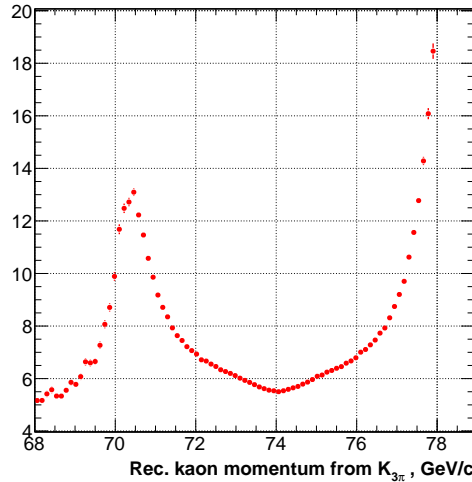
Figure 3.8: Data to MC ratio of the kaon momentum distribution reconstructed using $K_{3\pi}$ events [72]. The formula for the weight is chosen to flatten the parabolic-like shape visible in the distribution.

3.1.6 Signal event reconstruction and kinematics

The reconstruction of the $K_{e2\gamma}^+$ (SD$^+$) events is performed using the information of the candidate positron and the cluster associated to the candidate photon. The positron 4-momentum, P_e, is reconstructed by using the momentum and directions (earth field corrected) of the track measured by the spectrometer (in the hypothesis of the positron mass), while the photon 4-momentum, P_γ, is computed using the energy

and the position of the LKr cluster, as well as the decay vertex position. The slopes of the photon trajectory, $(dx/dz)_\gamma$ and $(dy/dz)_\gamma$, are reconstructed with the corrected position of the photon cluster (x_{cl}, y_{cl}, z_{cl}) at the LKr calorimeter and the position of the decay vertex $(x_{vtx}, y_{vtx}, z_{vtx})$:

$$(dx/dz)_\gamma = \frac{x_{cl} - x_{vtx}}{z_{cl} - z_{vtx}}, \quad (dy/dz)_\gamma = \frac{y_{cl} - y_{vtx}}{z_{cl} - z_{vtx}}.$$

The photon 3-momentum, $\vec{p}_\gamma$, can be expressed as:

$$\vec{p}_\gamma = \frac{E_\gamma}{\sqrt{1 + (dx/dz)_\gamma^2 + (dy/dz)_\gamma^2}}((dx/dz)_\gamma, (dy/dz)_\gamma, 1).$$

The $K^+_{e2\gamma}$ (SD$^+$) kinematic variables x and y are reconstructed using the formulae (see Eqs. 1.11-1.13):

$$x = \frac{2E^*_\gamma}{m_K} = \frac{2P_K \cdot P_\gamma}{m_K^2}, \quad y = \frac{2E^*_e}{m_K} = \frac{2P_K \cdot P_e}{m_K^2},$$

where E^*_γ and E^*_e are respectively the photon and positron energies in the kaon rest frame and P_K is the kaon 4-momentum taken from the database. In the kaon rest frame, the $K^+_{e2\gamma}$ (SD$^+$) events are mainly confined in a kinematic region of the x-y plot where the photon and the positron are emitted almost anti-parallel, with a relative angle $\theta^*_{e\gamma} > 120°$ (in more than 95% of the cases) and with the positron energy spectrum peaking at $E^*_e = m_K/2 \cdot (1 + r_e)$ or $y = 1 + r_e$ ($r_e \equiv (m_e/m_K)^2 = 1.07 \cdot 10^{-6}$). On the other hand, the IB and SD$^-$ components are concentrated along the line $x + y = 1$ (see Fig. 1.2). As already mentioned, the main backgrounds to $K^+_{e2\gamma}$ (SD$^+$) are due to the $K^+ \to \pi^0 e^+ \nu_e$ and $K^+ \to \pi^+ \pi^0$ decays (followed by $\pi^0 \to \gamma\gamma$), when a photon from π^0 remains undetected. The kinematic endpoints of $K^+ \to \pi^0 e^+ \nu_e$ and $K^+ \to \pi^+\pi^0$ backgrounds are (assuming the electron hypothesis for the track): $y^{max}(K^+ \to \pi^0 e^+ \nu_e) = 0.925$ and $y^{max}(K^+ \to \pi^+\pi^0) = 0.920$. A cut at $y > y^{max}(K^+ \to \pi^0 e^+ \nu_e)$ is therefore necessary to reject most of the background. The following kinematic cuts define the signal region:

- a lower limit $x > 0.2$ is chosen to reduce the IB background that increases at low x: the x-y distribution for the MC $K^+_{e2\gamma}$(IB) background is shown in Fig. 3.9 (bottom-left panel).

- the y resolution varies from $\sigma_y = 0.006$ at low momenta ($p_{trk} < 20\text{GeV}/c$), where it is dominated by the reconstruction of the momentum directions, up to $\sigma_y = 0.015$ at high momenta ($p_{trk} > 50\text{GeV}/c$), where the component from
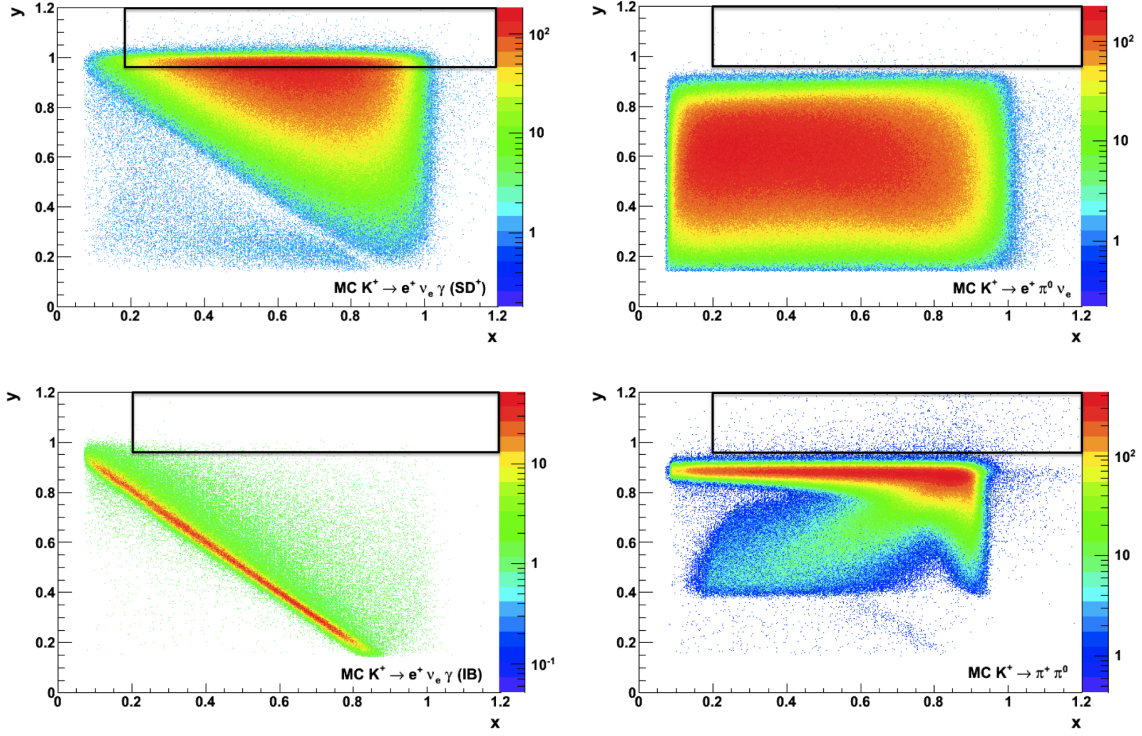
Figure 3.9: Distribution of reconstructed x and y kinematic variables for the signal $K^+_{e2\gamma}(\text{SD}^+)$ (top-left) and background $K^+ \to \pi^0 e^+ \nu_e$ (top-right), $K^+_{e2\gamma}(\text{IB})$ (bottom-left) and $K^+ \to \pi^+ \pi^0$ (bottom-right) MC events (logarithmic colour scale). The overlay regions define the analysis kinematic region.

the spectrometer resolution is not negligible. Assuming a fixed lower cut at $y > y_{min}$, with $y_{min} = 0.95$, and a y resolution of $\sigma_y \approx 0.01$, the kinematic end-points $y^{max}(K^+ \to \pi^0 e^+ \nu_e) = 0.925$ and $y^{max}(K^+ \to \pi^+ \pi^0) = 0.920$ are about $2.5\sigma_y$ and $3\sigma_y$, respectively, away from the chosen signal region; a residual background contamination is expected due to y resolution tails. A fixed y cut is not optimal over the full momentum range of the analysis, $p_{trk} = (10, 55) \text{ GeV}/c$, and two regions have been considered:

1. for $10 \text{ GeV}/c \le p_{trk} < 35 \text{ GeV}/c$ the y resolution is $0.006 \le \sigma_y < 0.010$ and a fixed lower cut at $y > 0.950$ ensures more than $3\sigma_y$ separation between signal and background components;

2. for $35 \text{ GeV}/c \le p_{trk} < 55 \text{ GeV}/c$ the y resolution is $0.010 \le \sigma_y < 0.015$ and the lower cut at $y > y_{min}$ varies in four p_{trk} bins of $5 \text{ GeV}/c$ width according to the y resolution; y_{min} is chosen as $y_{min} = 3\sigma_y + y^{max}(K^+ \to \pi^0 e^+ \nu_e)$ and

the explicit values are: $y_{min} = (0.954, 0.959, 0.964, 0.969)$.

The x-y distributions for the MC $K^+ \to \pi^0 e^+ \nu_e$ and $K^+ \to \pi^+ \pi^0$ backgrounds passing the event selection described up to this point with a lost photon, are shown in Fig. 3.9. The $K^+ \to \pi^0 e^+ \nu_e$ distribution (top-right panel) has a nearly rectangular shape covering the whole x (photon energy spectrum) and y (positron energy spectrum) ranges. The kinematic endpoints in x and y are smeared by resolution effects. No events are reconstructed in the regions $y < 0.15$ and $x < 0.08$, corresponding to low-momentum (< 40 MeV) kaon decay products in the kaon rest frame: this is because such particles travel in the beam pipe and miss the detector. The x-y distribution for MC $K^+ \to \pi^+ \pi^0$ (bottom-right panel) covers the whole x range but only populate high momenta ($0.8 < y < 0.9$): this is a consequence of the closed kinematics of the process (two-body decay) and the lost photon.

- $|m^2_{miss}| < 0.01$ GeV^2/c^4, where $m^2_{miss} = (P_K - P_e - P_\gamma)^2$ is the reconstructed squared missing mass, already introduced in Sec. 3.1.2, corresponding to the mass of the neutrino for the $K^+_{e2\gamma}$ (SD$^+$) decay (see Fig. 3.10).
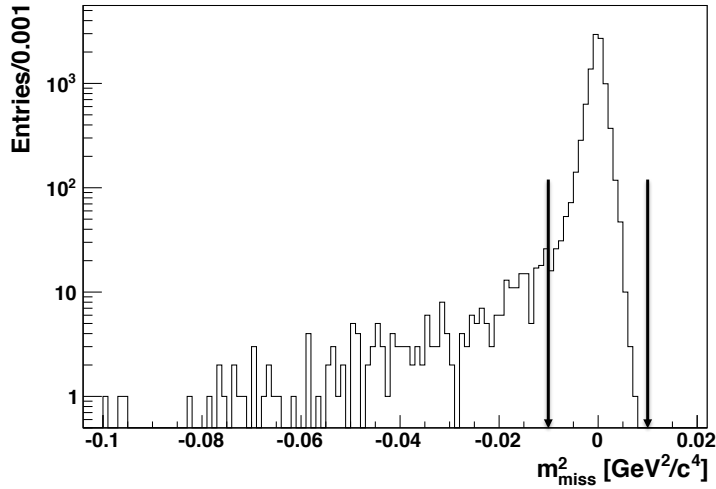
Figure 3.10: Squared missing mass m^2_{miss} distribution for data (log scale). The complete list of cuts for the charged-track, photon and kinematic selections of $K^+_{e2\gamma}$ (SD^2) events is applied. The arrows represent the m^2_{miss} cut chosen for the event selection.

The x-y distribution for the signal MC $K^+_{e2\gamma}$(SD$^+$) is shown in Fig. 3.9 (top-left panel), this has a nearly triangular shape and peaks at high y values ($E^*_e = m_K/2$) corresponding to high positron energy. The origin of events reconstructed in the region below

56

the diagonal $x + y = 1$ has been found to be related to energy losses produced by interactions in the detector material (e.g. the DCH flanges), positron bremsstrahlung and $\gamma \rightarrow e^+e^-$ conversion. The first two processes are treated with specific cuts, as shown in Sec. 3.1.2, while the photon conversions are included in the reconstruction efficiency of the detector. The number of $K^+_{e2\gamma}$ (SD$^+$) candidates passing the event selection is $N(K^+_{e2\gamma}, SD^+) = 9835$. The study and the evaluation of the background will be described in Sec. 3.4.

3.2 Normalization mode

3.2.1 $K^+ \rightarrow \pi^0 e^+ \nu_e$ event selection

The kaon flux is evaluated by counting the $K^+ \rightarrow \pi^0 e^+ \nu_e$ decays (followed by $\pi^0 \rightarrow \gamma\gamma$) and taking their BR from the Particle Data Group (PDG Review [16]). This decay has a signature similar to the signal, with one charged track in the final state, and it has been acquired with the same trigger chain[4]. It differs from the signal by the presence of two photons in the final state, coming from the $\pi^0 \rightarrow \gamma\gamma$ decay, instead of a single one. Due to its relatively high branching ratio ($\sim 5\%$), the $K^+ \rightarrow \pi^0 e^+ \nu_e$ decay can be selected with a negligible background contamination ($\sim 10^{-4}$).

The charged track selection and the kaon decay vertex reconstruction, for this analysis, are the same as for the signal event selection (Sec. 3.1.2), so that no systematic effects related to the difference between the signal and the normalization channel selections are introduced. The same photon selection as the one reported in section 3.1.3 is applied to reconstruct two clusters in the LKr calorimeter, which are generated by a $\pi^0 \rightarrow \gamma\gamma$ decay. An additional requirement on the time difference between the two photon clusters, being within 3 ns, ensures their common origin. A minimum distance of 20 cm between the two photon clusters at the LKr calorimeter is also required in order to avoid energy sharing effects between the photon electromagnetic showers. The signal di-photon mass range is determined by fitting the $\gamma\gamma$ mass distribution (shown in Fig. 3.11) and keeping events within 5 standard deviations of the distribution peak: $125 \, \text{MeV}/c < M(\gamma\gamma) < 145 \, \text{MeV}/c$.

The $K^+ \rightarrow \pi^+ \pi^0$ decay contributes as a background to $K^+ \rightarrow \pi^0 e^+ \nu_e$ events if the charged pion is mis-identified as a positron. This contribution, reported in Tab. 3.1, is the dominant one and its treatment is explained in Sec. 3.4.1. A kinematic separation

---

[4]The K_{e2} main trigger.
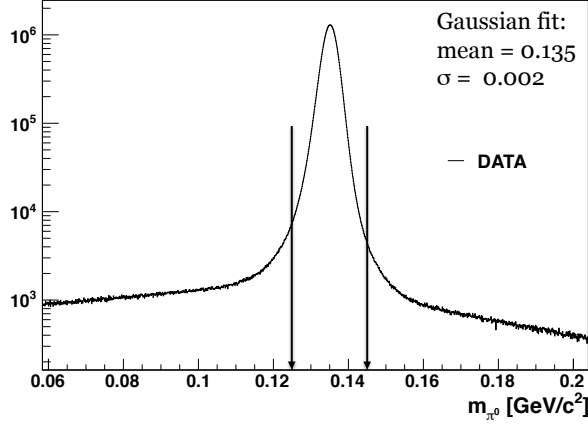
Figure 3.11: $\gamma\gamma$ mass distribution for data (logarithmic scale) passing the $K^+ \to \pi^0 e^+ \nu_e$ event selection cuts described up to this point.

of $K^+ \to \pi^0 e^+ \nu_e$ and $K^+ \to \pi^+ \pi^0$ decays is achievable by constraining the missing transverse momentum p_T calculated with respect to the kaon direction. In the $K^+ \to \pi^0 e^+ \nu_e$ decay, the neutrino in the final state is undetectable and it produces a loss of transverse momentum, while in the $K^+ \to \pi^+ \pi^0$ decay all the particles in the final state are visible by the detector and can be reconstructed. The kinematic separation of $K^+ \to \pi^0 e^+ \nu_e$ and $K^+ \to \pi^+ \pi^0$ is illustrated in Fig. 3.12. The p_T spectrum for $K^+ \to \pi^+ \pi^0$ MC events is mainly constrained at zero and a lower limit $p_T > 0.02$ GeV$/c$ is applied to reject this background.

Another source of background comes from $K^+ \to \pi^0 e^+ \nu_e$ followed by the $\pi^0 \to e^+ e^- \gamma$ Dalitz decay (combined branching ratio BR $= 6 \cdot 10^{-4}$): when one of the two leptons from the Dalitz decay is lost, the π^0 is wrongly reconstructed with the photon and the remaining lepton. This background contribution, reported in Tab. 3.1, is the second main one. A kinematic background rejection is obtained by constraining the reconstructed squared missing mass: $|m^2_{miss}| = |(P_K - P_e - P_{\gamma\gamma})^2| < 0.01$ GeV$^2/c^4$. Fig. 3.13 shows the m^2_{miss} distributions for MC $K^+ \to \pi^0 e^+ \nu_e$ ($\pi^0 \to \gamma\gamma$) and $K^+ \to \pi^0 e^+ \nu_e$ ($\pi^0 \to \gamma e^+ e^-$) Dalitz events. The former distribution (left panel) represents the neutrino invariant mass and m^2_{miss} peaks at 0 GeV$^2/c^4$, while the latter (right panel) shows no peak and a tail at positive m^2_{miss} values as a consequence of the π^0 mis-reconstruction.

A dedicated background study for $K^+ \to \pi^0 e^+ \nu_e$ ($\pi^0 \to \gamma\gamma$) events, labelled as K_{e3}, is performed with MC simulations. For each source the background over signal
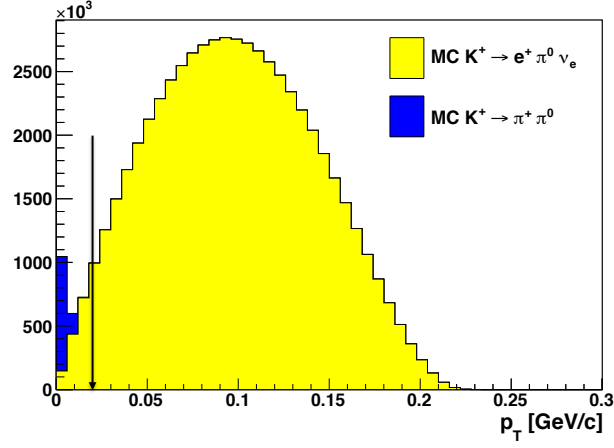
Figure 3.12: p_T distributions for $K^+ \to \pi^0 e^+ \nu_e$ (signal, yellow) and $K^+ \to \pi^+ \pi^0$ (background, blue) MC events. The difference in the spectra suggests for the signal selection a cut at $p_T > 0.02$ GeV/c in order to reject the background contamination from $K^+ \to \pi^+ \pi^0$ events.
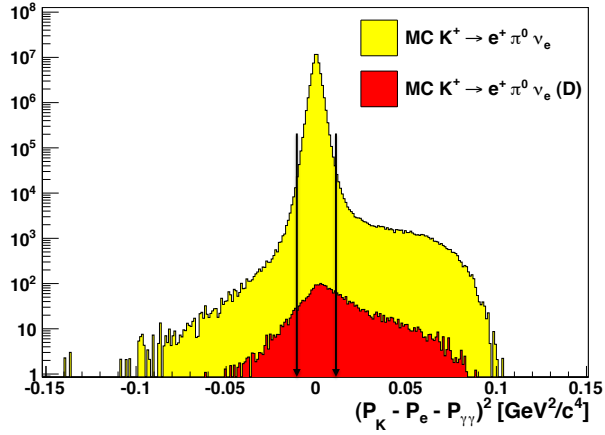
Figure 3.13: $m_{miss}^2 = (P_K - P_e - P_{\gamma\gamma})^2$ distributions for MC (signal, yellow) $K^+ \to \pi^0 e^+ \nu_e$ ($\pi^0 \to \gamma\gamma$) and (background, red) $K^+ \to \pi^0 e^+ \nu_e$ ($\pi^0 \to e^+ e^- \gamma$) Dalitz events. The difference in the spectra suggests a narrow cut at $m_{miss}^2 < 0.01$ GeV^2/c^4 in order to reduce this background contamination.

ratio is computed as:

$$\alpha = \frac{Acc(bkg) \times BR(bkg)}{Acc(K_{e3}) \times BR(K_{e3})}.$$

The geometrical acceptances, $Acc(bkg)$ and $Acc(K_{e3})$, are evaluated with MC simulations; the explicit expression for the signal acceptance is defined below and reported

59

in Tab. 3.1:

$$Acc(K_{e3}) = \frac{N_{MC}(K_{e3})}{N_{MC}(-2000\text{cm} < z_{gen} < 9000\text{cm})},$$ (3.3)

where $N_{MC}(-2000\text{ cm} < z_{gen} < 9000\text{ cm})$ is the number of generated $K^+ \to \pi^0 e^+ \nu_e$ ($\pi^0 \to \gamma\gamma$) MC events in the given fiducial decay region $-2000\text{ cm} < z_{gen} < 9000\text{ cm}$, with z_{gen} being the z coordinate of the generated decay vertex. $N_{MC}(K_{e3})$ is the number of selected $K^+ \to \pi^0 e^+ \nu_e$ ($\pi^0 \to \gamma\gamma$) MC events within the same sample. The cut on the reconstructed z_{vtx} at the numerator is $-1600\text{ cm} < z_{vtx} < 9000\text{ cm}$, the same as the one defined in Sec. 3.1.2 for the signal selection. The same acceptance definition is applied to the background sources. $Acc(K_{e3})$ and $Acc(bkg)$ are reported in Tab 3.1, together with the branching ratios, $BR(K_{e3})$ and $BR(bkg)$, taken from the PDG [16]. The α ratios for these backgrounds are also summarized in Tab. 3.1.

Decay	Acceptance	BR (%)	α
$K^+ \to \pi^0 e^+ \nu(\pi^0 \to \gamma\gamma)$	0.11	5	$-$
$K^+ \to \pi^+ \pi^0(\pi^0 \to \gamma\gamma)$	1.2×10^{-6}	20	$\sim 4 \times 10^{-5}$
$K^+ \to \pi^0 e^+ \nu(\pi^0 \to \gamma e^+ e^-)$	2.2×10^{-4}	0.06	$\sim 2 \times 10^{-5}$

Table 3.1: Signal and background sources to $K^+ \to \pi^0 e^+ \nu_e$ ($\pi^0 \to \gamma\gamma$) events: acceptances at the end of the full selection, branching ratios (BR) and α ratios.

The total background contamination to K_{e3} events amounts to $\alpha < 10^{-4}$; it counts for a negligible contribution when compared with the overall expected precision of this analysis. For this reason it will be neglected in the measurement of the kaon flux.

3.2.2 Kaon flux computation

The kaon flux in a given fiducial decay region, for a general case, can be calculated using the formula:

$$\Phi(K^+) = \frac{N(K_{e3}) - N(bkg)}{BR(K_{e3}) \times Acc(K_{e3}) \times \varepsilon_{K_{e3}}},$$ (3.4)

where $N(K_{e3})$ is the number of selected $K^+ \to \pi^0 e^+ \nu_e$ ($\pi^0 \to \gamma\gamma$) candidates; $N(bkg)$ is the number of background events passing the event selection; $\varepsilon_{K_{e3}}$ is the trigger efficiency for $K^+ \to \pi^0 e^+ \nu_e$ ($\pi^0 \to \gamma\gamma$) events. The latter relies on a minimum bias trigger configuration ensuring high efficiency and is measured directly from data, as described in Sec. 3.3. The quantity $N(bkg)$ can be written in terms of the single background components as: $\sum_i \Phi(K^+) Acc_i(bkg) BR_i(bkg)$, where the index i runs over the

background sources to $K^+ \to \pi^0 e^+ \nu_e$ ($\pi^0 \to \gamma\gamma$) events. Substituting this expression in Eq. 3.4 and solving the equation for $\Phi(K^+)$ one obtains:

$$\Phi(K^+) = \frac{N(K_{e3})}{(BR(K_{e3}) \times Acc(K_{e3}) \times \varepsilon_{K_{e3}}) + \sum_i Acc_i(bkg)BR_i(bkg)}. \tag{3.5}$$

Using the following values:

$$N(K_{e3}) = 56,645,739;$$

$$BR(K_{e3}) = (0.0501 \pm 0.0004);$$

$$Acc(K_{e3}) = (11.180 \pm 0.002)\%;$$

$$\epsilon_{K_{e3}} = (0.99451 \pm 0.00013)$$

and neglecting the background term, which amounts to $\sum_i Acc_i(bkg)BR_i(bkg) < 4 \times 10^{-7}$, a result for the kaon flux is obtained:

$$\Phi(K^+) = (10.17 \pm 0.08) \cdot 10^9. \tag{3.6}$$

The flux uncertainty accounts only for the uncertainties on the quantities appearing in Eq. 3.4 and is computed propagating the errors in quadrature. The relative error on the flux appears to be 0.8% and is dominated by the uncertainty on BR(K_{e3}). The kaon flux obtained corresponds to the number of kaon decays in the fiducial decay region $-2000\,\mathrm{cm} < Z_{vtx} < 9000\,\mathrm{cm}$ during the analysed data taking period.

3.2.3 Data-MC comparison

The reliability of the MC simulation has been checked using the normalization channel. The MC distributions have been normalised using the kaon flux $\Phi(K^+)$, as computed in Eq. 3.6, and the branching ratios reported in Tab. 3.3. The data-MC comparisons of events passing the K_{e3} selection for the most relevant variables of the analysis are shown in Figs. 3.14,3.15,3.16,3.17.

All Data/MC ratio disagreements are outside the signal region defined for the selection of the normalization decay channel.

3.3 Trigger efficiency studies

The trigger used for the selection of $K^+_{e2\gamma}$ (SD$^+$) events was originally implemented and optimised for the acquisition of $K^+ \to e^+ \nu_e$ events and it is called the "K_{e2} main
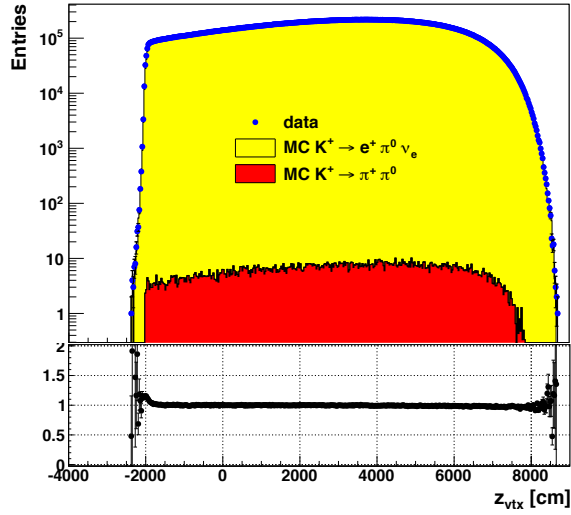
Figure 3.14: Reconstructed z_{vtx} distributions of $K^+ \rightarrow \pi^0 e^+ \nu_e$ candidates compared with the sum of normalised estimated signal and background components (logarithmic scale). Data/MC ratio shows that the agreement fails for resolution effects outside the signal region: $-2000 \, \text{cm} < z_{vtx} < 8000 \, \text{cm}$.
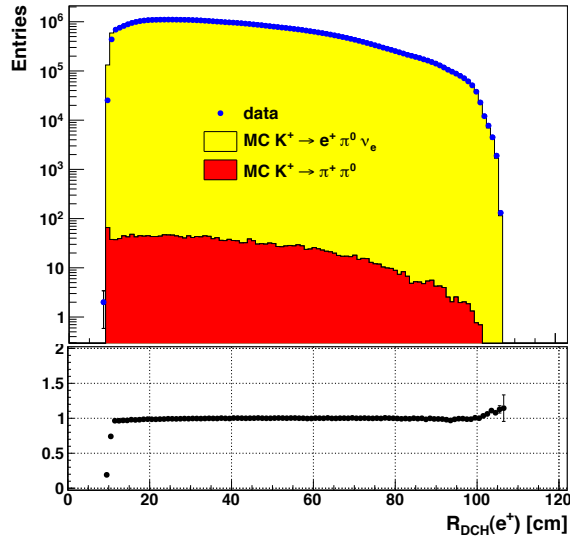
Figure 3.15: Reconstructed positron radius at DCH1, $R_{DCH}(e^+)$, distributions of $K^+ \rightarrow \pi^0 e^+ \nu_e$ candidates compared with the sum of normalised estimated signal and background components (logarithmic scale). Data/MC ratio shows that the agreement fails for $R_{DCH}(e^+) < 12 \, \text{cm}$, which is understood to be caused by particle interactions in the DCH1 flange.

62
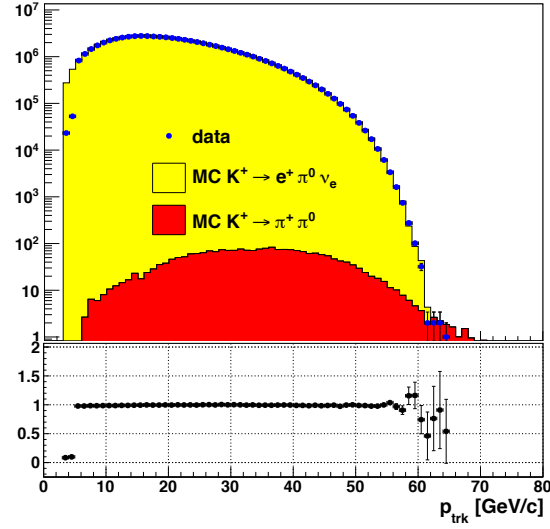
Figure 3.16: Reconstructed track momentum distributions of $K^+ \to \pi^0 e^+ \nu_e$ candidates compared with the sum of normalised estimated signal and background components (logarithmic scale). Data/MC ratio shows a disagreement for $p_{trk} < 5$ GeV/c, which might be due to low-momentum positrons interacting in the detector material on the beam line.
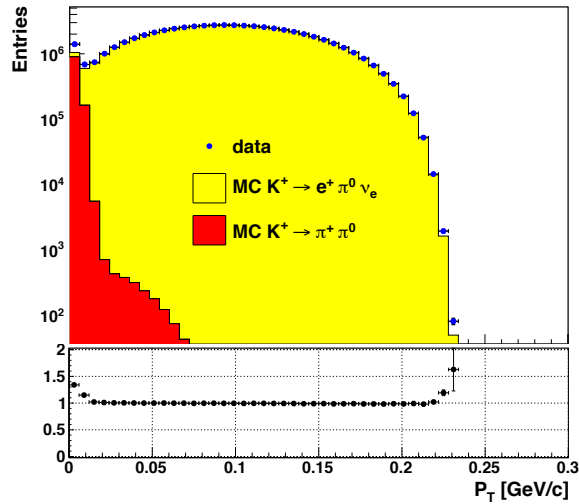
Figure 3.17: Reconstructed transverse momentum, P_T, distributions of $K^+ \to \pi^0 e^+ \nu_e$ candidates compared with the sum of normalised estimated signal and background components (logarithmic scale). Data/MC ratio shows a disagreement for $P_T < 0.01$ GeV/c, which might be due to a non perfect rejection of the $K^+ \to \pi^+ \pi^0$ decay peaking in this P_T region.

63

trigger". As introduced in Sec. 2.6, the trigger signal consists of the coincidence between three sub-signals: $Q1 \times E_{LKr} \times 1TRKLM$.

The trigger efficiency has been directly measured with data. The procedure can be summarised as follows: selection of a control data sample and counting of the number of events, among those that passed the event selection, for which the trigger condition is satisfied. The trigger structure allows studying the efficiencies for the "K_{e2} main trigger" and for the single sub-signal components: each trigger condition is stored by means of pattern units (PU), a digital register which allows accessing each bit of the trigger word (TW) produced by the trigger supervisor (TS) during the data taking.

Control trigger signals are available and can be used to select control data samples. In this analysis the control signal is the NHOD, introduced in Sec. 2.6, provided by the "neutral hodoscope" and triggering on a shower in the LKr calorimeter. This choice is reasonable for both the signal ($K_{e2\gamma}^+$, SD$^+$) and the normalisation mode (K_{e3}) as the decay products (e^+ and γ) are expected to release their energy in the LKr calorimeter. The NHOD trigger rate is higher compared with the triggers to be measured and the control data sample has been downscaled ($D = 150$). The trigger efficiency for the sub-signal i (e.g. Q1) is determined by the ratio:

$$\varepsilon_i = \frac{N_{PU(i)*NHOD}}{N_{NHOD}} , \tag{3.7}$$

where $N_{PU(i)*NHOD}$ is the number of selected events in the control data sample satisfying the trigger condition i, taken from the pattern units, and N_{NHOD} is the total number of selected events in the control data sample. The "K_{e2} main trigger" efficiency is measured by requiring the coincidence, in a 75 ns readout window, of the three trigger conditions for events within the same control data sample:

$$\varepsilon = \frac{N_{PU(Q1)*PU(1TRK)*PU(LKr)*NHOD}}{N_{NHOD}} . \tag{3.8}$$

The error assigned to the trigger efficiency is binomial and is given by:

$$\delta\varepsilon = \sqrt{\frac{\varepsilon(1-\varepsilon)}{N_{NHOD}}} . \tag{3.9}$$

The measurement of the $K_{e2\gamma}^+$(SD$^+$) trigger efficiency is constrained by the statistically poor data sample of $K_{e2\gamma}^+$(SD$^+$) candidates ($\sim 10,000/D$ events). The trigger efficiency can be measured for the normalisation channel only. The sample of K_{e3} candidates comprises about 380,000 events and the measured trigger inefficiencies ($1 - \varepsilon$) are reported in Tab. 3.2.

Trigger signal	Inefficiency $(1 - \varepsilon)$
$Q1$	2.8×10^{-3}
$1TRKLM$	1.2×10^{-3}
E_{LKr}	0.1×10^{-3}
Time mis-alignment	1.4×10^{-3}
Total "K_{e2} main trigger"	5.5×10^{-3}

Table 3.2: Trigger inefficiencies measured with reconstructed K_{e3} events; an additional source of inefficiency, due to the time mis-alignment between the single sub-signals within the readout window, is reported.

3.3.1   Q1 trigger efficiency

The $Q1$ trigger signal requires at least one coincidence between horizontal and vertical scintillators within the same hodoscope sub-quadrant. The $Q1$ inefficiency accounts for $\sim 50\%$ of "K_{e2} main trigger" inefficient events. The distribution of $Q1$ inefficient events at the HOD front plane is shown in Fig. 3.18. Two components can
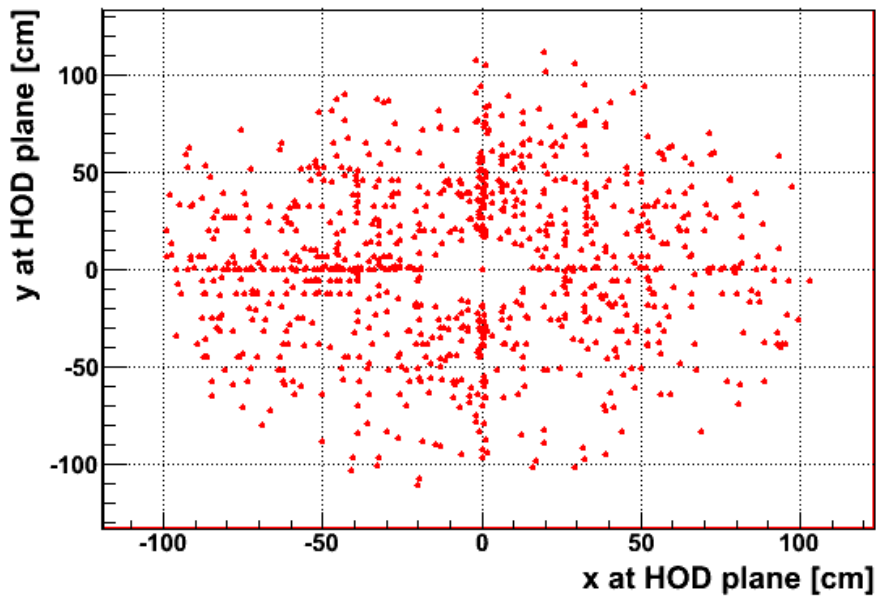
Figure 3.18: The Q1 inefficiency as a function of the track impact point on the HOD, evaluated using K_{e3} events.

be distinguished:

- one is uniform on the HOD plane and it amounts to $1 - \varepsilon = 2.2 \times 10^{-3}$;

- the other is localized on the HOD plane, it amounts to the remaining $1 - \varepsilon = 5.6 \times 10^{-4}$, and it is due to coincidences of small "cracks" in the horizontal and vertical scintillator slabs.

The former component can be assumed to be the same for K_{e3} and $K_{e2\gamma}^+$ (SD$^+$) events. The latter component determines an accumulation of Q1 inefficient events in the (x, y) regions of the HOD plane defined by $(0, \pm 2\text{cm})$ and $(\pm 2\text{cm}, 0)$. Being geometrical, the inefficiency depends on the event kinematics; the spatial distribution of K_{e3} events on the HOD plane is different for $K_{e2\gamma}^+$ (SD$^+$). This inefficiency has been simulated with K_{e3} events by tuning the MC in order to obtain the same inefficiency value as the one measured with data. The simulated inefficiency corresponds to a 100% inefficiency in $200\,\mu$m wide strips in the vertical and horizontal planes of the HOD: the value obtained with K_{e3} MC events is $1 - \varepsilon = 6.2 \times 10^{-4}$. The inefficiency simulated for $K_{e2\gamma}^+$ (SD$^+$) MC events gives the following value: $1 - \varepsilon = 5.8 \times 10^{-4}$. The difference between the two inefficiency estimations (with K_{e3} and $K_{e2\gamma}^+$ (SD$^+$) MC events) is $\sim 8\%$ relative and it implies a correction to events showing the Q1 localized trigger inefficiency, which amounts to $\sim 5 \times 10^{-5}$ and can be neglected. As a consequence, the trigger efficiency component coming from Q1 can be assumed to be the same for K_{e3} and $K_{e2\gamma}^+$ (SD$^+$) events.

Fig. 3.19 shows the Q1 trigger efficiency for K_{e3} events plotted as a function of the track momentum: no dependence is observed. Using Eq. 3.7 the following measurement is achieved: $\varepsilon_{Q1} = 0.99724 \pm 0.00009_{stat}$.

3.3.2 $E_{LKr}(10\text{ GeV})$ trigger efficiency

The $E_{LKr}(10\text{ GeV})$ trigger signal requires a minimum energy deposit of $10\,$GeV in the LKr calorimeter. The selection criteria described in Sec. 3.1.2 and applied in both $K_{e2\gamma}^+(\text{SD}^+)$ and K_{e3} event selections, namely $(10 < p_{trk} < 55)\,$GeV$/c$ and $E_\gamma > 5\,$GeV, have been chosen in order to guarantee an energy deposition in the LKr calorimeter above the 10 GeV trigger energy threshold. Fig. 3.20 shows the $E_{LKr}(10\text{ GeV})$ trigger efficiency for K_{e3} events plotted as a function of the track momentum. The efficiency is very high and flat on the full momentum range; using Eq. 3.7 the following measurement is achieved: $\varepsilon_{E_{LKr}(10\,GeV)} = 0.999908 \pm 0.000017_{stat}$.
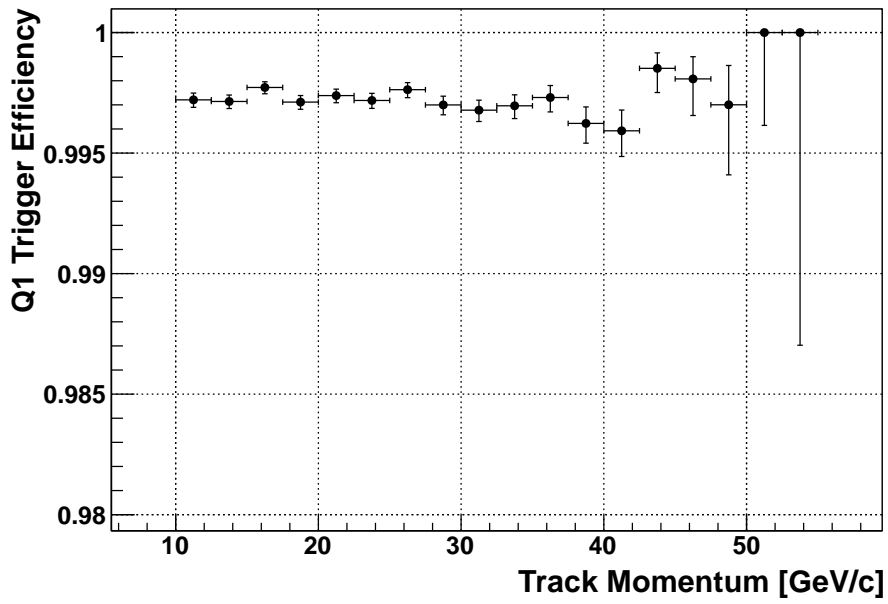
Figure 3.19: The Q1 trigger efficiency as a function of the track momentum measured using K_{e3} events.
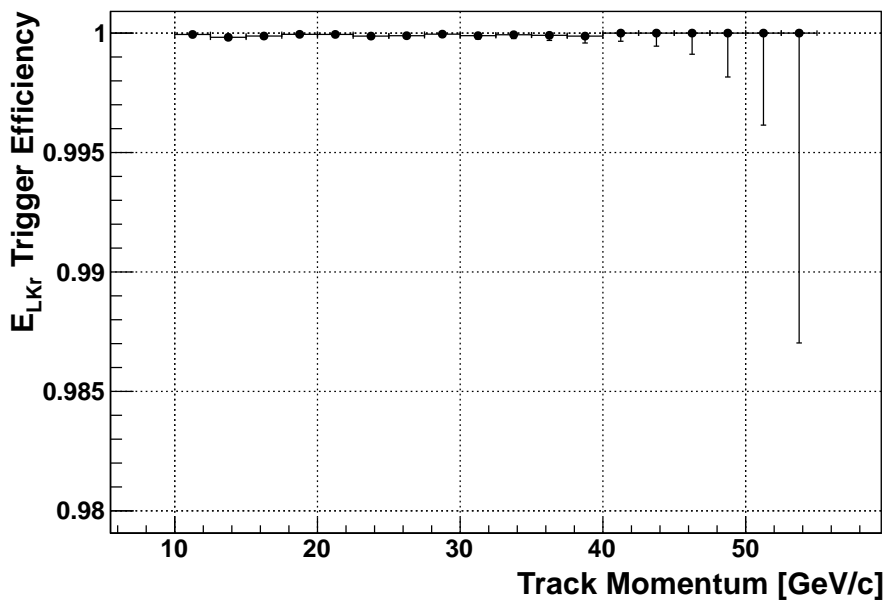
Figure 3.20: The $E_{LKr}(10\,\text{GeV})$ trigger efficiency as a function of the track momentum measured using K_{e3} events.

3.3.3 1TRKLM trigger efficiency

The 1TRKLM trigger signal constrains the number of hits in DCH1,2 and 4 determining the suppression of events with high and low activity in the drift chambers. The 1TRKLM trigger condition is highly efficient for K_{e3} events: Fig. 3.21 shows that it is independent on the track momentum. Using Eq. 3.7 the following estimation is obtained: $\varepsilon_{1TRKLM} = 0.99867 \pm 0.00006_{stat}$.
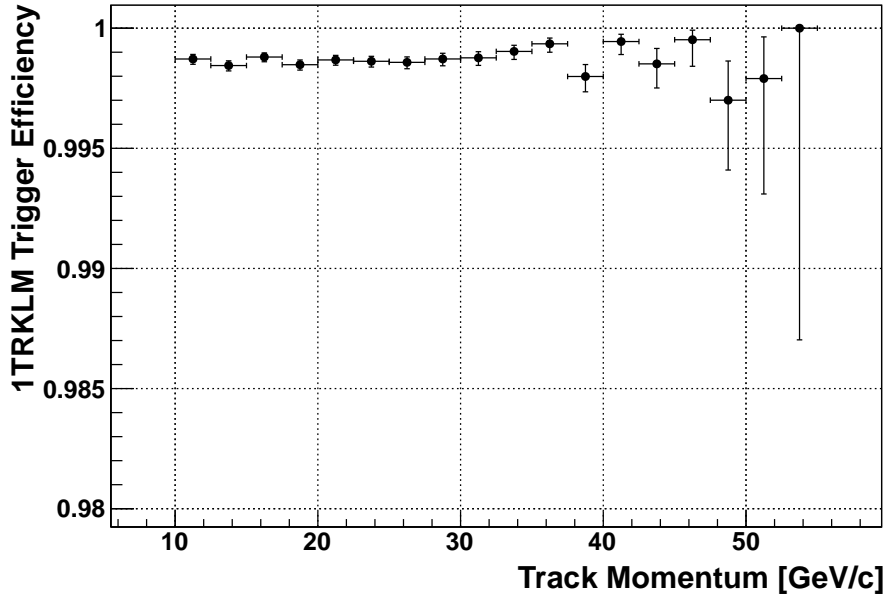
Figure 3.21: The 1TRKLM trigger efficiency as a function of the track momentum measured using K_{e3} events.

3.3.4 Main trigger efficiency

The efficiency of the total "K_{e2} main trigger" (namely the $Q1 \times E_{LKr}(10GeV) \times 1TRKLM$ trigger efficiency) for K_{e3} events ($\varepsilon_{K_{e3}}$) has been measured:

$$\varepsilon_{K_{e3}} = 0.99451 \pm 0.00013.$$

This efficiency differs from the product of the single sub-signal efficiencies because it is affected by the time mis-alignment between the sub-signal components, namely events for which $Q1$, $1TRKLM$ and E_{LKr} are efficient, within a certain readout window; those events are reported in Tab. 3.2 and amount to 1.4×10^{-3}.
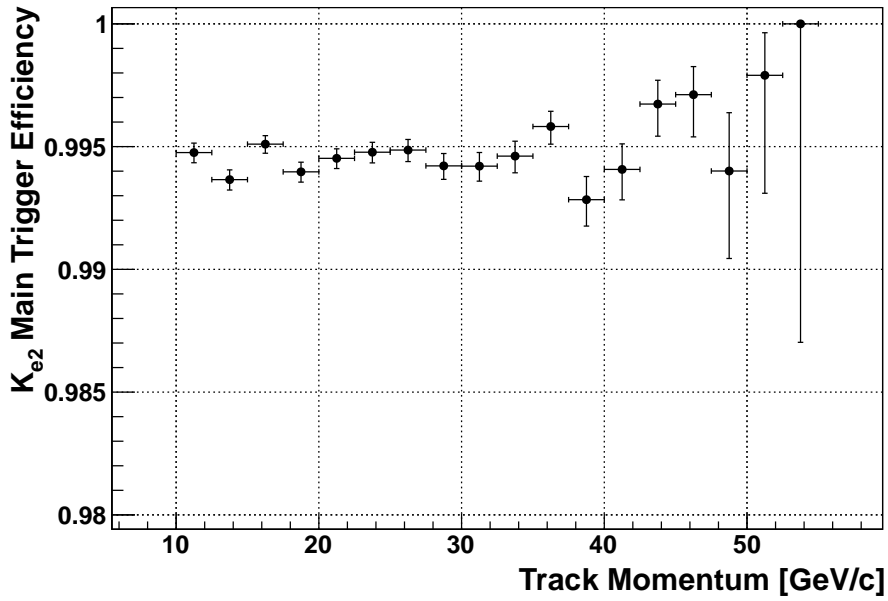
Figure 3.22: The total "K_{e2} main trigger" efficiency as a function of the track momentum measured using K_{e3} events.

Stability checks of the total "K_{e2} main trigger" efficiency confirm that $\varepsilon_{K_{e3}}$ does not depend on the relevant variables of the analysis: the track momentum (Fig. 3.22), the photon energy in the lab frame and the kinematic variable y proportional to the positron energy in the kaon rest frame (Fig. 3.23).
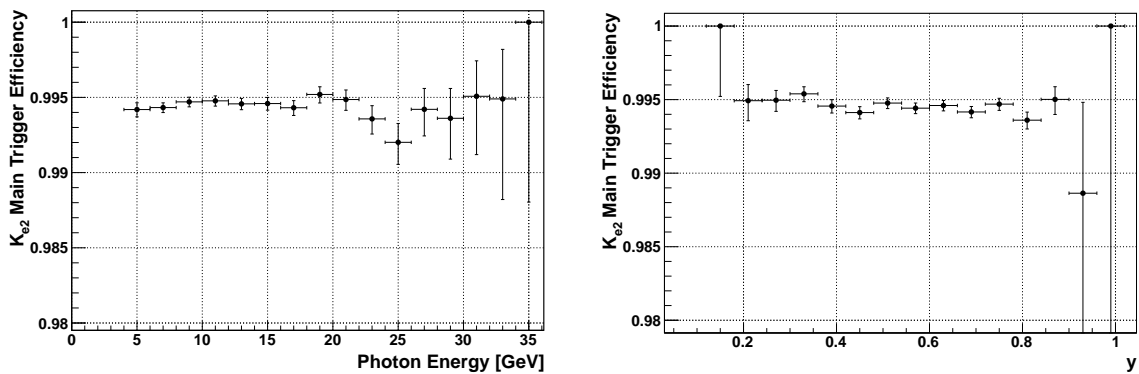
Figure 3.23: The total "K_{e2} main trigger" efficiency vs the photon energy in the lab frame (left) and the y variable in the kaon rest frame (right) for K_{e3} events.

3.3.5 Conclusions

The evaluation of the trigger efficiency for $K^+_{e2\gamma}(\mathrm{SD}^+)$ events is affected by the limited statistics of the sample of $K^+_{e2\gamma}(\mathrm{SD}^+)$ candidates. The trigger efficiency has been measured for the normalisation channel (K_{e3}). The trigger inefficiency $\varepsilon_{K_{e3}}$ is dominated by the Q1 component, which is in turn dominated by a diffuse component due to the intrinsic HOD inefficiency. Due to the topological similarity between K_{e3} and $K^+_{e2\gamma}$ (SD^+) and a carefully designed trigger logic, the trigger efficiencies for both decay modes are expected to be similar. In particular, the $1TRKLM$ component relies on the track reconstruction in DCHs and K_{e3} and $K^+_{e2\gamma}$ (SD^+) events have a common charged track selection. The E_{LKr} inefficiency is negligible for K_{e3} events and so is for $K^+_{e2\gamma}$ (SD^+); due to the event selection requirements on the photon energy (at least $5\,\mathrm{GeV}$ in the lab frame) and on the lower limit of the track momentum (at least $10\,\mathrm{GeV}/c$), the overall energy released in the calorimeter by selected $K^+_{e2\gamma}$ (SD^+) events is above the $10\,\mathrm{GeV}$ energy trigger threshold. Moreover, the time mis-alignment component does not depend on the decay mode and it can be assumed to be the same for K_{e3} and $K^+_{e2\gamma}$ (SD^+) events. In this scenario, as the "K_{e2} main trigger" efficiency cancels between signal and normalization channels, the residual systematic effects are negligible.

3.3.6 Trigger efficiency for backgrounds

The 1TRKLM trigger efficiency has been studied in a control sample obtained using the $K^+_{e2\gamma}(\mathrm{SD}^+)$ event selection (reported in Sec. 3.1) with no kinematic cuts on m^2_{miss}, x and y variables applied. The control sample is dominated by the background; the selected events are mainly $K^+ \to \pi^0 e^+ \nu_e$ and $K^+ \to \pi^+ \pi^0$ decays with a lost photon from the $\pi^0 \to \gamma\gamma$ decay. Fig. 3.24 shows the 1TRKLM trigger efficiency as a function of the photon energy in the lab frame and the kinematic variables (x,y) in the kaon rest frame.

A dependence of the trigger efficiency on the photon energy in the lab frame is visible and the inefficiency increases up to 10% at low energies of the detected photon. This is due to the lost photon carrying most of the π^0 energy, thus travelling nearly parallel to the beam pipe. The photon is more likely to interact with the material of the detector, produce a shower and thus high multiplicity in the drift chambers; such events are more likely to be rejected by the 1TRKLM trigger component. The above dependence is also visible in the kaon rest frame, where the 1TRKLM trigger efficiency decreases at low values of x (proportional to the energy of the detected photon in
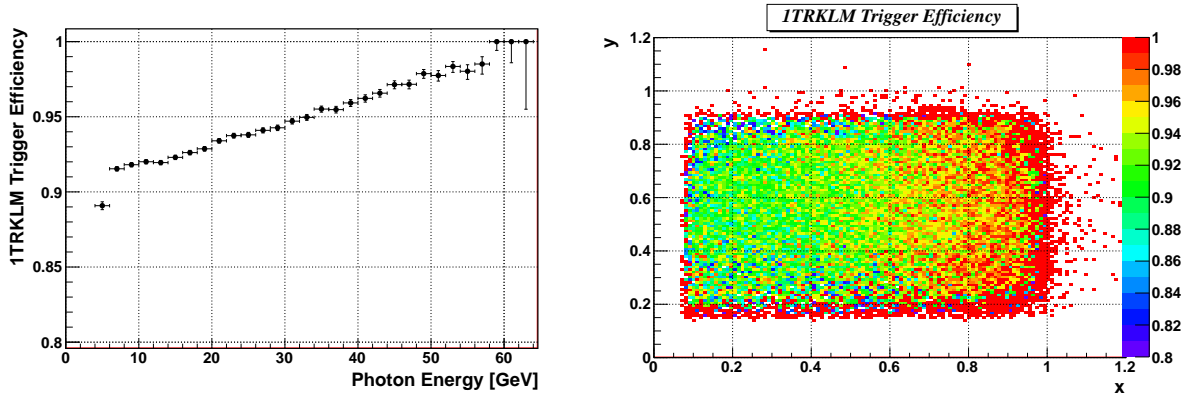
Figure 3.24: The 1TRKLM trigger efficiency vs photon energy in the lab frame (left) and on the (x,y) plot (right) evaluated using the $K_{e2\gamma}^+(\mathrm{SD}^+)$ event selection with no kinematic cuts (m_{miss}^2, x and y).

the kaon rest frame). To evaluate the effect on $K_{e2\gamma}^+(\mathrm{SD}^+)$ events, this dependence is taken into account by weighting the background MC distributions for the 1TRKLM trigger efficiency as a function of x. This correction and more studies, reported in Sec. 3.6.2, have been performed to estimate the related systematic uncertainties on the measurement of the $K_{e2\gamma}^+(\mathrm{SD}^+)$ form factors and to assess to what precision the trigger inefficiency is controlled.

3.4 $K^+ \rightarrow e^+\nu_e\gamma$ (SD$^+$) Background Evaluation

A summary of the background sources, with their short notations and branching ratios, is reported in the first three columns of Tab. 3.3. A model independent background evaluation is performed in terms of the ratio, $N(bkg)/N_{tot}$, between the computed number of background events, as expected in the signal region, and the number of signal events selected from data. The ratio is computed as:

$$\frac{N(bkg)}{N_{tot}} = \frac{\Phi(K^+) \cdot BR(bkg) \cdot Acc(bkg)}{N(K_{e2\gamma}^+, SD^+)}, \tag{3.10}$$

where the denominator represents the number of $K_{e2\gamma}^+(\mathrm{SD}^+)$ data candidates passing the event selection and reported at the end of Sec. 3.1.6; the kaon flux $\Phi(K^+)$ has been computed in Eq. 3.6; the branching ratio $BR(bkg)$ is taken from Tab. 3.3; the geometrical acceptance $Acc(bkg)$ in the given fiducial region is evaluated with MC using the explicit expression in Eq. 3.3 and it includes the trigger efficiency for backgrounds through the correction introduced in Sec. 3.3.6.

71

Backgrounds	Short notation	Branching Ratio (BR)	$N(bkg)/N_{tot}$
$K^+ \to \pi^0 e^+ \nu_e$ ($\pi^0 \to \gamma\gamma$)	K_{e3}	$(5.01 \pm 0.04) \times 10^{-2}$	0.018
$K^+ \to \pi^+ \pi^0$ ($\pi^0 \to \gamma\gamma$)	$K_{2\pi}$	$(20.42 \pm 0.08) \times 10^{-2}$	0.004
$K^+ \to \pi^0 e^+ \nu_e$ ($\pi^0 \to e^+ e^- \gamma$)	K_{e3D}	$(5.97 \pm 0.05) \times 10^{-4}$	$2 \cdot 10^{-4}$
$K^+ \to \pi^+ \pi^0$ ($\pi^0 \to e^+ e^- \gamma$)	$K_{2\pi D}$	$(24.32 \pm 0.09) \times 10^{-4}$	$2 \cdot 10^{-5}$
$K^+ \to e^+ \nu_e \gamma$ (IB)	$K^+_{e2\gamma}$(IB)	$(1.581 \pm 0.008) \times 10^{-5}$	$1 \cdot 10^{-4}$
$K^+ \to e^+ \nu_e \gamma$ (SD$^-$)	$K^+_{e2\gamma}$(SD$^-$)	$(2.58 \pm 0.26) \times 10^{-6}$	$4 \cdot 10^{-4}$
$K^+ \to \pi^0 \mu^+ \nu_\mu$ ($\pi^0 \to \gamma\gamma$)	$K_{\mu 3}$	$(3.31 \pm 0.03) \times 10^{-2}$	$< 10^{-7}$
$K^+ \to \pi^0 \mu^+ \nu_\mu$ ($\pi^0 \to e^+ e^- \gamma$)	$K_{\mu 3D}$	$(3.95 \pm 0.04) \times 10^{-4}$	$< 10^{-7}$

Table 3.3: Background sources analysed for the $K^+_{e2\gamma}$ (SD$^+$) analysis with their branching ratios [16] and $N(bkg)/Ntot$ values. BR($K^+_{e2\gamma}$, SD$^-$) is not measured and χPT expectations at $\mathcal{O}(p^6)$ are used (see Tab. 1.3) with a 10% relative uncertainty.

The main background comes from the K_{e3} decay; its branching ratio is a factor of ~ 3000 higher than that of the signal. The decay may lead to a $K^+_{e2\gamma}$ signature if one photon from the π^0 decay is undetected (absorbed before the LKr, or out of the calorimeter acceptance) or if the π^0 decays in the Dalitz mode, $\pi^0 \to e^+ e^- \gamma$, and the $e^+ e^-$ pair is undetected. K_{e3} and $K^+_{e2\gamma}$ decays are found to be kinematically[5] compatible if the positron undergoes large multiple Coulomb scattering (MCS) in the detector material. In particular, MCS at the kevlar window and DCH1 affects the reconstruction of the track direction, which is used for the computation of the decay vertex and CDA parameter; to confirm this statement, Fig. 3.25 shows that the CDA distribution for background K_{e3} events passing the signal selection has a significantly larger mean value than that of the signal $K^+_{e2\gamma}$(SD$^+$).

Non-Gaussian tails of MCS are simulated with a limited precision and the effect on K_{e3} background has been investigated with two specific MC K_{e3} samples, in which the theories describing the MCS include Gaussian tails only, in one case, and extra terms associated to the non-Gaussian tails [80], in the other one (default sample). Using Eq. 3.10, the background evaluations at CDA $= 3$ cm, which is the value chosen for the signal event selection, are the following:

$$\frac{N(K_{e3} - \text{default sample})}{N_{tot}} = 1.8\%; \quad \frac{N(K_{e3} - \text{Pure Gaussian})}{N_{tot}} = 0.5\%.$$

The K_{e3} background evaluations obtained with the two MC samples show that the K_{e3}

---

[5] The event kinematic selection is described in Sec. 3.1.6.
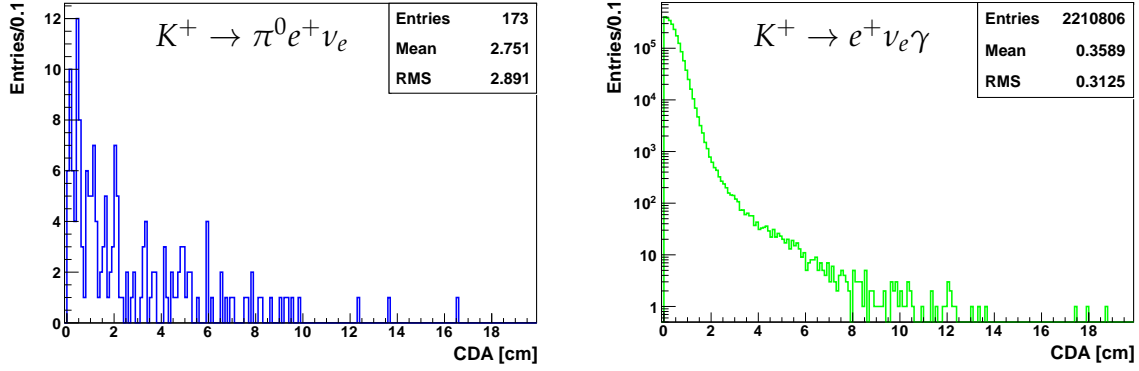
Figure 3.25: CDA distributions for K_{e3} (left, background) and $K^+_{e2\gamma}$ (right, signal) MC events. The observable is sensitive to MCS of the positron in the kevlar window and DCH1; the difference in the mean value of one order of magnitude confirms large MCS as the origin of K_{e3} events passing the signal selection.

background, in the assumption of non-Gaussian tails of MCS, is enhanced by a factor of ~ 4 with respect to a model assuming pure Gaussian tails. The dependency of the systematic error on form factors from the uncertainty of the fraction of K_{e3} events has been studied and is reported in Sec. 3.6.3.

The second main source of background comes from the $K_{2\pi}$ decay; its branching ratio is a factor of ~ 12000 higher than that of the signal. The decay may contribute to the background if one photon from the π^0 decay is undetected and the charged pion is mis-identified as a positron because it deposits $> 95\%$ of its energy in the LKr calorimeter. As known from previous analyses [1], the study of the $K_{2\pi}$ background contamination is biased by the MC reliability in the simulation of hadronic cascade development in the LKr calorimeter. To compute the number of expected $K_{2\pi}$ events passing the signal selection, the identification of the MC charged track by means of the reconstructed E_{LKr}/p_{trk} variable (introduced in Sec. 3.1.2) is not performed and the MC events are corrected for the measured probability to mis-identify a pion as a positron. A discussion about this probability ($P(\pi \to e)$) and the correction applied to this background contribution is reported in Sec. 3.4.1.

Looking at the MC $K_{2\pi}$ events arriving at the end of the signal selection without any requirement on E_{LKr}/p_{trk}, two contributions are identified: those are represented in Fig. 3.26, where the quantity defined as $\Delta p = p_{trk}(rec) - p_{trk}(true)$ is plotted for those events. A component peaks at $\Delta p = 0$ with a r.m.s. of ~ 1 GeV/c, which is about one order of magnitude larger than the expected spectrometer resolution at
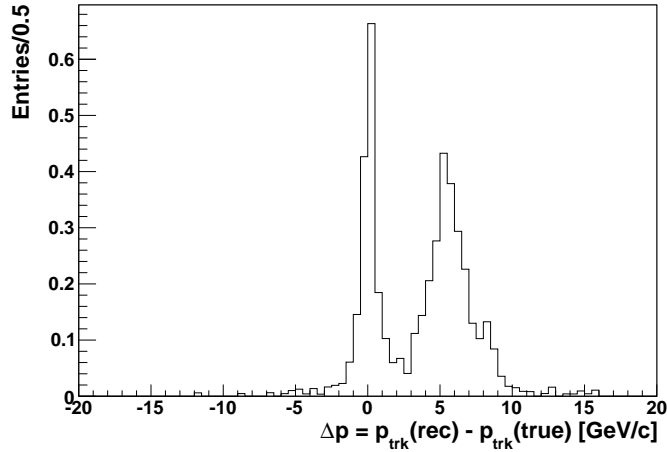
Figure 3.26: $\Delta p = p_{trk}(rec) - p_{trk}(true)$ for $K_{2\pi}$ MC events passing the signal event selection (no E_{LKr}/p_{ptrk} cut applied).

high momenta[6] (e.g. $\sigma_p \sim 100$ MeV at 50 GeV/c). Another component peaks around 5 GeV/c. To explain the origin of such background one can argue that the first component is due, as for K_{e3}, to non Gaussian MCS in the detector material before the magnet (kevlar window and DCH1), while the second component is due to non Gaussian MCS in the detector material after the magnet (DCH2-3 and Helium). In the first case, the MCS mainly affects the reconstruction of the decay vertex and the CDA parameter, while in the second case the MCS induces a mis-measurement of the bending angle, thus of the reconstructed track momentum. Moreover, the presence of a peak at positive Δp results from to the positive correlation between Δp and y and from the signal selection criteria based on a lower limit requirement on y (see Sec. 3.1.6). The probability ($P(\pi \to e)$) based on E_{LKr}/p_{trk} depends on Δp: to account for such correlation a correction has been applied to MC $K_{2\pi}$ events, on top of the correction for ($P(\pi \to e)$). The discussion and evaluation of $K_{2\pi}$ background are reported in Sec. 3.4.1.

Another source of background comes from the $K_{2\pi D}$ decay, in which the π^0 decays in the Dalitz mode $\pi^0 \to e^+ e^- \gamma$; two different components can be distinguished according to the way this decay chain may lead to a $K_{e2\gamma}^+$ signature:

- the charged pion is mis-identified as a positron and the $e^+ e^-$ pair is undetected;

- the charged pion and the electron are undetected.

Both components have been addressed with a specific $K_{2\pi}$ MC sample in which the π^0

---

[6]In Sec. 3.1.2 has been shown that $K_{2\pi}$ events contribute only at high momenta.

undergoes the Dalitz decay $\pi^0 \to e^+e^-\gamma$. The background evaluation of the former contribution exploits the approach explained in Sec. 3.4.1 and gives a negligible result $N(K_{2\pi D})/N_{tot} = 2 \cdot 10^{-5}$. The latter contribution is found to be kinematically non compatible with the signal: the positrons from the π^0 Dalitz decays are produced in the y range from ~ 0.5 to ~ 0.9; the ratio $N(K_{2\pi D})/N_{tot} = 4 \cdot 10^{-8}$ has been computed for this component.

The $K_{e2\gamma}^+$ (IB and SD$^-$) components have the same particles in the final state as for the signal and their branching ratios are comparable to that of the signal. However the event kinematics are rather different: in the former decay the radiative photon is soft and its energy spectrum in the kaon rest frame peaks outside the signal region; in the latter decay the positron energy in the kaon rest frame peaks at $\sim 100\,\text{MeV}$ ($\sim M_K/4$), while in the signal the positron energy peaks at a value two times larger: $\approx M_K/2$ (kinematics discussed in Sec. 1.1.2). The $K_{e2\gamma}^+$ (IB) background is reduced to a negligible amount cutting on the variable x, proportional to the photon energy in the kaon rest frame (see Sec. 3.1.6); the background contribution has been studied with MC and amounts to $N(K_{e2\gamma}^+, IB)/N_{tot} = 1 \cdot 10^{-4}$. The phase space covered by the $K_{e2\gamma}^+$ (SD$^-$) background is kinematically overwhelmed by the K_{e3} decay, for which the rejection is achieved with a cut on the variable y, proportional to the positron energy in the kaon rest frame. The expected background contamination in the signal kinematic region is negligible; the background contribution has been studied with MC and amounts to $N(K_{e2\gamma}^+, SD^-)/N_{tot} = 4 \cdot 10^{-4}$.

Background channels with muons in the final state, such as the $K_{\mu3}$ and its Dalitz mode ($K_{\mu3}$ followed by $\pi^0 \to e^+e^-\gamma$), have also been considered. These channels may contribute to the background to $K_{e2\gamma}^+$ (SD$^+$) events if the muon is mis-identified as a positron and, in the first case, a photon from the π^0 decay is undetected, while in the second case the e^+e^- pair from the π^0 Dalitz decay mode is undetected. A μ^+ can be mis-identified as a positron if:

- it deposits $> 95\%$ of its energy in the LKr calorimeter through a "catastrophic" bremsstrahlung; this contribution is addressed with a similar approach to the one used for pions and explained in Sec. 3.4.1.

- it decays to a positron via the process $\mu^+ \to e^+\nu_e\bar{\nu}_\mu$.

The background contributions from $K_{\mu3}$ decays to $K_{e2\gamma}^+$ (SD$^+$) decay have been studied with specific MC samples and found to be negligible ($N(K_{\mu3})/N_{tot} < 10^{-7}$).

A summary of the background contributions to the total $K_{e2\gamma}^+$ (SD$^+$) data sample is shown in the third column of Tab. 3.3. The main components come from K_{e3} and

$K_{2\pi}$ events, while the others are considered negligible. The computation of errors (statistical) for the main background components is reported in Sec. 3.8.

3.4.1 Particle mis-identification probability

As shown in Fig. 3.3, $K_{2\pi}$ decays passing the signal event selection are mainly at high momentum ($p_{trk} > 50\text{GeV}/c$). Hadronic shower development produced by π^+ is poorly described in MC, thus the reconstruction of the energy deposition in the LKr may be biased and inadequate for the characterization of the $K_{2\pi}$ background. As a consequence, the background contributions to $K_{e2\gamma}^+$ (SD$^+$) events coming from $K_{2\pi}$ decays have been addressed with the following approach. Specific $K_{2\pi}$ and $K_{2\pi D}$ MC samples have been analysed with the signal event selection. The information from the LKr is not used to compute the reconstructed ratio E_{LKr}/p_{trk}, as discussed in section 3.1.2. From previous analyses [1], the probability for a pion to be mis-identified as an electron ($P(\pi \to e)$) has been measured directly from data by using a control samples of $K_{2\pi}$ and $K_L \to \pi^{\pm} e^{\pm} \nu_e$ events and counting the number of pions entering the signal region $0.95 < E_{LKr}/p_{trk} < 1.1$. For the $K_{e2\gamma}^+$ (SD$^+$) analysis presented in this thesis, the measured values of the probability (momentum dependent) are used as weights for MC events with a charged pion in the final state ($K_{2\pi}$, $K_{2\pi D}$). In particular, at high track momentum where $K_{2\pi}$ mainly contribute, $P(\pi \to e)$ was measured to be: $(0.41 \pm 0.02) \cdot 10^{-2}$ [81].

As shown in Fig. 3.26, about half of the $K_{2\pi}$ events passing the signal selection without requiring the E_{LKr}/p_{trk} cut are reconstructed with $\Delta p = p_{trk}(rec) - p_{trk}(true) > 2$ GeV/c. This is due to charged pions undergoing multiple Coulomb scattering in the detector material and being reconstructed with a different bending angle, thus with a different momentum. Due to the dependence of $P(\pi \to e)$ on Δp, a correction is needed to address this background component. A further weight f_{EoP} has been applied to $K_{2\pi}$ MC background events on top of the previous one. f_{EoP} depends on the "true" track momentum (p_{true}) and on the difference Δp (the weight is indicated as $f_{EoP}(p_{true}, \Delta p)$ in what follows). A standalone framework has been produced for the evaluation of $f_{EoP}(p_{true}, \Delta p)$: the E_{LKr}/p_{trk} probability distribution function (PDF) of pions has been simulated in the vicinity of $E_{LKr}/p_{trk} = 1$ as linearly dependent on (E_{LKr}/p_{trk}) and vanishing at $E_{LKr}/p_{trk} = 1$. The momentum and energy resolution, as expected from the detectors, are introduced to smear the PDF. The spectra of the simulated E_{LKr}/p_{trk} in the range ($0.5 \div 1$) are shown in Fig. 3.27 (left panel): the blue distribution corresponds to the "true" E_{LKr}/p_{trk} variable
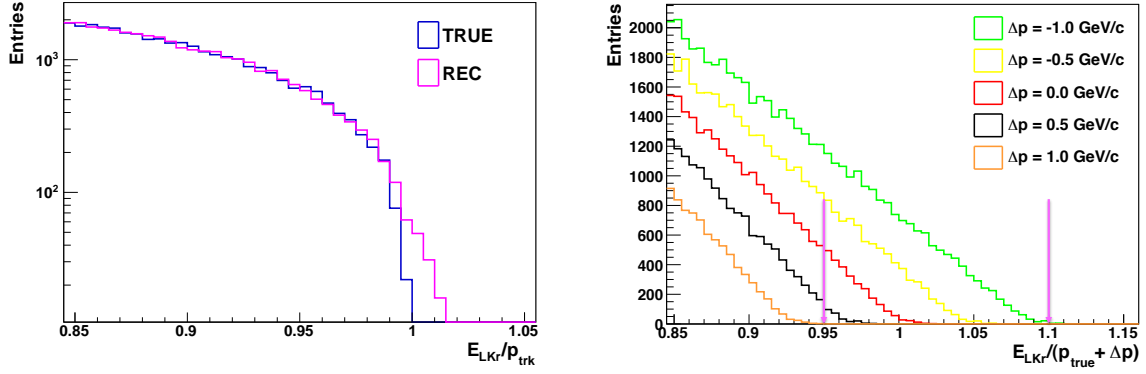
Figure 3.27: Left: simulated E_{LKr}/p_{trk} for "true" and reconstructed variables (log scale). Right: simulated $E_{LKr}/(p_{true} + \Delta p)$, where $\Delta p = -1, -0.5, 0, 0.5, 1\,\mathrm{GeV}/c$. The arrows indicate the "electron-like" region (0.95,1.10).

(vanishing at $E_{LKr}/p_{trk} = 1$ by construction); the magenta distribution represents the E_{LKr}/p_{trk} variable after the smearing introduced by the detector; as a result of resolution effects, the magenta distribution extends beyond $E_{LKr}/p_{trk} = 1$. A discrete set of $(p_{true}, \Delta p)$ has been chosen: 9 values of $p_{true} = 12.5, 17.5, ..., 52.5\,\mathrm{GeV}/c$ and 100 values of $\Delta p = -5, -4.9, ..., 5\,\mathrm{GeV}/c$. For each combination $(p_{true}, \Delta p)$ the corresponding $E_{LKr}/(p_{true} + \Delta p)$ is produced and the weight $f_{EoP}(p_{true}, \Delta p)$ is evaluated as the ratio between the number of entries in the "electron-like" region ($0.95 < E_{LKr}/(p_{true} + \Delta p) < 1.10$) and the total number of generated events, which is the same in all samples. In Fig 3.27 (right panel) the PDF of $E_{LKr}/(p_{true} + \Delta p)$ is plotted for $p_{true} = 10\,\mathrm{GeV}/c$ and $\Delta p = -1, -0.5, 0, 0.5, 1\,\mathrm{GeV}/c$.

The factors $f_{EoP}(p_{true}, \Delta p)$ are plotted in Fig. 3.28 for the fixed 9 values of p_{true} and as functions of Δp. These factors are applied as weights to MC $K_{2\pi}$ events depending on the "true" momentum of the charged pion and the difference $\Delta p = p_{rec} - p_{true}$ between the reconstructed and "true" pion momentum. Fig. 3.29 shows the effect of the correction on the Δp distribution of $K_{2\pi}$ MC background events passing the signal selection without E_{LKr}/p_{trk} cut. The $K_{2\pi}$ component peaking at $5\,\mathrm{GeV}/c$ completely disappeared after the correction. This is due to the anti-correlation between E_{LKr}/p_{trk} and Δp such that: for Δp increasing E_{LKr}/p_{trk} decreases and it goes below the lower limit $E_{LKr}/p_{trk} = 0.95$ of the "electron-like" region. The overall effect is large and implies a background reduction from $N(K_{2\pi})/N_{tot} = 0.8\%$ to $N(K_{2\pi})/N_{tot} = 0.4\%$, before and after the correction (Tab. 3.3).

As the MC simulation of the shower development produced by muons in the LKr
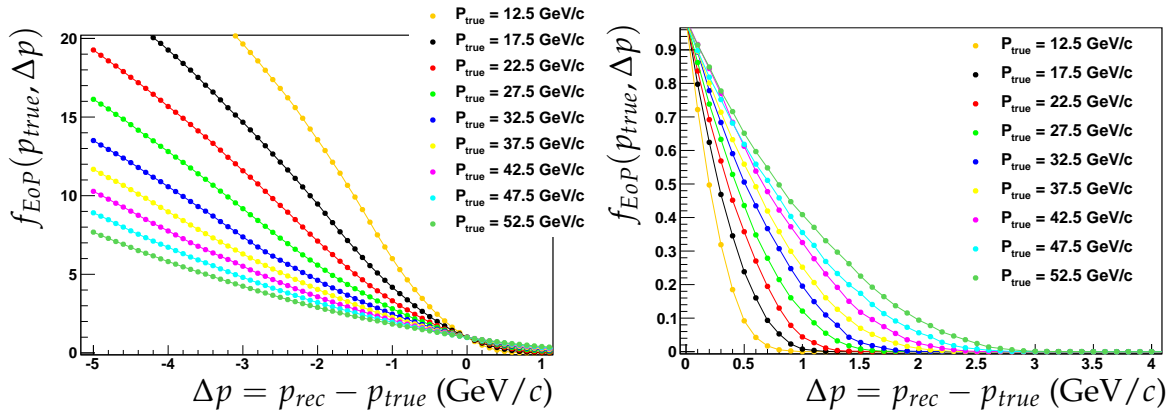
Figure 3.28: Correction factors, $f_{EoP}(p_{true}, \Delta p)$, as functions of (left panel) positive and (right panel) negative $\Delta p = p_{rec} - p_{true}$, for 9 bins of p_{true} momentum in the range $(10 - 55)\, \text{GeV}/c$.
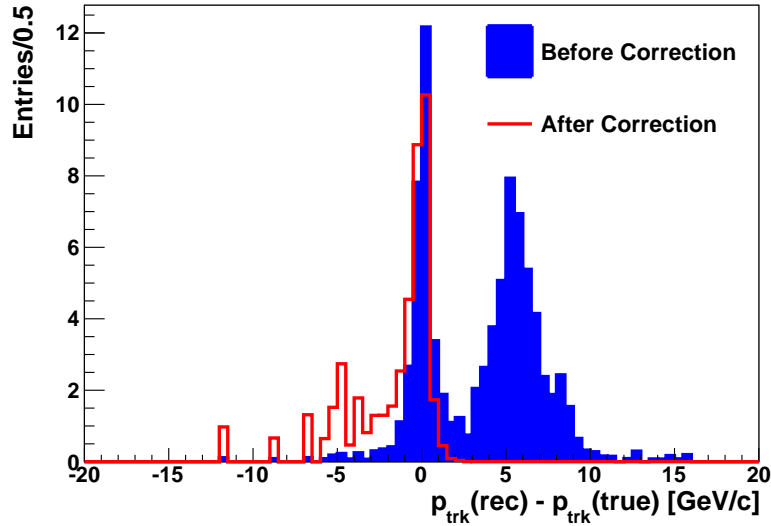
Figure 3.29: $\Delta p = p_{trk}(rec) - p_{trk}(true)$ distributions for $K_{2\pi}$ MC events passing the signal event selection (without E_{LKr}/p_{ptrk} cut) before (blue) and after (red) the correction for the dependence of $P(\pi \to e)$ on Δp. The effect of the correction is visible as the peak at $5\, \text{GeV}/c$ disappeared due to the anti-correlation between E_{LKr}/p_{trk} and Δp.

calorimeter suffers of the same problem discussed for the pions, the background contributions to $K_{e2\gamma}^+$ (SD$^+$) events coming from the $K_{\mu3}$ decays have been addressed with a similar approach. Specific $K_{\mu3}$ and $K_{\mu3D}$ MC samples have been analysed with the signal event selection without requiring the E_{LKr}/p_{trk} cut. From previous studies [82] the probability for a muon to be mis-identified as an electron $P(\mu \to e)$ was mea-

sured to be $\sim 10^{-6}$. Background MC samples with a muon in the final state have been weighted with the measured value of $P(\mu \to e)$. Due to the smallness of such probability the background contributions from $K_{\mu3}$ decays are negligible (see Tab. 3.3).

3.5 $K^+ \to e^+\nu_e\gamma(\text{SD}^+)$ form factors measurement

As described in Sec. 1.1, the $K^+_{e2\gamma}$ (SD^+) decay amplitude can be parameterized by the vector and axial-vector form factors, $F_V(x)$ and $F_A(x)$ respectively. The evaluation of the $K^+_{e2\gamma}$ (SD^+) form factors requires a theoretical effort due to the non-perturbative behaviour of the strong interactions at low energies. In this respect, χPT provides predictions of the $K^+_{e2\gamma}$ form factors up to $\mathcal{O}(p^6)$. A measurement of the $K^+_{e2\gamma}$ (SD$^+$) form factors with a precision below the theoretical one (discussed in Sec. 1.1.3) represents an important test of χPT . The description of the fitting method and the preliminary results of the form factor measurement are discussed below.

3.5.1 Definition of the fitting procedure

A model dependent procedure has been established to measure the form factors. This can be summarized into three steps:

- the computation of the number of $K^+_{e2\gamma}$ (SD^+) decays predicted by the theoretical model in bins of x;

- the convolution (folding) of the theoretical model with the detector acceptance and resolution, as simulated by the MC, to evaluate the reconstructed $K^+_{e2\gamma}$ (SD$^+$) events;

- fit of the measured events (data) with the reconstructed events (MC).

The effects of resolution and acceptance are encoded in a folding matrix P_{ij} (left panel in Fig. 3.30), which is used to smear the theoretical expectations. The matrix represents the probability that an event will be found with reconstructed value x in bin j, given that the true value was in bin i. The matrix depends on the theoretical model implemented in the MC[7], which is a-priori unknown; this dependence cancels out if the matrix binning is small enough that the resolution is approximately constant over the bin i. In principle the binning used for the fit can be different from the one applied

---

[7]The signal MC sample is generated assuming the form factors as measured by KLOE [21]

in the folding. In this procedure the fit binning (k) is chosen in order to perform the measurement with a reasonable statistical uncertainty ($\sim$ few %) in each bin of x.
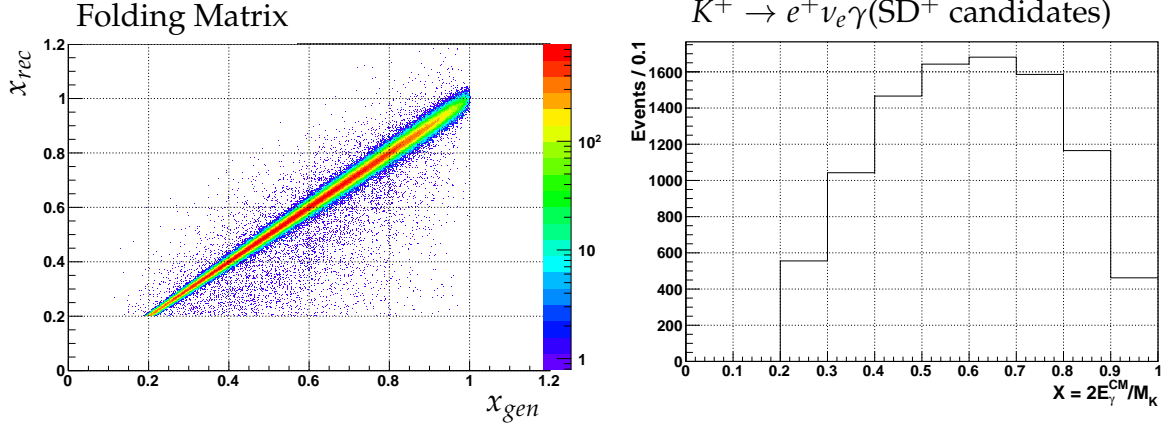
Figure 3.30: (Left) Folding matrix of the x distribution. Events reconstructed with an energy lower than the true energy are visible (mis-reconstructed events). (Right) Distribution of the $K_{e2\gamma}$ candidates over x.

The number of generated $K_{e2\gamma}^{+}$ (SD^{+}) decays in a given i bin of x is computed according to the theoretical differential decay rate with the vector form factor F_V expanded at the first order of x: $F_V = V_0(1 + \lambda(1 - x))$ and the axial-vector form factor $F_A(p^2) = F_A(0)$ as predicted by χPT at $\mathcal{O}(p^6)$. The number of events is normalized using the kaon flux $\Phi(K^+)$:

$$N_{gen}(x_i) = \Phi(K^+) \cdot dBR(x_i) \tag{3.11}$$

where $dBR(x_i) = \frac{dBR}{dx_i} \cdot \Delta x$ is the SD^+ theoretical differential branching ratio (introduced in Eq. 1.21) evaluated in bin centre and multiplied by the bin width Δx. The reconstructed distribution of the signal, $N_{rec}(x_j)$, is obtained by convoluting the theoretical spectrum with the folding matrix:

$$N_{rec}(x_j) = \sum_i P_{ij} \cdot N_{gen}(x_i).$$

Using Eq. 3.11 one can write:

$$N_{rec}(x_j) = \Phi(K^+) \sum_i P_{ij} \cdot dBR(x_i)$$

The expected number of $K_{e2\gamma}^{+}$ (SD^+) events, N_k^{exp}, is showed in Fig. 3.30 (right panel) and is obtained by re-binning the reconstructed distribution of the signal $N_{rec}(x_j)$ from $j \rightarrow k$ in order to match the fit binning. The choice of the bin width used for the

fit is dictated by the limited statistics of the SD^+ candidates. The x distribution has been divided in bins of width $\Delta x = 0.1$ (about 10 times larger than the average x resolution) and the fit has been performed over 8 bins ($0.2 < x < 1$). The total number of background events in bin k (N_k^{bkg}) is estimated according to the Eq. 3.12 and is subtracted to the number of data in bin k (N_k^{data}); the latter is then compared with the expected number of $K_{e2\gamma}^+$ (SD^+) events. The best value of the form factors compatible with the data is found by minimizing the χ^2 function:

$$\chi^2 = \sum_{k=1}^{8} \frac{(N_k^{data} - N_k^{exp})^2}{\sigma_{N_k^{data}}^2 + \sigma_{N_k^{exp}}^2}$$

assuming the $\sigma_{N_k^{exp}}^2$ to be negligible. The average number of candidates falling in each bin is about 1000 events/bin (Fig. 3.41).

3.6 Systematics effects

Several effects have been analysed for the evaluation of the systematic error associated to the measurement of the form factor parameters (V_0, λ). These are grouped in four categories:

- kaon flux computation (with the normalization channel);

- trigger efficiency;

- background subtraction;

- other systematic effects.

The contributions are reported with a precision of 10^{-4} and 10^{-3} for V_0 and λ, respectively. Although the rounding may be too generous for some effects, the choice is adopted because the statistical errors on V_0 and λ are one order of magnitude larger than the above precisions (see Eq. 3.13).

3.6.1 Kaon flux computation

The kaon flux $\Phi(K^+)$, introduced in Sec. 3.2, has been evaluated with K_{e3} decays. The branching ratios, BR($K^+ \to \pi^0 e^+ \nu_e$) = (0.0507 ± 0.0004) and BR($\pi^0 \to \gamma\gamma$) = (0.98823 ± 0.00034) [16], have been used to compute $\Phi(K^+)$ and the result is reported in Eq. 3.6. The relative error $\delta\Phi(K^+)/\Phi(K^+) = 0.8\%$ is dominated by the

limited precision at which $BR(K^+ \to \pi^0 e^+ \nu_e)$ is known. The dependence of the V_0 and λ results on this external parameter has been studied by looking at their variation when increasing $BR(K^+ \to \pi^0 e^+ \nu_e)$ by its uncertainty. One obtains the following variations: $\delta V_0 = 5.8 \cdot 10^{-3}$ and $\delta\lambda = 3 \cdot 10^{-3}$, which are considered as contributions to the systematic error (see Tab. 3.4).

3.6.2 Trigger efficiency

In the selection of $K^+_{e2\gamma}$ (SD$^+$) events, without x, y and m^2_{miss} cuts, a dependence of the 1TRKLM trigger efficiency on the energy of the photon candidate has been observed (see Sec. 3.3.6). Such dependence is due to background contaminations from $K_{2\pi}$ and K_{e3} decays, followed by $\pi^0 \to \gamma\gamma$ with a lost photon. The reliance of the measured 1TRKLM efficiency on the variable x has been considered; MC K_{e3} and $K_{2\pi}$ background events are weighted with a linear function of x obtained by fitting the slope. The correction has been quantified by comparing the form factor parameters achieved with and without applying the weight; the following variations have been observed: $\Delta V_0 = +1.8 \cdot 10^{-3}$ and $\Delta\lambda = -6 \cdot 10^{-3}$.

A residual systematic error associated to the correction has been evaluated. To account for the y cut missing in the procedure, the phase space of the y variable has been divided into 9 regions, defined by $(y_i, y_i + 0.1)$ with $y_i = 0.1, 0.2, ..., 0.9$ and the stability of the 1TRKLM efficiency (x dependent) has been studied as a function of y.

The measured 1TRKLM trigger efficiency is plotted in Fig. 3.31 as a function of x in 9 regions of y and its dependence on x (slope) is different in each y region. The 9 measured efficiencies, fitted with a linear function, have been applied as weights, in the same way as explained above, and 9 independent measurements of the form factor parameters, V_0 and λ, have been performed. Analogously, to account for the m^2_{miss} cut not applied in the procedure, 4 control regions of the m^2_{miss} variable have been chosen: $\{(-0.01, 0.01); (0.01, 0.03); (0.03, 0.05); (0.05, 0.07)\}$ GeV$^2/c^4$. The first m^2_{miss} region corresponds to the signal one. In the same way as performed with the y variable, the stability of the 1TRKLM efficiency (x dependent) has been studied as a function of m^2_{miss}. The measured 1TRKLM efficiency is shown in Fig. 3.32 as a function of x in the 4 regions of m^2_{miss}. Fitting the trigger dependence on x and applying the fit function as a weight to K_{e3} and $K_{2\pi}$ MC events with a lost photon, allows performing 4 independent measurements of the form factor parameters (V_0, λ).

The results (from both y and m^2_{miss} studies) are shown in the (V_0, λ) plane, in Fig. 3.33, where 14 values are plotted: 9 corresponding to the y regions (green markers),
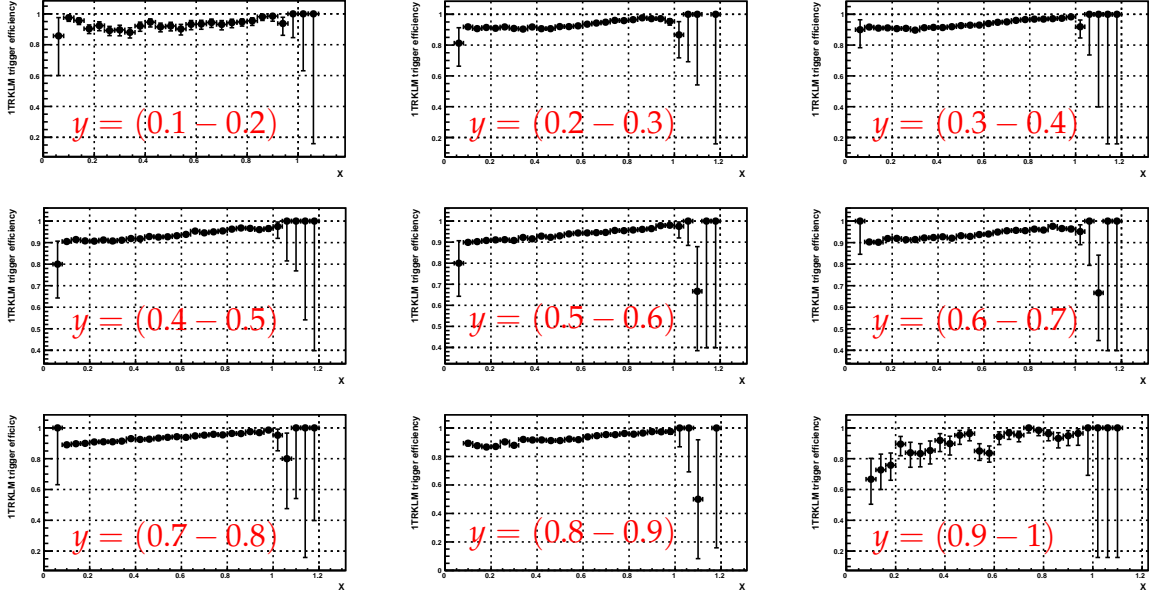
Figure 3.31: 1TRKLM trigger efficiency versus x for events passing the $K^+_{e2\gamma}$ (SD$^+$) event selection without kinematic cuts; the plots correspond to 9 regions of y defined as $(y_i, y_i + 0.1)$ with $y_i = 0.1, 0.2, ..., 0.9$.

one to the whole y spectrum (red marker) and the remaining 4 (blue markers) to the m^2_{miss} regions. Two systematic uncertainties have been assigned separately to the two sets of measurements because the corresponding studies have been performed at different stages of the analysis. Half of the maximum spread between the measurements in each set for each parameter is considered a systematic uncertainty. The following variations are obtained: $\delta V_0 = 0.1 \cdot 10^{-3}$ and $\delta \lambda = 4 \cdot 10^{-3}$ (for the study in y strips); $\delta V_0 = 0.1 \cdot 10^{-3}$ and $\delta \lambda = 2 \cdot 10^{-3}$ (for the study in m^2_{miss} regions). The contributions are summed up in quadrature and the correction for the trigger efficiency and its systematic uncertainty are summarised as follows: $\Delta V_0 = (+1.8 \pm 0.1) \cdot 10^{-3}$ and $\Delta \lambda = (-6 \pm 4) \cdot 10^{-3}$.

3.6.3 Background subtraction

The background contamination to $K^+_{e2\gamma}$ (SD$^+$) events amounts to $N(bkg)/N_{tot} = 2.3\%$. As explained in Sec. 3.4, the main component is due to K_{e3} events, $N(K_{e3})/N_{tot} = 1.8\%$, which enter the signal region via resolution effects and non-Gaussian tails of multiple Coulomb scattering (MCS) of the track. The study of the standard simulation with non-Gaussian tails of MCS shows that this background component is enhanced
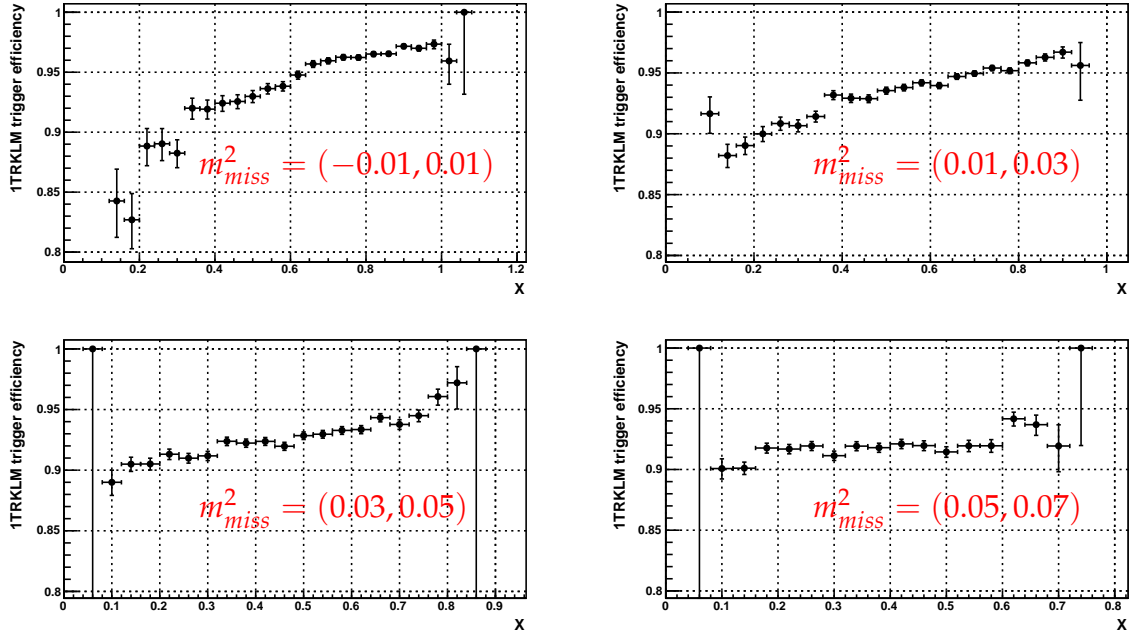
Figure 3.32: 1TRKLM trigger efficiency versus x for events passing the $K^+_{e2\gamma}$ (SD$^+$) event selection without kinematic cuts; the plots correspond to 4 control regions of the m^2_{miss} variable. The top-left panel corresponds to the signal region.
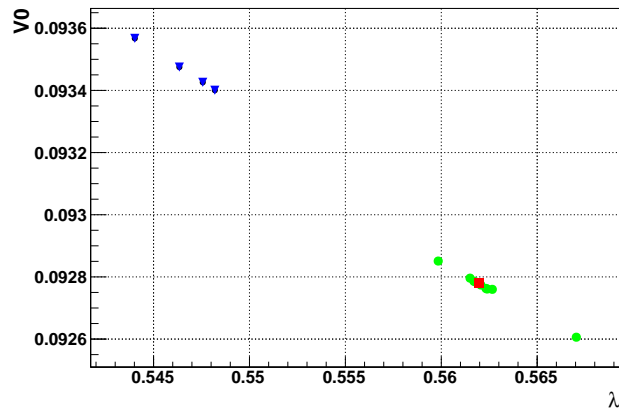
Figure 3.33: (V_0, λ) results obtained by correcting the $K_{2\pi}$ and K_{e3} background MC events with a lost photon for the 1TRKLM trigger efficiency dependence on x. The measurements are performed in 9 different kinematic regions of y (green markers), in the whole y spectrum (red marker) and in 4 different kinematic regions of m^2_{miss} (blue markers).
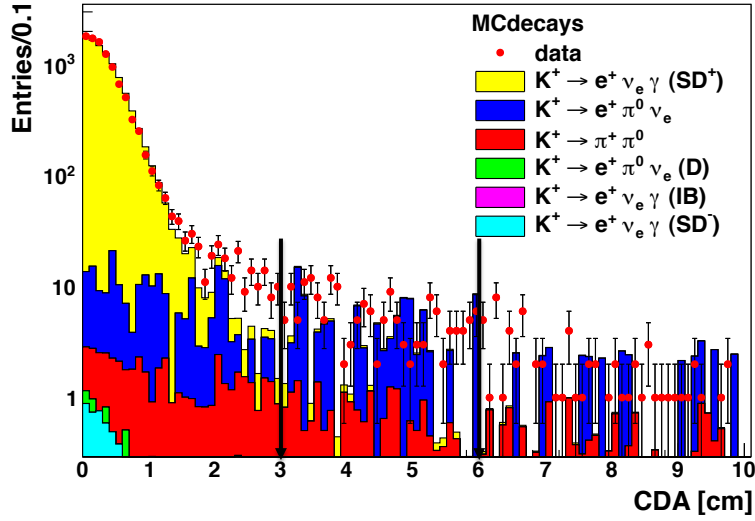
Figure 3.34: Reconstructed CDA distributions of $K^+_{e2\gamma}$ (SD^2) candidates compared with the sum of normalised estimated signal and background components (logarithmic scale). The deficit of reconstructed MC events in the region above 2 cm is due to resolution effects dominated by non-Gaussian tails. Detailed studies of such effects are on still going. The arrows represent the side-band chosen for the study of the background from non-Gaussian tails of MCS.

by a factor of 4 with respect to a model assuming pure Gaussian tails (see Sec. 3.4). The data-MC comparison for the CDA[8] parameter shows that the standard MC K_{e3} sample leads to an under-estimation of the tails. The same effect is observed in other relevant distributions, such as m^2_{miss} and x (see Figs. 3.35, 3.36). The dependence of the systematic error on (V_0, λ) from the uncertainty of the fraction of K_{e3} events have been studied. When comparing the two MC K_{e3} samples, a factor of 4 less background induces the following variations: $\delta V_0 = 19.7 \times 10^{-3}$ and $\delta\lambda = 63 \times 10^{-3}$.

Non-Gaussian tails are simulated with a limited precision and the number of K_{e3} events can be enhanced in data due to MCS and tails of the reconstructed momenta. Studies to address these points with different models (i.e. Geant4) are ongoing and will be completed after the submission of the present thesis. However, the CDA distributions for data and expected normalised[9] MC background components in Fig. 3.34 shows that a study of the side-bands of such observable may allow the background

---

[8]The CDA parameter is an observable sensitive to MCS.

[9]All the MC distributions but the signal have been normalised by means of the kaon flux and branching ratios. The MC $K^+_{e2\gamma}$ (SD$^+$) sample has been normalised to $N_{tot} - \sum_{bkg_i} N(bkg_i)$.

contaminations to be evaluated using data. Selecting a region $3\,\mathrm{cm} < \mathrm{CDA} < 6\,\mathrm{cm}$ populated by background only, one can infer that the discrepancy between data and MC standard simulations including non-Gaussian tails is about 80% of the discrepancy between the models used to evaluate the background. As a preliminary conclusion on the K_{e3} contamination, one can scale the above variations ($\Delta V_0, \Delta \lambda$) by a factor of 0.8 and include the results in Tab. 3.4 as estimations of the systematic errors on the form factor parameters due to the main background component. This contribution is the largest to the systematic error.
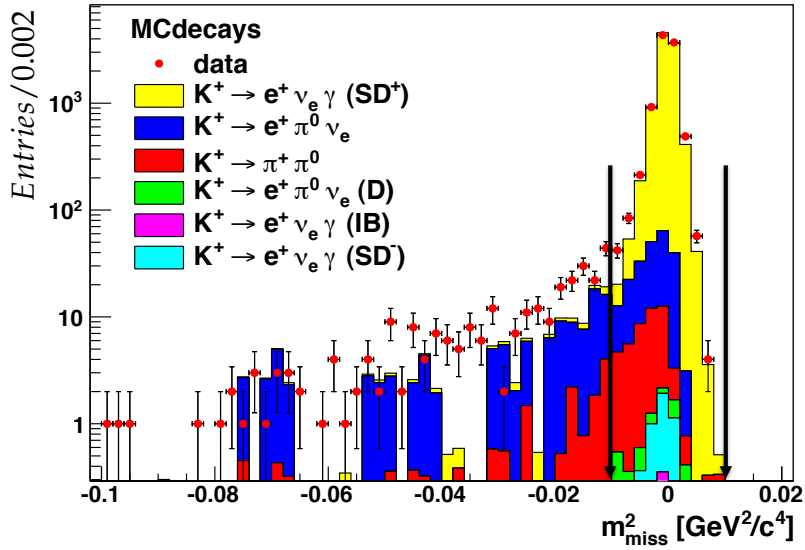
Figure 3.35: Reconstructed m^2_{miss} distributions of $K^+_{e2\gamma}$ (SD^2) candidates compared with the sum of normalised estimated signal and background components (logarithmic scale). The arrows define the signal region chosen for the analysis. The deficit of reconstructed MC events in the region below $0.01\,\mathrm{GeV}^2/c^4$ is mostly outside the signal region and due to resolution effects dominated by non-Gaussian tails. Such effects are being investigated.

The second main component of the residual background contamination in the selected $K^+_{e2\gamma}$ (SD$^+$) sample is due to $K_{2\pi}$, $N(K_{2\pi})/N_{tot} = 0.4\%$. This background depends on the pion mis-identification probability, introduced in Sec. 3.4.1. This probability has been measured to be 0.4% with a $\sim 5\%$ relative precision. The measured value (momentum dependent) has been applied as a weight to $K_{2\pi}$ MC events passing the signal selection without requiring any identification for the charged track (no E_{LKr}/p_{trk} cut). The size of the correction is not quoted because it is too large and
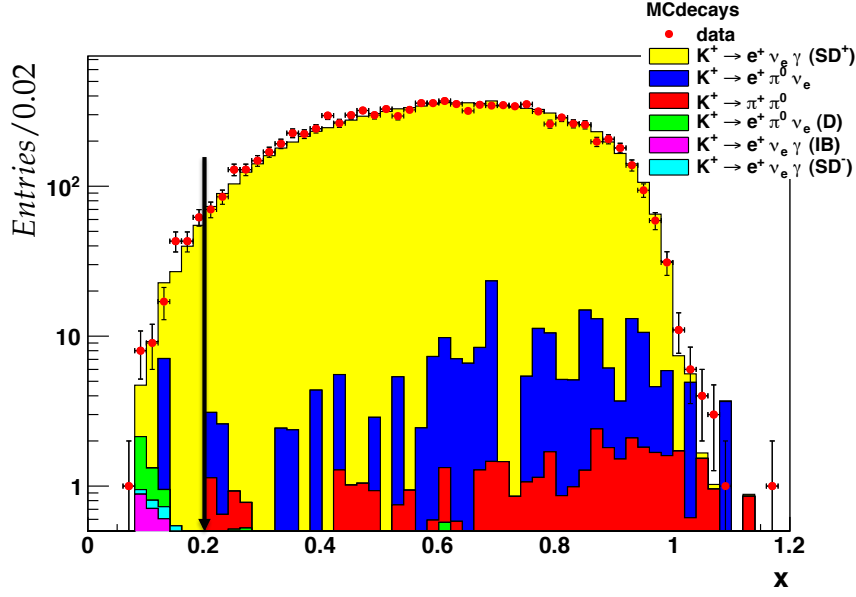
Figure 3.36: Reconstructed x distributions of $K^+_{e2\gamma}$ (SD^2) candidates compared with the sum of normalised estimated signal and background components (logarithmic scale). The x variable is proportional to the photon energy in the kaon rest frame. The arrow represents the lower limit: $x = 0.2$ applied in the event selection and corresponding to a lower limit on the photon energy in the kaon rest frame of about 50 MeV.

meaningless to the discussion of systematic effects. A residual systematic error has been assigned to the $K_{2\pi}$ background by studying the effect of the limited precision of the pion mis-identification probability on the final V_0 and λ results. When shifting the weights by their uncertainty the following variations are observed: $\delta V_0 = 0.2 \times 10^{-3}$ and $\delta\lambda = 1 \times 10^{-3}$.

As explained in Sec. 3.4, the study of this background allows to identify a component for which the track (the charged pion) is reconstructed with a momentum significantly higher than the true one ($\Delta p = p_{trk}(rec) - p_{trk}(true) > 2$ GeV, see Fig. 3.26). The measured pion mis-identification probability depends on Δp. To take into account the anti-correlation between the observables E_{LKr}/p_{trk} and p_{trk}, a weight depending on the true momentum and Δp has been applied to background $K_{2\pi}$ MC events on top of the previous weighting (see Sec. 3.4.1). The size of this correction is large and it amounts to: $\Delta V_0 = +11.8 \times 10^{-3}$ and $\Delta\lambda = -49 \times 10^{-3}$, when comparing the results before and after the correction. Possible sources of residual systematic errors associated to this correction have been considered.

- The E/p probability distribution function (PDF) of pions from $K_{2\pi}$ decays has

been simulated as linearly dependent on (E/p) and vanishing in the vicinity of $E/p = 1$. This assumption has been tested by looking at the variation of the form factors when modifying the dependence to a quadratic one $\sim (1 - E/p)^2$. The following systematic errors have been calculated: $\delta V_0 = 0.3 \times 10^{-3}$ and $\delta \lambda = 1 \times 10^{-3}$.

- The momentum and energy resolutions of the detector, quoted in Sec. 2.2 and Sec. 2.4, respectively, have been applied to smear the simulated PDF. This assumption has been tested by evaluating the variation of (V_0, λ) when shifting the resolutions by 1 unit in the least significant digit. The contributions from the momentum and energy resolutions have been studied separately and give the same systematic errors: $\delta V_0 = 0.2 \times 10^{-3}$ and $\delta \lambda = 1 \times 10^{-3}$.

The above uncertainties related to the $K_{2\pi}$ background are summed in quadrature and introduced in Tab. 3.4 as a single entry. These uncertainties are understood to be too optimistic and more investigations on systematic effects related to the $K_{2\pi}$ background component are foreseen.

3.6.4 Other systematic effects

Source	$\Delta V_0 (10^{-3})$	$\pm \delta V_0 (10^{-3})$	$\Delta \lambda (10^{-3})$	$\pm \delta \lambda (10^{-3})$
BR($K^+ \to \pi^0 e^+ \nu_e$) external parameter	-	± 5.0	-	± 3
Trigger efficiency	$+1.8$	± 0.1	-6	± 4
$K^+ \to \pi^0 e^+ \nu_e$ background	-	± 15.8	-	± 50
$K^+ \to \pi^+ \pi^0$ background	-	± 0.5	-	± 2
Spectrometer alignment	$+0.9$	± 0.1	-5	± 1
$P_K(\beta)$ correction	-	± 3.5	-	± 11
Beam simulation	-	± 1.0	-	± 5
LKr non-linearity	-2.3	-	$+6$	-
PID efficiency	-	± 1.2	-	< 1
LKr energy calibration	-0.7	-	$+1$	-
Corrections to LKr cluster positions	-	± 1.0	-	± 5

Table 3.4: Summary of corrections and systematic uncertainties evaluated for the $K_{e2\gamma}^+$ (SD$^+$) analysis. All reported uncertainties $(\delta V_0, \delta \lambda)$ are taken into account in the final results.

Several dependence studies of the results on the corrections applied to the $K^+_{e2\gamma}$ (SD$^+$) event selection and background rejection have been performed.

1. As explained in Sec. 3.1.5.3, a correction has been applied to the measured track momentum to take into account the internal mis-alignment of the drift chambers and the mis-calibration of the magnetic field in the spectrometer. The effect is quantified by looking at the variation of the results when removing the correction for the data; the values obtained are: $\Delta V_0 = 0.9 \times 10^{-3}$ and $\delta\lambda = 5 \times 10^{-3}$. A residual systematic uncertainty is assigned by evaluating the variation of the results when removing the correction for both data and MC events. The correction and its systematic uncertainty are reported in Tab. 3.4 (Spectrometer alignment): $\Delta V_0 = (+0.9 \pm 0.1) \times 10^{-3}$ and $\Delta\lambda = (-5 \pm 1) \times 10^{-3}$.

2. As described in Sec. 3.1.5.3, a β correction has been applied to the average kaon momentum, which is computed from reconstructed $K^+ \to \pi^+\pi^+\pi^-$ decays (see Sec. 3.1.4). The systematic uncertainty associated is quantified by evaluating the variations $(\delta V_0, \delta\lambda)$ when removing the correction, which is applied to both data and MC. The following values are obtained and reported in Tab. 3.4 ($P_K(\beta)$ correction): $\delta V_0 = 3.5 \times 10^{-3}$ and $\delta\lambda = 11 \times 10^{-3}$.

3. As discussed in Sec. 3.1.5.5 a difference between the widths of data and MC kaon momentum distributions has been observed by reconstructing $K \to \pi\pi\pi$ events. The difference lies in the core width of the distributions (around the nominal value of $74\,\mathrm{GeV}/c$) and also in the momentum tails, as shown in Fig. 3.8. To account for this effect, a weight w have been applied to signal and background MC events: w is reported in Eq. 3.2 and depends on the generated kaon momentum and a time-dependent parameter τ. At first order for the data sample analysed in this thesis, $\tau = 0.07\,\mathrm{GeV}^{-2}$ allows to adjust the discrepancy in the core width. At second order extra factors are added to adjust the discrepancy in the momentum tails. The associated systematic uncertainty has been evaluated by comparing the results obtained with the first- and second-order implementations of the correction. The following variations are observed and reported in Tab. 3.4 (Beam simulation): $\delta V_0 = 1.0 \times 10^{-3}$ and $\delta\lambda = 5 \times 10^{-3}$.

4. As explained in Sec. 3.1.5.1, a correction has been applied to the reconstructed LKr cluster energy for data to account for the non-linearity in the calorimeter response and not simulated in the MC. The effect is negligible for cluster energies above $10\,\mathrm{GeV}$; a possible source of systematic uncertainty due to energy

depositions in the LKr below this threshold has been considered. When removing the correction the following variations are observed and reported in Tab. 3.4 (LKr non-linearity): $\Delta V_0 = -2.3 \times 10^{-3}$ and $\Delta\lambda = +6 \times 10^{-3}$. The size of the correction $(\Delta V_0, \Delta\lambda)$ allows neglecting a possible systematic error associated.

5. In previous analyses [72] the positron identification probability was measured from reconstructed K_{e3} events ($\sim 99\%$). In this analysis such probability is applied as a weight to signal and background MC events with a positron in the final state. A systematic error on form factor parameters has been evaluated by varying the weight by its uncertainty ($\sim 0.05\%$ relative). The following contributions are obtained and reported in Tab. 3.4 (PID efficiency): $\delta V_0 = 1.2 \times 10^{-3}$ and $\delta\lambda = 0.4 \times 10^{-3}$.

6. As discussed in Sec. 3.1.5.1), a LKr cell-by-cell energy calibration has been performed to improve the homogeneity of the LKr response and increase the positron identification probability. A correction depending on the track impact point at the LKr front plane, thus on the LKr cells involved into the development of the electromagnetic shower, has been applied to the data. The effect has been quantified by looking at the variation of the results when removing the correction. The following values are obtained and reported in Tab. 3.4 (LKr energy calibration): $\Delta V_0 = -0.7 \times 10^{-3}$ and $\Delta\lambda = +1 \times 10^{-3}$. The size of the correction $(\Delta V_0, \Delta\lambda)$ allows neglecting a possible systematic error associated.

7. The positions of LKr clusters reconstructed for data and MC events have been corrected according to the procedure described in Sec. 3.1.5.2 and accounting for: the DCH-LKr alignment; the LKr projectivity structure; the LKr shower development. The correction has been quantified by studying the variation of the form factor parameters when the correction is not applied. The following values are obtained and reported in Tab. 3.4 (LKr cluster position): $\delta V_0 = 1.0 \times 10^{-3}$ and $\delta\lambda = 4 \times 10^{-3}$.

3.7 Stability checks

The stability of the final V_0 and λ results with respect to several cuts chosen for the event selection and the background rejection has been studied.

The uncertainties associated to the detector acceptance and the spectrometer reconstruction have been evaluated by varying:

- the upper cut applied on the reconstructed CDA parameter, introduced in Sec. 3.1.2 (see Fig. 3.37). The nominal cut is: CDA < 3 cm.

- lower and upper cuts on the reconstructed longitudinal coordinate of the decay vertex Z_{vtx} (see Figs. 3.38, 3.39). The nominal cut, defined in Sec. 3.1.2, is: -16 m $< Z_{vtx} < 90$ m.

The form factor variations resulting from the above studies are within the statistical errors associated to V_0 and λ at the nominal cuts.
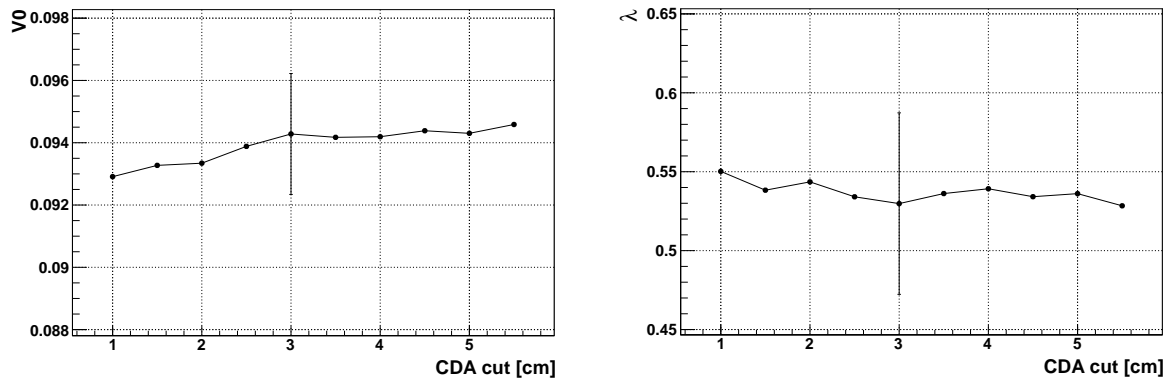
Figure 3.37: Stability check of the form factor parameters on the CDA cut. The variations of V_0 and λ are within the statistical errors associated for the nominal upper cut: CDA $= 3$ cm. No systematic uncertainties are considered.
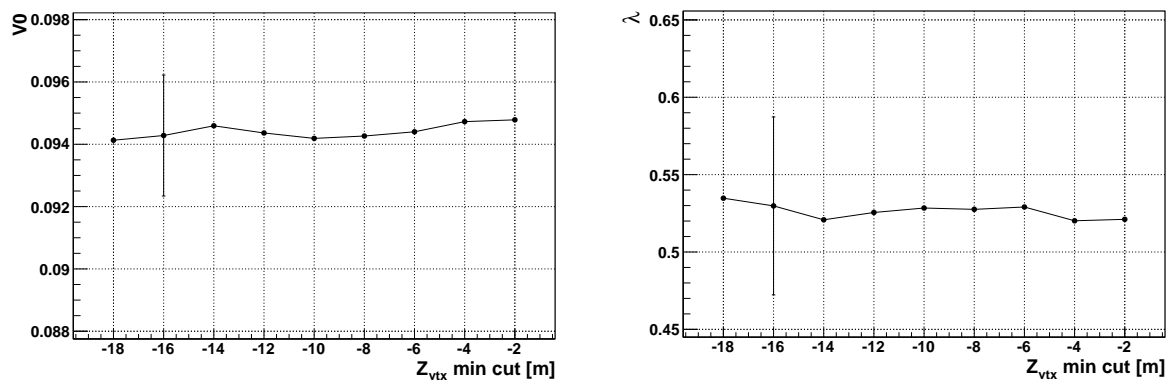
Figure 3.38: Stability check of the form factor parameters on the lower limit of the Z_{vtx} cut. The variations of V_0 and λ are within the statistical errors associated for the nominal lower cut: $Z_{vtx} = -16$ m. No systematic uncertainties are considered.
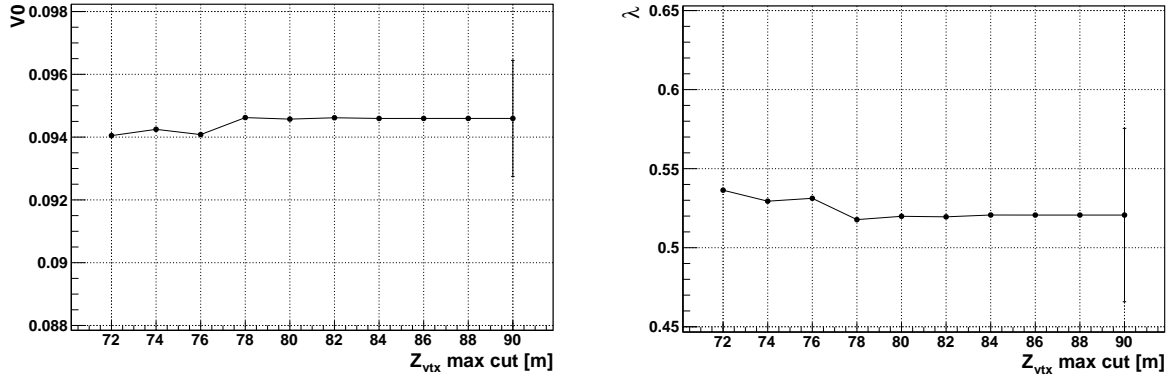
Figure 3.39: Stability check of the form factor parameters on the upper limit of the Z_{vtx} cut. The variations of V_0 and λ are within the statistical errors associated for the nominal upper cut:$Z_{vtx} = 90$ m. No fluctuations are observed in the last 4 points because the Z_{vtx} distribution for signal events at the end of the selection ends at 80 m. No systematic uncertainties are assigned.
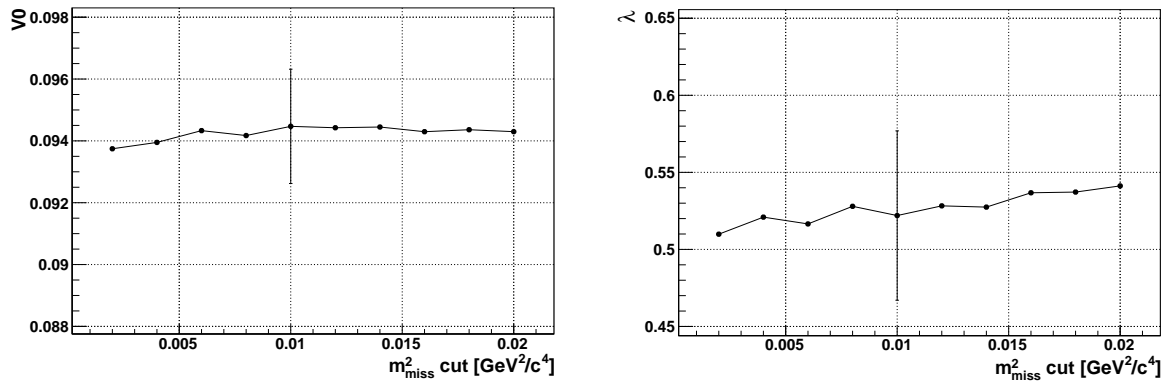
Figure 3.40: Stability check of the form factor parameters on the $|m^2_{miss}|$ cut. The variations of V_0 and λ are within the statistical errors associated for the nominal cut: $|m^2_{miss}| < 0.01 \, \mathrm{GeV}^2/c^4$. No systematic uncertainties are considered.

The dependence of the final result on the signal kinematics has been investigated by varying lower and upper cuts on the reconstructed missing mass $m^2_{miss} = (P_K - P_e - P_\gamma)^2$ (see Fig. 3.40). The nominal cut, defined in Sec. 3.1.6, is $|m^2_{miss}| < 0.01 \, \mathrm{GeV}^2/c^4$. The form factor variations observed are within the statistical errors associated to V_0 and λ at the nominal cut. No systematic uncertainties are added to the ones in Tab. 3.4.

3.8 Results

The number of $K^+_{e2\gamma}$ (SD$^+$) data candidates, the signal acceptance[10] and the expected number of residual events for the main background components and the total are summarised in Tab. 3.5.

$N(K^+ \to e^+\nu_e\gamma, SD^+)$	9835
$Acc(K^+ \to e^+\nu_e\gamma, SD^+)$	0.06156 ± 0.00004
N(K_{e3}) bkg	178 ± 20
N($K_{2\pi}$) bkg	43 ± 4
$N_{tot}(bkg)$	221 ± 20

Table 3.5: Summary of the $K^+_{e2\gamma}$ (SD$^+$) data candidates, the signal acceptance, the main background components and the total background contamination; all errors are statistical.

The total background $N_{tot}(bkg)$ is evaluated using the usual formula:

$$N_{tot}(bkg) = \Phi(K^+) \times \sum_{bkg_i} BR(bkg_i) \times Acc(bkg_i) \tag{3.12}$$

where $\Phi(K^+)$ is the kaon flux, $BR(bkg_i)$ is the branching ratio of the single decay channel contributing to the background and $Acc(bkg_i)$ is the corresponding geometrical acceptance. All acceptances for background and signal processes are computed by MC simulations. The errors associated to the residual backgrounds, reported in Tab. 3.5, are the statistical errors computed by error propagation of the terms in Eq. 3.12.

3.8.1 Fit to the χPT at $\mathcal{O}(p^6)$

The result of the fit using χPT at $\mathcal{O}(p^6)$ with $F_V(0)$ and λ as free parameters is shown in fig.3.41. The following results are obtained:

$$V_0 = 0.0946 \pm 0.0018_{stat} \pm 0.0170_{syst}$$
$$\lambda = 0.521 \pm 0.055_{stat} \pm 0.052_{syst} \tag{3.13}$$

with $\chi^2/ndf = 6.27/6$ and a statistical correlation coefficient between the parameters of -0.94; the systematic errors are $\sim 100\%$ correlated.

---

[10]The signal acceptance is reported here for completeness and is evaluated with MC assuming the form factors as measured by KLOE (Eq. 1.22).

χ^2 / ndf	6.273 / 6
V0	0.0946 ± 0.0018
lambda	0.5205 ± 0.0548
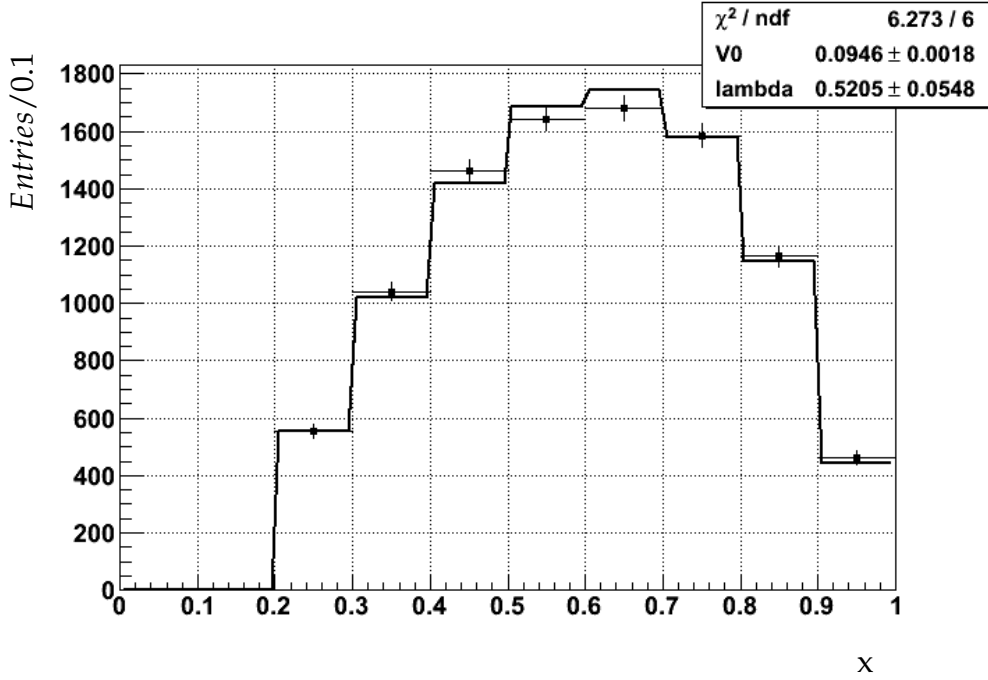
Figure 3.41: Fit to χPT at $\mathcal{O}(p^6)$. The fit parameters are the vector form factor V_0 and the "slope" λ, while the axial form factor is fixed to its $\mathcal{O}(p^6)$ value $F_A(q^2) = F_A(0) = 0.034$.

The fit results are the form factor parameters (V_0, λ) and their correlation, which can be represented with confidence interval contours in two dimensions (2D). The contours at 39.4%, 68.3%, 95% confidence levels (CL), are drawn in Fig. 3.42; the above numbers come from a general rule for the construction of confidence interval ellipses (2D case) of $n\sigma$: the probability is written as $P(n\sigma) = 1 - \exp(-n^2/2)$. As a consequence a 1σ ellipse ($n = 1$) corresponds to $P(1\sigma) = 1 - \exp(-0.5) = 39.4\%$. Similarly, 2σ and 3σ ellipses correspond to $P(2\sigma) = 68.3\%$ and $P(3\sigma) = 95\%$. The centre of the ellipse corresponds to the measured (V_0, λ), while the semi-axes are functions of the errors on (V_0, λ) and the angle ϕ between the major semi-axis and the V_0 axis. The angle ϕ satisfies the following relation:

$$tan(2\phi) = \frac{2\rho\sigma_{V_0}\sigma_\lambda}{\sigma_{V_0}^2 - \sigma_\lambda^2}.$$

The geometrical contours are evaluated from the matrix of second derivatives at the minimum point (χ^2_{min}). It is possible to compare NA62 and KLOE results in terms of confidence interval contours in the (V_0, λ) plane (Fig. 3.42). The NA62 and KLOE contours do not overlap: for KLOE the ellipses are constructed with the combination of statistical and systematic errors, while for the NA62 ellipses only the statistical errors

are implemented, for the time being. For the $K^+_{e2\gamma}$ (SD$^+$) form factor measurement the data sample selected by NA62 is a factor of ~ 8 larger than the one selected by KLOE. This makes the NA62 statistical precision better than the current PDG [16] average value[11] on this measurement. Nevertheless, at the present time the systematic error is dominating and the combined (stat+syst) result has a precision comparable to the one reported in the current PDG.
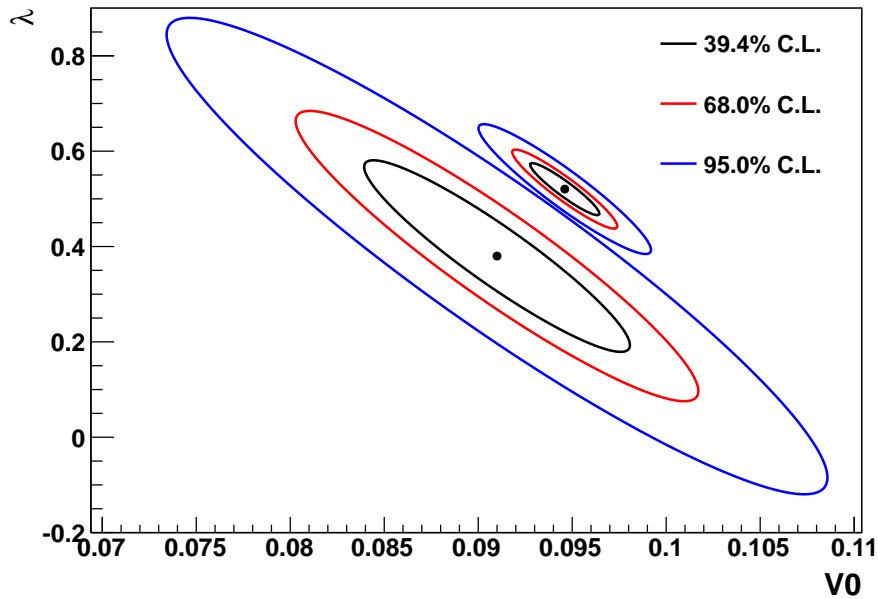
Figure 3.42: Comparison between NA62 and KLOE $K^+_{e2\gamma}$ (SD$^+$) form factor measurements. Confidence interval ellipses in the (V_0, λ) plane at 1σ, 2σ, 3σ (2D case).

---

[11]The PDG 2012 average is based on the measurement performed by KLOE.

Chapter 4

The NA62 experiment at CERN SPS

The main aim of the NA62 experimental programme is the study of the rare decay $K^+ \rightarrow \pi^+ \nu \bar{\nu}$ using an upgraded setup. The final goal is to measure BR($K^+ \rightarrow \pi^+ \nu \bar{\nu}$) with a 10% accuracy. The NA62 strategy foresees the collection of ~ 100 events of the $K^+ \rightarrow \pi^+ \nu \bar{\nu}$ decay, with a Signal to Background ratio (S/B) of 10/1, in two to three years of data taking starting at the end of 2014 [83]. This measurement can provide decisive tests of SM predictions in rare kaon decays or lead to a discovery of deviations from the SM that turns into indirect evidence of new physics. The new NA62 beam line and experimental apparatus are described in this chapter.

4.1   The experimental strategy and detector

To collect ~ 100 $K^+ \rightarrow \pi^+ \nu \bar{\nu}$ events, assuming a branching ratio of $\sim 10^{-10}$ and a detector acceptance of $\sim 10\%$, at least 10^{13} kaon decays are needed in the fiducial decay region. To measure BR($K^+ \rightarrow \pi^+ \nu \bar{\nu}$) with a 10% accuracy, the background must be controlled at the challenging level of 10^{12}. The two undetectable neutrinos and the presence of a single charged track in the final state require a new experimental design with redundant measurements of the event kinematics, excellent tracking and particle identification (PID) systems, as well as hermetic vetoes.

The kinematics of the $K^+ \rightarrow \pi^+ \nu \bar{\nu}$ decay is schematically sketched in Fig. 4.1: the momentum of the incoming kaon P_K, the momentum of the outgoing pion P_π and the angle between the mother and the daughter particles $\theta_{\pi K}$ are the only measurable quantities. It is convenient to use the squared missing mass kinematic variable, m_{miss}^2,
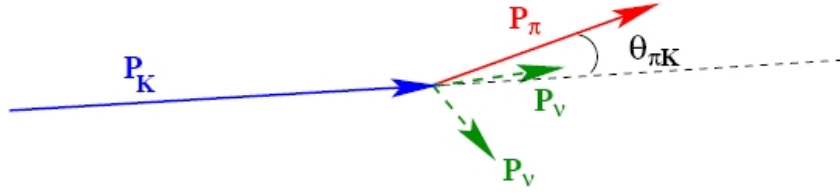
Figure 4.1: Kinematics of the $K^+ \to \pi^+ \nu \bar{\nu}$ decay.

defined as follows:

$$m_{miss}^2 = (E_K - E_\pi)^2 - (P_K - P_\pi)^2$$
$$= (E_K - E_\pi)^2 - (P_K^2 + P_\pi^2 - 2|P_K||P_\pi|\cos\theta_{\pi K}),$$

where

$$(E_K - E_\pi)^2 = m_K^2 + P_K^2 + m_\pi^2 + P_\pi^2 - 2|P_K||P_\pi|\sqrt{\left(1 + \frac{m_K^2}{P_K^2}\right)\left(1 + \frac{m_\pi^2}{P_\pi^2}\right)}.$$

In the above equations:

- $|P_K|$ is measured with a beam spectrometer (GTK, Sec. 4.1.3) located upstream the kaon decay region;

- $|P_\pi|$ is measured with a spectrometer (STRAW, Sec. 4.1.3) positioned downstream the kaon decay region;

- the angle, $\theta_{\pi K}$, is computed from the measurements of the kaon and pion directions, which are performed by the two spectrometers.

The m_{miss}^2 variable allows to distinguish between two background categories in the $K^+ \to \pi^+ \nu \bar{\nu}$ analysis: the main one accounts for 92% of charged kaon decays and consists of channels which are kinematically constrained ($K^+ \to \mu^+ \nu_\mu$, $K^+ \to \pi^+ \pi^0$, $K^+ \to \pi^+ \pi^+ \pi^-$ and $K^+ \to \pi^+ \pi^0 \pi^0$); the second one includes the remaining 8% of charged kaon decays, whose kinematics cannot be constrained by the m_{miss}^2 variable.

Fig. 4.2 shows the m_{miss}^2 distributions for $K^+ \to \pi^+ \nu \bar{\nu}$ and the background channels kinematically constrained, for $P_K = 75$ GeV/c. If resolution effects are ignored the $K^+ \to \pi^+ \pi^0$ decay is constrained to a line at $m_{miss}^2 = m_{\pi^0}^2$ and the m_{miss}^2 of the $K \to \pi\pi\pi$ decays shows a lower bound. The m_{miss}^2 of $K^+ \to \mu^+ \nu_\mu$ does not appear as a line at $m_{miss}^2 = 0$ because it is wrongly evaluated under the assumption that the track
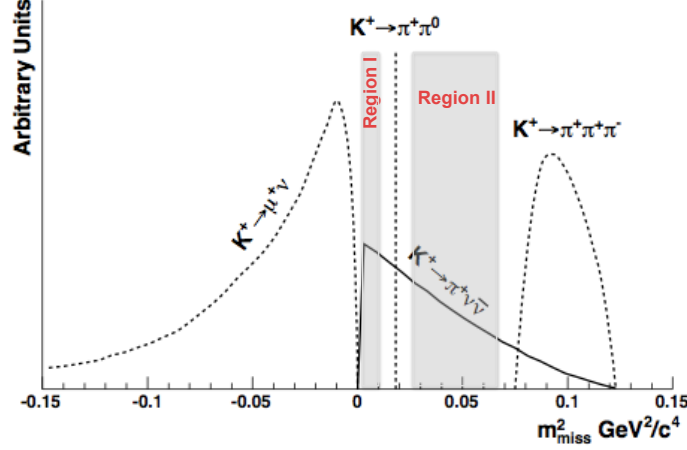
Figure 4.2: Distributions of the m^2_{miss} variable, as expected under the assumption that the detected charged particle in the final state is a pion, for the signal (solid curve) and the kaon decays kinematically constrained (dotted curves). The spectra are plotted in arbitrary units and neglecting the resolution effects introduced by the detector. The $K^+ \to \pi^+\pi^0$ kinematic signature forces the analysis region to be split into two parts: "Region I" and "Region II" (grey areas) [84].

is a pion; the spectrum has $m^2_{miss} = 0$ as the upper boundary. The rejection of these backgrounds relies on the reconstruction of the m^2_{miss} variable defined above. Nevertheless, to guarantee the background rejection at the required level of 10^{12}, kinematic constraints must be used in conjunction with PID and veto systems.

Fig. 4.3 shows the m^2_{miss} distributions for $K^+ \to \pi^+\nu\bar{\nu}$ and the background channels with non-constrained kinematics, for $P_K = 75$ GeV/c. The domain of the m^2_{miss} kinematic variable for these decays intersects the one for the signal $K^+ \to \pi^+\nu\bar{\nu}$. Some examples are: $K^+ \to \pi^0 l^+\nu_l$ and $K^+ \to \pi^+\pi^- l^+\nu_l$ with $l = e, \mu$; the radiative decays $K^+ \to \mu^+\nu_\mu\gamma$ and $K^+ \to \pi^+\pi^0\gamma$. To push down the level of these backgrounds, PID and veto detectors are the only experimental tools. However, with respect to the kinematically constrained background, here the rejection benefits from the smaller branching ratios of the channels. In Tab. 4.1 the dominant K^+ decay modes are reported, together with the techniques intended to reject them.

By looking at Fig. 4.2 one can define the signal region as the region of m^2_{miss} values for the $K^+ \to \pi^+\nu\bar{\nu}$ decay. The signal region needs to be as free as possible from the background. Due to the $K^+ \to \pi^+\pi^0$ kinematics, which produces a spike in the middle of the signal region, it is necessary to define two separate kinematical regions for the $K^+ \to \pi^+\nu\bar{\nu}$ acceptance (indicated as "Region I" and "Region II" in Fig. 4.2).
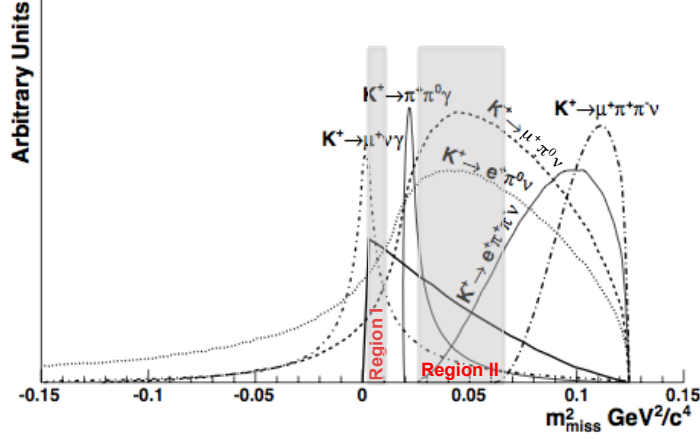
Figure 4.3: Distributions of the m_{miss}^2 variable, as expected under the assumption that the detected charged particle in the final state is a pion, for the signal (solid curve) and the kaon decays not kinematically constrained (dashed curves). The spectra are plotted in arbitrary units and neglecting the resolution effects introduced by the detector. The analysis regions: "Region I" and "Region II" are indicated with grey areas [84].

Decay	BR	Rejection mode
$K^+ \to \mu^+ \nu_\mu$	63%	Kinematics + μ-PID
$K^+ \to \pi^+ \pi^0$	21%	Kinematics + γ-Veto
$K^+ \to \pi^+ \pi^+ \pi^-$	6%	Kinematics + π^--Veto
$K^+ \to \pi^+ \pi^0 \pi^0$	2%	Kinematics + γ-Veto
$K^+ \to \pi^0 e^+ \nu$	5%	e-PID + γ-Veto
$K^+ \to \pi^0 \mu^+ \nu$	3%	μ-PID + γ-Veto

Table 4.1: Dominant kaon decays, their branching ratios and corresponding rejection techniques. The first four channels are kinematically constrained (their branching ratio sums up to 92%), while the last two channels are kinematically non-constrained.

Depending on the m_{miss}^2 resolution achievable for the signal ($\sim 10^{-3}$ GeV^2/c^4) upper and lower limits of the two signal regions will be defined in order to minimize the background contributions from gaussian tails due to the m_{miss}^2 of $K^+ \to \mu^+ \nu_\mu$, $K^+ \to \pi^+ \pi^0$ and $K \to \pi\pi\pi$ events. Fig. 4.4 shows the m_{miss}^2 total resolution (black circle) as a function of the pion momentum. The different components contributing to the resolution and coming from the kinematic variables P_K, P_π, θ_K and θ_π, namely the kaon and pion momenta and directions, are plotted as a function of the pion momentum.
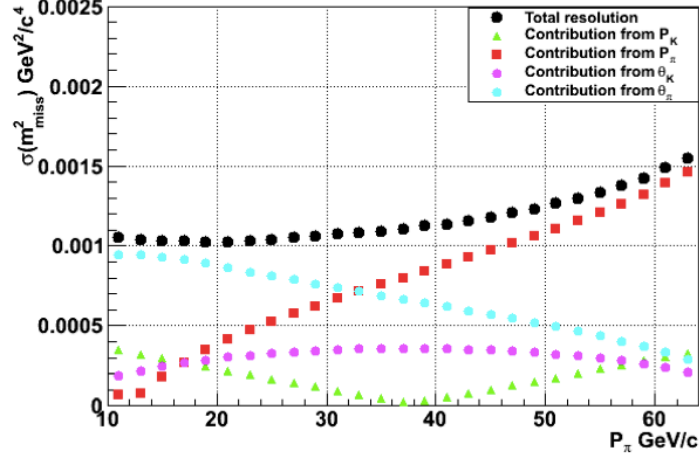
Figure 4.4: The m_{miss}^2 total resolution (black circle) as a function of the pion momentum (P_π). Single components contributing to the resolution from the measurement of P_K (green triangle), P_π (red square), θ_K (magenta circle) and θ_π (cyan circle), i.e. the kaon and pion momenta and directions, as a function of P_π [85].

4.1.1 The NA62 beam line

NA62 will use a kaon decay-in-flight technique. A secondary kaon beam will be produced from primary protons at 400 GeV/c delivered by the SPS and impinging on a beryllium target.

The advantage of using a high energy proton machine is that the kaon production cross-section increases with the proton energy, so fewer protons are needed to achieve a given kaon flux, thus reducing the non-kaon related accidental activity in the detector. The measured particle production data [86] established that, in the given length of the fiducial decay volume (~ 100 m), the number of K^+ (K^-) decays is maximum for $p_K \sim 0.23 p_0$ ($\sim 0.15 p_0$), where p_K and p_0 are the kaon and proton beam momenta respectively. Ultimately, 75 GeV/c is the maximum momentum value achievable to contain the required stages (momentum selection, K^+ tagging, momentum measurement and tracking) in the 102 m existing length between the production target and the beginning of the decay fiducial volume [87].

A drawback arising when performing the experiment at high momentum is that kaons cannot be efficiently separated from other charged hadrons (mainly pions and protons) at the beam level. As a consequence, upstream detectors are exposed to a particle flux larger[1] than the single component made of kaons. According to the NA62

---

[1] At 75 GeV/c the total beam particle flux is about 17 times higher than the kaon flux.

beam specifications the primary beam amounts to $\sim 7 \times 10^{12}$ protons per pulse (ppp) on the target. The total particle rate of a selected $75\,\mathrm{GeV}/c$ secondary hadron beam is about $750\,\mathrm{MHz}$; the single component rates are: protons at $173\,\mathrm{MHz}$, K^+ at $45\,\mathrm{MHz}$, π^+ at $525\,\mathrm{MHz}$, μ^+ at $6\,\mathrm{MHz}$ and e^+ $0.3\,\mathrm{MHz}$. The number of K^+ decays integrated over a year[2] in $60\,\mathrm{m}$ of decay fiducial length is 4.5×10^{12}; considering the signal branching ratio BR$(K^+ \to \pi^+ \nu \bar{\nu}) \sim 10^{-10}$ and the detector acceptance $\sim 10\%$, this translates into ~ 45 events collected in one year (i.e. ~ 100 events in two years).

For the secondary unseparated NA62 beam of $75\,\mathrm{GeV}/c$ central momentum the choice to select a positive rather than a negative beam is motivated by the following reasons:

- the K^+ production cross section is higher: $K^+/K^- \sim 2.1$;

- the fraction of kaons with respect to the total beam flux and with respect to the dominant (pion) component is the same for both charges.

The schematic layout of the NA62 experiment comprising the target, the beam line, the decay fiducial region and detectors is shown in Fig. 4.5.

After the production target quadrupole magnets are used to focus hadrons towards the centre of a beam dump stage (labelled with TAX). The latter is an achromatic corrector composed by four dipole magnets and a momentum-defining slit in the middle, which allows to select a narrow momentum band ($\simeq 1\% \Delta p/p$). More quadrupoles focus the beam towards two collimators acting in both vertical and horizontal planes and align the beam to the optical axis of a Cherenkov differential (CEDAR) counter, which is used to tag the K^+ in the beam. The next stage on the beam line is a particle tracking system composed by a second achromatic corrector, made of four dipole magnets and three stations of GigaTracKer (GTK) detector. This stage, discussed in more detail in Sec 4.1.3, provides the momentum and direction measurements for all particles in the beam. The third GTK station is positioned right after a final collimator on the beam line and is followed by a veto detector (CHarged ANTI - CHANTI), which surrounds the beam in vacuum and is designed to reject charged particles produced by the beam scattering into the GTK detector material (see Sec. 4.1.5).

4.1.2 The detector overview

An extensive discussion on the individual components can be found in [87]. The decay fiducial region, whose beginning is marked by the exit of the final collimator, is

---

[2]The NA62 strategy foresees a 100-days running time per year with an effective duty cycle of 20%.
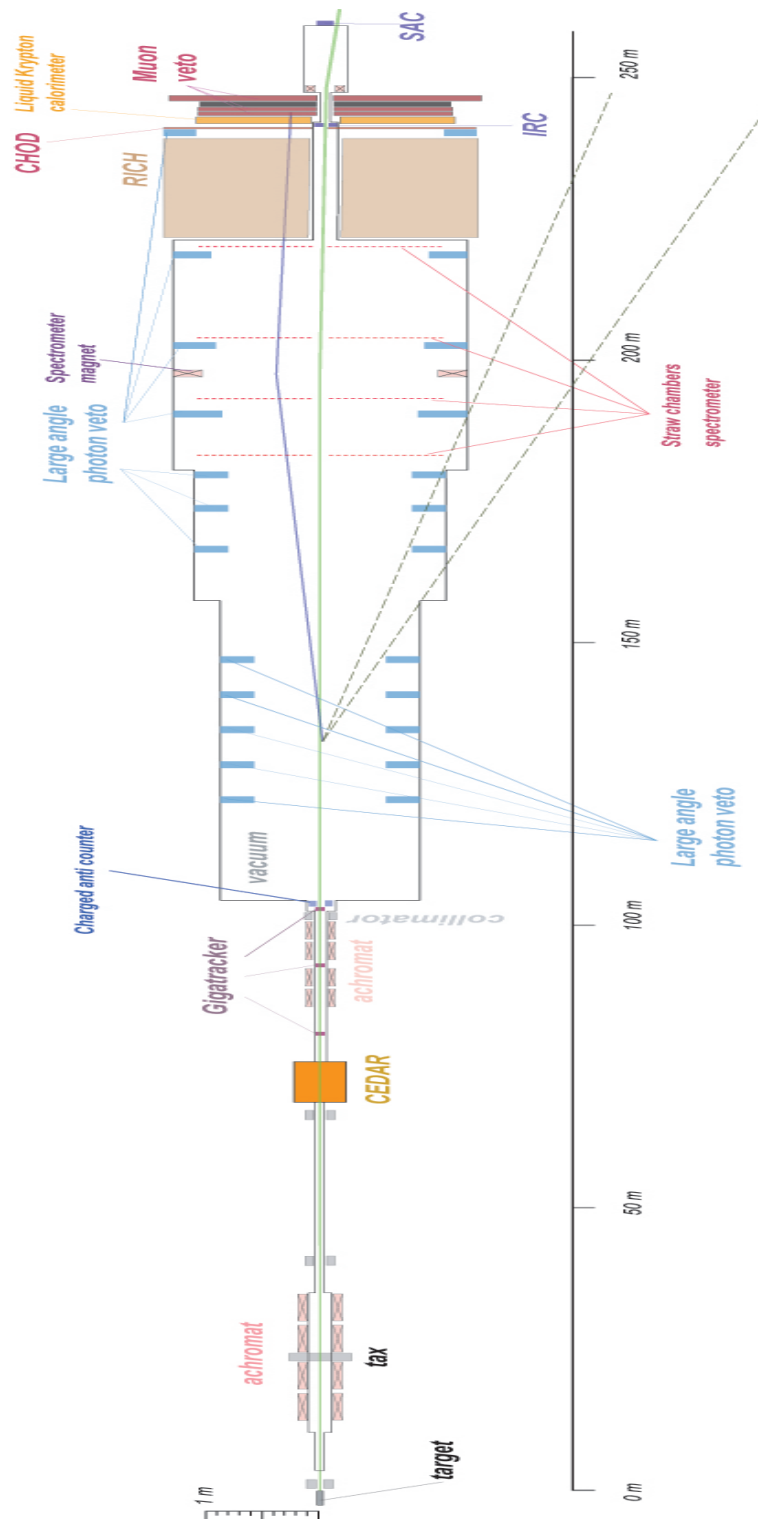
Figure 4.5: Schematic layout of the NA62 experiment including the beam line, the decay fiducial region and detectors.

contained in the first 60 m of a large vacuum tank, $\sim$ 120 m long. The beam is transported in vacuum through the downstream detectors with a thin-walled aluminium

beam tube of inside diameter of $\sim 156\,\text{mm}$.

A magnetic spectrometer, composed of four straw-tubes chambers (STRAW) and a large-aperture dipole magnet, is responsible for the detection and tracking of the charged decay products inside the vacuum tank (see Sec. 4.1.3). The magnet provides a horizontal transverse momentum kick of $270\,\text{MeV}/c$, thereby deflecting the $75\,\text{GeV}/c$ beam by 3.6 mrad.

After the spectrometer, a Ring Imaging CHerenkov (RICH) counter, further discussed in Sec. 4.1.4, provides the identification of pions from kaon decays and the separation π/μ, necessary to reject the $K^+ \rightarrow \mu^+ \nu_\mu$ decays, in the pion momentum range (15;35) GeV/c. As a consequence, for kaon decays with K^+ at $75\,\text{GeV}/c$, the decay products, other than the accepted π^+, will carry an energy of at least 40 GeV, which helps the background rejection. As an example, the probability that both photons from a 40 GeV π^0 decay are left undetected because of detector inefficiencies is below 10^{-8}. The RICH is followed by a "charged" hodoscope (CHOD), similar to the hodoscope employed in the NA48/2 detector and described in Sec. 2.3.

The vacuum tank, the magnetic spectrometer, the RICH and CHOD are interspaced by twelve stations of ring-shaped Large Angle photon Veto (LAV) detectors. The LAV is designed to reject the second main background due to $K^+ \rightarrow \pi^+ \pi^0$ decays, followed by $\pi^0 \rightarrow \gamma\gamma$; together with the LKr electromagnetic calorimeter, which is inherited from the predecessor experiment and described in Sec. 2.4, it covers the angular region of photon emission up to 50 mrad. In the forward region the detection of photons is rendered hermetic by means of an Intermediate Ring Calorimeter (IRC), placed between the CHOD and the LKr, and a Small-Angle Calorimeter (SAC), positioned on the beam line at the downstream end of it. The LAV, LKr, IRC and SAC detectors compose the photon veto system, addressed in Sec. 4.1.5. The beam is finally absorbed in a beam dump composed of iron surrounded by concrete.

4.1.3 Tracking systems

The GigaTracKer (GTK) detector plays a fundamental role in the NA62 measurement strategy, which relies on the tracking of K^+ under the following conditions:

- high and non-uniform beam rate (750 MHz over $1620\,\text{mm}^2$ - $1.3\,\text{MHz}/\text{mm}^2$ peak value);

- minimal amount of material ($< 1\% X_0$) on the beam line to preserve the beam divergence and limit beam hadronic interactions;
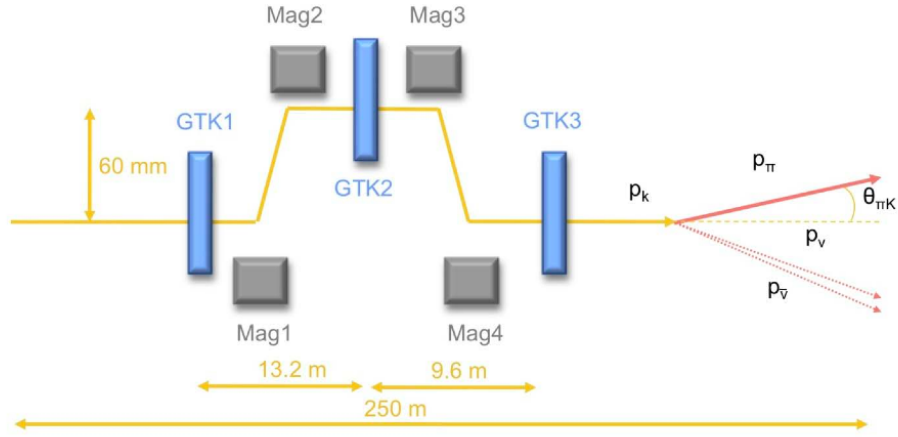
Figure 4.6: Schematic layout of the Gigatracker stations and sketch of the $K^+ \to \pi^+ \nu \bar{\nu}$ decay.

- excellent time resolution ($\sim$150 ps) matching the pion tracking information from downstream detectors;

The GTK is composed of three stations (GTK1, GTK2 and GTK3) placed along the beam line and mounted in between four achromat magnets (Fig. 4.6). The measurement of the particle momentum and direction is obtained through a magnetic field bending the path of the particle, which traverses it, in proportion to its momentum. In the middle of the four magnets the beam is displaced by 60 mm. Simulation studies of kaon decays in the detector, assuming the expected resolution from downstream detectors tracking the pions, has established the following required resolutions on beam momentum and direction: $\sigma(p_K)/p_K \sim 0.2\%$ relative and 16 μrad, respectively. Each GTK station is a hybrid silicon pixel detector containing 18,000 pixels of size 300×300 μm^2, arranged in a matrix of 90×200 elements. The pixel thickness is 200 μm and it corresponds to $0.22\% X_0$. Including the material budget for the pixel readout and cooling, the total amount per station is below $0.5\% X_0$.

To measure the momentum and direction of secondary charged particles originating from the decay region, a downstream magnetic spectrometer is employed. It is composed of a high aperture dipole magnet, providing a vertical B-field of 0.36 T, and four tracking chambers. To minimise multiple scattering effects, the spectrometer will work in vacuum. Straw-tube chambers are considered optimal tracking detectors to cover large areas and operate in vacuum. Each chamber is equipped with 1,792 straw tubes, which are positioned in four "Views" (see Fig. 4.7) providing measurements of two couple of orthogonal coordinates (x,y ; u,v): this is necessary to eliminate the
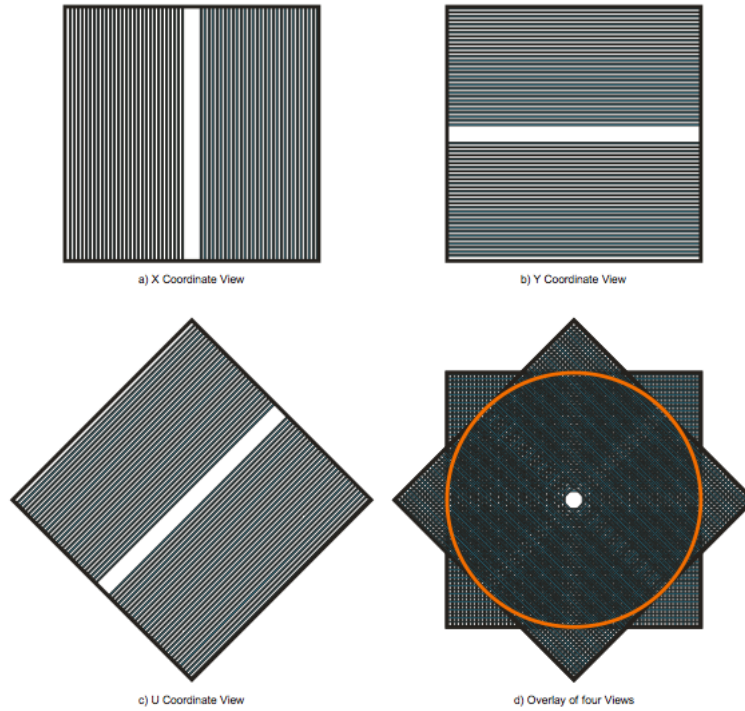
Figure 4.7: Straw chamber four "Views" assembly: a) the x "view" with straws vertically oriented; b) the y "view" with horizontal straws; c) the u "view" with straws rotated by 45 degrees with respect to the straws in the y "view" (the v "view" is rotated by 90 degrees with respect to the u "view"); d) One straw chamber assembly made of the four "Views"; each chamber has an active area of 2.1 m diameter. The central hole allows the beam passage.

ambiguity in the track assignment in case of multiple hits. The central part of the chamber is not equipped with straw tubes in order to allow the beam pipe passing through. The determination of each coordinate is obtained combining the information from four layers of straw tubes: this resolves the left-right ambiguity in the corresponding coordinate. The physics performances of NA62 imply several requirements on the Straw Tracker design:

- use of minimum amount of material ($\leq 0.5\% X_0$ for each chamber) along the particle trajectory to minimise multiple Coulomb scattering;

- a spatial resolution ($\leq 130 \mu$m per coordinate and $\leq 80 \mu$m per space point) to reconstruct precisely the intersection point between the decay and parent particle;

- operation with an average particle rate of 40 kHz and up to 500 kHz for straws

106

close to the beam;

- capability to veto events with multiple charged particles.

4.1.4 Particle identification detectors

The first PID detector on the NA62 beam line is the CEDAR: a Cherenkov diffe-rential counter proposed for the charged kaon identification and tagging. The CEDAR represents the detector whose upgrade, development and test I was directly involved into. An extensive discussion about its operation mode, features and usage in NA62 will follow in Chp. 5.
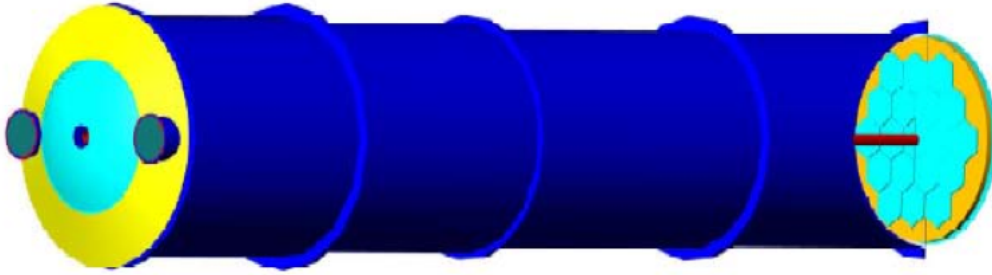
Figure 4.8: Schematic layout of the NA62 RICH detector: the right section of the vessel is cut to show the spherical mirror and the beam pipe.

The kaon decay channel $K^+ \rightarrow \mu^+ \nu_\mu$ represents the main source of background to $K^+ \rightarrow \pi^+ \nu \bar{\nu}$ events: $\text{BR}(K^+ \rightarrow \mu^+ \nu_\mu) \sim 63\%$ and it may lead to a signal event if the μ^+ is mis-identified as a π^+. The usage of a RICH counter (introduced in Sec. 4.1.2) has been proposed to reject the muon in the final state. In a Cherenkov detector the PID exploits the formation of light cones due to the Cherenkov effect. That is, a charged particle traversing a medium, with a velocity β larger than the speed of light c in the medium, emits a Cherenkov radiation at an angle θ_c with respect to the particle trajectory such that:

$$\cos \theta_c = 1/n\beta \,, \tag{4.1}$$

where β is normalised to c and n is the index of refraction of the medium. In a RICH detector, the light cone image is reflected by a spherical mirror, placed at one end of the vessel (see Fig. 4.8), on a photon detector located at the opposite end of the same volume. The photon detector sits on the mirror focal plane (the plane orthogonal to

the optical axis and passing through the focal point[3]) and if the particle trajectory is parallel to the optical axis, the cone image is a ring of radius: $r = f \tan \theta_c \sim f \theta_c$, for small θ_c angles[4] and where f is the focal length of the mirror (equal to half of its curvature radius). Once the optical path, defined as $f \times n$, is fixed, the Cherenkov ring radius depends only on the particle velocity β. If the particle has mass m, its momentum p is given by:

$$p = m\gamma\beta = \frac{m\beta}{\sqrt{1 - \beta^2}} \tag{4.2}$$

where γ is the Lorentz factor; it follows that for a given value of p the Cherenkov angle θ_c, thus the ring radius r, is only a function of the particle mass.

According to the NA62 measurement strategy the requirements to be fulfilled by the RICH detector are:

- π^+/μ^+ separation in the momentum range $(15,35)\,\text{GeV}/c$ providing a muon suppression factor of at least 10^{-2};

- time measurement with a resolution of at least $100\,\text{ps}$;

To be fully efficient on particles of momentum p, the threshold p_t, defined as $p_t = \beta_t m$, where $\beta_t = 1/n$ (from Eq. 4.1) is the threshold velocity below which no Cherenkov radiation is emitted, must be about 20% smaller than the actual particle momentum p. From similar considerations applied to the pion momentum range, it follows the choice of the gas. In particular, the lower limit $p = 15\,\text{GeV}/c$ implies $p_t \sim 12.5\,\text{GeV}/c$, which leads to a refractive index such that: $(n-1) = 62 \times 10^{-6}$, corresponding to Neon gas at atmospheric pressure.

The photon detector technology is based on Hamamatsu R7400U-03 photomultiplier tubes (PMTs). Assuming a single-photon detection, the time resolution on the pion crossing time[5], $\sigma_\pi(t)$, is proportional to the time resolution of PMTs, $\sigma_{PMT}(t)$, according to the formula: $\sigma_\pi(t) = \sigma_{PMT}(t)/\sqrt{N_{pe}}$, where N_{pe} is the number of photoelectrons produced by photons impinging on the photon detector. The time resolution requirement thus leads to the choice of fast single anode PMTs and to the usage of a copious number of them, which decreases the probability of pile-up and multi-photon detection. Moreover, the granularity of the photon detection is also important to optimize the angular resolution of the detector; this implies a solution with the PMTs

---

[3]The focal point is where the light incident the mirror and travelling parallel to the optical axis will impinge after the reflection.

[4]This is generally the case in gas radiators.

[5]The pion crossing time is defined by the photon arrival times at the photon detector plane.

arranged in a compact configuration. According to simulations, a total of 2000 PMTs is sufficient to match the detector requirements. The same photon detector technology will be used for the CEDAR detector, so more details on PMT operations, performances and features can be found in Chpt. 5. Assuming a RICH filled with Neon at 1 atm and with a mirror focal length of 17 m, the Cherenkov ring radius (left) and N_{pe} (right) are shown in Fig. 4.9 as a function of the momentum for a pion and a muon.
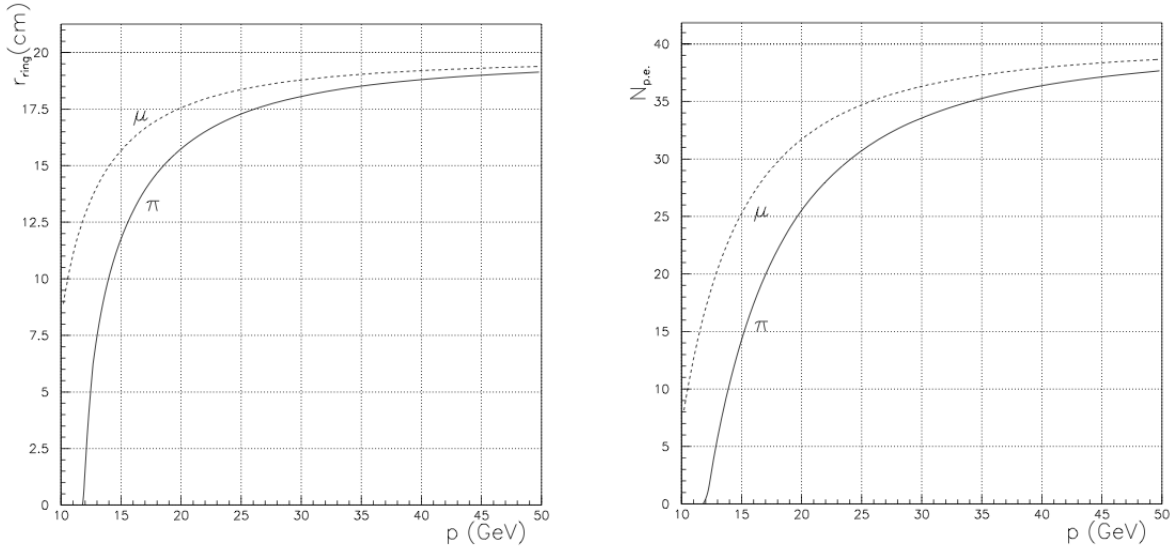
Figure 4.9: Ring radius (left) and N_{pe} (right) as a function of momentum, for a pion (solid line) and a muon (dashed line), for a RICH filled with Neon at 1 atm and with focal length of 17 m.

In 2009 a test beam was performed with a RICH prototype equipped with 414 Hamamatsu R7400U-03 PMTs. A time resolution of 65 ps was measured and the π/μ separation was scanned in the range (15,35) GeV/c. The μ suppression factor was estimated to be 10^{-2} integrated in the momentum range of interest [88].

In order to suppress $K^+ \rightarrow \mu^+\nu_\mu$ events, in addition to the kinematic rejection (STRAW) and the π^+/μ^+ separation (RICH), a further muon reduction of the order of 10^{-5} with respect to pions is required and achieved by means of a muon veto system. If the charged particle is a muon the energy deposit in the LKr calorimeter is small and the particle traverses a thick layer of iron without being absorbed. To ensure the required S/B ratio, special cases, in which muons undergo catastrophic bremsstrahlung or direct pair production and deposit a major fraction of their energy in the calorimeter, must be vetoed. To reject these events, electromagnetic muon showers must be distinguished from hadronic pion showers by measurements of the shower shape.
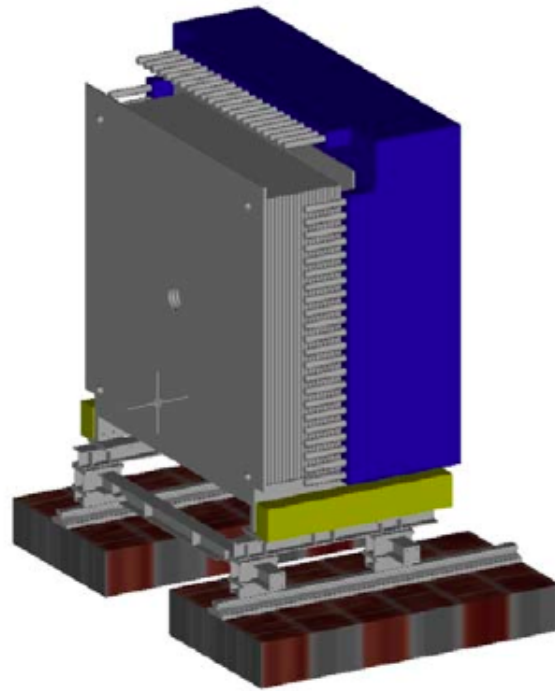
Figure 4.10: Schematic view of MUV1 (grey) and MUV2 (blue). The beam is coming from the left.

To partially suppress muon events already at the first trigger level, a fast muon veto detector is needed. This sub-detector should have a time resolution below 1 ns to reject events with coincident signals in the GTK and the CEDAR. The muon veto system (MUV), shown in Fig. 4.10 consists of three distinct parts, called MUV1, MUV2, and MUV3, according to their longitudinal position along the beam axis. The first two modules, MUV1 and MUV2, follow directly the LKR calorimeter and work as hadronic calorimeters for the measurement of deposited energies and shower shapes of incident particles. Both modules are iron-scintillator sandwich calorimeters with 24 (MUV1) and 22 (MUV2) layers of scintillator strips. In both modules, the scintillator strips are alternatively oriented in the horizontal and vertical directions. After MUV1 and MUV2 and an 80 cm thick iron wall, the MUV3 module, or Fast Muon Veto, detects non-showering muons and acts as muon veto detector at trigger level. To achieve the required time resolution at each transversal position, scintillator tiles are used and arranged in order to minimise differences in the light path trajectories.

4.1.5 Vetoes
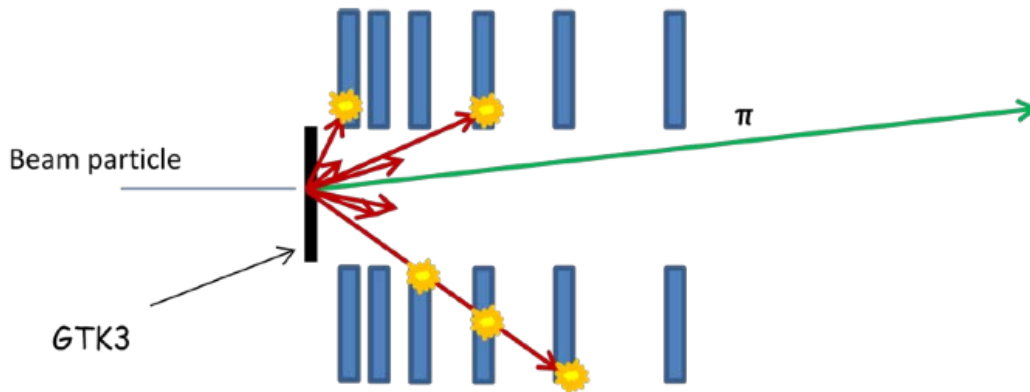
Figure 4.11: Sketch of beam particles undergoing inelastic interactions in the GTK material. The scattered particles are detected in the CHANTI detector placed immediately after GTK3.

Despite the fact that GTK stations are thin, beam particles can undergo inelastic interactions in the GTK material. The most critical events take place in GTK3: the scattered particles, pions or muons, if emitted within the straw acceptance, can mimic a kaon decay in the fiducial region. If no other track is detected these events lead to a $K^+ \rightarrow \pi^+ \nu \bar{\nu}$ signature. The probability of kaon inelastic scattering is $\sim$ 1%: thus, to achieve the required S/B ratio, the combined rejection factors from analysis cuts and veto efficiency must reach a level of 10^{-8}. To this purpose, the CHANTI detector, introduced in Sec. 4.1.1, has been proposed; it consists of six stations of scintillator bars surrounding the beam and placed inside a single vacuum tight vessel, together with the GTK3 station. The CHANTI is also used to veto beam halo (muons) in the region closest to the beam. The expected rate of particles, from inelastic interactions and beam halo, releasing enough energy to be detected, is $\sim 2\,\mathrm{MHz}$ [87]. The CHANTI is able to veto about 95% of kaon inelastic interactions in GTK3. This vetoing efficiency reaches almost 99% if one restricts to potentially signal-like events, namely the ones where the kaon either did not survive the inelastic interaction or did not decay in the fiducial volume and one track is reconstructed by the STRAW tracker at the same time.

The kaon decay channel $K^+ \rightarrow \pi^+ \pi^0$ represents the second main source of background to $K^+ \rightarrow \pi^+ \nu \bar{\nu}$ events: BR($K^+ \rightarrow \pi^+ \pi^0$) $\sim$ 21% and it can contaminate the signal region if the two photons from the $\pi^0 \rightarrow \gamma\gamma$ decay are not detected. The cut on the charged pion momentum between $15\,\mathrm{GeV}/c$ and $35\,\mathrm{GeV}/c$ provides a kinematic
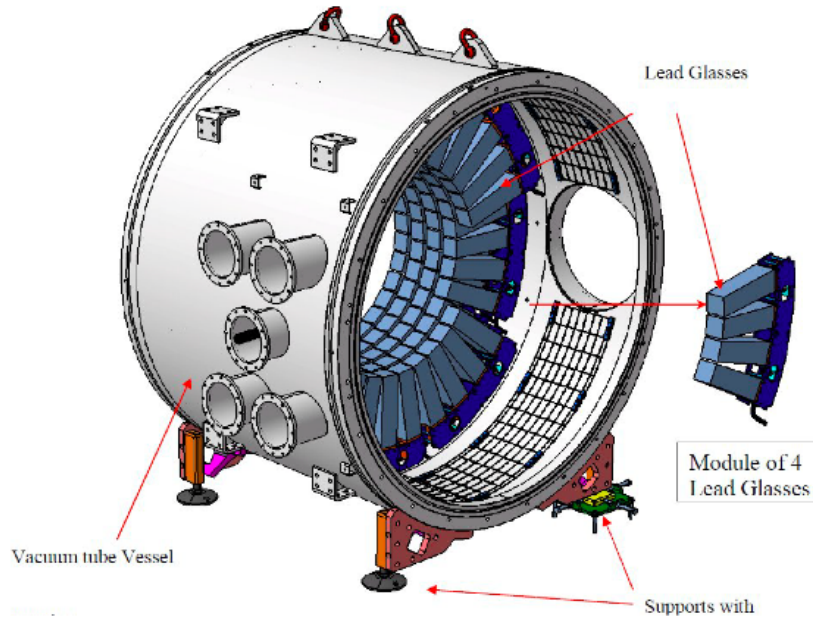
Figure 4.12: Layout of one LAV station.

rejection factor on $K^+ \to \pi^+\pi^0$ events of order of 10^{-4}. To ensure the signal over background ratio ($S/B \sim 10/1$) required by the NA62 measurement strategy and control the $K^+ \to \pi^+\pi^0$ backbround, it is essential to keep the average inefficiency on the rejection of the π^0 down to a level of 10^{-8}. To this end, an hermetic photon veto system has been proposed to detect photons produced in the fiducial decay region. The geometry of the experiment suggests a partition of the veto system into three different angular regions, each one instrumented with three different detector technologies:

- 12 Large Angle Veto (LAV) stations distributed along the decay volume and covering the angular region: (8.5÷50) mrad;

- a LKr calorimeter, inherited from the predecessor experiment and explained in Sec. 2.4, providing photon veto in the angular region: (1÷8.5) mrad;

- a Inner Radius Calorimeter (IRC) and a Small Angle Calorimeter (SAC) addressed to photons emitted at small angle (< 1 mrad) and designed to cover the zone around the inner radius of the LKr calorimeter.

The LKr, IRC, SAC and the last station of LAV are positioned outside the vacuum tank. Photons coming from the π^0 decays are distributed at different angles with different energy spectra. The photon energy distribution in the LAV covers the range between

112

10 MeV and 30 GeV. The minimum photon energy in the LKr calorimeter is 1 GeV, while in the IRC and SAC it is ~ 6 GeV. The major contribution (0.2%) to the global photon veto inefficiency is due to π^0 decays in which one photon is emitted at low energy and is either outside the acceptance of the LAV or inside it, but with high inefficiency, while the other photon is mainly impinging the LKR calorimeter, with an energy larger than 35 GeV, or the IRC with an energy larger than 60 GeV [87]. It is then mandatory to have an inefficiency of the LKR lower than 10^{-5}, at those energies, to reduce the contribution from these events to the average π^0 rejection inefficiency.

The LAV basic building blocks are lead glass crystals from the former OPAL electromagnetic calorimeter [89]. Four crystal detectors (lead glass crystals + PMTs) are mounted on a common support structure forming an azimuth segment. Inside the vacuum tube the segments are assembled to form a complete ring of lead glass blocks. Each LAV stations is made up of 4 or 5 rings, which are staggered in the azimuthal direction providing complete hermeticity.

The photon veto system is complemented by two additional detectors, IRC at intermediate radii and SAC at very small angles. These two small detectors will have a single-photon detection efficiency better than 10^{-5} for photon energies above several GeV. While this thesis is being written (September 2012) the construction technology for these two detectors is still under discussion, but it will be probably based on alternating layers of lead and scintillator, read out via wavelength shifter fibers. For a full general description of this type of calorimeter see [90].

4.1.6 Trigger and Data Acquisition System

The intense flux needed in rare decay experiments implies the design of high-performance triggering and data acquisition systems, which minimise the dead time while maximising data collection reliability.

The proposed solution is a combined trigger and data acquisition (TDAQ) system [91], assembling trigger information from readout-ready digitized data. A common clock, with a frequency of ~ 40 MHz, is optically distributed to all systems by means of a Timing, Trigger and Control (TTC) electronic module designed for LHC experiments [92]. The TTC clock will be the common time reference for all sub-detectors. The trigger hierarchy is made of three logical levels:

- a hardware L0 trigger, based on the input from a few sub-detectors;

- a software L1 trigger, based on information computed independently by each

113

sub-detector system;

- a software L2 trigger, based on assembled and partially reconstructed events;

The hardware L0 trigger uses the input from the HOD, the MUV, the LKr, the RICH, the LAV, and the STRAW. The primary trigger corresponds to events with a single track in the HOD, nothing in the MUV and no more than one cluster in the LKr. The inclusion of other sub-detector information is possible, both to refine the primary trigger and to implement secondary triggers for control samples, as well as for different physics goals.

The L1 trigger is based on simple correlations between independently-computed conditions by single sub-detectors. Some examples are: an equal number of tracks in the front and back of the STRAW spectrometer, no showers in the LAV, a hit multiplicity and pattern consistent with a charged pion in the RICH and a positive indication of at least one in-time kaon in the CEDAR.

The L2 trigger is based on more complex correlations between different sub-detectors and it provides the final trigger decision. All data associated with events satisfying the L2 trigger conditions will be logged to tape.

Chapter 5

The CEDAR Detector

This chapter will focus on a detector which is essential for both the $K^+ \rightarrow \pi^+ \nu \bar{\nu}$ event reconstruction and the background suppression. As explained in Sec. 4.1.1, in the secondary beam that will be used in NA62, kaons are not separated from the other particles produced at the proton interactions in the target. The main beam components consist of 70% of pions, 20% of protons and 6% of kaons with a central momentum of 75 GeV/c and r.m.s spread of 1%; the total beam rate amounts to 750 MHz [86]. A beam particle (mainly a pion) interacting with the residual gas in the vacuum tank[1] may lead to a $K^+ \rightarrow \pi^+ \nu \bar{\nu}$ signature, if no other visible particles are produced in the same event. This source of background, with probability $\sim 10^{-4}$, can be kept below one fake event per year by evacuating the tank at a pressure less than 6×10^{-8} mbar. The vacuum requirement can be relaxed by at least an order of magnitude, if the kaons are tagged in the beam. Hence, a crucial aspect of the NA62 experiment is to perform a positive identification of the minority particles of interest in the beam, namely the kaons, in this high rate environment before their decay. The task will be achieved by means of a gas-filled differential Cherenkov counter (CEDAR)[2] placed in the beam line (see Fig. 4.5).

CEDAR counters [93] have been constructed and used at CERN since the early '80s for SPS secondary beam diagnostics. There are two versions of the CEDAR detector, "North" and "West", designed to be used with different gases and suitable to operate in different energy regimes. In 2006 a test run at CERN demonstrated the CEDAR capability to distinguish the main beam components (pions, kaons and protons). The test was performed with a "West" version of the detector, which was then confirmed for usage in NA62. The CEDAR "West" is designed to be filled with nitrogen gas

---

[1]The vacuum tank housing the fiducial decay volume.
[2]The acronym CEDAR stands for ChErenkov Differential counter with Achromatic Ring focus.

and is optimised for low beam momenta: it is able to separate kaons and pions up to $150 \, \text{GeV}/c$ and detect protons down to $12 \, \text{GeV}/c$. Preliminary simulations have shown that the same counter, filled with hydrogen instead of nitrogen, at an absolute pressure of $3.6 \, \text{bar}$, can function well for NA62 purposes. The choice of the gas is imposed by the necessity to keep a minimal amount of material on the beam line: an H_2-filled volume corresponds to $\sim 0.2\% X_0$, while a N_2-filled one to $\sim 3\% X_0$. This requirement reduces the scattering of beam particles in the radiator, which is necessary to control the beam divergence in the sub-detectors placed further down the beamline.

5.1 The CEDAR requirements in NA62

In NA62 the kaon tagging and time information, in conjunction with the timing from other components, is necessary to reconstruct the $K^+ \rightarrow \pi^+ \nu \bar{\nu}$ decay and to guarantee the rejection of background induced by accidental overlap of events in the detector. For that purpose, the GTK spectrometer (see Sec. 4.1.3) and the Cherenkov counters (the RICH in Sec. 4.1.4 and the CEDAR) will play an essential role in NA62 by providing fast PID information.

The NA62 experimental strategy requires the following conditions to be satisfied by the CEDAR detector:

- a kaon tagging efficiency, defined in Sec. 5.6, of at least 95%;

- a kaon crossing time measurement, defined in Sec. 5.2, with a resolution better than $100 \, \text{ps}$;

- a pion and proton rejection with minimal accidental mis-tagging ($\sim 10^{-4}$);

- a capability to stand a high radiation level;

- stable and reliable operations over time.

5.2 Principle of operation

The CEDAR principle of operation for the particle identification is almost the same as the one described for the NA62 RICH detector (see Sec. 4.1.4); it exploits the formation of light cones due to the Cherenkov effect. As already mentioned, for a given beam momentum, the Cherenkov light produced by a charged particle traversing the

gas (at a given pressure) is emitted with an angle θ_c (Cherenkov angle) that only depends on the mass of the particle and the wavelength of the Cherenkov light. Differential Cherenkov counters have an internal optical system focusing the light on the photon detector plane and giving a ring image so that particles of different velocities can be distinguished by the diameter of the light rings.

For an annular aperture of fixed[3] radius, R_c, (thus θ_c is fixed) particles of different masses are selected by varying the gas pressure, and hence the refractive index, in order to fulfil the equation 4.1. The radius R_c is defined by a mechanical diaphragm with variable annular aperture of width, w_D, varying in the range between 0 and 20 mm. For an operating angle $\theta_c = 30.9$ mrad and a radius $R_c = 100$ mm the effective focal length f of the optical system, according to the formula $R_c = f\theta_c$, is $f = 3.3$ m.

An important quantity to consider is the difference between the ring radius of two particles of masses m_1 and m_2 in a beam of momentum p, which can be expressed as:

$$\Delta R_c = f\Delta\theta_c = \frac{f}{\theta_c}\frac{m_2^2 - m_1^2}{2p^2},$$

Two rings, and the corresponding particles, can be distinguished if their radii differ by $\Delta R > w_D$. Thus, closing the diaphragm aperture gives the rejection of unwanted particles. As an example, using kaons and pions ($m_\pi = 0.1395$ GeV^2, $m_K = 0.4937$ GeV^2) of momentum 75 GeV/c and the same values as above for the operating angle θ_c and the focal length f, one obtains $\Delta R_{K,\pi}$ of about 2 mm. The diaphragm aperture width, w_D, should be set at less than this value to ensure that no light from pions is detected, when the pressure is set to detect kaons. However, the light ring of a single kind of particle is broadened by various mechanisms, so that closing the light diaphragm too much reduces the efficiency of detecting the desired particle.

The most severe of such effects is the chromatic dispersion, which occurs because the index of refraction of the gas n varies with the wavelength λ of the light. For a given gas, the chromatic dispersion only depends on the γ of the particle, so a fixed chromatic corrector can be used to compensate for the chromaticity in a particular regime, i.e. separating kaons and pions at high momentum. In the original version of the CEDAR "West", filled with nitrogen at 1.7 bar, the contribution from chromatic dispersion to the radius is $\Delta_R = 2$ mm (comparable with the distance $R_{K,\pi}$). A chromatic corrector lens in the CEDAR optical system corrects for this effect and the correction factor achieved is ~ 10. Simulations have shown that, with the CEDAR filled with hydrogen gas at 3.8 bar and the chromatic corrector in place, the light ring width is

---

[3]The radius is fixed up to the width of the aperture.

about 3 mm on the kaon peak and is dominated by chromatic dispersion, as the optical system is not optimise for this radiator.

The second effect comes from the beam divergence; the light rings are concentric only when particles in the beam travel parallel to each other. If that is not the case then the projected angle of a particle trajectory results in a displacement of the centre of the light ring. Considering the projected angle averaged over the beam particles ($\Delta\theta_x = \Delta\theta_y = 70\,\mu$rad [87]) the contribution to the radius is given by $\Delta_R = \sqrt{\Delta_x^2 + \Delta_y^2}$ =0.3 mm (r.m.s.), where $\Delta_{x,y} = f\Delta\theta_{x,y}$.

Additional minor effects broadening the width of the light ring are due to: the multiple scattering incurred by the beam during its traversal of the gas radiator and the momentum spread of the beam ($\Delta p/p \sim 1\%$). The former contribution to the light radius R is evaluated using the typical deviation of a particle trajectory due to multiple scattering through small angles [80], which depends on the beam momentum. At 75 GeV/c and with an amount of material of $\sim 0.3\% X_0$, one obtains a contribution of $\Delta_R = 0.05$ mm (r.m.s.). The latter contribution can be computed using the Lorentz relation for a relativistic particle velocity, $\beta = \frac{1}{\sqrt{1+(m/p)^2}}$, in Eq. 4.1; one obtains $\Delta_R = 0.05$ mm (r.m.s.).

The number of photons N emitted through a radiator thickness x depends on the wavelength λ (or energy E), the index of refraction n, the Cherenkov angle θ_c and is given by the Frank-Tamm equation (assuming a single charge particle):

$$\frac{d^2N}{dEdx} = \frac{2\pi\alpha}{hc}sin^2\theta_c \simeq 370\ sin^2\theta_c\ eV^{-1}cm^{-1}\ , \tag{5.1}$$

where α is the fine-structure constant and h the Planck constant. This equation can also be written in terms of the wavelength λ as:

$$\frac{d^2N}{d\lambda dx} = \frac{2\pi\alpha}{\lambda^2}sin^2\theta_c\ . \tag{5.2}$$

A common principle of operation in both NA62 Cherenkov counters (RICH and CEDAR) is that the photons emitted by the particle traversing the radiator are reflected into a mirror placed at one end of the vessel and travel all the way back, in the opposite direction along the vessel, before impinging on the photon detector plane. By construction, photons produced at the beginning of the vessel (earlier) travel for a longer distance with respect to photons produced at the end of it (later) and they all arrive at the same time on the photon detector plane. As a result, the arrival time of photons produced by a particle traversing the radiator does not depend on the photon production point along the vessel and it is used to define the particle crossing time.

Assuming a photon detector technology with single photon counting capability, the corresponding time resolution on the kaon crossing time can be calculated using the equation:

$$\sigma_{T,K} = \frac{\sigma_{T,\gamma}}{\sqrt{N_\gamma}} , \qquad (5.3)$$

where $\sigma_{T,\gamma}$ is the time resolution on single photon detection, determined by the chosen technology, and N_γ is the number of photons detected per kaon.

5.3 Detector overview
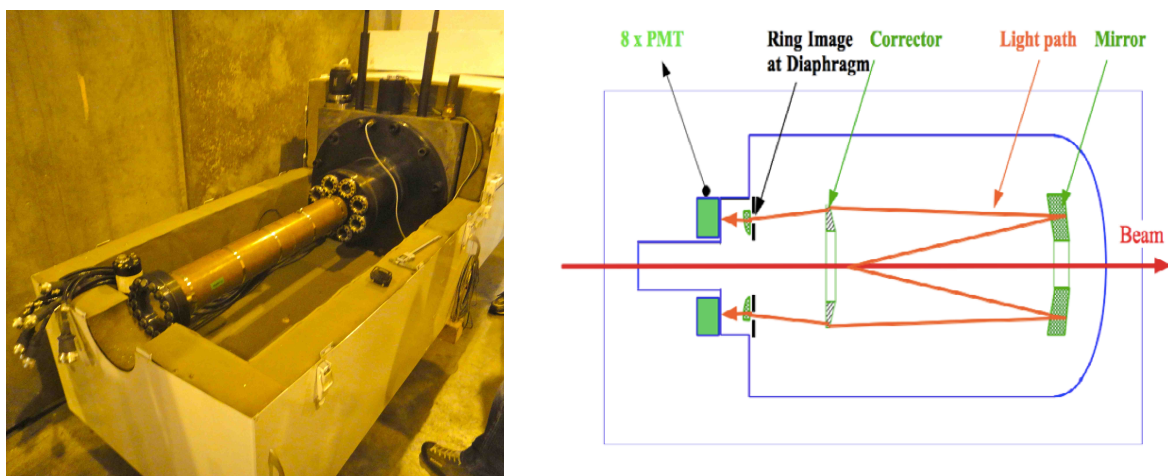
Figure 5.1: CEDAR counter: (left) upstream end view of the vessel with the nose and the quartz windows; (right) schematic layout of a standard West version.

The CEDAR counter is a steel vessel filled with gas of controlled pressure. It has a diameter of about 60 cm and it is closed by a $\sim$ 1 m-long nose with eight quartz windows at the upstream end (see left picture in Fig. 5.1); it terminates with a spherical head at the downstream end. The length of the vessel is 4.5 m, while the overall length of the detector sums up to $\sim$ 6 m when including the nose. As illustrated in the right panel of Fig. 5.1, the Cherenkov light produced in the gas is reflected by a mirror, then passes through a corrector lens and finally through a diaphragm, and via additional lenses onto eight spots where the photon detectors (PMTs) are located. The optical components (Mangin mirror, chromatic corrector, condensor lenses and quartz windows) are shown in Fig. 5.2; a sketch of the optical path of two Cherenkov photons is provided. The mirror and the condensors are mounted onto the same optical axis, which is attached to the diaphragm and fixed without constraint to the vessel. Hence,
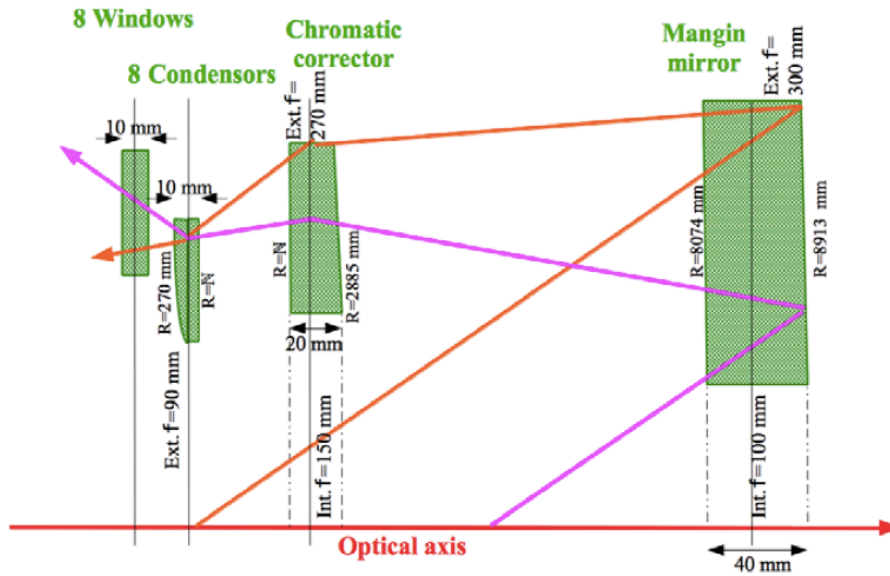
Figure 5.2: Schematic layout of the optical elements inside the CEDAR vessel and a sketch of the light path.

possible pressure and temperature variations do not affect the optical axis. The chromatic corrector is mounted off-axis and it is designed to match the dispersion curve of the gas[4] to compensate the effect of the chromatic dispersion. The corrector lens ensures that the Cherenkov light, emitted at all wavelengths, arrives at the same radius on the diaphragm plane. As a consequence, the light from unwanted particles hits the diaphragm at different radii from that of wanted particles; it does not pass through the annular aperture at the diaphragm plane and does not contribute to the rate on PMTs. That is why the detector is well suited to tag minority particles in a high-intensity beam. For a correct CEDAR operation all light rings produced at the diaphragm plane must be concentric; as mentioned in Sec. 5.2 this happens when all beam particles travel parallel to each other. To this end the optical axis of the counter must be precisely aligned with the beam axis.

In a CEDAR "West" counter, designed for use with nitrogen gas, the chromatic corrector does not work under optimal conditions with any other radiator. Fig 5.3 shows the distributions of the Cherenkov ring radius at the diaphragm plane as expected for kaons and pions; the spectra are obtained by operating the CEDAR "West" counter with nitrogen, N_2, gas at an absolute pressure of 1.7 bar and hydrogen, H_2, gas at an

---

[4]The dispersion curve of the gas describes the dependence of the index of refraction n on the wavelength λ of the light.
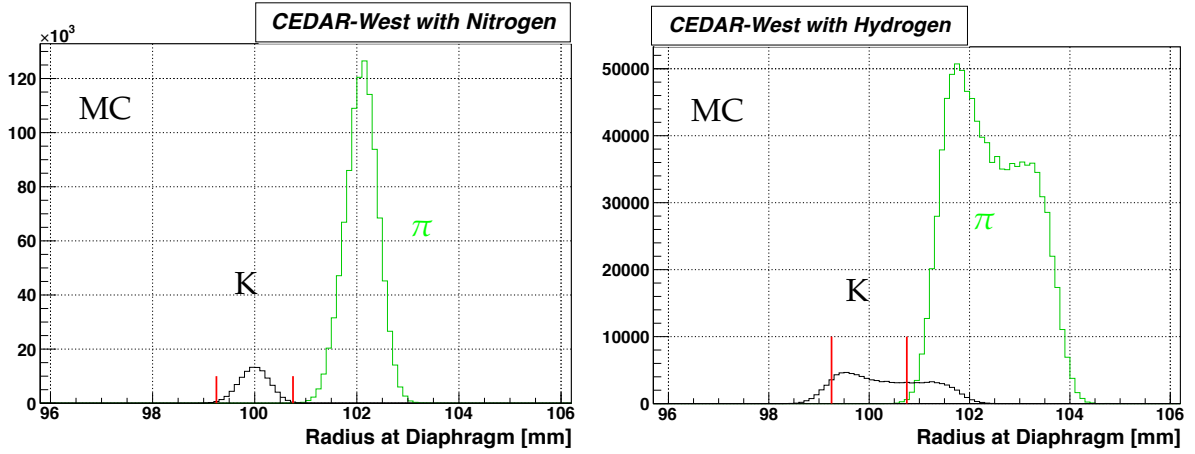
Figure 5.3: Cherenkov photon ring radius at the diaphragm plane expected for kaons (black) and pions (green). Left: CEDAR operating with N_2 gas at an absolute pressure of 1.7 bar. Right: CEDAR operating with H_2 gas at an absolute pressure of 3.3 bar. The standard annular aperture ($w_D = 1.5$ mm) is represented by red lines.

absolute pressure of 3.3 bar. The effect of the chromatic corrector is visible with N_2 (left panel): in agreement with what stated in Sec. 5.2, the width of the kaon and pion ring radius distributions is ~ 0.2 mm (r.m.s.), corresponding to a factor $1/10$ of the distance between the kaon and pion peaks ($R_{K,\pi} \sim 2$ mm). On the contrary, the chromatic dispersion effects are not compensated with H_2 (right panel) and the width of the kaon and pion ring radius distributions is broadened with respect to the one obtained with N_2. The shoulder appearing with H_2 in the distribution of the kaon ring radius (above 101 mm) is mainly populated by low wavelength Cherenkov photons ($\lambda < 260$ nm) and contaminates the radius region expected from Cherenkov photons produced by pions. The $K - \pi$ separation is achieved by setting the diaphragm aperture width at $w_D = 1.5$ mm, as indicated by the red lines in Fig. 5.3. The resulting light loss ($\sim 30\%$) does not compromise the correct (even if not under optimal optical conditions) operation of the CEDAR. Besides, as it will be seen in the next section, within NA62 the counter will work in a high rate environment and the amount of Cherenkov light, passing through the diaphragm and reaching the PMTs, induces several limitations and modifications to be applied. As a consequence, a $\sim 30\%$ light loss can be simply ignored.

5.3.1   Upgrade for NA62

To meet the requirements listed in Sec. 5.1 some modifications to the original CEDAR detector design are needed. The proposed version of the counter relies on new photon detector, readout, mechanics, cooling and safety systems. Some upgrades are finalised (photon detector and readout), while some are still under optimisation at the time of the present thesis. In this chapter the new photon detector and readout electronics is discussed being the result of part of the work carried out during my PhD. The NA62 Technical Design document [87] describes all the modifications that will be applied to the CEDAR counter in order to be adapted for usage with hydrogen gas, instead of nitrogen, on the NA62 beam line. The main parameters of the hydrogen-filled CEDAR "West" counter, proposed for application in NA62, are listed in Tab. 5.1.

Parameter	Value
Gas type	H_2
$n-1$	$\sim 142 \times 10^{-6}$
Nominal pressure (for kaons)	3.86 bar
θ_c	30.9 mrad
Kaon rate (average)	50 MHz
Time resolution	100 ps
$\Delta\theta_c/\theta_c$	4.8×10^{-3}
$\Delta\beta/\beta$	5×10^{-6}

Table 5.1: Requirements and resolutions of the CEDAR detector.

Only Cherenkov photons originating from kaons are selected at the diaphragm plane, excluding light induced by pions and protons; the expected average kaon rate is 50 MHz. The Cherenkov light distribution at the eight quartz windows is presented in Fig. 5.4; the light spots cover eight 30×10 mm^2 rectangular areas. In the original version of the CEDAR "West" counter each light spot is readout by one PMT. Assuming a light yield of about 200 photons per kaon at the exit windows of the CEDAR and distributed among the eight spots,the expected mean rate of single photons is about 4 MHz/mm^2, without considering accidental and thermal noise (dark counts). The original CEDAR PMTs are inadequate to cope with such a high and localised photon rate; new photon detectors and associated readout are needed to operate at the required rate. Moreover, integrating the expected rate of single photons over a PMT's
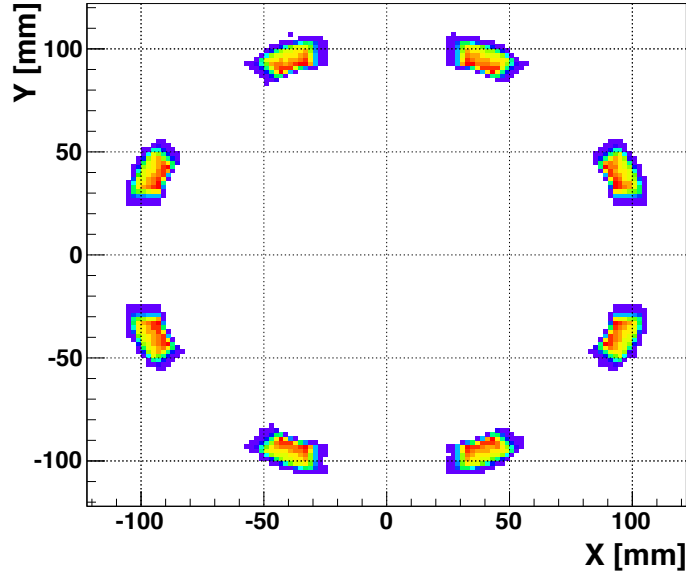
Figure 5.4: Cherenkov light distribution at the eight CEDAR quartz windows.

active area of $\sim 50\,\mathrm{mm}^2$, one obtains a single photon rate per PMT device $> 200\,\mathrm{MHz}$. In this regime, the anode current would be only an order of magnitude below the maximum sustainable value and this is considered not a safe operational mode. Typical modern PMTs are rated at a maximum anode current in the region of 100 μA and a gain in the region of 10^6.

Figures 5.5 show the new solution proposed for the CEDAR photon detector to reduce the rate on a single PMT device (of $\sim 50\,\mathrm{mm}^2$ active area) to a more acceptable value of $\sim 5\,\mathrm{MHz}$. The 90 degrees reflection in external mirrors is necessary to spread the Cherenkov light over large collection areas and keep the longitudinal dimension of the counter within certain limitations [87]. Referring to the drawing in Fig. 5.5 (left-panel), the Cherenkov light, selected at the CEDAR diaphragm and passing through the quartz windows (blue), is projected on the plane of the new PMTs (green) and distributed, by means of additional external mirrors (red), over larger collection areas. The new photon detector design consists of a compact array of new and small PMTs at each spot; this configuration allows to reduce the photon rate and average anode current per PMT. A careful design of external optics and light collection cones is required to keep the light collection efficiency at the same level as that of the original PMTs and to reduce the effect of dead areas. The assembly of the new photon detector at the CEDAR nose is shown in the mechanical design in Fig. 5.5 (right-panel). At the time of the present thesis the choice of the best configuration for the light transport and

collection systems are under optimization with a Geant4-based study including most of the modifications concerning the CEDAR detector. The photon detector technology was tested at CERN: the dark count, the response in charge and the time resolution for CEDAR PMTs are discussed in Sec. 5.5. The number of PMTs has been decided with a Monte-Carlo simulation of the CEDAR photon detector, explained in Sec. 5.6. Cross checks and validations will follow from the Geant4 simulation of the whole apparatus. New electronics is needed to cope with a $\sim$ few MHz rate on single device (i.e. per readout channel). The proposed readout system design, introduced in Sec. 5.4.2, was tested in a test beam described in the next chapter.

5.4 The CEDAR PMT

The photodetector choice must accommodate all CEDAR working requirements. Photomultiplier Tubes, or PMTs, are electron tube devices which convert light (photons) into a measurable electric current (electrons)[5]. PMTs have a high resistance to the damage by radiation and a low ($\sim$ few Hz) dark-count rate. In addition, PMTs with quartz input windows are sensitive to UV and near-UV wavelengths. The re-

---

[5]The reader can refer to [94] for details on the main characteristics of a PMT and its operation mode.
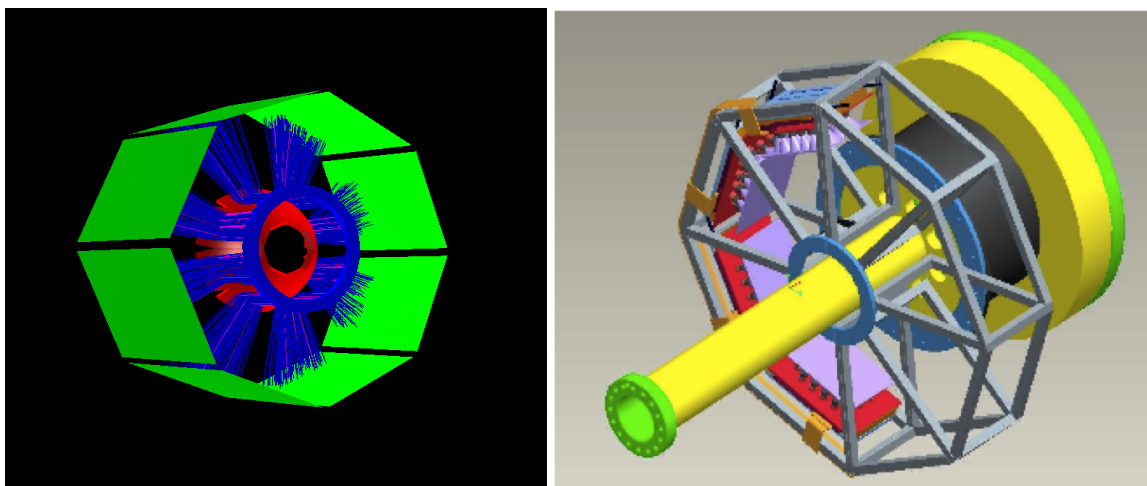
Figure 5.5: Simulation of Cherenkov photons (left-panel) with the ray tracing from the CEDAR quartz windows (blue), to the external mirrors (red) and to the new PMT planes (green). Mechanical design of the new CEDAR photon detector (right-panel) with the main structure positioned after the quartz windows, surrounding the nose and housing external mirrors, light collection cones and PMTs.

quired combination of pico-second time resolution, high rate and reliable operation over many years implies a careful evaluation of the behaviour and features of PMTs and the development of an optimization procedure to establish the minimum number of PMTs necessary to achieve the desired kaon efficiency, while minimising the dead time and accidental noise.

5.4.1 Technology overview

The technology under discussion is based on PMTs already used for the NA62 RICH detector [95]. It consists of metal package photomultipliers of the HAMA-MATSU [96] R7400 series, U-03 (quartz window) type, which were chosen for their compactness, speed and relative cheapness. The R7400 PMT has a polyoxymethylene insulation cover of roughly cylindrical shape, 15.9 ± 0.4 mm wide and 11.5 ± 0.4 mm long. The eight PMT dynodes are properly supplied through a HAMAMATSU high voltage divider ($2.8 M\Omega$ total resistance), which has a cylindrical shape 17.0 ± 0.2 mm wide and 15.0 ± 0.5 mm long and three cables: one cable for the signal output and two cables for the high (negative) voltage supply and grounding. The photocathode (with 8 mm minimum active diameter) is bialkali type and has a typical photocathode sensitivity of $S_k = 62$ mA/W, at $\lambda = 420$ nm, corresponding to a Quantum Efficiency value of $QE \sim 20\%$. The former quantity, S_k, is defined as the ratio between the photocathode current $I_k(Ampere)$ and the incident electron flux $\Phi_e(Watt)$; it is quoted for a specific wavelength when the photocathode is not uniformly sensitive to the spectral composition of the incident light. The latter quantity, QE, is defined as the ratio between the number of electrons[6] emitted at the photocathode and the number of incident photons; it is a characteristic of the photocathode material and is related to S_k. The typical PMT gain is $G \simeq 1 \cdot 10^6$ at a high-voltage value of $V_{HV} = 900$ V (maximum safe V_{HV} is 1000 V). The R7400 typical rise time is 0.78 ns and the transit time is 5.4 ns (definitions for the mentioned properties can be found in [94]).

5.4.2 PMT Readout

The PMT output (anode) signal is shown in Fig. 5.9 (top waveform); it has a roughly triangular shape with the same rise time as the PMT (0.78 ns average) and a fall time about twice this. At $V_{HV} = 900$V, corresponding to an average gain of $1.0 \cdot 10^6$, the output charge is about 240 fC and is represented by a negative peak volt-

---

[6]One can refer to such electrons as photoelectrons.

age of 10 mV over a 50 Ω resistance. In order to benefit from the fast PMT response, the 8-channel NINO ASIC [97] is used as discriminator; this chip, originally developed for the output signal of multigap resistive plate chambers, has a differential input and an intrinsic time resolution of 50 ps. Two readout options are under consideration for the PMT-NINO coupling:

- the PMT output signal is sent to a current amplifier with differential output before reaching the NINO;

- the PMT is directly connected to the NINO.

In the former solution the amplification stage is based on a 24-channel (customised) printed circuit, originally designed for the NA62 RICH prototype photon detector readout system, but radiation hardened; the number of channels is optimised to couple with a board containing three NINO ASIC chips. The latter solution is feasible only if the standard Hamamatsu high voltage divider is replaced with a customised printed circuit board with differential anode output. The NINO chip will operate in *Time-Over-Threshold* (TOT) mode and its *Low Voltage Differential Signal* (LVDS) output will be sent to a 128-channel *Time to Digital Converter* (TDC) module, working in a trigger matching mode. The TDC module contains four *High Performance Time to Digital Converter* (HPTDC) chips for precise time tagging of electronics signals. Both the leading and trailing edges of the LVDS output will be recorded providing information on the width of the PMT output signal.

5.5 Validation of the CEDAR PMT

In preparation for the test beam a preliminary test programme was set up at CERN in order to investigate PMT time performances and readout coupling. In the experimental setup, shown in pictures 5.6 and 5.7, a laser produced light pulses in the wavelength region of ~ 105 nm, with a Full Width at Half Maximum of ~ 50 ps and a repetition rate of 5 MHz (chosen in the available range from the single shot to 80 MHz). The light was then attenuated with an optical filter of $(80 \div 20)\%$ transparency and collected with a PMT HAMAMATSU R7400/U-03 series. A (*Keithley SourceMeter*) was used as a HV power supply for the PMT and a (*LeCroy LC574AL*) digital oscilloscope (with $1 GHz$, four channels, capable of a maximum effective sampling rate of $1\,GS/s$ and MATACQ performances) was employed as Analogic to Digital Converter (ADC)

to acquire and analyse the analogical anode signal. The test was organized in several steps, each of them focusing on a CEDAR specific key point.

Figure 5.6: Left side: Dark box, Laser control system and HV power supply. Right side: ADC sampling oscilloscope.
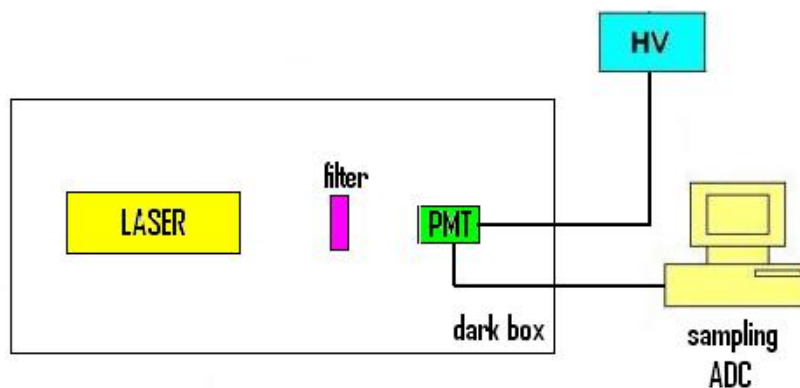
Figure 5.7: Experimental setup at CERN.

5.5.1 Dark current

Even in total darkness, a relatively small electric current can be detected at the anode of a PMT: this is called *dark current*. The major source is the thermionic emission from the photocathode and the dynodes. The dark current depends on the composition of the photocathode and dynodes and obviously varies with the gain, giving a considerable contribution in the high gain working region. Even though the dark current is specified by the manufacturer in the datasheet [96], it can change over the time depending on the use, the supply voltage applied and the exposure of the pho-

tocathode to the light. Therefore it is mandatory to check the dark current each time a PMT is turned on.
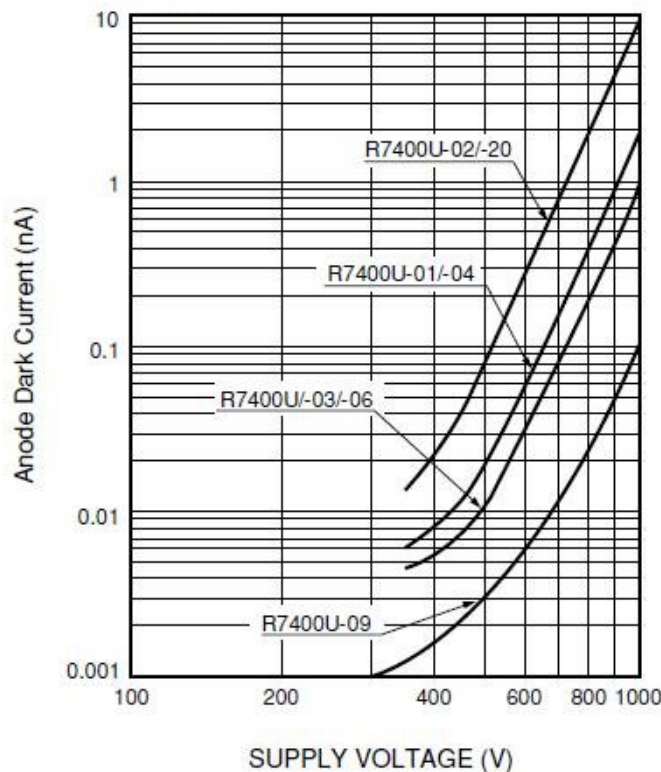
Figure 5.8: HAMAMATSU specification: *Anode Dark Current* versus the supply voltage applied, each trend corresponding to a different PMT of the R7400/U series [96].

The dark current is measured using the PMT output signal when there is no light impinging on it. To this end, a light tight housing was needed. The *dark box* (Fig. 5.6) used during the test had a removable side plate allowing for the assembling of the equipment. Once the PMT was in the dark box the anode current was measured using the following formula 5.4:

$$I_D = \frac{V_{mean} \pm \frac{V_{RMS}}{2}}{R_{trans}} \, , \tag{5.4}$$

where $R_{trans} = 50 \ \Omega$; V_{mean} is the average DC voltage over one sample set and it corresponds to the dark current of the tube; V_{RMS} is the average fluctuation of the signal and is related to the error associated to the mean voltage.

The dark current was evaluated at different values of the supply voltage applied to the PMT and results were found to be compatible with the specified values in the datasheet. Figure 5.8 shows how the anode dark current is expected to vary with

128

the supply voltage according to the manufacturer specifications. The measured dark current at the PMT working region ($HV = 900$ V) was $I_D = 0.20 \pm 0.02$ nA; looking at Fig. 5.8 the value is within the corresponding manufacturer specification.

5.5.2 Single photoelectron Response (SER) and Spectrum (SES)

The CEDAR photodetector must be able to perform single photon counting, that is detecting individual photo-electrons. According to the manufacturer, HAMAMATSU, the PMTs used in this thesis are especially optimised for single photon counting applications in which single photo-electron pulses are well separated in time. To allow the single photo-electron detection, optical filters were used to attenuate the light source. Using the same experimental setup, as in Fig. 5.7, the next step was to turn on the laser, with low intensity.

5.5.2.1 SES measurement process

The *SES* is defined as the amplitude distribution of single photo-electron pulses. The secondary electron emission process, happening at the dynodes, has a stochastic nature affecting the *SES* and inferring very large amplitude fluctuations. With a minimum level of illumination, such that the probability of more than one photo-electron being emitted at the photocathode is very small one obtains SER anode signals and can achieve a SES measurement by calculated the anode charge, integrated over a fixed time window. The procedure was to measure the area, A, in pV $\times$ sec, of the region defined by the PMT anode signal (top waveform in Fig. 5.9) and divide it by the product of the impedance $R_{trans} = 50\Omega$ and the acquisition time window $\Delta T = 10ns$ according to the equation (5.5):

$$Q = \int I dt = \int \frac{A}{R_{trans}.\Delta T} dt. \tag{5.5}$$

The anode charge distribution (spectrum) was then displayed and acquired, as shown by the oscilloscope snapshot (bottom distribution) in Fig. 5.9.

To check if the experimental setup was really producing a SES measurement for the PMT under study, the spectrum was analysed according to the following procedure. The photon emission is a random process: both fluctuations in the number of photons striking the cathode and the number of emitted photo-electrons can be described with a poisson distribution if the PMT input system collection efficiency is uniformly distributed over the whole cathode surface, which is the case for the PMTs used in this
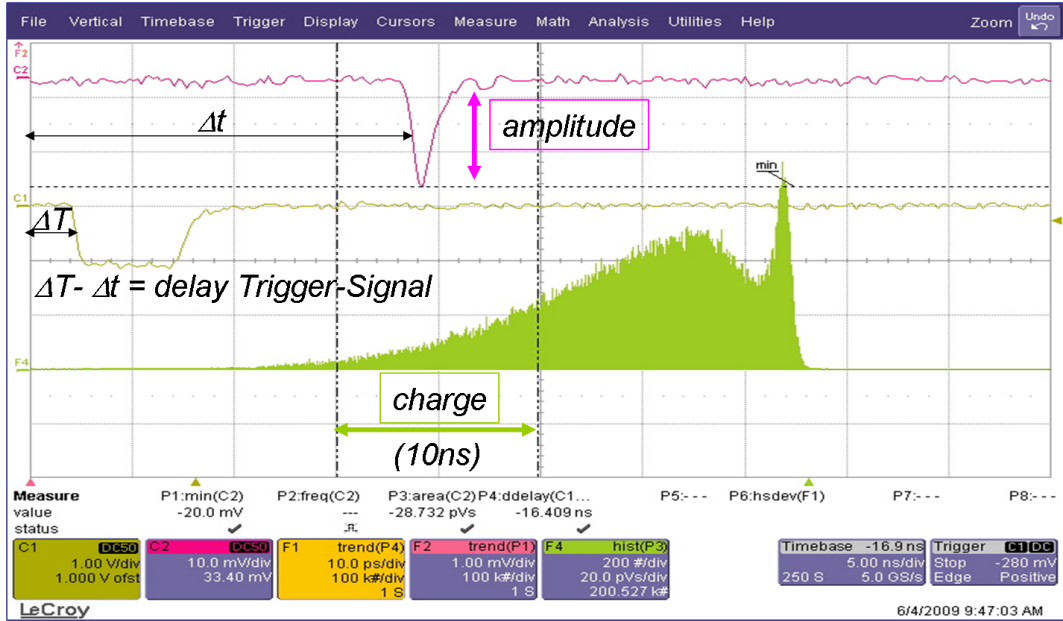
Figure 5.9: Digital sampling oscilloscope snapshot (time scale $5ns/div$): PMT anode signal (top waveform, voltage scale $10mV/div$), laser signal (central waveform, voltage scale $1V/div$), anode charge spectrum (bottom distribution) and fixed time window for charge integration ($10ns$).

thesis. It is then possible to work out an analytical condition for the SES spectrum to be fulfilled. Indicating with:

$$P(N) = \frac{\mu^N e^{-\mu}}{N!}$$

the probability to have N emitted photo-electrons, where μ is the mean parameter of the distribution, it is a fair approximation to ask for a SES spectrum which satisfy the condition $\frac{P(2)}{P(1)} < 5\%$. This condition implies $\frac{\mu}{2} < 5\%$, where the μ parameter can be easily worked out when considering the equation $P(0) = e^{-\mu}$. The probability $P(0)$ to have zero photo-electrons events is directly evaluated from the spectrum as the ratio between the number $N(0)$ of zero photo-electrons events (pedestal entries) and the total number N_{TOT} of events (total entries). Using this expression for the parameter: $\mu = -ln\frac{N(0)}{N_{TOT}}$, one has $-ln\frac{N(0)}{N_{TOT}} < 10\%$ which results in the analytical SES condition:

$$N(0) \sim 90\% N_{TOT}. \tag{5.6}$$

5.5.2.2 Data collection and results

The PMT was set to a gain value of 10^6 and data were collected using several optical filters of different transparency: $80\%, 50\%, 20\%$. The PMT anode charge spectrum

for different values of the light attenuation is shown in Figs. 5.10 (a), (b) and (c). It is clear that the ratio $\frac{N(0)}{N_{TOT}}$ is getting bigger as more light is filtered. Looking at Fig. 5.10 (c) the analytical SES condition, eq. (5.6), is met when the laser is strongly attenuated with a 20% filter. This spectrum (SES), shown again in Fig. 5.10 (d), is zoomed in the SER region by eliminating pedestal entries; the integral of SER events (noticable in the plot legend) is found to be $\sim 10\%$ of the total entries.

(a) Filter 80%$->$ $\frac{N(0)}{N_{TOT}} \sim 50\%$

(b) Filter 50%$->$ $\frac{N(0)}{N_{TOT}} \sim 80\%$

(c) Filter 20%$->$ $\frac{N(0)}{N_{TOT}} > 90\%$

(d) Single photoElectron Spectrum
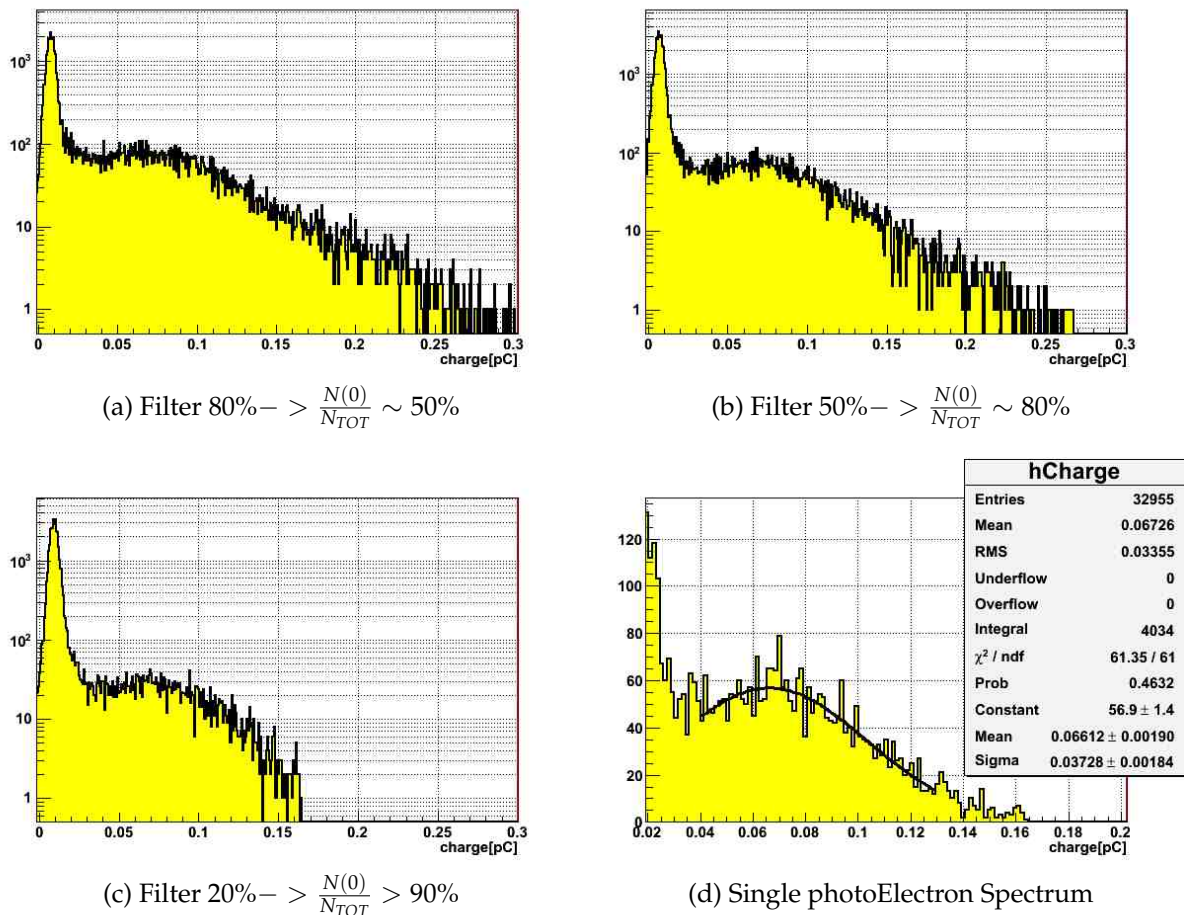
Figure 5.10: PMT anode charge spectra measured at a gain of 10^6 ($V_{HV} = 900$ V) for different values of the light attenuation.

The SER event peak, in Fig. 5.10 (d), is well separated from pedestal events. Considering the PMT anode signal as a gaussian and relying on the fact that the PMTs used are low noise devices, a gaussian fit to the SER peak was performed. The fit parameters (mean and sigma) are shown in the plot legend in Fig. 5.10 (d), which gives $Q(\text{SER}) = (0.07 \pm 0.04)$ pC. This is compatible within ~ 2 sigma with the expectation value for the PMT anode charge response Q to the emission of a single photo-electron

of charge $q_e = 1.6 \cdot 10^{-19}$ C at a gain value of $G = 1.0 \cdot 10^6$ [94]:

$$Q = q_e \times G \sim 0.16 \text{ pC} .$$

5.5.3 Time resolution

The CEDAR photodetector must achieve a time resolution of ~ 100 ps. The kaon time resolution ($\sigma_{T,K}$) is proportional to the single photo-electron time resolution ($\sigma_{T,\gamma}$), according to the relation [98]:

$$\sigma_{T,K} = \frac{\sigma_{T,\gamma}}{\sqrt{N_\gamma}} , \tag{5.7}$$

where N_γ is the number of photo-electrons detected per kaon. In the next chapter, with the help of a MonteCarlo simulation to describe the CEDAR photodetector layout, the kaon tagging requirement will be fixed at a minimum value of $N_{\gamma min} = 9$. Therefore, to get the aimed $\sigma_{T,K}$ from the equation (5.7), the $\sigma_{T,\gamma}$ should not exceed 300 ps at the chosen working supply voltage.

5.5.3.1 Time Resolution measurement process

The $\sigma_{T,\gamma}$ corresponds to the PMT time resolution[7] and is defined as the Full Width at Half Maximum (FWHM) of the transit-time distribution for identical light pulses striking the same part of the photocathode[8]. Under the assumption of a transit-time distribution approximately gaussian, with standard deviation σ_R, the PMT time resolution can be evaluated as:

$$\sigma_{T,\sigma} \simeq 2.36\sigma_R . \tag{5.8}$$

It is positively correlated to $1/\sqrt{n_{k,i}}$, where $n_{k,i}$ is the number of electrons in the anode charge pulse, thus improves when increasing the supply voltage applied to the PMT. To get the time distribution of SER events, the delay $(\Delta T - \Delta t)$, indicated in Fig. 5.9, between the laser signal (used as a trigger signal), ΔT, and the anode signal, Δt, was recorded and plotted. A gaussian fit to the peak allowed to determine the standard deviation, σ_R, of the SER time distribution; the $\sigma_{T,\gamma}$ is obtained from the equation 5.8.

5.5.3.2 Data collection and results

Figures 5.11 show two SER time distributions corresponding to different supply voltage values: (a) $V_{HV} = 800$ V and (b) $V_{HV} = 900$ V. A gaussian fit to the peaks

---

[7]The R7400 typical PMT time resolution or transit time jitter is 0.28 ns.
[8]The transit time can change depending on which part of the photocathode is illuminated.

(a)   (b)
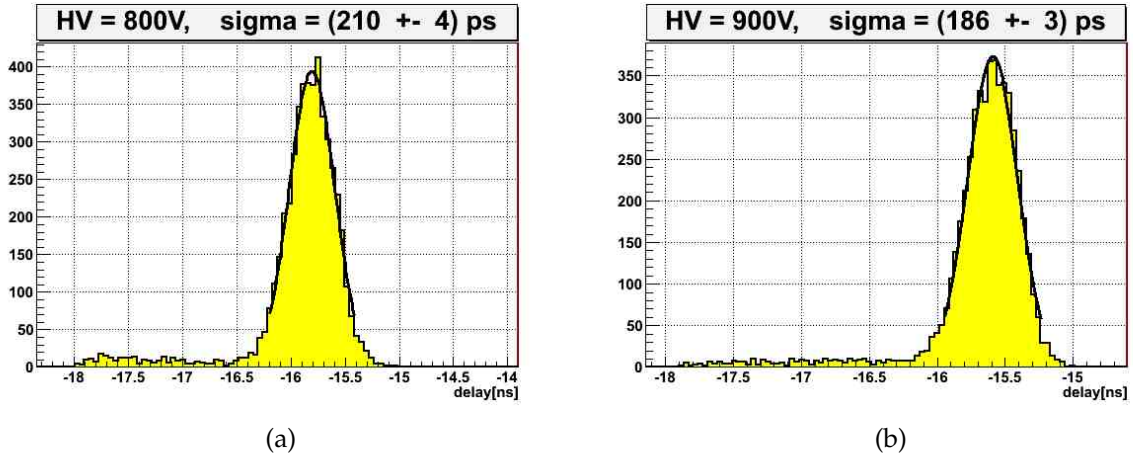
Figure 5.11: PMT response time distributions with a 20% light attenuation optical filter at V_{HV} values: 800 V, 900 V.

allowed to determine the standard deviation of the SER time distributions, indicated with "sigma" in the figure label; the $\sigma_{T,\gamma}$ is obtained from the equation 5.8 by replacing σ_R with "sigma". The SER time distributions show how the standard deviation is getting smaller, as well as the PMT time resolution, as V_{HV} increases, which confirms the dependence mentioned above. The values $\sigma_{T,\gamma} \simeq 495$ ps and $\sigma_{T,\gamma} \simeq 440$ ps are calculated using $\sigma_R = 210$ ps and $\sigma_R = 186$ ps corresponding to $V_{HV} = 800$ V and $V_{HV} = 900$ V, respectively. Both $\sigma_{T,\gamma}$ values are found to be greater than 300 ps; time slewing corrections, expected to get the peak narrower, are not applied yet. The results are in agreement with previous SER time resolution measurements, without time-slewing corrections, performed by the NA62 RICH detector working group with the same PMTs [95].

5.5.4   Results and conclusions

HAMAMATSU R7400/U-03 PMTs "*specially selected for photon counting applications*" [96] are indeed powerful devices for Single photoElectron Response (SER) measurements:

- The dark current contribution, including thermionic emission and leakage current, is within the manufacturer specification.

- SER peak, Fig. 5.10 (d), is well separated from pedestal events. Considering the PMT anode signal as a gaussian and relying on the fact that the PMTs used are

133

low-noise devices, a gaussian fit to the SER peak gives a charge value $Q(e) = (0.07 \pm 0.04)$ pC. This is to be compared with the PMT anode charge response Q to the emission of a single photoelectron of charge $q_e = 1.6 \cdot 10^{-19}$ C at a gain value of $G = 1.0 \cdot 10^6$ [94]:

$$Q = q_e \times G \sim 0.16 \ pC \ .$$

A consistency within 2σ is observed.

- The SER time resolution is dependent on the supply voltage applied to the PMT, improving at high values. The values $\sigma_{T,\gamma} \simeq 495$ ps and $\sigma_{T,\gamma} \simeq 440$ ps are calculated, from eq. (5.8), using $\sigma_R = 210$ ps and $\sigma_R = 186$ ps obtained in the previous section and corresponding to $V_{HV} = 800$ V and $V_{HV} = 900$ V, respectively. Both $\sigma_{T,\gamma}$ values are in good agreement with SER time resolution measurements, without time-sleewing corrections, made by the NA62 RICH detector working group with the same PMTs [95].

As a first approximation, a good $\sigma_{T,\gamma}$ is achieved for $V_{HV} = 900$ V, which corresponds to a gain value of $G = 1 \cdot 10^6$ and to the optimal working supply voltage value specified in the datasheet [96].

5.6   Montecarlo Simulation for the CEDAR PMT

The CEDAR detector is required to achieve a kaon tagging efficiency of at least 95% with a time resolution of at least 100 ps. The kaon tagging efficiency is defined as the number of kaon events satisfying a given tagging condition and normalised to the total number of kaon events. The tagging condition is subject to definition criteria not strictly fixed yet and it can change according to trigger purposes and the type of PMTs and gas used. The above criteria are:

- the number N_S of hit spots per kaon event must be above the minimum number $\overline{N_S}$ required for the Cherenkov ring reconstruction. Any simple algorithm for the ring reconstruction suggests this number to be $\overline{N_S} = 3$. Nevertheless, the test run in 2006 with the CEDAR "West" counter - filled with nitrogen and equipped with standard CEDAR PMTs - have pushed the requirement up to the value $\overline{N_S} = 6$ in order to render negligible the contributions coming from gas scintillation, PMT dark counts and pion light rings.

- the number N_γ of photo-electrons detected per kaon event must be above the minimum number $\overline{N_\gamma}$ required to achieve a kaon time resolution of $\sigma_{T,K} \sim 100$ ps. According to Eq. 5.7, given a time resolution on single photon detection of 300 ps, the kaon crossing time will be measured with a resolution of $300\,\text{ps}/\sqrt{N_\gamma}$, where N_γ is the number of detected photo-electrons per kaon. This implies the requirement $\overline{N_\gamma} = 9$.

The single photon rate, $4\,\text{MHz/mm}^2$, implies several limitations on photodetector performances involving event pile-up, dead time, anode current and smearing effects on the readout system. The single photon rate affects the number of detected photons per kaon; the real kaon detection efficiency obviously depends on it. A simulation based on a toy Montecarlo was developed to study all these contributions and to predict the configuration of PMTs necessary to optimize the CEDAR photodetector performance.

5.6.1 Number of photo-electrons

The number of Cherenkov photons emitted from the kaon particle passing through the radiator is of order of ~ 200 photons [93]. The number of detected photons (photo-electrons) depends on a quality parameter N_0 which can be factorized in several contributions coming from the optical system (mirror reflectivity, medium transparency, photon collection efficiency and geometrical acceptance) and above all from the photodetector choice (quantum efficiency which will depend on the photon energy). MonteCarlo simulations on existing CEDAR applications within the NA62 experiment at CERN [93] had determined the distribution of the total number of photo-electrons seen on the photodetector plane per kaon event (Fig. 5.12).
Those photons were generated according to:

- Cherenkov radiation trajectory $cos\theta_c = 1/\beta n$;

- Frank Tamm equation $\frac{dN}{d\lambda} = N_0 \cdot L \cdot sin^2\theta_c$ with $N_0 = 370\ \text{eV}^{-1}$, as mentioned in Sec. 5.2;

- wavelength $\sim 1/\lambda^2$ in the range $[2000, 6000]$ Å, hence $\Delta E = 4.13$ eV;

- QE of PMT as a function of λ (see Fig. 5.13).

Further simulation studies on the new CEDAR optical system [98] quote a factor of 80% that must be applied to the number of photons impinging the photodetector plane
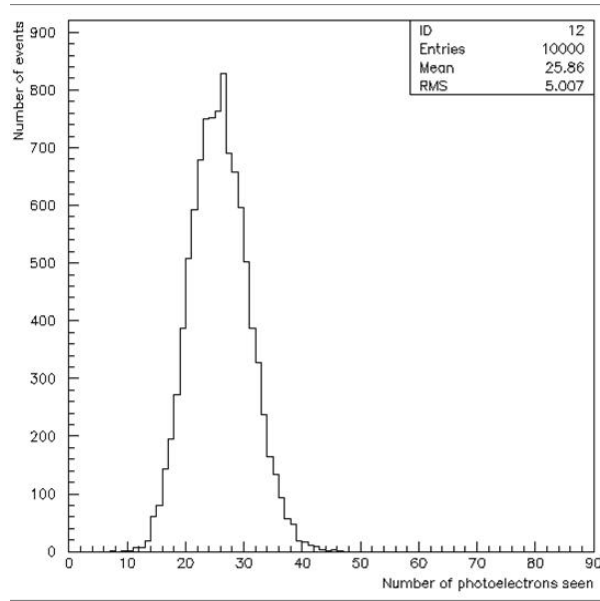
Figure 5.12: Number of photo-electrons seen per kaon event: plot taken from a Montecarlo simulation on the existing CEDAR [93].
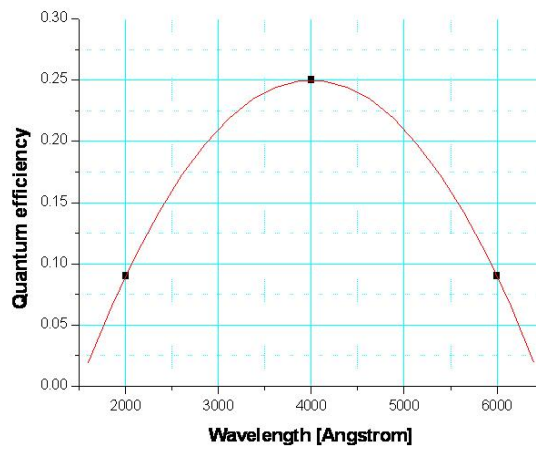
Figure 5.13: Photodetector Quantum Efficiency (QE) as a function of emitted photon's Cherenkov wavelengths.

to take into account the total acceptance of the new optical system. Moreover, it was proved that the light coming from each spot is not uniformly distributed on the photodetector plane, but mostly concentrated in the central region of the spot, as shown in Fig. 5.14.
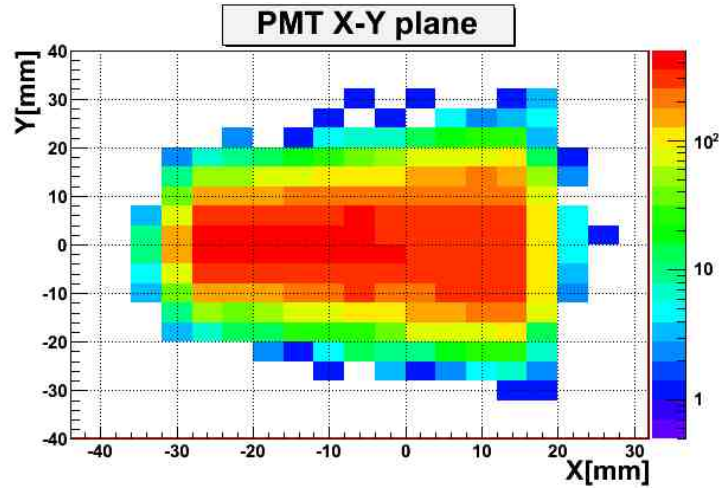
Figure 5.14: One-Spot light distribution on the X-Y photodetector (PMT) plane.

5.6.2 Toy Montecarlo inputs

The development of the parametric model starts reproducing the time distribution of kaons on the beam line. Assuming an exponential probability density function

$$f(t) = \frac{1}{\tau}e^{-t/\tau} \, ,$$

the "Inverse function" Montecarlo method is applied to evaluate the time intervals

$$\Delta t_i = -\tau ln(u_i) \, ,$$

where u_i are numbers randomly generated and τ is the inverse of the exponential distribution frequency (i.e the kaon rate): $\tau = \frac{1}{50 \, MHz} \simeq 20$ ns.

The kaon time distribution is generated according to the following procedure:

$$t_0 = 0, t_1 = \Delta t_1, t_2 = \Delta t_1 + \Delta t_2, ..., t_N = \sum_{i=1}^{N} \Delta t_i$$

and plotted in Fig. 5.15.

The number of photons N_γ is generated for each kaon according to:

- QE as a function of the kaon's emission wavelength (Fig. 5.13);

- the distribution of the number of photo-electrons seen per kaon event (Fig. 5.12);

- 80% factor to include optics acceptance.
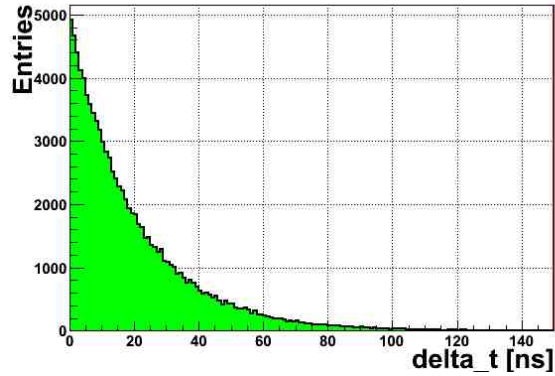
Figure 5.15: Kaon arrival time distribution.
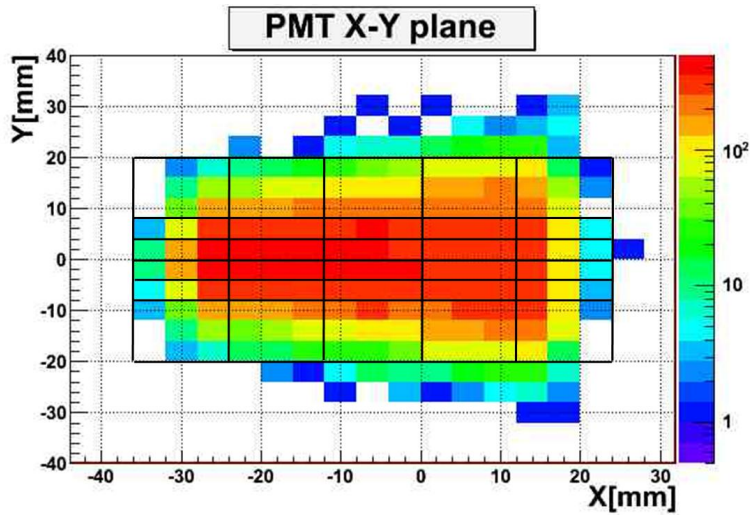
Figure 5.16: One-Spot light distribution on the X-Y photodetector plane: a matrix of 30 PMTs allows to define different sized regions of light collected by PMTs.

Those photons are then uniformly distributed among the eight spots. To reduce the photon rate over the spot a photodetector layout with a 6×5 matrix of R7400/U-03 PMTs is proposed.

As shown in Fig. 5.16 the suggested PMT layout does not provide the photon collection at the borders of the spot. Although this choice implies a light loss of $\sim 1\%$, it consistently helps to spread the light distribution on the PMT X-Y plane. The number of PMTs collecting photons from the high intensity light region (central part of the spot in Fig. 5.16) is such that the photon (photo-electrons) rate on single PMT is ≤ 5 MHz everywhere on the spot.

Due to the non uniform light distribution on the spot the single PMT rate is now de-
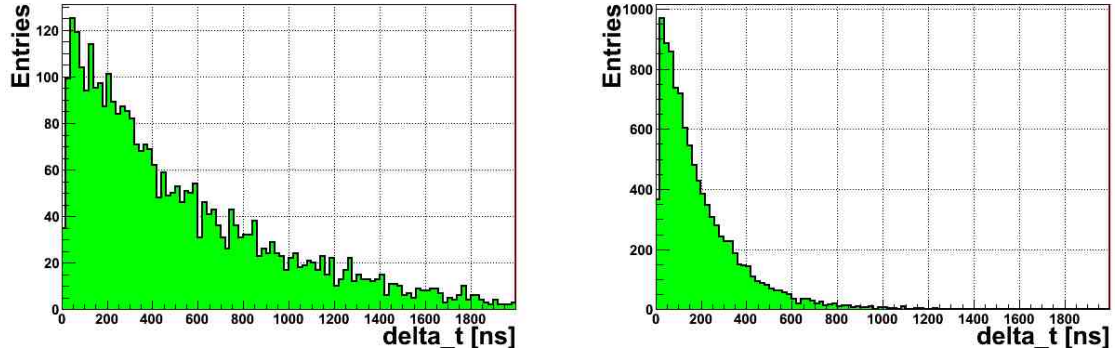
Figure 5.17: Photon arrival time distribution for PMTs collecting light from the border (a) and the central (b) parts of the spot.

pendent on the PMT X-Y position on the PMT plane: ranging from $R_1 = 1/\tau_1 \simeq 2$ MHz for PMTs situated on the border side (Fig. 5.17 (a)) to $R_2 = 1/\tau_2 \simeq 5$ MHz for PMTs situated in the centre of the spot (Fig. 5.17 (b)).

5.6.3   Pile-up inefficiency

Assuming that a single PMT gives a single hit even if more than one photon impinges on it, the actual number of hits per kaon event is smaller than the number of photo-electrons considered so far (see Fig. 5.12). The probability to have photons overlapping on PMTs (pile-up) within the same kaon event is shown in Fig. 5.18.
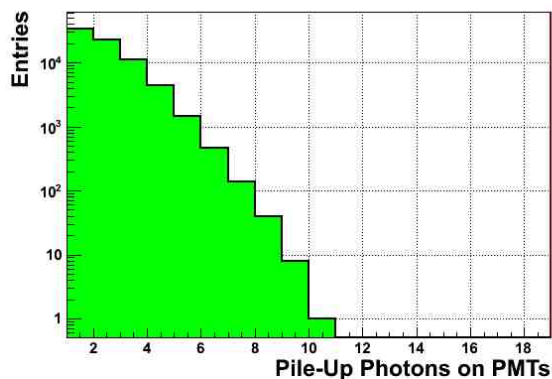
Figure 5.18: Pile-up photons on PMTs within the same kaon event.

Approximately $\sim 78\%$ of kaons show pile-up on at least one PMT which means that $\sim 78\%$ of kaons lose at least one photon.

139

Similarly a single PMT gives a single hit even when more than one photon impinges on it within a certain time interval (dead time). Hamamatsu R7400/U-03 PMTs were tested and their parameters put in the parametric model; their dead time is fixed at $T_D = 20$ ns in order to cover for:

- PMT Transit Time = 5.4 ns (see Sec. 5.4.1);

- Stretching Time = 11 ns introduced by the NINO to allow TDC time measurements; [9]

- Anode signal Time Over Threshold (TOT) $\simeq$ few ns.

The probability to have photons coming from different kaons and overlapping on PMTs (pile-up) within T_D is shown in Fig. 5.19:
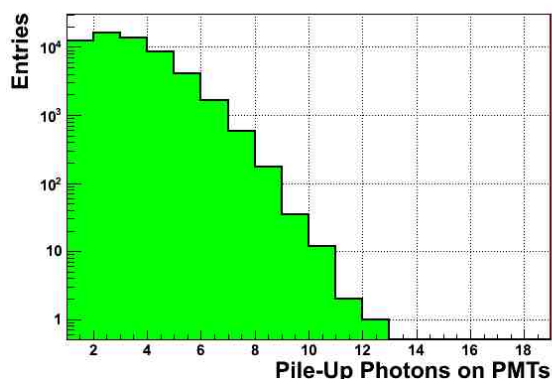
Figure 5.19: Pile-up photons on PMTs within the dead time.

Approximately $\sim 58\%$ of kaons show an inefficiency in at least one PMT, which means that $\sim 58\%$ of kaons lose at least one photon.

Both pile-up effects cause a decrease in the number of PMT hits per kaon, which is plotted in Fig. 5.20 and has to be compared with the one in Fig. 5.12.

5.6.4 Photon collection efficiency

Both pile-up photons on PMTs within the same kaon event and with a $\Delta T \leq T_D$ are considered as inefficiency. Both pile-up photons on PMTs with a $\Delta T > T_D$ and NO pile-up photons are considered as *"Good"*, each of them indeed corresponding to a single PMT hit. The values reported in Tab. 5.2 are evaluated with respect to the total number of produced photons.

---

[9] This time was measured in NINO applications within the NA62 RICH detector [95].
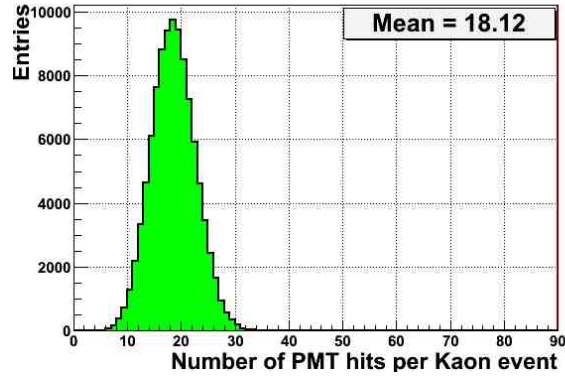
Figure 5.20: Number of photo-electrons detected per kaon event.

Inefficient Photons	Pile-Up/same Kaon event	Pile-Up with $\Delta T \leq T_D$
	$\sim 7\%$	$\sim 8\%$
"Good" Photons	Pile-Up with $\Delta T > T_D$	No Pile-Up
	$\sim 5\%$	$\sim 80\%$

Table 5.2: Photon collection efficiency.

5.6.5 PMT anode current

The average/peak anode current for Hamamatsu R7400/U-03 PMT is limited to 0.1 mA [96]. This is directly dependent on the photo-electron rate (peRate) on single PMT and indirectly dependent on the PMT working supply voltage. As a result of the previous chapter, high gain values are needed to optimize photodetector single counting performances such as a good separation between SER and pedestal event peaks, as well as a reasonably small time resolution. Indeed a gain value of $1 \cdot 10^6$, corresponding to $V_{HV} = 900$ V, is choosen to mostly achieve the desired CEDAR photodetector requirements. The anode current is evaluated using the relation:

$$Average/Peak \; Anode \; current \; \alpha \; peRate/mm^2 \times q(pe). \tag{5.9}$$

The rate $peRate/mm^2$ is calculated using the maximum possible value of ~ 5 MHz obtained in the central regions of the spot (Fig. 5.17) and dividing it by the size of the central light collection regions. The anode charge due to a photoelectron $q(pe)$ can be calculated by the equation: $q(pe) = 1pe \times G \times q_e$, using the electron charge $q_e = 1.6 \cdot 10^{-19}$ C and a gain value $G = 1 \cdot 10^6$. The anode current value is evaluated from Eq. 5.9 and a value of $\simeq 0.8 \ \mu$A is obtained. This value turns out to be orders

of magnitude smaller than the maximum sustainable value of 0.1 mA quoted in the manufacturer specifications [96].

5.6.6   Limitations of the PMT readout system

The photodetector readout system illustrated in the Sec. 5.4.2 includes HPTDC chips for the time measurements [99]. Each HPTDC has a maximum bandwith available of 40 MHz and inefficiencies are present if information is collected at rates higher than 1 MHz. The architecture of the data driver can be summarized in the following key points:

- Information from 8 channels (8 PMTs) are stored in a common latency buffer so that, in theory, the maximum bandwith available per HPTDC channel is $\sim$ 40 MHz/8 = 5 MHz.

- In practice, a probability of hit loss can already be observed for rates above 1 MHz, the reason for it is mainly due to the channel occupancy.

- The channel occupancy is given by a buffer of 4 memory locations; when the buffer is full and a new hit arrives, it is simply ignored.

- For CEDAR purposes both leading and trailing edge measurements will be performed, which means that one hit (one photon) will occupy two locations in the buffer and one HPTDC channel (one PMT) will be full (busy) after only two photons have impinged on it.

- If fewer than 8 channels are occupied (per each group of 8 HPTDC channels), the maximum bandwith available per HPTDC channel increases; in particular, choosing the first channels per each group helps data to flow quicker.

- The hit loss probability also depends on the correlation between hits, increasing for correlated hits on HPTDC channels.

Tests were made at the "University of Pisa" (Italy) by myself and local researchers in order to measure the hit loss probability, for correlated hits on HPTDC channels, using a different number of HPTDC channels at different hit rates. Test results are reported in Tab. 5.3. The only possibility for the photodetector readout to stand an average rate of $\sim$ 5 MHz, with relatively small ($\sim$ 1%) hit losses, is by connecting to

Hit Rate[MHz]	#2 channels	#3 channels	#4 channels
1	No Hit Loss	No Hit Loss	No Hit Loss
2	No Hit Loss	No Hit Loss	No Hit Loss
3	No Hit Loss	No Hit Loss	No Hit Loss
4	1%	1%	10%
5	1%	10%	20%

Table 5.3: Hit loss probability values measured with different numbers of HPTDC channels at different rates; the results are evaluated with respect to ~ 100 hits so that "No Hit Loss" means $< 1\%$.

PMTs only 2 channels per each group of 8 HPTDC channels. This implies doubling the readout electronic system and it will be mandatory in order to minimize the contribution coming from this kind of inefficiency.

A hit loss probability value of $\sim 1\%$ is also considered, as an upper limit, for uncorrelated hits on HPTDC channels. The number of PMT hits per kaon event, after applying both inefficiencies for correlated and uncorrelated hits on HPTDC channels at 5 MHz, is shown in Fig. 5.21.
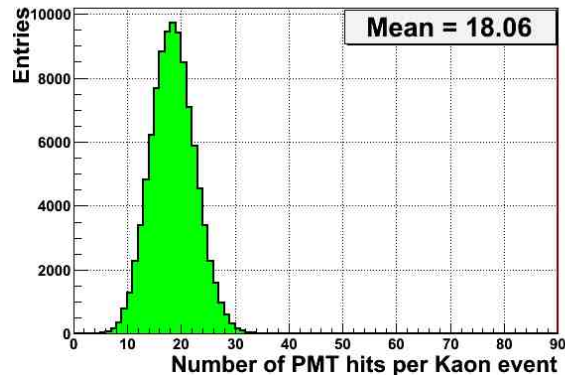
Figure 5.21: Number of photo-electrons detected per kaon event.

This distribution, together with the number of hit spots per kaon event (Fig. 5.22) will be used in the next section to evaluate the kaon inefficiency.

5.6.7 Kaon inefficiency

The kaon tagging inefficiency is defined as $(1 - \epsilon_K)$, where ϵ_K is the kaon tagging efficiency introduced in Sec. 5.6. Kaon tagging inefficiency values for different N_S and
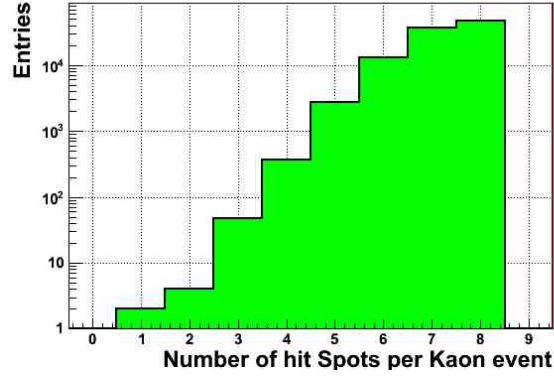
Figure 5.22: Number of hit spots per kaon event.

N_γ thresholds are evaluated with the Montecarlo and reported in Tab. 5.4. For each N_γ

AND	$N_\gamma \geq 8$ $\sigma_{T,K} \simeq 106ps$	$N_\gamma \geq 9$ $\sigma_{T,K} \simeq 100ps$	$N_\gamma \geq 10$ $\sigma_{T,K} \simeq 95ps$	$N_\gamma \geq 11$ $\sigma_{T,K} \simeq 90ps$
$N_S \geq 3$	(3.05 ± 0.17) $\times 10^{-3}$	(6.64 ± 0.26) $\times 10^{-3}$	(1.45 ± 0.04) $\times 10^{-2}$	(2.74 ± 0.05) $\times 10^{-2}$
$N_S \geq 4$	(3.19 ± 0.18) $\times 10^{-3}$	(6.74 ± 0.26) $\times 10^{-3}$	(1.46 ± 0.04) $\times 10^{-2}$	(2.75 ± 0.05) $\times 10^{-2}$
$N_S \geq 5$	(6.02 ± 0.24) $\times 10^{-3}$	(9.01 ± 0.29) $\times 10^{-3}$	(1.63 ± 0.04) $\times 10^{-2}$	(2.87 ± 0.05) $\times 10^{-2}$
$N_S \geq 6$	(3.19 ± 0.06) $\times 10^{-2}$	(3.34 ± 0.06) $\times 10^{-2}$	(3.83 ± 0.06) $\times 10^{-2}$	(4.77 ± 0.07) $\times 10^{-2}$
$N_S \geq 7$	(1.609 ± 0.012) $\times 10^{-1}$	(1.613 ± 0.012) $\times 10^{-1}$	(1.627 ± 0.012) $\times 10^{-1}$	(1.663 ± 0.012) $\times 10^{-1}$
$N_S \geq 8$	(5.305 ± 0.016) $\times 10^{-1}$	(5.305 ± 0.016) $\times 10^{-1}$	(5.306 ± 0.016) $\times 10^{-1}$	(5.311 ± 0.016) $\times 10^{-1}$

Table 5.4: Kaon identification inefficiency values for different definition criteria of inefficient kaon events.

144

value the corresponding kaon time resolution is calculated using the equation (5.7):

$$\sigma_{T,K} = \frac{\sigma_{T,\gamma}}{\sqrt{N_\gamma}}$$

where $\sigma_{T,\gamma}$ is the single photon time resolution of $\sim$ 300 ps measured for HAMA-MATSU R7400/U-03 PMT.

5.6.8 Contamination to the kaon identification

Photodetector thermal noise (dark count) could in principle contribute to the kaon identification giving spurious coincidences. Comparing with the intrinsic kaon rate $R_K \sim 50$ MHz, Hamamatsu R7400/U-03 PMT has an extremely low typical dark count rate of $R_{dark} \sim 80$ Hz at the typical gain value of 10^6 [96]. Even so, any possible contribution to the kaon identification inefficiency and the kaon rate is considered.

The probability to lose a photon coming from a kaon because it impinges at the same time with a dark noise photon on the same PMT, within a time $T \leq T_D$ ns, can be evaluated analytically as the ratio of $R_{dark}/R_K \sim 2 \times 10^{-6}$.

The probability to have a spurious concidence of dark noise photons that simulates a kaon event is shown in Fig. 5.23. The implementation of dark-dark events coincidences, within the single photon time resolution of $\sigma_{T,\gamma} \simeq 300$ ps, results in 12 double coincidences found out of 10^6 dark photons, which corresponds to a probability of $\sim 5 \times 10^{-6}$, while no multiple dark coincidences are found.
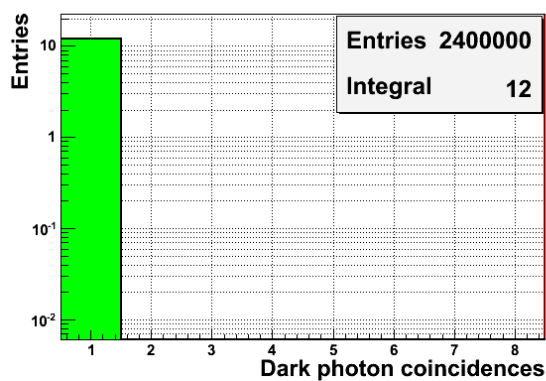
Figure 5.23: Dark photon event coincidences: the first bin is filled if a double coincidence is found.

Considering a data acquisition rate of $\sim$ 1 MHz and recording events for a 75 ns period (readout time window), the probability to have dark photons within the

145

readout time window is shown in Fig. 5.24. Only 6 dark photons are found in 2000 readout time windows which corresponds to a contribution of order of $\sim 0.3\%$ to the total rate in the readout system.
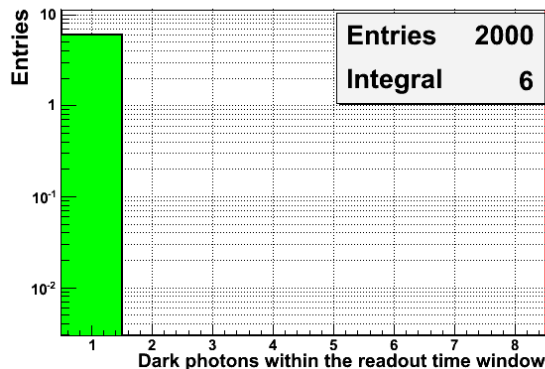
Figure 5.24: Dark photon events within readout time windows.

As a result, for CEDAR purposes the dark noise rate gives a negligible contribution.

5.6.9 Conclusions

The CEDAR detector to be used in the near-future NA62 research programme is required to achieve a kaon identification efficiency of at least 95% with a time resolution of at least 100 ps. The original CEDAR light spots will be exposed to a very high photon rate and existing photomultipliers are unsuitable for CEDAR requirements and need to be replaced.

A MonteCarlo simulation has been developed to study the optimal configuration for the CEDAR photodetector. A proposed solution is a matrix of HAMAMATSU R7400/U-03 PMTs collecting the light at each spot. Due to the non-uniform light distribution on the PMT plane, a new optical system and a careful design of light collection cones is addressed. This solution helps to spread the photon rate over the spot and to reduce the photon flux at each PMT to $\sim$ 5 MHz, keeping the PMT anode current within a safe limit. Despite that, the photon rate implies several limitations on photodetector performances. Inefficiencies coming from event pile-up in PMTs and smearing effects in the HPTDC readout system decrease the number of photo-electrons detected per kaon, contributing to the kaon identification inefficiency. Such contributions are studied in the MonteCarlo simulation and the number of detected photo-electrons and hit spots per kaon event, after applying such inefficiencies, are

shown in Figs. 5.21 and 5.22. The inefficiency values reported in Tab. 5.4 indicate that it is feasible to require up to 6 spots in coincidence to 11 PMTs as a kaon tagging condition, ensuring a kaon identification efficiency of $\sim 95\%$ and a kaon time resolution $\sigma_{T,K} \leq 100ps$. Any possible contribution coming from photodetector thermal noise (dark count) is also studied in the MonteCarlo simulation and verified to be negligible.

Future improvements will involve:

- Simulation of Cherenkov photons emitted by the pion component of the beam. The CEDAR is supposed to be insensitive to pion Cherenkov light rings, but pions are the dominant particles of the beam. For this reason it is mandatory to check that the kaon mis-identification probability is negligible.

- Rate tests on the electronic readout chain (NINO+HPTDC). Similarly to the test made in Pisa, they will be performed to investigate limitations of the complete PMT readout system.

- Development of a Geant4 simulation for the CEDAR within the final Geant4 global simulation called *NA62MC*.

Chapter 6

The CEDAR test beam at CERN

In October 2011 a test beam with a CEDAR "West" counter was performed at CERN. The first task was to become familiar with the operation of the actual CEDAR (identified as WEST-01) to be used in NA62. Then, detailed measurements were made of new hardware and electronics designed specifically for NA62 to operate at high beam flux.

The test was organised in three phases. First, the CEDAR detector was installed with its standard PMTs and readout system. Once all the alignment procedures had been carried out, PMT efficiencies were measured and a pressure scan was performed so that the velocity (and hence the mass) resolution of the detector could be observed. Next, the new front-end and read-out electronics were installed and independent measurements with the standard CEDAR PMTs (EMI 14 dynodes) were made. Finally, one of the standard PMTs was replaced with an assembly of three of the new PMTs specified for NA62 and further investigations were carried out, including measurements of time distributions for the PMT response.

6.1   Phase 1 - Operation with standard components

6.1.1   Installation

The CEDAR was installed on the H6 beam line (left picture in Fig. 6.1) in building 887(EHN1) located in the North Area. Some manual adjustment was required to align the optical axis of the CEDAR with the beam axis. This was achieved by lowering the nose by about 5 mm with a jack.

6.1.2   Experimental Layout
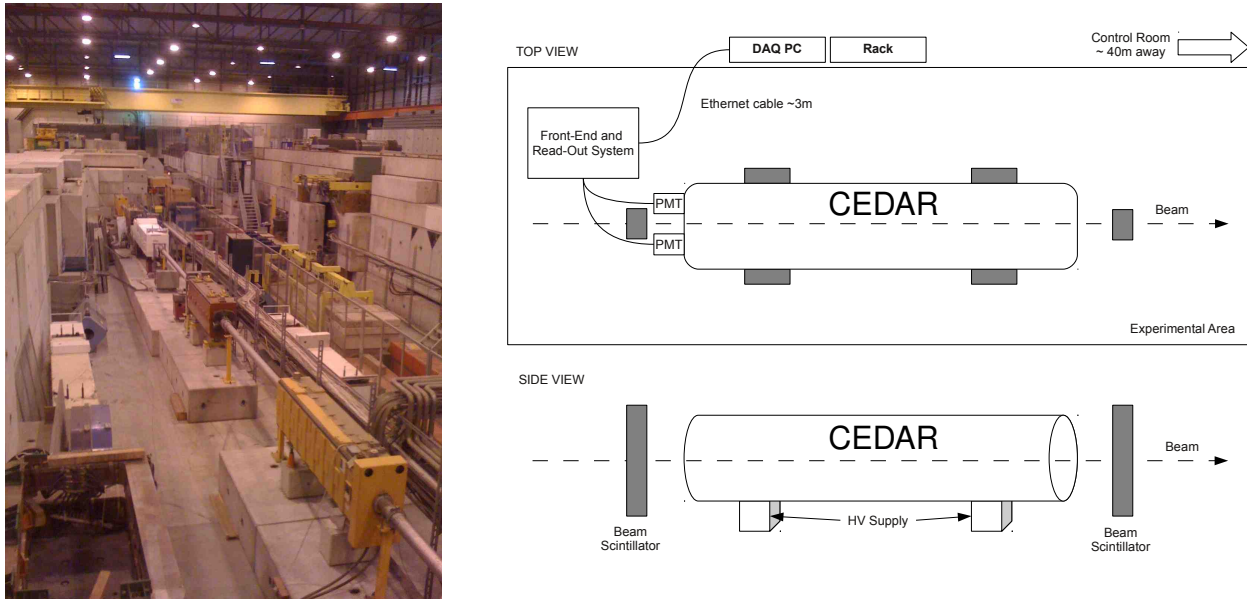
Figure 6.1: Left: CEDAR counter (white rectangular box) positioned on the H6 beam line. Right: schematic layout used for the CEDAR test beam (top view, side view, not to scale).

The experimental layout is shown in Fig. 6.1 (right). In the final set-up, the new front-end and read-out electronics were placed close to the detector to reduce time delays. The PC for data acquisition was positioned at a safe distance from the beam line and connected by a 100 m ethernet cable to another PC located in the control room. Scintillators were placed at either end of the CEDAR to provide the trigger and measure the beam particle flux. In the first phase, the experimental set-up comprehended:

Scintillators The signal coincidence of the two beam scintillators was used as a strobe input for the coincidence of PMT signals.

Photomultiplier Tubes Eight standard CEDAR PMTs were screwed onto the eight quartz windows at the exit of the CEDAR.

Discriminator The signals from the 8 PMTs were shaped by fast discriminator modules[1] operating at low threshold before being split into two: one for measuring coincidences and one for system diagnostics.

---

[1]A discriminator module is a device generating logic pulses (hig-low level) in response to analog input signals exceeding a certain threshold.

Coincidence module One set of PMT signals was sent to a logic unit, which could provide three levels of coincidence (sixfold, sevenfold and eightfold). The counts of each level of coincidence were used to evaluate the average number of photo-electrons (NPE) seen by the PMTs (see Sec. 6.1.3).

Scaler counter The other set of PMT signals was sent to a coincidence module strobed with the beam scintillators coincidence signal. The output, i.e. the coincidence between signals from each PMT and the beam scintillators, was recorded on 8 scaler counters[2] to extract information on single PMT efficiencies, which are defined as the number of the above coincidence signals normalised to the total number of signals from the beam scintillators.

In the first phase, both control of the CEDAR and data acquisition were achieved with the standard interface, "CESAR" [93], integrated into the main SPS software for the beam monitoring and control. This software was used for fine tuning of the CEDAR alignment (Sec. 6.1.4), for measuring PMT efficiencies (Sec. 6.1.3) and performing the pressure scan (Sec. 6.1.5); such software will not be available in future and it will be replaced.

6.1.3 Individual PMT Efficiencies

A measurement of individual PMT efficiencies can be performed by setting the gas pressure to detect a certain particle and by comparing the number of PMT counts, i.e. PMT output signals in response to photons, with the particle ratio expected from the beam composition. It is recommended to perform the above measurement with the CEDAR set at the nominal value of gas pressure corresponding to the most abundant particle in the beam, so that the measurement is less affected by statistical fluctuations and tails of Cherenkov light distributions from other particles in the beam. PMT counts are normalised to the number of triggers recorded by the scintillators. If the beam composition is known, the PMT counting efficiency is given by:

$$\text{PMT counting efficiency} = \frac{\text{PMT hits / 100 triggers}}{\text{beam fraction of particle}}. \tag{6.1}$$

Individual PMT counting efficiencies are dependent on:

· The spectrum of Cherenkov light transmitted through the CEDAR quartz windows;

---

[2]A scaler counter is a device counting pulses occurring too rapidly to be recorded individually. It operates by grouping them into bunches of a pre-definite number of pulses.

· The geometrical acceptance of the light-guide channelling light onto the PMTs;

· The quantum efficiency of the PMT as a function of the wavelength.

Tab. 6.1 shows the results of measurements made after setting the gas pressure on the proton peak. The PMT counts (first row), normalised to the number of triggers, are expressed as a percentage. Calculations based on empirical data [86] show that the expected proton beam fraction at the source is 0.226. Taking into account the pion and kaon lifetimes, the expected proton fraction at the CEDAR, 500 m downstream, is 0.257^3. The PMT counting efficiencies (Tab. 6.1, second row) are calculated assuming this beam fraction, so 25.7 PMT counts per 100 triggers would imply 100% PMT counting efficiency. The uncertainty assigned to those efficiencies is dominated by a $\sim 2\%$ systematic error due to a non correct PMT equalisation and evaluated as the spread between the farthest measurements.

Appendix B describes how the measured efficiencies can be related to the number of photo-electrons produced per particle (reported in Tab. 6.1, third row). It can be shown that, if η is the PMT counting efficiency, the mean number of photo-electrons in this PMT per particle, ϕ, is given by:

$$\phi = -\ln(1 - \eta). \tag{6.2}$$

If all PMTs can be assumed to have identical efficiencies, then appendix B describes an alternative method which can be used to calculate the average efficiency based on the ratios of 6-fold and 7-fold to 8-fold coincidences. The relative efficiencies are also useful for the alignment procedure described below.

	Ch 0	Ch 1	Ch 2	Ch 3	Ch 4	Ch 5	Ch 6	Ch 7
PMT counts (%)	21	21	21	23	19	22	21	22
PMT Counting Efficiency	0.82	0.82	0.82	0.90	0.74	0.86	0.82	0.86
Mean number of photo-electrons	1.71	1.71	1.71	2.27	1.35	1.95	1.71	1.95

Table 6.1: PMT counts, counting efficiencies and derived number of photo-electrons per proton per PMT. The acquisition corresponds to the CEDAR aligned with the aperture width, w_D, set at 8 mm.
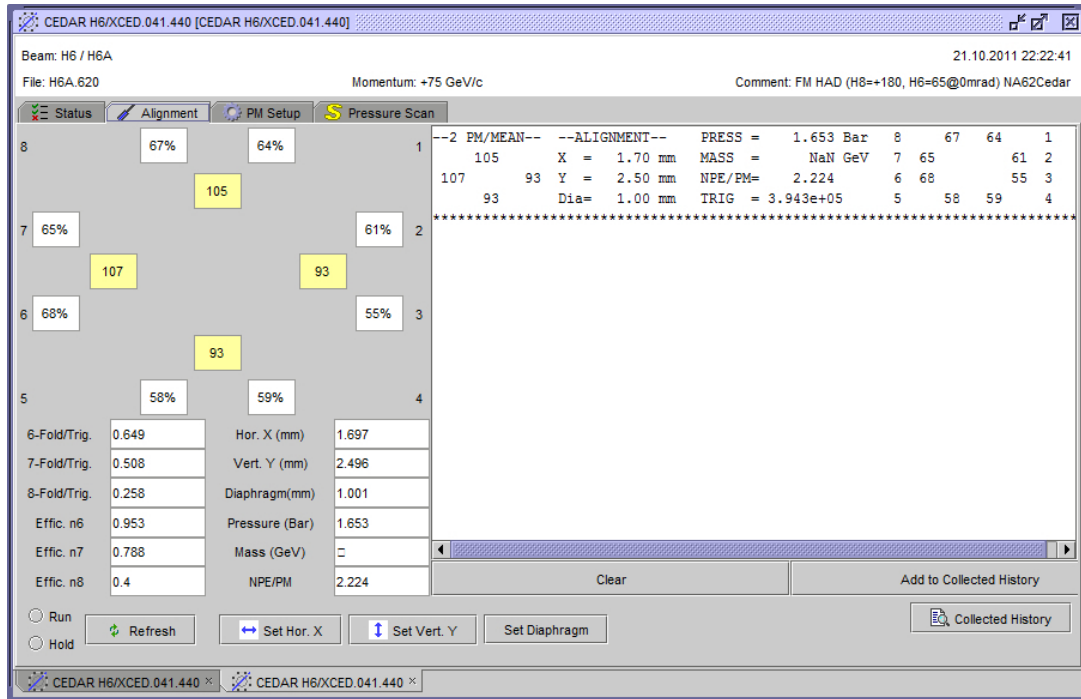
Figure 6.2: Standard "CESAR" software interface screenshot: (left-up side) counting rates for eight standard PMTs written on white boxes which are displaced in circle; counting rates for four grouped PMTs written on yellow boxes arranged on an inner circle; (left-down side) indicators for 6-, 7- and 8-fold coincidence rates; X-Y positions of the nose, diaphragm width, gas pressure; controls for the CEDAR alignment. In the right side of the screenshot a typical printout of the alignment procedure is showed; the CEDAR was set on the pion pressure and the counting rates (($55 \div 68$)%) reflect the pion fraction in the beam.

6.1.4 Alignment

The alignment system, as described in the CERN Yellow Report [93], allows the position of the nose of the CEDAR to be moved in x and y directions with an accuracy of 0.01 mm, corresponding to an angular resolution of 2.3 μrad. As a measure of the alignment, the "CESAR" software interface (Fig. 6.2) provides grouped count rates: up (U), down(D), left (L) and right (R), each calculated as the sum of two PMTs normalised to the average of all. The alignment procedure consists in equalising the ratios R/L and U/D with the diaphragm wide open, then reducing the width, w_D, of the diaphragm aperture and adjusting the alignment in order to reproduce the same

---

[3]The number of a given type of particle of mass m_i and lifetime τ_i remaining after x m is computed as $N_i(x) = N_i(0) \exp(-xm_i/pc\tau_i)$

values of R/L and U/D ratios as with the diaphragm wide open. The CEDAR alignment gets more and more difficult as the diaphragm is narrowed. The alignment was considered successful as the ratios R/L and U/D at $w_D = 1\,\text{mm}$ were compatible with those corresponding to a wide open diaphragm, $w_D = 8\,\text{mm}$. Tab. 6.2 shows the PMT counts as measured after the CEDAR alignment achieved at $w_D = 1\,\text{mm}$; with such narrow diaphragm aperture the amount of light collected by the PMTs is lower and so are the PMT counting efficiencies.

	Ch 0	Ch 1	Ch 2	Ch 3	Ch 4	Ch 5	Ch 6	Ch 7
PMT counts	19	20	20	20	18	20	18	20
PMT Counting Efficiency	0.74	0.78	0.78	0.78	0.70	0.78	0.70	0.78
Mean number of photo-electrons	1.35	1.51	1.51	1.51	1.21	1.51	1.21	1.51

Table 6.2: PMT counts, counting efficiencies and derived number of photo-electrons per proton per PMT after the CEDAR alignment with w_D set at 1 mm.

6.1.5 Pressure Scan

The possibility of vessel outgassing or gas pollution by air implies that the nominal pressures given by the "CESAR" software interface may be slightly wrong. A pressure scan provides a way to check this, as well as measuring the beam composition and demonstrating the resolution of the CEDAR. The P-SCAN subroutine performs a gas-pressure scan between two given limits and with a given number of steps. At each step, once the required statistics (determined by the number of triggers) is reached, the numbers of 6-fold, 7-fold and 8-fold coincidences recorded by the PMTs are displayed. As described in appendix B, the coincidence levels provide another way to calculate the number of photo-electrons per PMT, independent from the number of triggers.

During a pressure scan, care must be taken to maintain the thermal equilibrium since temperature fluctuations would affect the CEDAR resolution [93]. This is achieved by always running from high gas pressure to low gas pressure and leaving enough time after each pressure adjustment for equilibrium to be reached. Two pressure scans have been performed in different gas pressure ranges; the parameters used are shown in Tab. 6.3.

Fig. 6.3 shows the results of the pressure scan over the full range. Three peaks due to (from left) pions, kaons and protons are visible: the proton and kaon peaks are

	Full range scan	Partial range scan
Maximum pressure (bar)	2	1.796
Minimum pressure (bar)	1.6	1.605
Pressure step (mbar)	10	5
Diaphram aperture (mm)	1	0.8

Table 6.3: Parameters used for the pressure scans: the full range scan covered the pion, kaon and proton peak regions, the partial one was focused on the pion and kaon peaks in order to achieve a better resolution.
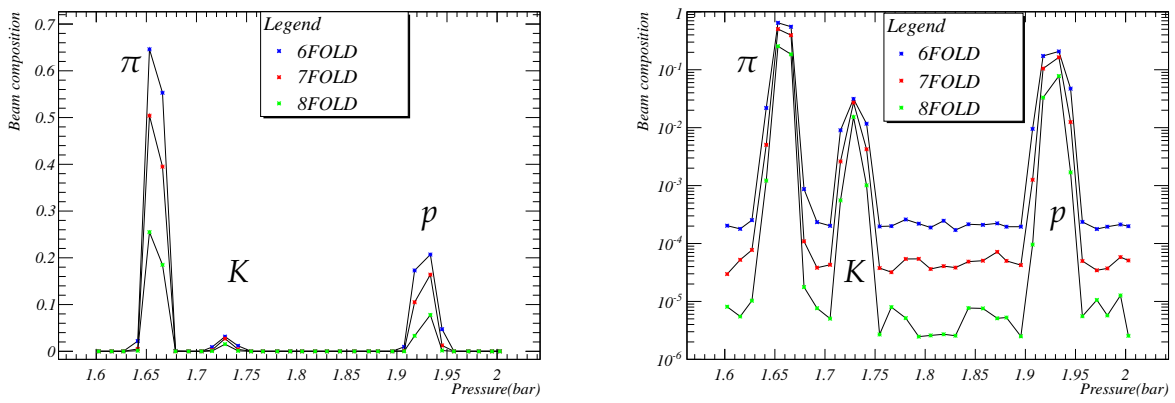
Figure 6.3: Pressure scan over the full range of gas pressures.

clearly separated, while the kaon and pion peaks are much closer and can only be better resolved using a smaller diaphragm aperture, thus worsening the light geometrical acceptance (see Sec. 5.2).

To further improve the separation of the peaks, the diaphragm aperture was reduced to 0.8 mm and a second pressure scan was performed in a partial pressure range. The results are showed in Fig. 6.4. The pion and kaon peaks are now clearly separated.

The effect of changing the aperture width was investigated by setting the pressure at the value corresponding to the pion peak and measuring the particle detection efficiency (defined as the ratio between the number of 6-fold coincidences and the number of triggers recorded by the scintillators) as w_D was increased from 0.4 mm to 2 mm. The results are shown in Fig. 6.5; the two trends correspond to separate measurements. The particle detection efficiency plateaued at around 63%, which is comparable with the maximum height of the pion peak in the pressure scans (Figs. 6.3, 6.4).
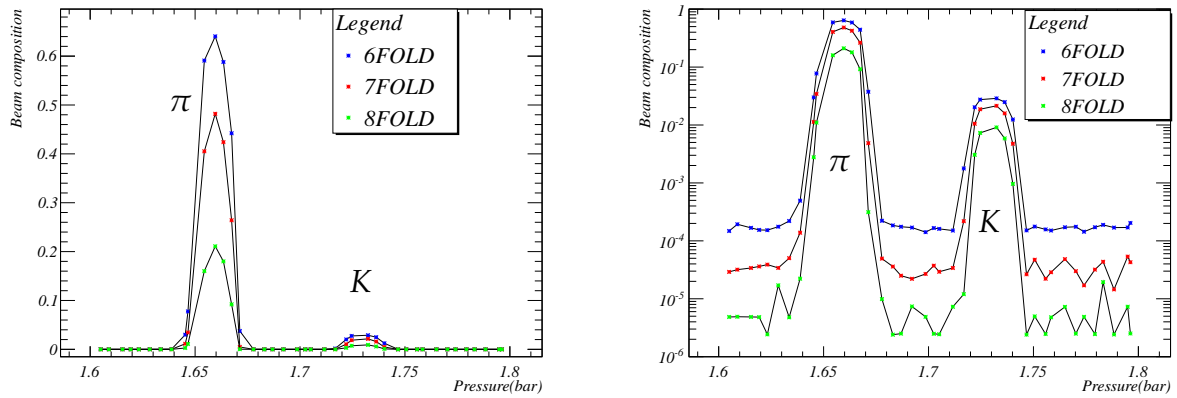
Figure 6.4: Pressure scan focused on separation of pion and kaon peaks.
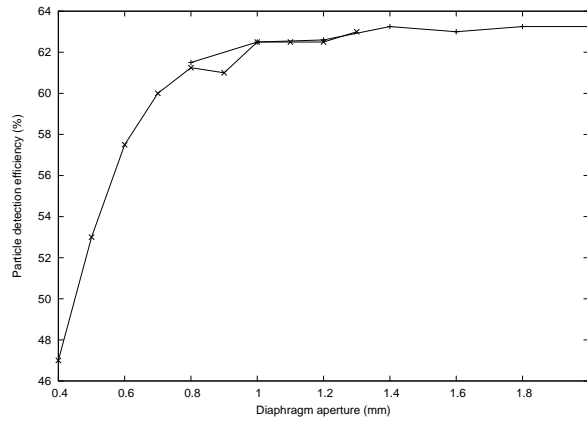
Figure 6.5: Detection efficiency as a function of the diaphram aperture at fixed gas pressure on the pion peak

6.2 Phase 2 - New Front-End and Readout Electronics
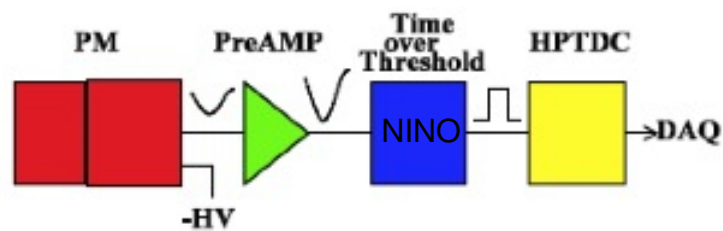
Figure 6.6: CEDAR new front-end and readout system designed for NA62.

After the first phase of the CEDAR commissioning in its standard version, a second phase followed, aiming to test the new front-end and readout system designed

for use in NA62. As discussed in details in Sec. 5.4.2, in the new design (Fig. 6.6) the typical PMT signal output produced by one photon is amplified, discriminated and time-stretched by a NINO ASIC [97] board to produce a LVDS output. As the NINO requires a differential input, a preamplifier and shaper board has been proposed to adapt the PMT output to the NINO input. The new readout chain is equipped with HPTDC chips (developed at CERN [99]) mounted on TDC boards. The data acquisition system is an Field Programmable Gate Array (FPGA) based TEL62 (Trigger ELectronics for NA62 [100]) mother board housing 4 TDC cards.

Figure 6.7: CEDAR new front-end and readout system designed for NA62.

In the NA62 experiment the front-end will be placed close to the PMTs and it must be radiation-hard. The NINO ASIC positively passed radiation tests up to a dose level of 7 krad (equivalent to 70 Gy), with no latch-up observed [101]. The preamplifier board has been designed with rad-hard components. The rest of the electronics will be positioned far enough from the beam not to require radiation hardness.

As the TEL62 board was still under development at the time of the test, its predecessor TELL1 (Trigger ELetronics for Level 1 [102]) board, originally designed for use on the LHC, was used. Two different front-end options, coupled with the NINO ASIC, were tested: a preamplifier board (Florence's[4]) made for use in the NA62 RICH detector and a custom rad-hard preamplifier board designed to withstand the radiation level at CEDAR.

During the test, the data acquisition was triggered by the coincidence of two beam scintillators positioned at both ends of the CEDAR counter. Fig. 6.8 (left panel) shows

---

[4]Labelled after the working group who realised it.

the CEDAR nose equipped with standard PMTs and passive splitters, which allowed the division of the PMT output into two signals: one cabled to the standard "CE-SAR" readout interface and the other one to the new front-end and readout system. The front-end, composed of attenuation modules, Florence's preamplifier and NINO board, was positioned inside the CEDAR insulation box, while the PMT high voltage system was sitting in a NIM crate below the CEDAR box. Fig. 6.8 (right panel) shows the TELL1 readout system and a PC for the data acquisition and the local data storage, as they were all located at about 3 m from the CEDAR along the H6 beam line. The data acquisition was driven remotely with another PC located in a control room about 40 m downstream from the experimental area. The two PCs were connected with a 100 m long ethernet cable, thus creating a fast data transferring local grid.

The official "NA62 Event Display" [105] software was implemented as a data-quality online monitor featuring the possibility to look at distributions updating in real-time during the data taking. An offline analysis software was ready to give a fast feedback on the acquired data. During the test beam about 500 GB of data were recorded in Castor to be available for the users.

6.2.1 Standard PMTs
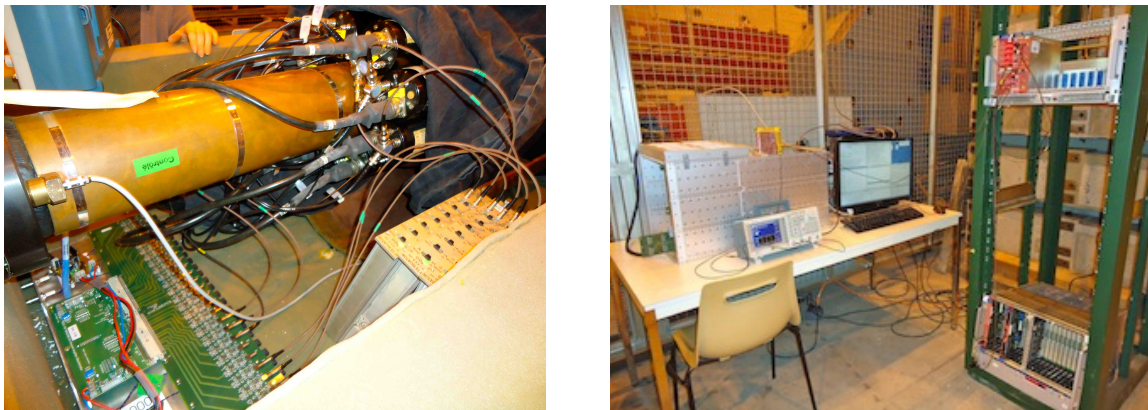
Figure 6.8: Left: CEDAR nose with standard PMTs; passive splitters to connect the signal with standard and new readouts; attenuator modules; Florence's preamplifier and NINO board. Right: TELL1 readout system; data acquisition PC and rack for additional electronics placed along the H6 beam line.

During this phase the CEDAR standard PMTs (EMI 14 dynodes) were coupled with the new front-end and readout system (as explained in the previous section). The same

signal treatment was applied to the beam scintillators upstream and downstream of the CEDAR detector.

The PMT efficiencies as well as the 6-,7-, and 8- fold coincidences resulting from both standard and new readout systems were compared. Fig. 6.9 shows the signal time distributions with respect to the trigger time for the eight CEDAR standard PMTs. The plot refers to the CEDAR at a gas pressure value set to detect pions and with the diaphragm aperture opened at $w_D = 1$ mm. It shows that the signal time distributions of the standard PMTs are aligned within a 15 ns time window and about 60 ns ahead the trigger signal from the scintillators (used as a reference time).
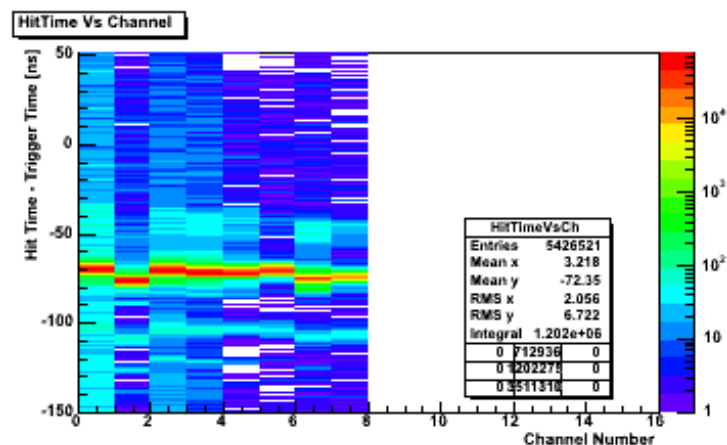
Figure 6.9: Channel occupancies (left plot) and signal time distributions with respect to the scintillator trigger (right plot) of standard CEDAR PMTs.

6.3 Phase 3 - New PMTs

The CEDAR photodetector choice is based on PMTs used for the NA62 RICH detector [95]: photomultipliers of the HAMAMATSU [104] R7400 series, U-03 (glass window) type. During this phase of the tests, one standard 5 cm diameter CEDAR PMT was replaced with an assembly of three Hamamatsu R7400U-03 PMTs. Fig. 6.10 shows the technical design for the assembly of new PMTs (left picture) and its positioning at the place of one standard CEDAR PMT (right picture).

The new PMT has an active photocathode diameter of 8 mm, corresponding to an active area of about 50 mm^2. The standard CEDAR PMTs were located about 150 mm upstream of the quartz windows, while the new PMTs were installed, in the same housing, about 340 mm upstream of the CEDAR quartz window using an extension tube (not shown in the right panel of Fig. 6.10). The assembly has been purposely

Figure 6.10: Left: the new-PMTs assembly layout and its relative position with respect to the Cherenkov light ring (red circle). Right: CEDAR setup with seven standard PMTs and the new-PMTs assembly.

designed with an adjustable orientation so that the light collection efficiency can be optimised. The Cherenkov light distributions at the new-PMT plane as predicted by a MC simulation, as well as the definition of the rotation angle φ of the assembly, are presented in Fig. 6.11.

Figure 6.11: NA62-MC simulation of the Cherenkov light at the new-PMT plane (with extension tube in place) overlaid with the PMT assembly in its nominal position (left) and rotated by 180 degree (right). The y-axis in the plots points radially but the actual prototype was rotated by 22.5^o with respect to the plot. The centre of rotation of the prototype was at $x = 0$, $y = 103$ mm.

6.3.1 PMT Efficiency

With the CEDAR tuned on 75 GeV/c pions, the response of the new PMTs as a function of the applied high voltage was measured. The left panel in Fig. 6.12 shows a high voltage scan in the range between 800 V and 900 V for one of the new PMTs (the central one within the assembly). The lower limit is the minimum voltage at which the PMT output signal is visible in Single photo-Electron Response (SER) regime[5], while the upper limit is the maximum working voltage according to the datasheet. The new-PMT counting rate is defined as the ratio between the number of PMT counts and the number of triggers[6]; it includes the geometrical acceptance and reflects the particle fraction in the beam when the CEDAR is correctly aligned. The value chosen as the PMT working voltage was 900 V.

The dependence of the new-PMT response on the diaphragm aperture width w_D was also studied. The right panel in Fig. 6.12 shows how the new-PMT counting rates increase when changing the diaphragm aperture from 1 mm to 6 mm. The four sets of measurements refer to:

· the new-PMT assembly in two different positions with respect to the Cherenkov light ring transverse plane: tangent ($\varphi = 180°$) and radial ($\varphi = 270°$);

· two different run conditions: with the standard PMTs switched ON and OFF;
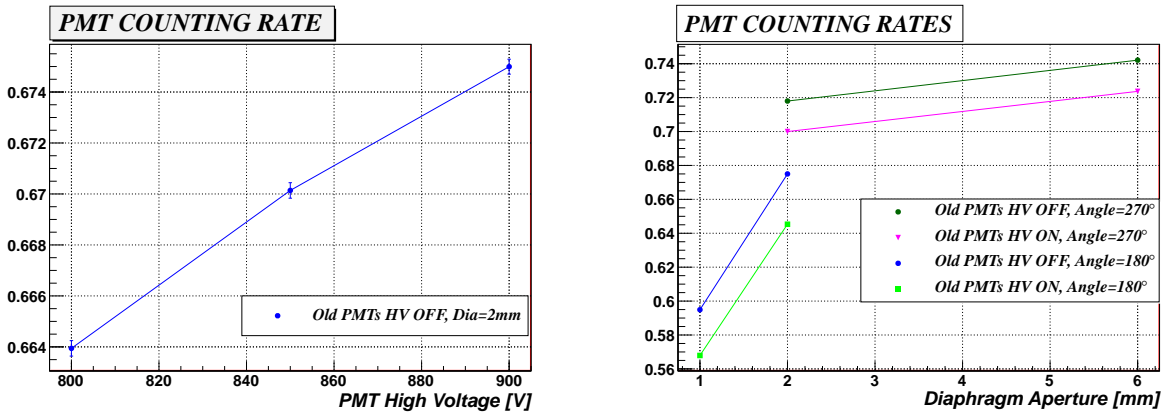
Figure 6.12: Left: new-PMT high voltage scan. Right: new-PMT response dependence on the diaphragm aperture w_D.

---

[5]R7400U-03 Hamamatsu PMTs will be applied for single photon detection as the final configuration of the CEDAR photon detector will be optimized for a light yield of at most 1 photon per PMT.

[6]The trigger signal is the coincidence between upstream and downstream beam scintillators.

The first set of measurements was performed to show how the PMT counting rates are affected by the geometrical acceptance of the assembly in the two orientations (see Fig. 6.11). At a diaphragm aperture of $w_D = 2\,\text{mm}$, the two circle markers in Fig. 6.12 (right panel), representing data acquisitions under the same conditions apart from the prototype orientation, show a 0.04 discrepancy. The second set of measurements was performed because, during the data taking, the counting rate of the three new PMTs was observed to vary depending on whether the seven remaining, standard PMTs were switched on or off. This was discovered to be a consequence of the cross-talk induced by the standard PMTs on new PMTs: the cross-talk interfered destructively with the new-PMT signals resulting in reduced efficiency. The overall result is a shift of 0.02 for the new-PMT counting rate when the standard PMTs are turned off (right plot in Fig. 6.12).

6.3.2 Data/MC comparison of the PMT counting rates

To compare the Cherenkov light spot with the NA62MC predictions, a study of the new-PMT counting rates as a function of the angle of rotation φ of the assembly has been performed.

The measured counting rates for each of the three new PMTs normalised to the number of beam particles are shown in Fig. 6.13. In order to compare these measurements to the MC predictions for a pion beam, they have been scaled by the inverse fraction of pions in the beam ($f_1 = 1/0.7$) and by an empirical factor accounting for the loss of signal due to the standard PMTs being switched on.
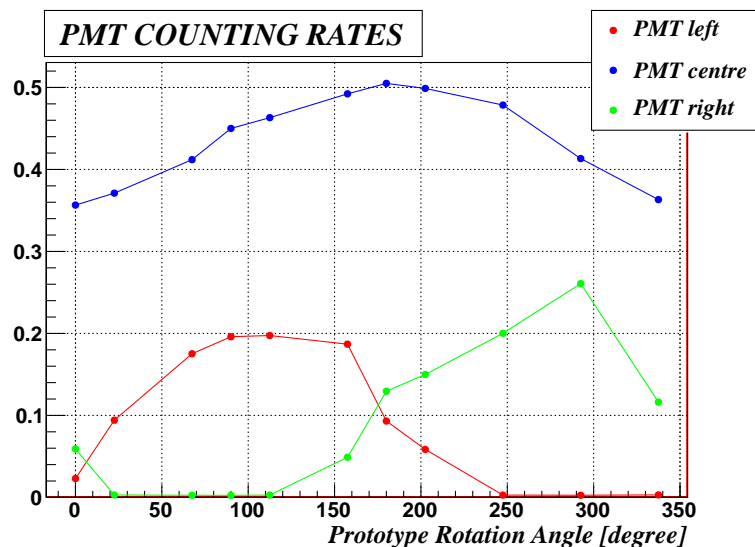
Figure 6.13: New PMTs: study of counting rates vs the orientation of the assembly.

The MC predictions for counting rates per beam pion (ε) vs the prototype rotation angle φ for the central PMT and one of the side PMTs, assuming different reflectivities of the aluminium cones[7], are shown in Fig. 6.14. The corresponding mean numbers of photoelectrons per beam pion, computed as $\lambda = -\ln(1 - \varepsilon)$, as functions of the prototype rotation angle φ are displayed in Fig. 6.15. The MC predictions for the two side PMTs are identical up to a reflection around $\varphi = 180°$, so only one side cone is shown.
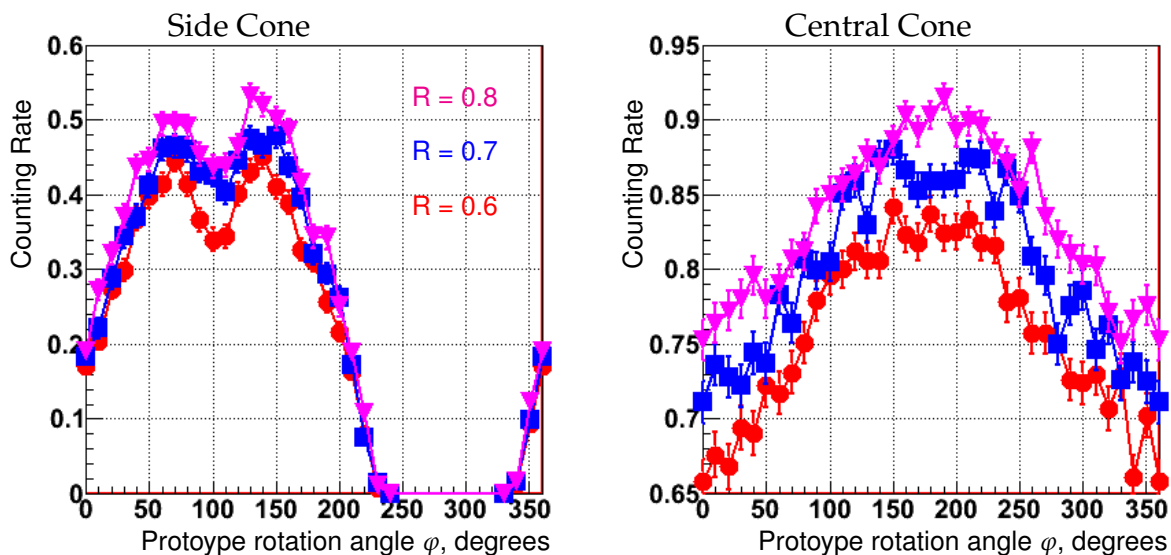
Figure 6.14: MC predictions for counting rates per beam pion, as a function of prototype rotation angle φ for different reflectivites (R) of the aluminium cones.

The data and MC (assuming cone reflectivity of 70%) mean numbers of photoelectrons per beam pion for the central PMT and a side PMT are shown in Fig. 6.16.

The data/MC ratios of the mean numbers of photoelectrons per beam pion for the central and one side PMTs and for three considered values of cone reflectivity $(0.6, 0.7, 0.8)$ are displayed in Fig. 6.17.

In conclusion, we observe a $\sim$ 30% Cherenkov photon deficit in the test beam data with respect to the NA62MC predictions. A part of this deficit can be explained by electronics thresholds, which are not currently simulated, the other part is being investigated. The ratio of data and MC figures for mean numbers of photoelectrons is approximately constant as the prototype is rotated, suggesting that the shape of the central part of the light spot is well simulated. In the side cones, the ratio varies with rotation angle, suggesting that edges of the light spot are less well simulated.

---

[7]The new-PMT assembly layout is equipped with polished aluminium cones (Fig. 6.10).
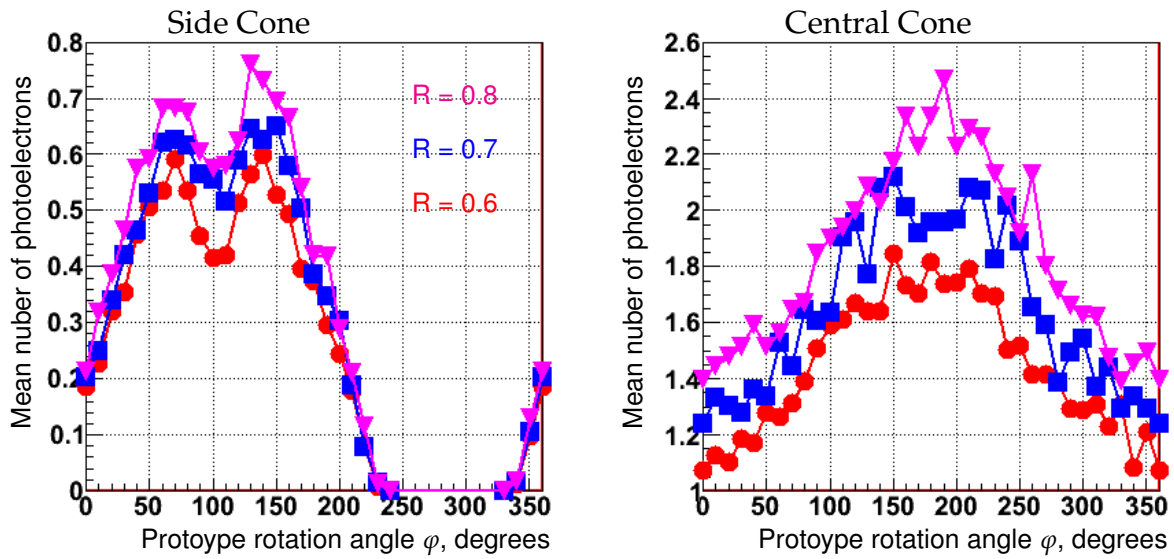
Figure 6.15: MC predictions for mean number of photoelectrons per beam pion, as a function of prototype rotation angle φ for different reflectivites (R) of the aluminium cones.
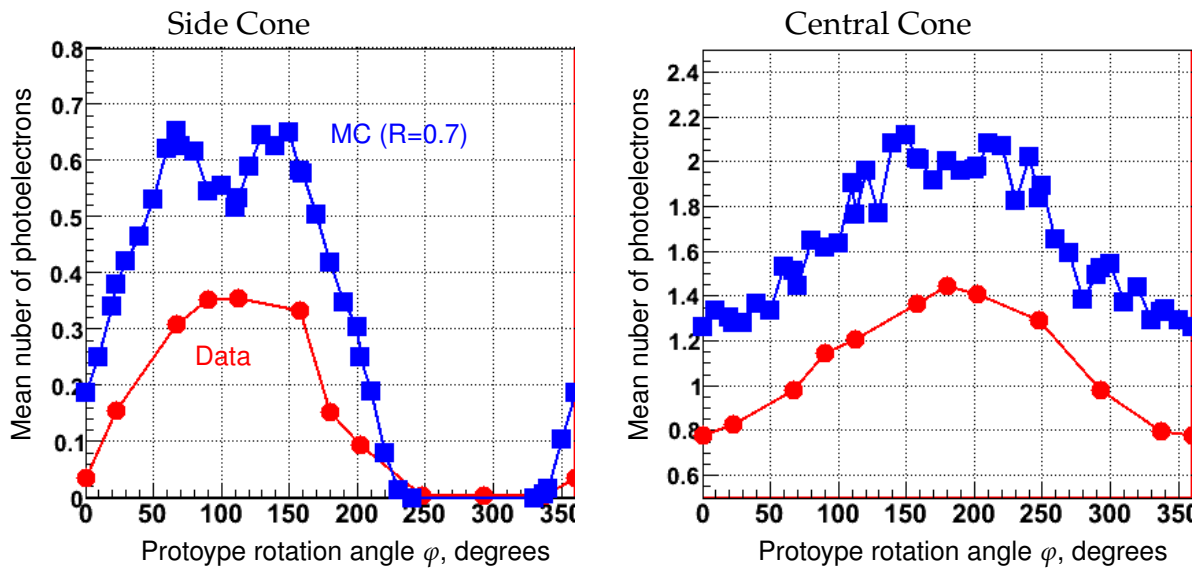
Figure 6.16: Data and MC comparison for mean numbers of photoelectrons per beam pion (assuming cone reflectivity of 0.7).
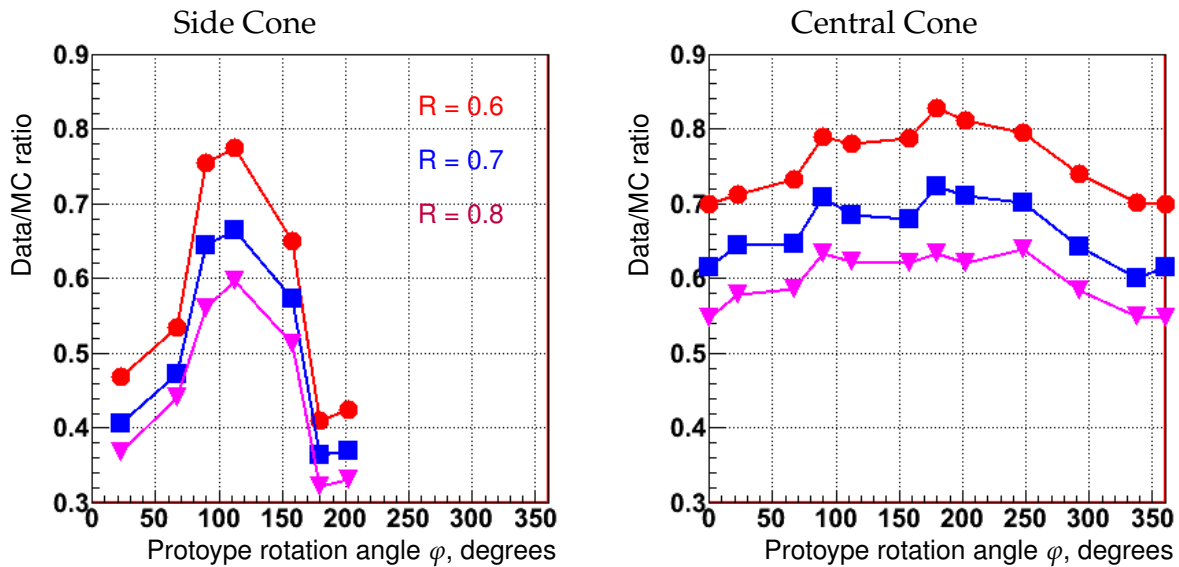
Figure 6.17: Data/MC ratios for mean numbers of photoelectrons per beam pion, as a function of prototype rotation angle φ for different reflectivites (R) of the aluminium cones.
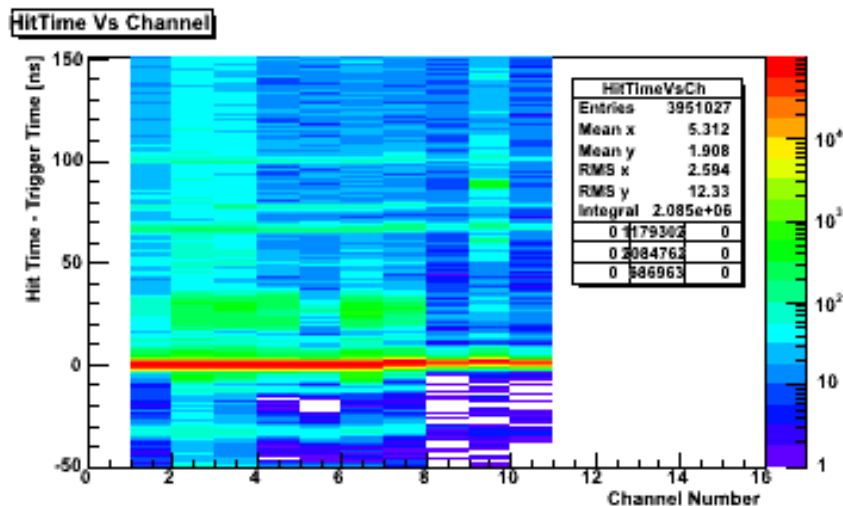
Figure 6.18: Signal time distributions with respect to the trigger time: standard PMTs in channels $1 - 7$ and new PMTs in channels $8 - 10$.

6.3.3 PMT Time Resolution

The time resolution of the new PMTs was measured. The plot in Fig. 6.18 shows that all the times of PMT signals were aligned with the trigger time. The width of the time distributions is dominated by the time resolution of the beam scintillators used for the trigger signal. To correct for the time-slewing induced by the amplitude

165

fluctuations, the correlation between the leading time and the time width (trailing edge - leading edge of the PMT signal pulse) is fitted and the result is used to correct the pulse leading times. The effect of the time slewing corrections was small with respect to the contribution of the beam scintillators.

Entries	244804
Mean	-0.092
RMS	0.4302
Underflow	41
Overflow	28
Integral	2.447e+05
χ^2 / ndf	228 / 7
Constant	3.461e+04 $\pm$ 1.011e+02
Mean	-0.091 $\pm$ 0.001
Sigma	0.2549 $\pm$ 0.0007
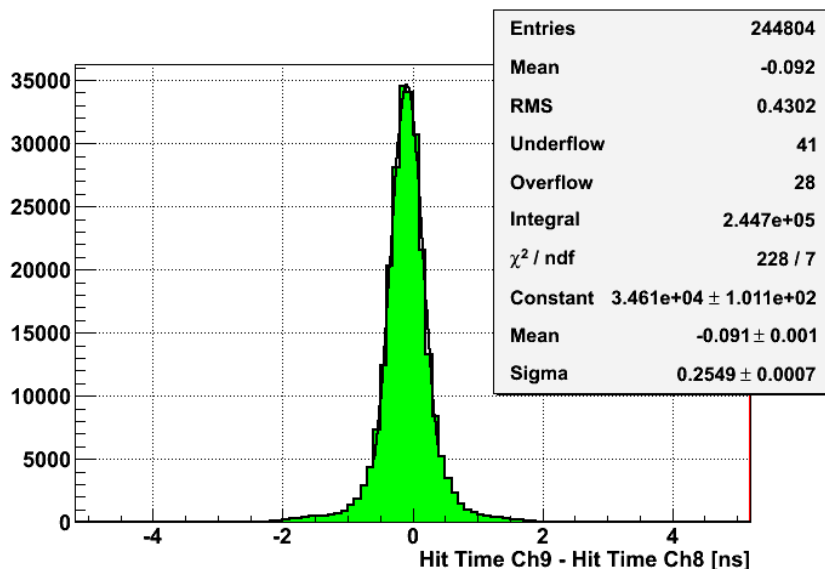
Figure 6.19: Time difference of new PMTs in channels 8 and 9. Solid line corresponds to a gaussian fit of the core of the distribution.

The PMT time resolution is measured by using the time difference between two PMTs; a preliminary value of $\sigma_{T1-T2}(T) = 255\,\mathrm{ps}$ is obtained with a gaussian fit of the core of the distribution after applying the time slewing corrections (Fig. 6.19). The PMT time resolution, $\sigma_{PMT}(T)$, is proportional to the Full Width at Half Maximum (FWHM) of the time distribution in Fig. 6.19 according to the formula $\sigma_{PMT}(T) = \frac{2.35 \times \sigma_{T1-T2}(T)}{\sqrt{2}}$. In Tab. 6.4, the values obtained for new PMTs with the data collected during the test beam are compared with those measured in a previous test beam in 2006 for the same photodetector technology.

	2006	2011 (Ch9 - Ch8)	2011 (Ch9 - Ch10)
$\sigma_{T1-T2}(T)$	325 ps	255 ps	251 ps
$\sigma_{PMT}(T)$	541 ps	424 ps	418 ps

Table 6.4: Width of time distributions for the differences between new-PMT channels $\sigma_{T1-T2}(T)$ and PMT time resolutions $\sigma_{PMT}(T)$ measured during two CEDAR test beams, in 2006 and 2011, using the same PMTs.

All the results achieved in 2011 are better than the ones obtained in 2006. The PMT time resolution ($\sigma_{PMT}(T)$) measurements, second row in Tab. 6.4, are affected by the time resolution of the coincidence signal from the beam scintillators (expected to be $\sim$350 ps). The contribution from the beam scintillators is embedded into the results of $\sigma_{PMT}(T)$ and can only be eliminated when performing the time difference between two PMTs, which carry the same contribution from the beam scintillators. For this reason, the time differences between two new-PMT channels ($\sigma_{T1-T2}(T)$), first row in Tab. 6.4, are the results to be compared with the time resolution of HAMAMATSU R7400-U03 PMT as measured by the NA62 RICH working group ($\sigma_{T,\gamma} \approx 300$ ps) [95]. The results are compatible within the errors.

6.3.4 Front-End Comparison
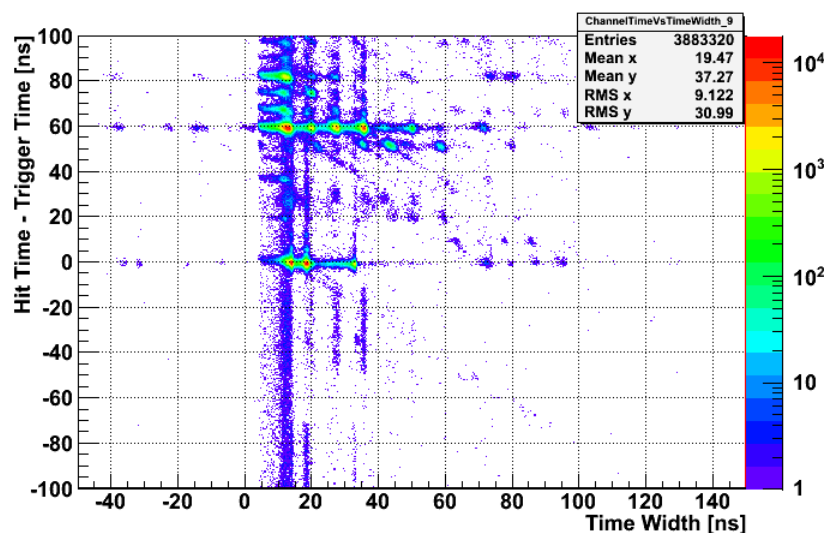
Figure 6.20: Signal time vs time width (trailing - leading) distributions for one new PMT.

The output signal of new PMTs was also cabled to the custom rad-hard preamplifier board (mentioned in Sec. 6.2) proposed as a front-end system to withstand the radiation level at CEDAR. This option gave different results with respect to the other front-end system (Florence's) as it was provided with a higher signal amplification factor. Fig. 6.20 shows the signal time distribution, with respect to the trigger time, for one new PMT versus its time width (time difference between trailing and leading edges). The double time structure, in time with the trigger and appearing for time

widths of about 15 ns and 20 ns, is most likely due to re-firings of the NINO ASIC board. The multiple time structures, delayed with respect to the trigger of about 60-80 ns, are understood to be produced by the cross-talk effect induced by the standard PMTs when they were switched on.
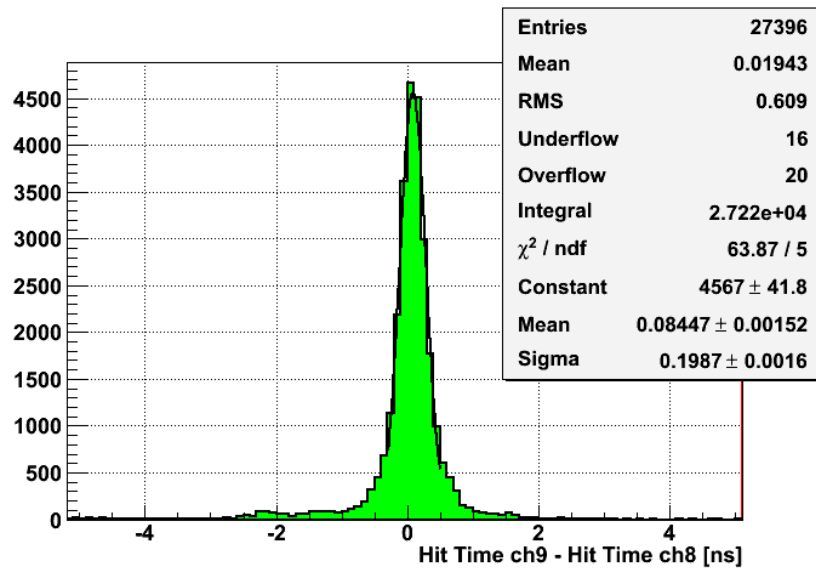
Figure 6.21: Time difference of new PMTs in channels 8 and 9 with the rad-hard front-end option. Solid line is the Gaussian fit of the central part of the distribution.

The time resolution of new PMTs is measured, again, by using the time difference between two PMTs; a preliminary value of $\sigma_{T1-T2}(T) = 199$ ps is obtained with a gaussian fit of the core of the distribution after applying the time slewing corrections (Fig. 6.21). The PMT time resolution achieved with the rad-hard preamplifier board, $\sigma_{PMT}(T) = 330$ ps, is better compared with the ones reported in Tab. 6.4. This means that the signal amplitude fluctuations are smaller than those observed with the "Florence's" pre-amplifier, which in turns implies that the PMT output signal is more amplified by this front-end option and its amplitude is bigger than the one expected in single photoelectron regime. However, the presence of NINO re-firings, probably induced by noise along the signal path, was difficult to be kept under control; it almost doubled the rate on the readout system. As a consequence, this front-end option is unsuitable for future applications in the high rate environment of NA62.

6.3.5 Additional measurements

Some additional measurements were taken to look for any effects which might be dependent on the beam intensity. A pressure scan was performed over the full range with a beam particle rate of 120 kHz instead of the original 40 kHz. The results in Fig. 6.22 show no significant deviation from those obtained at lower intensity. Nevertheless, this higher rate is still a long way below the future expected one at CEDAR and so rate dependent effects could still appear at higher intensities.
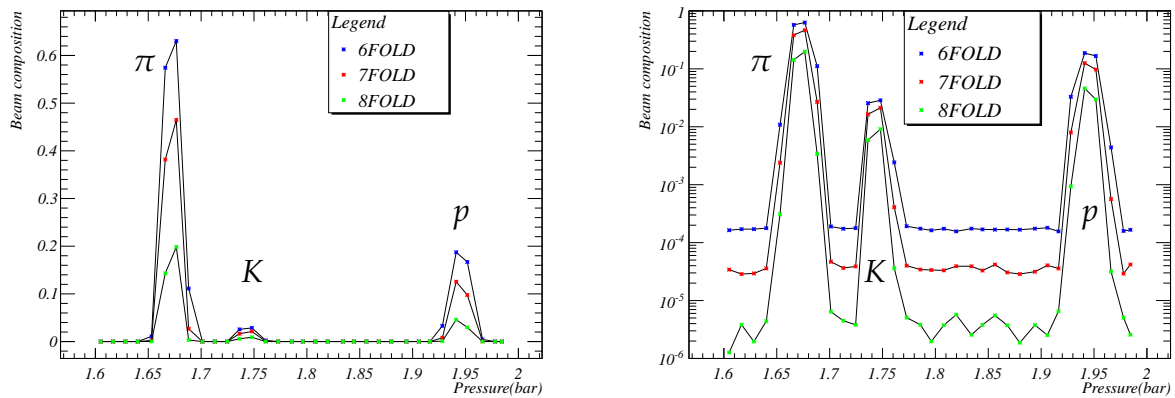
Figure 6.22: Pressure scan over the full range of gas pressures.

6.4 Conclusions

The commissioning of the CEDAR detector for NA62 has been successfully completed during a test beam in October 2011. Several pressure scans confirmed the counter ability to distinguish between kaons and pions.

Hamamatsu PMTs (R7400-U03), mounted in a three-PMTs assembly with light collection cones, designed and built in Liverpool, have been tested. Their counting efficiency includes geometrical acceptance effects and is affected by cross-talk induced by the standard CEDAR PMTs. Their time resolution is measured and found to be compatible with what expected from previous applications of the same technology, under similar conditions. Moreover, the results achieved for the time resolution are better than those obtained in a previous CEDAR test beam performed in 2006. The new front-end and readout system, designed for use in NA62, was installed and tested. Two different options of preamplifier boards, to be coupled with the NINO ASIC board, were considered:

- Florence's preamplifier: its performances result compatible with those expected from previous applications in the NA62 RICH detector;

- Rad-hard preamplifier: its performances turn out to be better in terms of signal amplification but worse in terms of noise.

An important outcome of the test was to acknowledge the possibility of a direct differential coupling between the PMT output signal and the NINO ASIC board, with no intermediate amplification stage. This alternative solution most certainly helps in reducing the NINO re-firings, as less noise is introduced in the signal electronics path, but there are some implications that must be taken into account:

1. the modification of the standard (lemo) Hamamatsu PMT output signal;

2. the stability of the differential coupling;

3. the amount of SER spectrum which is cut away by the NINO threshold.

The first two points are minor implications as the modifications proposed for the standard CEDAR, to cope with the NA62 working requirements, already foresee the replacement of the Hamamatsu high voltage divider with a custom PCB. This is currently under development and test, thus easy to be re-adapted. The third point is quite important and delicate; it might work out as a show-stopper in case it is understood to cause a worsening of the overall efficiency. Since then, tests at CERN have been devoted to address and investigate on this issue. At the time of the thesis submission we are aware that the direct coupling between PMT and NINO board is feasible and compatible with the expected CEDAR performances. The production of PMT high voltage divider PCBs with differential output has already started. However, the underlying study made at CERN is not reported in here as I was not directly involved in it.

Conclusions

A comprehensive study of the process $K^+ \to e^+ \nu_e \gamma$ (SD$^+$) is being performed with a partial (40%) data sample collected by the NA62 collaboration at CERN in 2007. A signal acceptance of 6.2% is achieved and the sample comprises 9,835 candidates with a background contamination of 2.3% mainly due to the $K^+ \to \pi^0 e^+ \nu_e$ and $K^+ \to \pi^+ \pi^0$ decay channels. A χ^2 fit has been performed to the measured x spectrum using the distribution expected from χPT models. The estimated form factors with their uncertainties are reported:

$$V_0 = 0.0946 \pm 0.0018_{stat} \pm 0.0170_{syst}$$
$$\lambda = 0.521 \pm 0.055_{stat} \pm 0.052_{syst},$$

with a statistical correlation between parameters of -0.94 and $\sim 100\%$ correlation between systematic errors. The result receives a significant contribution from the systematic uncertainty, mainly due to the background subtraction; the statistical uncertainty benefits from the large number of candidates, a factor of ~ 8 larger than the one analysed by the KLOE collaboration, whose results are the current world PDG average. At the time of submission the systematic error is dominating and the combined (statistical + systematic) result has a precision comparable to that achieved by KLOE.

The Cherenkov detector to be used in the near-future NA62 research programme for the charged kaon identification is required to achieve a kaon tagging efficiency of at least 95% with a time resolution of at least 100 ps. A Monte-Carlo simulation has been developed to study the optimal configuration for the Cherenkov photo-detector. A solution with a new optical system and light collection cones is found to be feasible while ensuring the detector performances needed. The Cherenkov detector commissioning has been successfully completed during a test beam in October 2011. Several pressure scans confirmed the counter ability to distinguish between kaons and pions.

Hamamatsu PMTs (R7400-U03) have been tested; their counting efficiency and time resolution have been measured and found to be compatible with what expected from previous applications of the same technology, under similar conditions.

171

The new front-end and readout system, designed for use in NA62, was installed and tested. An important outcome of the test was to acknowledge the possibility of a direct differential coupling between the PMT output signal and the NINO ASIC board, with no intermediate amplification stage.

Bibliography

[1] C. Lazzeroni *et al.*, Phys. Lett. **B698**, 105 (2011).

[2] S. Weinberg, Phys. Rev. Lett. **19**, 1264 (1967).

[3] S. Weinberg, *Physica* **A96**, 327 (1979).

[4] J. Bijnens, C. Ecker and J. Gasser, Nucl. Phys. **B396**, 81 (1993).

[5] J. Bijnens and U. Meissner, [arXiv:hep-ph/9901381].

[6] J. Gasser, Nucl. Phys. **B86**, 257-266 (2000).

[7] J. Gasser and H. Leutwyler, Ann. Phys. **158**, 142 (1984).

[8] C. Q. Geng and S. K. Lee, Phys. Rev. **D51**, 99 (1995).

[9] C. H. Chen, C. Q. Geng and C. C. Lih, Phys. Rev. **D77**, 014004 (2008).

[10] J. T. Goldman and W. J. Wilson, Phys. Rev. **D15**, 709 (1977).

[11] D. A. Bryman *et al.*, Phys. Rept. **88**, 151 (1982).

[12] M. Gell-Mann and F. Low, Phys. Rev. **84**, 350 (1951).

[13] C. Q. Geng, I. L. Ho and T. H. Wu, Nucl. Phys. **B684**, 281 (2004).

[14] F. Halzen, A. D. Martin, in *Quarks & Lepton: An introductory Course in Modern Particle Physics*, pag 102-103, John Wiley & Sons (1984).

[15] J. Bijnens, G. Colangelo, G. Ecker and J. Gasser [arXiv:hep-ph/9411311], in L. Maiani, G. Pancheri and N. Paver (Eds.) *The Second Daphne Physics Handbook*, Laboratori Nazionali di Frascati (1995).

[16] J. Beringer *et al.* [Particle Data Group], PR **D86**, 010001 (2012) *(http://pdg.lbl.gov)*.

[17] O. Strandberg [arXiv:hep-ph/0302064].

[18] C. Ametler *et al.*, Phys. Lett. **B303**, 140 (1993).

[19] V. Cirigliano *et al.*, *Kaon Decays in the Standard Model*, [arXiv:1107.6001v2] (2011).

[20] C. Gatti, *Monte Carlo simulation for radiative kaon decays*, [arXiv:hep-ph/0507280] (2005).

[21] F. Ambrosino *et al.*, Eur. Phys. J. **C64**, 627 (2009).

[22] K. S. Heard, *et al.*, Phys. Lett. **B55**, 324 (1975).

[23] J. Heintze, *et al.*, Nucl. Phys. **B149**, 365 (1979).

[24] S. C. Adler *et al.*, Phys. Rev. Lett. **85**, 2256 (2000).

[25] A. A. Poblaguev *et al.*, Phys. Rev. Lett. **89**, 061803 (2002).

[26] O. Tchikilev *et al.*, [arXiv:1001.0374] (2010).

[27] V. A. Duk *et al.*, Phys. Lett. **B695**, 59 (2011).

[28] G. D'Ambrosio, G. Isidori, Phys. Lett. **B530**, 108-116 (2002).

[29] J. Brod, M. Gorbahn, and E. Stamou, Phys. Rev. **D83**, 034030 (2011).

[30] G. Buchalla and A. J. Buras, Phys. Rev. **D54** 6782-6789 (1996).

[31] N. Cabibbo, Phys. Rev. Lett. **10**, 531 (1963).

[32] M. Kobayashi, T. Maskawa, Prog. Theor. Phys. **49**, 652 (1973).

[33] L. Wolfenstein, Phys. Rev. Lett. **51**, 1945 (1983).

[34] A. Ceccucci, Z. Ligeti and Y. Sakai, *The CKM quark-mixing matrix*, **PDG**(2012).

[35] F. Ambrosino *et al.*, Phys. Lett. **B632**, 76 (2006) [hep-ex/0509045].

[36] E. Blucher and W. J. Marciano, $V_u d$, $V_u s$, *the Cabibbo Angle and CKM Unitarity*, **PDG**(2012).

[37] Heavy Flavor Averaging Group, updates for Rare Decays, *http://www.slac.stanford.edu/xorg/hfag/rare/index.html*.

[38] A. J. Buras *et al.*, Phys. Rev. Lett. **95**, 261805 (2005) [hep-ph/0508165].

[39] M. Misiak *et al.*, Phys. Rev. Lett. **98**, 022002 (2007) [hep-ph/0609232].

[40] R. Aaij *et al.* [LHCb Collab.], arXiv:1203.4493; S. Chatrchyan *et al.* [CMS Collab.], arXiv:1203.3976; G. Aad *et al.* [ATLAS Collab.], arXiv:1204.0735.

[41] A. Abulencia *et al.*, Phys. Rev. Lett. **97**, 242003 (2006) [hep-ex/0609040].

[42] Aaij *et al.*, Phys. Lett. **B709**, 177 (2012) [arXiv:1112.4311].

[43] M. Battaglia *et al.*, *The CKM matrix and the unitarity triangle* [hep-ph/0304132].

[44] G. Isidori, "Invited talk at the Workshop on the CKM Unitarity Triangle", IPPP Durham, (2003) [hep-ph/0307014v2].

[45] M. Misiak and J. Urban, Phys. Lett. **B451** 161(1999) [hep-ph/9901278].

[46] G. Buchalla and A. J. Buras, Nucl. Phys. **B548** 309 (1999) [hep-ph/9901288].

[47] A. J. Buras, M. Gorbahn, U. Haisch and U. Nierste, Phys. Rev. Lett. **95**, 261805 (2005) [hep-ph/0508165].

[48] G. Isidori *et al.*, Nucl. Phys. **B718** 319 (2005).

[49] G. Buchalla and A. J. Buras, Nucl. Phys. **B412** 106 (1994).

[50] G. Buchalla and A. J. Buras, Nucl. Phys. **B398** 285 (1993); **400** 225 (1993).

[51] F. Mescia and C. Smith, Phys. Rev. **D76**, 034017 (2007).

[52] U. Camerini, *et al.*, Phys. Rev. Lett. **23**, 326 (1969).

[53] G. D. Cable *et al.*, Phys. Rev. D **8**, 3807 (1973).

[54] Y. Asano *et al.*, Phys. Lett. B **107**, 159 (1981).

[55] S. Adler *et al.*, Phys. Rev. Lett. 88, 041803 (2002).

[56] S. Adler *et al.*, Phys. Rev. Lett. 79, 2204 (1997).

[57] V. V. Anisimovsky et al., Phys. Rev. Lett. **93**, 031801 (2004).

[58] A. V. Artamonov *et al.*, Phys. Rev. D **79**, 092004 (2009).

[59] Y. Grossman and Y. Nir, Phys. Lett. B **398**, 163 (1997).

[60] A. Alavi-Harati *et al.*, Phys. Rev. D **61**, 072006 (2000).

[61] J. K. Ahn *et al.*, Phys. Rev. D **81**, 072004 (2010).

[62] J. Comfort *et al.*, *Proposal for $K_L^0 \to \pi^0 \nu \bar{\nu}$ Experiment at J-Parc*, J-PARC Proposal 14 (2006).

[63] G. Anelli *et al.*, *Proposal to measure the rare decay $K^+ \to \pi^+ \nu \bar{\nu}$ at the CERN SPS*, CERN-SPSC-2005-013, SPSC-P-326 (2005).

[64] V. Fanti *et al.*, Nucl. Instrum. Methods A **574**, 433 (2007).

[65] R. Batley *et al.*, Eur. Phys. J. C **52**, 875 (2007).

[66] D. Bédérède *et al.*, Nucl. Instrum. Meth. A **367**, 88 (1995).

[67] C. Biino *et al.*, *COmPACT 7.3 User's Guide* (2007).

[68] G. Barr *et al.*, Nucl. Instrum. Meth. A **370**, 413 (1996).

[69] V. Fanti *et al.*, *Proposal for a Precision Measurement of ϵ'/ϵ in CP violating $K^0 \to 2\pi$ decays* CERN-SPSC-90-22 (1990).

[70] M. De Beer, *NASIM User's Guide*, NA48 internal note, NA48-00-23 (2000).

[71] R. Brun *et al.*, *Detector Description and Simulation Tool* (1993).

[72] E. Goudzovski, [http://goudzovs.web.cern.ch/goudzovs/ke2/mc.html].

[73] M. Piccini, *"NA62 Analysis Meeting"* (25-10-2007).

[74] B. Bloch-Devaux, *"NA62 Analysis Meeting"* (08-02-2007/13-12-2007).

[75] E. Goudzovski, *"NA62 Analysis Meeting"* (17-07-2008).

[76] E. Goudzovski, *"NA62 Analysis Meeting"* (28-02-2009).

[77] G. Lamanna, *"Search for Direct CP violation in charged Kaons with NA48/2 experiment"* (PhD thesis - 2006).

[78] B. Bloch-Devaux, *"NA48 Internal Note 05-05"* (24-11-2005).

[79] E. Goudzovski, *"NA62 Analysis Meeting"* (12-02-2009).

[80] H. A. Bethe, Phys. Rev. **89**, 1256-1266 (1953).

[81] A. Winhart, *"NA62 Analysis Meeting"* (12-02-2009).

[82] S. Balev, *"NA62 Analysis Meeting"* (29-05-2008).

[83] A. Ceccucci *et al.*, *NA62 Status Report to the CERN SPSC*, CERN-SPSC-2012-2011, SPSC-M-778 (2012).

[84] A. Ceccucci *et al.*, *NA62/P-326 Status Report*, CERN-SPSC-2007-035 SPSC-M-760 (2007).

[85] G. Ruggiero, *"NA62 Physics Working Group"*, NA62 Collaboration Meeting, (07-09-2011).

[86] H. W. Atherton *et al.*, *Precise Measurements of Particle Production by 400 GeV/c Protons on Beryllium Targets*, CERN Yellow Report: CERN 80-07 (1980).

[87] E. Cortina *et al.*, *NA62: Technical design document*, NA62-10-07, CERN, (2010).

[88] B. Angelucci *et al.*, *Pion-Muon separation with a RICH prototype for the NA62 experiment*, Nucl. Instrum. Meth. A **621**, pp. 205-211 (2010).

[89] K. Ahmet *et al.*, Nucl. Instrum. Meth. A bf 305, 275 (1991).

[90] G. S. Atoian *et al.*, Nucl. Instrum. Meth. A **531**, 467 (2004).

[91] Sozzi, M. *A concept for the NA62 Trigger and Data Acquisition*. NA62 Note 07-03 (2007).

[92] [http://ttc.web.cern.ch/TTC/intro.html], *TTC: Timing, Trigger and Control Systems for LHC Detectors*.

[93] C. Bovet *et al.*, *The CEDAR Counters for Particle Identification in the SPS Secondary Beams*, CERN Report: CERN 82-13 (1982).

[94] S. O. Flyckt, C. Marmonier, *Photomultiplier Tubes: Principles and Applications* Photonis, Re-edited (2002).

[95] G. Anzivino *et al.*, *Construction and Test of a RICH Prototype for the NA62 experiment*, (2008), [doi:10.1016/j.nima.2008.05.029].

[96] HAMAMATSU PHOTONICS K. K., **314-5**, Shimokanzo, Toyooka-village, Iwata-gun, Shizuoka-ken, **438-0193**, Japan (*www.hamamatsu.com*).

[97] F. Anghinolfi, P. Jarron, A. N. Martemiyanov, E. Usenko, H. Wenninger, M. C. S. Williams and A. Zichichi, *NINO: an ultrafast low-power front-end amplifier/discriminator ASIC designed for the multigap resistive plate chamber*, Nucl. Instrum. Meth. A **533**, 183-187 (2004).

[98] C. Lazzeroni, D. J. Munday, N. K. Watson, N. H. Brook, H. F. Heath, D. Britton, J. B. Dainton and J. R. Fry, *Search for a new physics in kaon rare decays with the NA62 experiment at CERN* (2009).

[99] J. Christiansen *et al.*, *HPTDC High Performance Time to Digital Converter* User Manual v2.2 (2004), *Digital Microelectronics Group*, CERN.

[100] E. Pedreschi, M. Sozzi, F. Spinella, *From TELL1 to TEL62* NA62 Note 10-06, October 6 (2010).

[101] ALICE Collaboration, *Time of flight system, technical design report*. Technical Report ALICE TDR 8, CERN, LHCC/2000-12.

[102] G. Haefeli, A. Bay, A. Gong, H. Gong, M. Muecke, N. Neufeld, O. Schneider, *The LHCb DAQ interface board TELL1*, Nucl. Instrum. Meth. A **560**, 494 - 502 (2006).

[103] B. Hallgren, *CEDAR Readout using the LHCb TELL1 and 1GHz ADC Mezzanine Board*, NA48 Note 05-02, May 9 (2005).

[104] HAMAMATSU, User's Data Sheet, *Metal Package Photomultiplier Tube R7400U Series*, Hamamatsu Photonics K.K. (2001) "http://www.hamamatsu.com".

[105] *NA62MC*, [http://sergiant.web.cern.ch/sergiant/NA62FW/html/index.html].

Appendix A

The chiral theoretical framework

χPT is an effective quantum field theory (EQFT): in a given energy range few degrees of freedom are set and relevant, while the remaining ones, which describe the more general theory, can be integrated out. Below the scale of chiral symmetry breaking the dynamics of strong interactions cannot be treated in terms of partonic degrees of freedom. However, at this low-energy scale, the hadronic spectrum only comprises the octet of light pseudoscalar mesons (K, π, η) and those are assumed as the new degrees of freedom which allows the QCD to be treated in a perturbative way. In χPT this assumption relies on the smallness of the pseudoscalar meson constituent quark masses ($m_{u,d,s} << \Lambda_\chi$) compared with the typical hadronic scale; this implies that the quark mass terms, originally responsible for the chiral symmetry breaking, can be treated as small perturbations.

A.0.1 Effective chiral lagrangians

The effective chiral lagrangian at *leading order* can be written as [7]:

$$L_2 = \frac{F^2}{4} Tr(D_\mu U D^\mu U^\dagger + \chi U^\dagger + U \chi^\dagger) \tag{A.0}$$

The elements entering the lagrangian are:

1. A unitarity 3×3 matrix U incorporating the octet of pseudoscalar Goldstone boson fields:

$U = e^{i\sqrt{(2)}\phi/F}$, with $\phi = \frac{1}{\sqrt{2}} \sum_i \lambda_i \phi^i = \begin{bmatrix} \frac{\pi^0}{\sqrt{2}} + \frac{\eta_8}{\sqrt{6}} & \pi^+ & K^+ \\ \pi^- & -\frac{\pi^0}{\sqrt{2}} + \frac{\eta_8}{\sqrt{6}} & K^0 \\ K^- & \bar{K}^0 & -\frac{2\eta_8}{\sqrt{6}} \end{bmatrix}$,

where η_8 is the octet component of the η meson;

2. the external fields([1]) v, a, s, p (Hermitian 3×3 matrices in flavour space) introduced to parameterise the quark mass breaking terms in the fundamental QCD lagrangian:

$$L_{QCD}(v, a, s, p) = L_{QCD}^0 + \bar{\psi}\gamma^\mu(v_\mu + a_\mu\gamma_5)\psi - \bar{\psi}(s - ip\gamma_5)\psi \qquad \text{(A.0)}$$

where L_{QCD}^0 is the QCD lagrangian with all quark masses set to zero.

3. The derivative operator $D_\mu : D_\mu U = \partial_\mu U - ir_\mu U + iUl_\mu$;

4. The external gauge fields of SM describing electromagnetic and semi-leptonic interactions:

$$r_\mu = v_\mu + a_\mu = -eQA_\mu,$$
$$l_\mu = v_\mu - a_\mu = -eQA_\mu - \frac{e}{\sqrt{(2)}sin\theta_W}(W_\mu^+ T_+ + h.c.)$$

with $Q = \frac{1}{3}diag(2, -1, -1)$ and $T_+ = \begin{bmatrix} 0 & V_{ud} & V_{us} \\ 0 & 0 & 0 \\ 0 & 0 & 0 \end{bmatrix}$,

where V_{ij} are Kobayashi-Maskawa matrix elements;

5. The scalar and pseudoscalar external fields: $\chi = 2B(s + ip)$;

6. The external parameters F and B, which are the only free constants at $\mathcal{O}(p^2)$. The former is related to the pion decay constant: $< 0|\bar{\psi}\gamma^\mu\gamma_5\psi|\pi^+(p) >= i\sqrt{2}F_\pi p^\mu$. F_π is experimentally known from the width of the process $\pi^+ \to \mu^+\nu_\mu$, which gives $F_\pi = 92.4$ MeV. The latter is related to the quark condensate $< 0|\bar{\psi}\psi|0 >$. It is not directly linked to any physical observable but one can assign constraints to the product $B \times m_q$ by means of experimental data.

The generating functional is given by the classical action $Z_2 = \int d^4x L_2(U, v, a, s, p)$ and is invariant under local $SU(3)_L \times SU(3)_R$ transformations. The *leading-order* effective chiral lagrangian L_2 is of order $\mathcal{O}(p^2)$. It is invariant under chiral symmetry and it is completely determined by chiral symmetry except for those two couplings.

Amplitudes at *next-to-leading-order* L_4 include several contributions:

- one-loop diagrams generated by the *leading* order lagrangian L_2;

- a local action at $\mathcal{O}(p^4)$ generated by the effective chiral lagrangian L_4 at the tree level;

---

[1]The vector, axial-vector, scalar and pseudoscalar fields.

- an additional term taking into account the chiral anomaly;

The one-loop graphs contributing at $\mathcal{O}(p^4)$ are ultraviolet divergent and need to be renormalised. The loop contributions are of order $\mathcal{O}(p^2)$ and are not dependent on the scale of the renormalisation; the loop function only involves internal, external momenta and the masses of pions and kaons. The lagrangian of order p^4, in the case of three light flavours, is the following [7]:

$$
\begin{aligned}
L_4 ={}& l_1 Tr(D_\mu U^\dagger D^\mu U)^2 + l_2 Tr(D_\mu U^\dagger D_\nu U) Tr(D^\mu U^\dagger D^\nu U) \\
&+ l_3 Tr(D_\mu U^\dagger D^\mu U D_\nu U^\dagger D^\nu U) + l_4 Tr(D_\mu U^\dagger D^\mu U) Tr(\chi^\dagger U + \chi U^\dagger) \\
&+ l_5 Tr(D_\mu U^\dagger D^\mu U(\chi^\dagger U + U^\dagger \chi)) + l_6 Tr(\chi^\dagger U + \chi U^\dagger)^2 + l_7 Tr(\chi^\dagger U - \chi U^\dagger)^2 \\
&+ l_8 Tr(\chi^\dagger U \chi^\dagger U + \chi U^\dagger \chi U^\dagger) - i l_9 Tr(F_R^{\mu\nu} D_\mu U D_\nu U^\dagger + F_L^{\mu\nu} D_\mu U^\dagger D_\nu U) \\
&+ l_{10} Tr(U^\dagger F_R^{\mu\nu} U F_{L\mu\nu}) + l_{11} Tr(F_{R\mu\nu} F_R^{\mu\nu} + F_{L\mu\nu} F_L^{\mu\nu}) + l_{12} Tr(\chi^\dagger \chi),
\end{aligned}
\tag{A.1}
$$

where

$$
\begin{aligned}
F_R^{\mu\nu} &= \partial^\mu r^\nu - \partial^\nu r^\mu - i[r^\mu, r^\nu], \\
F_L^{\mu\nu} &= \partial^\mu l^\nu - \partial^\nu l^\mu - i[l^\mu, l^\nu].
\end{aligned}
$$

This effective chiral Lagrangian L^4 is invariant under $SU(3)_L \times SU(3)_R$ local symmetry. The low-energy constants l_i are not constrained by chiral symmetry; they have been evaluated by comparing with experimental low-energy information. They are all divergent (expect l_3 and l_7) and the ones necessary to address radiative semi-leptonic decays are l_4, l_5, l_9, l_{10} [4]. The latter absorb the divergences of the one-loop graphs and produce an expansion of amplitudes in terms of renormalised and finite couplings. The knowledge of LECs $F, B, l_1, \ldots, l_{10}$ allows for a complete description of the low-energy behaviour of pseudoscalar meson interactions at $\mathcal{O}(p^4)$. The couplings l_{11} and l_{12} are the so-called "contact terms", which contain only the external fields and are not directly accessible by experiment. The chiral anomaly is due to the vacuum transition amplitude which appears not to be invariant under the same chiral symmetry, but on the vector symmetry only. The contributions from this anomaly to the expansion of amplitudes in χPT at $\mathcal{O}(p^4)$ are expressed by a generating functional constructed by Wess and Zumino and consequently represented by Witten [?,?]. This functional must be added into the *next-to-leading-order* calculations to take into account all anomalous contributions to electromagnetic and semi-leptonic weak meson decays. At *next-to-next-to-leading* order the terms contributing into the effective chiral lagrangian are:

- two-loop diagrams generated by the *leading-order* lagrangian L_2;

- one-loop diagrams generated by the *next-to-leading-order* lagrangian L_4;

- a local action at $\mathcal{O}(p^6)$ generated by the effective chiral lagrangian L_6 at the tree level;

- corrections to the Weiss-Zumino-Witten functional for the chiral anomaly.

The number of LECs is significantly increased (~ 100) at $\mathcal{O}(p^6)$ but not all of them are relevant to the same decay channel. Many of them are well determined with low-energy phenomenology and the χPT still offers a tool to precisely compute a wide range of leptonic and semi-leptonic interactions.

Appendix B

Average number of photo-electrons

The derivation can be found in the CEDAR Yellow Paper but is included here for reference. Assuming that the number of photoelectrons detected by a photomultiplier follows a Poisson distribution with a mean number ϕ per event, the probability of detecting n photo-electrons is given by:

$$P(n) = \frac{\phi^n}{n!} e^{-\phi} \tag{B.1}$$

The probability of missing an event is the probability of detecting no photo-electrons:

$$P(0) = e^{-\phi} \tag{B.2}$$

Thus the effiency η of a single photo-multiplier which detects on average ϕ photons is:

$$\eta = 1 - P(0) = 1 - e^{-\phi} \tag{B.3}$$

which is the expression for ϕ found in the text.

The situation of eight photomultipliers looking at the same event can be simplified by assuming equal efficiencies η for each PM. Defining $\varepsilon = 1 - \eta$ as the probability of missing an event, the probabilities of various levels of coincidence between PMTs can be read off from the binomial expansion:

$$(\eta + \varepsilon)^8 = \eta^8 + 8\eta^7\varepsilon + 28\eta^6\varepsilon^2 + 56\eta^5\varepsilon^3 + 70\eta^4\varepsilon^4 + 56\eta^3\varepsilon^6 + 28\eta^2\varepsilon^6 + 8\eta\varepsilon^7 + \varepsilon^8 \tag{B.4}$$

The probabilities of the various coincidence levels 8-fold, 7-fold, 6-fold are:

$$\eta_8 = \eta^8 \tag{B.5}$$

$$\eta_7 = \eta_8 + 8\eta^7\varepsilon \tag{B.6}$$

$$\eta_6 = \eta_7 + 28\eta^6\varepsilon^2 \tag{B.7}$$

$$\dots \tag{B.8}$$

183

Defining $J = \epsilon/\eta = e^{-\phi}/(1 - e^{-\phi})$ and solving for ϕ:

$$\phi = \ln(1 + J) - \ln J \qquad (B.9)$$

the average number of photo-electrons can be deduced from the measured numbers of 6-, 7- and 8-fold coincidences as follows:

$$\frac{\eta_7}{\eta_8} = 1 + 8J \qquad (B.10)$$

From equations B.9 and B.10 we find:

$$\phi = \ln\left(1 + \frac{8}{\eta_7/\eta_8 - 1}\right) \qquad (B.11)$$

With further algebra, a similar result can be found for η_6 and η_8:

$$\phi = \ln\left(1 + \frac{14}{\sqrt{4 - 7(1 - (\eta_6/\eta_8)} - 2}\right) \qquad (B.12)$$

The two equations B.11 and B.12 can be used as a consistency check.